

**Targeting the Bacterial Fatty-Acid Synthesis Pathway:
Towards the Development of Slow-Onset Inhibitors and the
Characterisation of Protein-Protein Interactions**

**Die bakterielle Fettsäurebiosynthese als Zielobjekt zur Entwicklung
langsam bindender Inhibitoren und zur
Charakterisierung von Protein-Protein-Wechselwirkungen**

Doctoral thesis

for a doctoral degree at the Graduate School of Life Sciences,

Julius-Maximilians-Universität Würzburg,

Section Biomedicine

submitted by

Sandra Eltschkner

from Rostock

Würzburg 2017

Submitted on:

Office stamp

Members of the *Promotionskomitee*:

Chairperson: Prof. Dr. Ulrike Holzgrabe

Primary Supervisor: Prof. Dr. Caroline Kisker

Supervisor (Second): Prof. Dr. Christoph Sotriffer

Supervisor (Third): Prof. Dr. Peter Tonge

Supervisor (Fourth): Prof. Dr. Winfried Hinrichs

Date of Public Defence:

Date of Receipt of Certificates:

ZUSAMMENFASSUNG

Seit Beginn der Anwendung antibiotischer Substanzen wie Arsphenaminen, z.B. *Salvarsan*, entwickelt von Paul Ehrlich [1], Sulfonamiden, z.B. *Prontosil*, dessen antibakterielle Wirksamkeit durch Gerhard Domagk nachgewiesen wurde [2], oder des von Alexander Fleming entdeckten Penicillins [3] zur effektiven Bekämpfung von Infektionskrankheiten Anfang des 20. Jahrhunderts findet ein kontinuierliches Wetttrüsten zwischen der Entstehung von Antibiotikaresistenzen in Bakterien und der Entwicklung neuer Antibiotika statt. Vor allem die zügige Entstehung von Resistenzen im Gegensatz zum eher stockenden Fortschritt der Entdeckung neuer Antibiotika stellt ein ernstzunehmendes Risiko für die menschliche Gesundheit dar. Einige stark lebensbedrohliche Infektionskrankheiten, darunter Tuberkulose und Melioidose, erfahren dadurch eine erhöhte Verbreitung. Ein Anstieg der Zahl der Tuberkuloseerkrankungen in Gebieten, in denen die Krankheit bereits als ausgerottet galt, beispielsweise in Europa; oder im Falle der Melioidose, eine Verbreitung in Gebiete, in denen die Krankheitserreger natürlicherweise nicht vorkommen; sind u.a. die Folgen fehlender Wirkstoffe zur Bekämpfung resistenter Stämme. Methicillinresistente *Staphylococcus-aureus*- (MRSA-) Stämme sind hingegen bereits fast weltweit in Krankenhäusern verbreitet und gelten dort als Quelle schwerer Infektionen, die vor allem für Patienten mit geschwächtem Immunsystem eine ernsthafte Bedrohung darstellen. Die mannigfaltigen Vorkommen resistenter Erreger und die eingeschränkten Behandlungsmöglichkeiten dadurch verursachter Infektionen machen die Entwicklung neuer, wirksamer Antibiotika dringend notwendig.

Ein zentraler Stoffwechselweg der Bakterien ist die Fettsäurebiosynthese II, die im Hinblick auf die Herstellung lang- und verzweigtkettiger Fettsäuren sowie von Mykolsäuren essentiell ist. Die Zusammensetzung der Fettsäuren trägt maßgeblich zur Funktionsfähigkeit der unentbehrlichen Schutzbarriere der Zelle – nämlich der Zellhülle – bei. Eine intakte Zellwand und deren assoziierte Membranen schützen die Zelle vor physikalischem Stress, vor dem Eindringen antibiotischer Substanzen und regulieren die Aufnahme anderer Kleinmoleküle und Ionen. Genau aus diesem Grunde stellt die Fettsäurebiosynthese ein attraktives Ziel für die Entwicklung von Antibiotika dar. Die Enoyl-ACP-Reduktase (ENR), welche den letzten und geschwindigkeitsbestimmenden Schritt des Synthesesyklus katalysiert, wurde als hervorragendes Zielmolekül identifiziert und wird unter anderem von Diphenylethern gehemmt. Diese Verbindungen sind von Triclosan abgeleitet, dessen Bindung an ENR-Enzyme als erstem Vertreter dieser Stoffklasse nachgewiesen werden konnte [4, 5].

Basierend auf dem Diphenylethergrundgerüst von Triclosan wurden Inhibitoren mit unterschiedlichen Substitutionsmustern bezüglich ihrer Bindungseigenschaften an die ENR-Enzyme von *Burkholderia pseudomallei* (bpFabI) und *Mycobacterium tuberculosis* (InhA) untersucht. Kritische Positionen dieses

Grundgerüsten wurden mit verschiedenen, chemischen Gruppen versehen und die Bindung an diese beiden Enzyme anschließend strukturell, kinetisch und am lebenden Organismus charakterisiert. In beiden Fällen üben die Substitutionsmuster einen beträchtlichen Einfluss auf die Assoziations- und Dissoziationsgeschwindigkeiten der verschiedenen Inhibitoren im Rahmen des verlangsamten Zweischrittassoziationsmechanismus aus, welche wiederum die Verweildauer des Inhibitors am Enzym und dessen pharmakokinetische Eigenschaften bestimmen. Die Beschaffenheit der 2'-Substituenten beeinflusst beispielsweise die Stabilität des Grund- sowie des Übergangszustandes im Bindungsgeschehen an bpFabI, wohingegen 4'-Substituenten hauptsächlich zu Stabilitätsänderungen im Übergangszustand beitragen [6]. Die Einführung des Triazolsubstituenten an der 5-Position des Diphenylethergerüsts führt zu einer signifikanten Erhöhung der Energiebarriere des Übergangszustandes im Bindungsprozess an InhA [7], was im Rückschluss zu einer ebenfalls verlangsamten Dissoziation des Enzym-Inhibitor-Komplexes führt. Zusätzlich wird dieser Effekt durch die Beschaffenheit des entsprechenden Substituenten an der 2'-Position noch verstärkt oder abgeschwächt. Dies erfolgt beispielsweise durch eine Stabilisierung des Grundzustandes und eine daraus resultierende, verlängerte Verweildauer des Inhibitors am Enzym.

Weitere, strukturelle Untersuchungen im Rahmen dieser Arbeit konnten den vorgeschlagenen Bindungsmodus [8] des neuartigen, speziell auf das ENR-Enzym von *Staphylococcus aureus* (saFabI) zugeschnittenen Inhibitors „55JS“ (auch „SKTS1“) bestätigen. Dieser Diphenyletherinhibitor besitzt an der 4'-Position einen Pyridonring, welcher die Wechselwirkungen mit dem Enzym verstärken soll. Aus den strukturellen und vorläufigen, kinetischen Daten geht hervor, dass dieser Inhibitor ebenfalls und in ähnlicher Weise an InhA bindet. Außerdem legt ein Vergleich mit Komplexstrukturen verschiedener ENRs in Verbindung mit AFN-1252 [9] die Vermutung nahe, dass auch 55JS an weitere ENR-Homologe binden könnte; denn jener Teil des AFN-1252-Inhibitors, der sich räumlich mit dem Pyridonring von 55JS überlagert, geht mit derselben Region im Protein ähnliche Wechselwirkungen ein. Es ist daher möglich, dass dieser Inhibitor das Potential birgt, durch entsprechende Optimierung als Wirkstoff gegen andere Pathogene zum Einsatz zu gelangen.

Beide dieser neuartigen, funktionellen Gruppen, die Triazol- und die Pyridongruppe, stellen einen guten Ansatzpunkt für die Weiterentwicklung von Diphenylethern bezüglich verbesserter kinetischer Eigenschaften gegenüber ENR-Enzymen dar.

Ein weiterer, interessanter Ansatz für die strukturbasierte Wirkstoffentwicklung ist durch die Interaktionsfläche zwischen ENR-Enzymen und dem Acyl-Carrier-Protein (ACP) gegeben. ACP transportiert die naszierende Acylkette von einem zum nächsten Enzym des dissoziierten Fettsäurebiosynthesezyklus, welche es wahrscheinlich anhand elektrostatischer Interaktionen erkennt. Die Kontaktfläche zwischen saACP und saFabI wurde hier mittels verschiedener Ansätze

untersucht, die sowohl Crosslinking-Experimente als auch die Generierung von Fusionsproteinen umfassten. In den verschiedenen Fusionskonstrukten wurden das ACP- und das ENR-Protein durch eine flexible Aminosäurekette unterschiedlicher Längen und Zusammensetzungen miteinander verbunden. Durch die Crosslinking-Experimente konnten Aminosäuren identifiziert werden, welche einen Teil einer vorgeschlagenen Interaktionsfläche [10] ausmachen und tatsächlich eine hohe Vernetzungseffizienz aufwiesen. Proteinkristalle des Komplexes, die entweder beide Einzelkomponenten oder das Fusionsprotein enthielten, zeigten jedoch nur schwache Beugungsmuster. Diese Beobachtung deckt sich mit der Annahme, dass die Komplexbildung äußerst kurzlebig ist. Die intrinsische Flexibilität beider Proteine erhöht zusätzlich die Schwierigkeit, wohlgeordnete Kristalle zu erhalten. Es wird deshalb notwendig sein, den Komplex in einem fixierten Zustand einzufangen. Die Verwendung eines hochaffinen Substrates, welches die Dissoziation des Komplexes unterbindet, beispielsweise ein acylgekoppelter Inhibitor [11] mit langer Verweildauer am Enzym, könnte hier von großem Nutzen sein und es damit erlauben eine detaillierte Kenntnis der ACP-FabI-Interaktionsfläche zu erhalten, die neue Perspektiven für eine gezielte Entwicklung von Inhibitoren der Fettsäurebiosynthese II eröffnen könnten.

SUMMARY

A continuous arms race between the development of novel antibiotics and the evolution of corresponding resistance mechanisms in bacteria has been observed, since antibiotic agents like arsphenamines (e.g. *Salvarsan*, developed by Paul Ehrlich [1]), sulphonamides (e.g. *Prontosil*, Gerhard Domagk [2]) and penicillin (Alexander Fleming [3]) were first applied to effectively cure bacterial infections in the early 20th century. The rapid emergence of resistances in contrast to the currently lagging discovery of antibiotics displays a severe threat to human health. Some serious infectious diseases, such as tuberculosis or melioidosis, which were either thought to be an issue only in Third-World countries in case of tuberculosis, or regionally restricted with respect to melioidosis, are now on the rise to expand to other areas. In contrast, methicillin-resistant *Staphylococcus aureus* (MRSA) is already present in clinical setups all over the world and causes severe infections in immunocompromised patients. Thus, there is an urgent need for new and effective antimicrobial agents, which impair vital functions of the pathogen's metabolism.

One central metabolic pathway is represented by the bacterial fatty-acid synthesis pathway (FAS II), which is essential for the synthesis of long and branched-chain fatty acids, as well as mycolic acids. These substances play a major role as modulating components of the properties of the most important protective barrier – the cell envelope. The integrity of the bacterial cell wall and the associated membrane(s) is crucial for cell growth and for protection against physical strain, intrusion of antibiotic agents and regulation of uptake of ions and other small molecules. Thus, this central pathway represents a promising target for antibiotic action against pathogens to combat infectious diseases. The last and rate-limiting step is catalysed by the *trans*-2-enoyl-ACP reductase (ENR) FabI or InhA (in mycobacteria), which has been demonstrated to be a valuable target for drug design and can be addressed, amongst others, by diphenyl ether (DPE) compounds, derived from triclosan (TCL) – the first one of this class which was discovered to bind to ENR enzymes [4, 5].

Based on this scaffold, inhibitors containing different combinations of substituents at crucial positions, as well as a novel type of substituent at position five were investigated regarding their binding behaviour towards the *Burkholderia pseudomallei* and *Mycobacterium tuberculosis* ENR enzymes bpFabI and InhA, respectively, by structural, kinetic and *in-vivo* experiments. Generally, substitution patterns modulate the association and dissociation velocities of the different ENR inhibitors in the context of the two-step slow-onset binding mechanism, which is observed for both enzymes. These alterations in the rapidity of complex formation and decomposition have a crucial impact on the residence time of a compound and hence, on the pharmacokinetic properties of potential drug candidates. For example, the substituents at the 2'-position of the DPE scaffold influence the ground-

and transition state stability during the binding process to bpFabI, whereas 4'-substituents primarily alter the transition state [6]. The novel triazole group attached to the 5-position of the scaffold, targeting the hydrophobic part of the substrate-binding pocket in InhA, significantly enhances the energy barrier of the transition state of inhibitor binding [7] and decelerates the association- as well as the dissociation processes. Combinations with different substituents at the 2'-position can enhance or diminish this effect, e.g. by ground-state stabilisation, which will result in an increased residence time of the respective inhibitor on InhA.

Further structural investigations carried out in this work, confirm the proposed binding mode of a customised saFabI inhibitor [8], carrying a pyridone moiety on the DPE scaffold to expand interactions with the protein environment. Structural and preliminary kinetic data confirm the binding of the same inhibitor to InhA in a related fashion. Comparisons with structures of the ENR inhibitor AFN-1252 [9] bound to ENR enzymes from other organisms, addressing a similar region as the pyridone-moiety of the DPE inhibitor, suggest that also the DPE inhibitor bears the potential to display binding to homologues of saFabI and InhA and may be optimised accordingly.

Both of the newly investigated substituents, the pyridone moiety at the 4'-position as well as the 5-triazole substituent, provide a good starting point to modify the DPE scaffold also towards improved kinetic properties against ENR enzymes other than the herein studied and combining both groups on the DPE scaffold may have beneficial effects. The understanding of the underlying binding mechanism is a crucial factor to promote the dedicated design of inhibitors with superior pharmacokinetic characteristics.

A second target for a structure-based drug-design approach is the interaction surface between ENR enzymes and the acyl-carrier protein (ACP), which delivers the growing acyl chain to each distinct enzyme of the dissociated FAS-II system and presumably recognises its respective interaction partner via electrostatic contacts. The interface between saACP and saFabI was investigated using different approaches including crosslinking experiments and the design of fusion constructs connecting the ACP and the FabI subunits via a flexible linker region of varying lengths and compositions. The crosslinking studies confirmed a set of residues to be part of the contact interface of a previously proposed complex model [10] and displayed high crosslinking efficiency of saACP to saFabI when mutated to cysteine residues. However, crystals of the complex obtained from either the single components, or of the fusion constructs usually displayed weak diffraction, which supports the assumption that complex formation is highly transient. To obtain ordered crystals for structural characterisation of the complex it is necessary to trap the complex in a fixed state, e.g. by a high-affinity substrate attached to ACP [11], which abolishes rapid complex dissociation. For this purpose, acyl-coupled long-residence time inhibitors might be a valuable tool to elucidate the detailed architecture of the ACP-FabI interface. This

may provide a novel basis for the development of inhibitors that specifically target the FAS-II biosynthesis pathway.

TABLE OF CONTENTS

1	<i>Introduction</i>	1
1.1	Spread of antibiotic resistances – a global threat to human health	1
1.1.1	Tuberculosis – a third-world issue?.....	1
1.1.2	Melioidosis – a neglected issue.....	3
1.1.3	Methicillin-resistant <i>Staphylococcus aureus</i> (MRSA) – a global issue.....	4
1.2	The bacterial fatty acid synthesis pathway (FAS II) as an attractive drug target	6
1.2.1	Enoyl-acyl-carrier protein (ACP) reductases.....	8
1.2.2	The acyl-carrier protein (ACP) and substrate delivery.....	14
1.2.3	Essentiality in bacteria and implications for ENRs as valid drug targets.....	17
1.3	Drug development and resistance emergence – an everlasting arms race	19
1.3.1	Mechanisms of antibiotic resistance in bacteria.....	19
1.3.2	Examples of drugs targeting the bacterial ENR enzymes.....	22
1.4	Research objective	24
2	<i>Materials and methods</i>	26
2.1	Materials	26
2.1.1	Consumables.....	26
2.1.2	Equipment.....	35
2.1.3	Software.....	38
2.2	Methods	40
2.2.1	Molecular biology.....	40
2.2.2	Protein purification.....	43
2.2.3	Biochemical and biophysical characterisation.....	49
2.2.4	Protein crystallisation.....	54
2.2.5	X-ray crystallography.....	56
3	<i>Results</i>	59
3.1	Purification and crystallisation of InhA	59
3.1.1	Purification of InhA.....	59
3.1.2	Crystallisation of InhA.....	60
3.2	Purification and crystallisation of different FabI enzymes	64
3.2.1	Purification and crystallisation of ecFabI.....	64
3.2.2	Purification and crystallisation of saFabI.....	66

3.3	Purification and modification of different ACP proteins	68
3.3.1	Purification and modification of saACP	68
3.3.2	Purification and modification of ecACP	72
3.4	Investigation of complex formation between the single ACP and FabI components	74
3.4.1	Analytical size-exclusion chromatography (aSEC)	74
3.4.2	Native PAGE analysis	77
3.4.3	Crosslinking of saACP and saFabI cysteine variants	78
3.4.4	Crystallisation of ACP-FabI complexes	81
3.5	Investigation of different ACP-FabI fusion constructs	83
3.5.1	Construct design	83
3.5.2	Cloning and expression of fusion constructs	84
3.5.3	Purification of fusion constructs	85
3.5.4	Thermofluor analysis of selected fusion constructs	90
3.5.5	MALS analysis of selected fusion constructs	92
3.5.6	Modification of fusion constructs	95
3.5.7	Intramolecular crosslinking of Ib_E47C _{ACP} -K17C _{FabI} – an initial attempt	100
3.5.8	Crystallisation of fusion constructs	103
4	<i>Rationalizing the Binding Kinetics for the Inhibition of the Burkholderia pseudomallei FabI Enoyl-ACP Reductase</i>	106
4.1	Abstract	108
4.2	Introduction	108
4.3	Materials and Methods	111
4.3.1	Materials	111
4.3.2	Expression and Purification of bpFabI1	111
4.3.3	Crystallization and Structure Determination of the bpFabI1 Ternary Inhibitor Complexes	111
4.3.4	Synthesis of Diphenyl Ethers	112
4.3.5	Inhibition Kinetics	112
4.3.6	Minimum Inhibitory Concentration (MIC) Determination	113
4.3.7	Evaluation of Efficacy in an Acute B. pseudomallei Mouse Model of Infection	114
4.4	Results	114
4.4.1	Mechanism of Inhibition	116
4.4.2	Structure–Kinetic Analysis of bpFabI1 Inhibition	117
4.4.3	Structural Elements and Key Residues Found in bpFabI1–Inhibitor Ternary Complexes	120
4.4.4	Most Diphenyl Ethers Displayed a Resistance Index against Bp400	125

4.4.5	Selected Diphenyl Ethers Demonstrate in-Vivo Efficacy in an Acute <i>B. pseudomallei</i> Infection Animal Model	126
4.5	Discussion	127
4.6	Associated Content.....	130
4.6.1	Supporting Information.....	130
4.7	Author Information	130
4.7.1	Corresponding Authors	130
4.7.2	Author Contributions	131
4.7.3	Funding.....	131
4.7.4	Notes	131
4.8	Acknowledgements	131
4.9	Supplemental Information	131
4.9.1	Supplemental Tables	131
4.9.2	Supplemental Figures.....	142
4.9.3	Supplemental Experimental Procedures.....	144
5	<i>Structural characterisation of different ENR-inhibitor complexes and implications for future drug design</i>	151
5.1	Binding characteristics of triazole-based DPE compounds to InhA.....	151
5.1.1	Structural comparison of different binding characteristics of PT91, PT119 and members of the PT500 series	152
5.1.2	Impacts of different substitution patterns on the kinetic behaviour of enzyme-inhibitor complexes	158
5.1.3	Comparison of inhibitor- and substrate binding to InhA	159
5.2	A novel type of DPE inhibitor displays binding to saFabI and InhA.....	160
5.3	Implications for future drug design	166
5.3.1	Drug residence time and the importance of pharmacodynamic properties.....	166
5.3.2	Molecular basis of residence-time modulation on enoyl-ACP reductases.....	168
5.3.3	Impact of residence-time optimisation on pharmacokinetics of ENR inhibitors	169
5.4	Lessons learned from the investigation of the ACP-FabI complex	172
5.5	Conclusion.....	175
6	<i>Bibliography</i>	<i>XI</i>
7	<i>Appendix</i>	<i>XXIII</i>

7.1	Abbreviations	XXIII
7.2	Screen compositions	XXV
7.3	Construct list	LIV
7.4	Data collection parameters from additional data sets	LV
7.5	Silver-stained SDS gel prepared from crystals of the fusion construct “lb”	LVI
7.6	Statement of individual author contributions and of legal second publication rights ...	LVII
7.6.1	Statement of individual author contributions to figures/tables/chapters included in the manuscripts	LVIII

1 Introduction

1.1 Spread of antibiotic resistances – a global threat to human health

Since the first application of antibiotics to treat infections in humans, there has been a great emergence of resistances in numerous bacterial species, including pathogens causing severe diseases. In the following, a selection of human pathogens, their spread and the diseases caused by them will be described.

1.1.1 Tuberculosis – a third-world issue?

The World Health Organization's (WHO's) "Global tuberculosis report 2016" [12] estimates show that the tuberculosis (TB) epidemic is larger than previously estimated. Although the numbers of TB incidences and deaths continue to fall globally due to major advances in TB prevention and care, TB remains one of the top-ten causes of death worldwide. There were about 10.4 million new cases (**Figure 1.1-Ia**) and estimated 1.4 million deaths (**Figure 1.1-Ib**) caused by the disease alone in 2015. Alarmingly, there is a rapid emergence of multidrug-resistant TB (MDR-TB) and rifampicin-resistant TB (RR-TB) infections which comprised 480 000 and 100 000 cases, respectively, in the same year. Only six countries (India, Indonesia, China, Nigeria, Pakistan and South Africa) accounted for 60 % of all newly reported incidences.

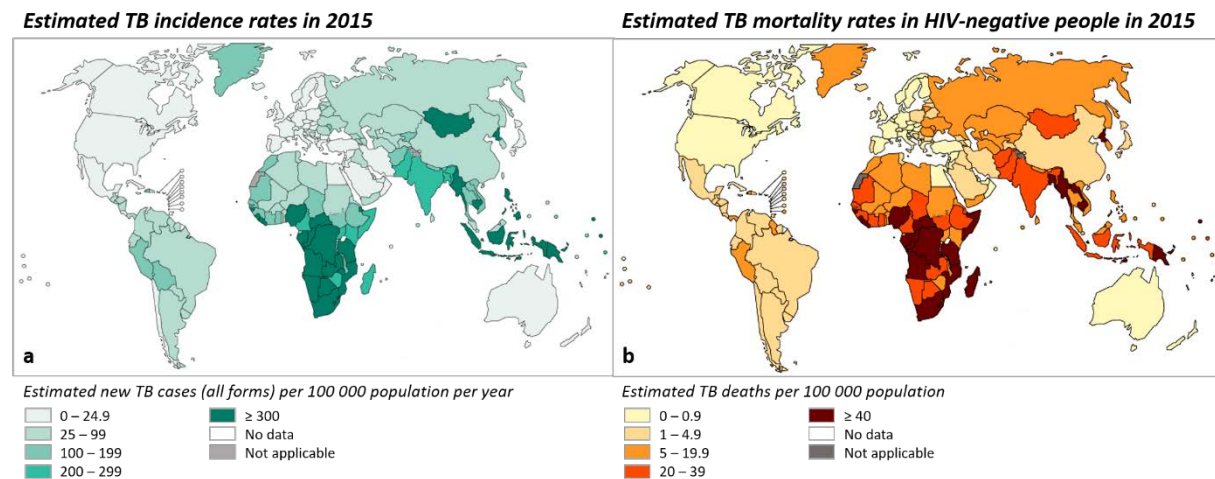


Figure 1.1-I: Global distribution of new TB cases (a) and fatalities (b) in 2015; derived from WHO Global tuberculosis report 2016 [12]

TB is an infectious disease that primarily affects the lungs, but infection of other tissues, such as pleura, lymph nodes or the genitourinary tract, is possible as well. The disease is caused by the pathogen *Mycobacterium tuberculosis* and although several anti-tuberculosis drugs have been available for more

than 50 years [13], TB still remains a major threat to human health. Presumably one third of the world's population carries a latent TB infection, but only 5 – 15 % of the carriers are expected to develop an active TB infection [12]. *M. tuberculosis* is usually transmitted via aerosol by coughing of the infected individual and subsequently being inhaled by other individuals. The pathogen is then incorporated by phagocytic cells in the lungs including macrophages, monocytes, neutrophils and dendritic cells [13]. Mechanisms for manipulation of the host cells allow reproduction of virulent mycobacteria inside these cells and promotes their spread to other cells. After a delayed onset of an adaptive immune response the bacterial growth can be arrested and the pathogen descends into a dormant stage which is referred to as latent TB infection. Reactivation of bacteria from the dormant stage results in progression to an active disease and normally takes place due to a weakened immunity as it is present in e.g. HIV patients [13]. In active TB mycobacteria are shed into respiratory secretions and infection of other individuals is possible.

The rapid emergence of multidrug- and extensively drug-resistant (MDR- and XDR-) TB strains presents a high risk. MDR-TB displays resistance at least to the first-line anti-TB drugs rifampicin (RMP) and isoniazid (INH), whereas in XDR-TB an additional resistance to fluoroquinolones (FQs) and at least one second-line injectable drug is present [14]. Interestingly, all acquired resistances of TB strains which have been reported so far, result from chromosomal mutations that arise under selective pressure imposed by the use of antibiotics [15]. The composition of the mycobacterial cell wall, which is an important determinant of passive resistance of *M. tuberculosis* to antibiotic compounds [15], displays a limiting factor regarding the acquisition of resistances via horizontal gene transfer [16]. Multidrug- and extensive drug resistances remarkably impede TB therapy, since treatment of drug-susceptible TB already requires a 6-month regimen consisting of the four first-line drugs isoniazid, rifampicin, ethambutol and pyrazinamide [12]. While the treatment success rate for TB totals about 83 %, MDR- and XDR-TB treatment successes decrease to 52 % and 28 %, respectively [12]. The recommended treatment alone for MDR-TB is very complicated, including at least pyrazinamide together with four second-line antibiotics, i.e. a fluoroquinolone, one injectable and two bacteriostatic agents [17, 18] for the course of 20 months or longer and requiring daily application [19]. In 2016 standardised short-course regimens lasting 12 months or less were recommended by the WHO for MDR- or RR-TB patients fulfilling special requirements, with RR-TB bearing resistance to rifampicin alone or combined with additional resistances to other drugs, except second-line antibiotics [12]. Although there are some new compounds like bedaquiline and delamanid available, which are active against MDR-TB, resistance mechanisms against these compounds are known [20]. So far, there is very limited experience in XDR-TB treatment both in general and in the use of bedaquiline and delamanid [17, 19]. Therefore, new drugs providing a less toxic, faster and saver regimen are urgently needed.

1.1.2 *Melioidosis – a neglected issue*

Burkholderia pseudomallei is a gram-negative bacterium occurring in muddy water and wet soil of tropical regions. The bacterium is mainly found in environmental water or soil, but is also able to survive in tap water [21] and is the major causative agent for melioidosis, which is prevalent in Singapore, Malaysia, Thailand, Vietnam, India and Northern Australia [22, 23] (**Figure 1.1-II**). Although morbidity and mortality rates have decreased due to better clinical management and advances in diagnostic techniques [22], melioidosis remains a severe threat in these regions. The pathogen's geographical spread is very narrow, but infection has also been detected outside the main endemic region, especially in travellers as well as in U.S. soldiers in Vietnam [24] and thus its global distribution is expanding [23].

Global distribution of melioidosis

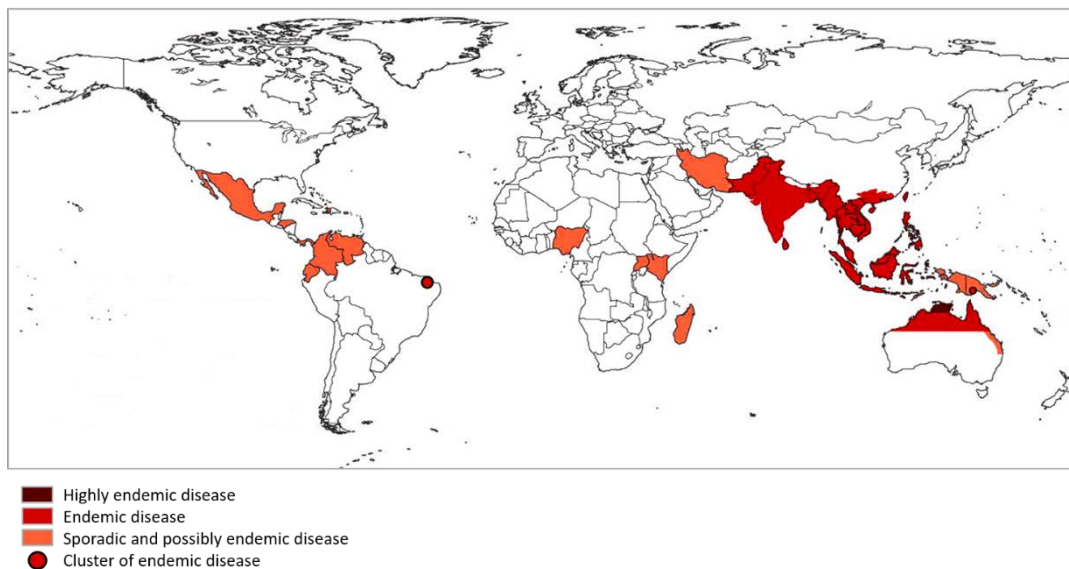


Figure 1.1-II: Global distribution of melioidosis; derived from Wiersinga et al., 2012 [23]

An elevated risk of infection is present in patients with open skin wounds, diabetes, lung disease, immune deficiency or chronic renal disease [22], the most common pre-existing condition being diabetes mellitus in 50 % of infected individuals [25]. A *B. pseudomallei* infection can be acquired through several routes. The most common way is by repeated inhalation during the rainy season [23, 24] when heavy rainfalls create aerosols contaminated with the organism. Another high risk of infections is present in people who are regularly exposed to contaminated soil and water, e.g. rice farmers, leading to cutaneous inoculation via injuries. Ingestion of bacteria through contaminated food or water is possible as well.

The most severe clinical manifestation of the disease is melioidosis septic shock, for which the mortality rates despite adequate treatment reaches about 40 % and the risk of relapse remains high

(4 – 20 %) in surviving patients, since persistence of bacteria within macrophages may progress to chronic infections [22]. Septicemia is often associated with pneumonia, leading to abscess formation and dissemination of bacteria to distant sites [22, 25]. Since the lungs are the most commonly affected organs and chronic lung disease can also occur, in some cases *B. pseudomallei* infection can be hardly distinguished from pulmonary TB.

Referring to *B. pseudomallei* as “the great mimicker” [25] describes the difficulty of identification and treatment of this particular infection. Besides a highly variable genome and the ability to evolve rapidly within the host [23, 26] the pathogen possesses a diversity of virulence mechanisms to escape the innate immune response of affected individuals. These include the manipulation of host-cell processes like DNA and protein synthesis [27], capsule formation preventing recognition of the bacterium by phagocytes [28] and the interference with the production of reactive nitrogen species (RNS) like NO, which play an important role in killing of intracellular bacteria [29]. *B. pseudomallei* is able to invade, survive and proliferate in many cell types, such as epithelial cells and phagocytes. It is also capable of escaping from these cells by either inducing apoptosis or by actin-associated membrane protrusion [30]. The formation of biofilms may also promote long periods of quiescent survival within the host [25]. All these mechanisms can expand the period between the actual exposure to the pathogen and the clinical manifestation of the infection, of which the longest reported time span is 62 years [31].

B. pseudomallei is intrinsically resistant to several antibiotics including most penicillins, first- and second-generation cephalosporins, rifamycins, macrolides and aminoglycosides [24], but is susceptible to chloramphenicol, tetracyclines, ureidopenicillins, third-generation cephalosporins and carbapenems [32]. In acute infections early-onset treatment is critical, since patients might die within hours or days. In any case a long-term antibiotic therapy of 20 weeks, comprising intravenous and oral treatments both with a combination of several different antibiotics, is mandatory for a complete cure and to prevent relapse. Unfortunately, these combination treatments are linked to strong side-effects and despite the multi-drug and long-lasting therapy complications and mortality associated with *B. pseudomallei* infections remain high. Combined therapies of antibiotics together with immunotherapeutic agents have been shown to be a promising alternative to exclusive antibiotic regimens [33, 34]. Although there is ongoing research [35], so far no effective vaccines are available for the protection against *B. pseudomallei* infections [22], which is critical since *B. pseudomallei* is also considered as a potential bioweapon [22-24, 36].

1.1.3 Methicillin-resistant Staphylococcus aureus (MRSA) – a global issue

As a ubiquitous and human commensal bacterium *S. aureus* is able to colonise the anterior nares and other skin areas of healthy individuals. Studies revealed that about 50 % of individuals are persistent

or intermittent nasal *S. aureus* carriers [37]. MRSA has been considered the prototype of multi-resistant nosocomial pathogens for many decades [38]. Due to its versatile arsenal of virulence factors and acquired genes for resistances against several antibiotics over time, MRSA managed to become a widely spread pathogen; not only in hospital setups (hospital-acquired (HA-) MRSA), but also among healthy individuals living in the community (community-acquired (CA-) MRSA). Today MRSA is a major cause of several infections such as skin and soft-tissue infections [39, 40] including abscesses and impetigo, as well as more severe diseases such as necrotising pneumonia [41], bloodstream infections [42], osteomyelitis, endocarditis and toxic shock syndrome [43].

Since the discovery of penicillin in 1928 [44], which represented the first effective antibiotic against *S. aureus*, the pathogen has started an extraordinary adaptation in terms of acquisition of new virulence traits as well as antibiotic resistance determinants, e.g. through exchange of genetic material. After becoming capable of destroying penicillin [45], *S. aureus* developed resistance against the follow-up compound methicillin which was designed to circumvent the effect of staphylococcal penicillinase, only two years after the introduction of methicillin for therapeutic use [46]. However, resistances in MRSA are not restricted to methicillin alone. The presence of the *mecA* gene, encoding PBP2a, an isoform of the methicillin-targeted penicillin-binding proteins (PBPs), renders MRSA unsusceptible to all β -lactam antibiotics, including synthetic penicillins, cephalosporins and carbapenems [38]. Additional resistances to a broad range of different antibiotic classes like fluoroquinolones, lincosamides, tetracyclines, macrolides and aminoglycosides have been reported as well [47, 48]. Even more alarming is the emergence of MRSA with resistance against the last-resort antibiotic vancomycin [49], which might probably have been acquired during an MRSA infection associated with vancomycin-resistant enterococcus (VRE) by plasmid transfer [48]. Thus, individualised dosing schedules as well as alternatives to vancomycin treatment like lipoglycopeptides are being considered [50].

Another risk is the ability of staphylococci to form biofilms, growing on wounds, scar tissue and medical implants such as joint prostheses and heart valves [51] and play a role in the course of many infections. Biofilms are highly resistant to antibiotics, since the cells are in a resting state in which the production of antibiotic target enzymes is down-regulated and the thickness of the cell envelope is increased. Additionally, biofilms serve as a reservoir for persister cells, which display a small subpopulation of cells resistant to antibiotic actions and are responsible for antibiotic tolerance in biofilms [52]. Interestingly, novel diarylquinoline derivatives display bactericidal activity against *S. aureus* biofilms [53], but it might be a matter of time until a resistance mechanism will be employed by *S. aureus* against these compounds as well.

Moreover, MRSA was found to colonise companion animals like pigs. The use of antibiotics to promote animal growth and prevent disease in crowded factories and farms benefits evolution of resistances.

Currently more than 50 % of the available antibiotics are used to promote animal growth [51]. The emergence of zoonotic strains displays a major reservoir of MRSA with the ability to cause human infections [54] and beings capable of inter-human transfer.

As stated by Pantosti et al. in 2007 [48]:

“Staphylococcus aureus can exemplify better than any other human pathogen the adaptive evolution of bacteria in the antibiotic era, as it has demonstrated a unique ability to quickly respond to each new antibiotic with the development of a resistance mechanism, starting with penicillin and methicillin, until the most recent, linezolid and daptomycin.”,

MRSA infections still remain a serious threat to human health, demonstrating the perseverative necessity to continually develop new methods to overcome infections caused by this “sophisticated” organism.

1.2 The bacterial fatty acid synthesis pathway (FAS II) as an attractive drug target

There are two different types of fatty acid (FA) biosynthesis “machineries” present in living organisms (**Figure 1.2-I**). Mostly in eukaryotes, but also in few bacterial species [55], the FA synthesis I (FAS I) pathway comprises one large, multifunctional complex, combining all of the required reaction centres for the production of a FA [56, 57]. The main product from the FAS-I multienzyme complex is usually palmitate [56].

In contrast, preferentially in bacteria, but additionally in specialised eukaryotic organelles like mitochondria and plastids of plants [55], the FAS-II pathway provides a huge variety of products and is capable to produce FAs of different chain lengths, unsaturated FAs (UFAs) and branched-chain FAs (BCFAs). Instead of utilising one single enzyme complex, FAS II consists of distinct enzymes, each of which carries out one single step in the catalytic cycle of FA synthesis. The growing acyl chain is transported by a small, acidic acyl-carrier protein (ACP) to which it is attached via a flexible phosphopantetheine linker. To deliver the substrate for catalysis, ACP transiently interacts with each single enzyme of FAS II. Due to its dissociated character and hence, its high mobility, substrates attached to ACP can be interchanged between different biosynthetic pathways. For example, acyl chains from FAS II can be utilised for polyketide-, lipid-A- and lipoic-acid synthesis [55].

One elongation cycle of FAS II is divided into two modules: the initiation and the elongation module [56]. The first and committed step of the initiation part comprises the conversion of acetyl-coenzyme A (acetyl-CoA) to malonyl-CoA, which is catalysed by the acetyl-CoA carboxylase (ACC). Simultaneously, ACP has to be conveyed from its *apo*-form to activated *holo*-ACP by attaching a 4'-phosphopantetheine prosthetic group from CoA to its designated serine residue (Ser36; *S. aureus* numbering). This step is

carried out by an ACP-synthase (AcpS). The subsequent transfer of the malonyl group from malonyl-CoA to *holo*-ACP is executed by FabD, the malonyl-CoA:ACP transacylase. An initial condensation step is conducted by the β -ketoacyl-ACP synthase III, FabH, transferring acetyl-CoA to malonyl-ACP. In mycobacteria these initial steps are catalysed by the FAS-I system, while further elongation of distinct FA precursors is executed via the FAS-II system (**Chapter 1.2.1.1**). In the following, mycobacterial enzyme denotations of the FAS-II elongation module will be referred to in parentheses.

The following elongation module has a cyclic character and contains four core enzymes (**Figure 1.2-I**). It is repeated several times until the desired acyl-chain length is achieved. In each cycle the acyl chain is elongated by two carbon atoms. β -ketoacyl-ACP (-AcpM) enters the modification cycle starting with a NADPH-dependent reduction step to gain β -hydroxyacyl-ACP, which is catalysed by the β -ketoacyl-ACP reductase FabG (MabA). Afterwards, water is derived from the substrate by a β -hydroxyacyl-ACP dehydratase, either FabA or FabZ (HadAB/BC), resulting in an unsaturated *trans*-2-enoyl-ACP product. The enoyl-ACP reductase FabI (InhA) catalyses the last and rate-limiting step, which is cofactor-dependent (either NADH or NADPH) and yields a saturated acyl ACP. The condensation steps of subsequent elongation cycles are, unlike the initial condensation reaction, carried out by the condensing enzymes FabB or FabF (KasA/B), the β -ketoacyl-ACP synthase I or II, respectively. In contrast to FabH, these enzymes process an acyl and a malonyl chain, which are attached to one ACP each, instead of condensing acetyl-CoA with a malonyl-ACP substrate.

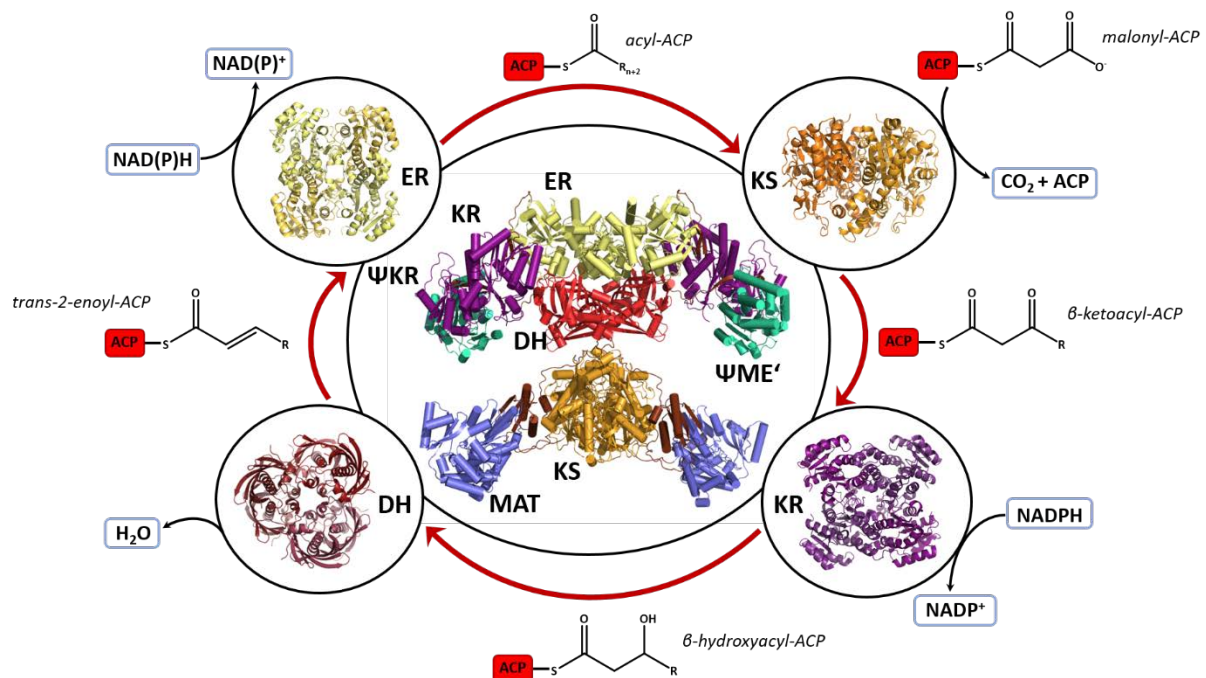


Figure 1.2-I: FAS-I and FAS-II reaction cycles: The FAS-I multienzyme complex is depicted in the inner circle with one set of domains labelled for one monomer or the other assigned with “Ψ”. The corresponding core enzymes of the FAS-II elongation cycle are shown in small circles surrounding the centre and are coloured according to the homologous domains of FAS I. KS: β -ketoacyl synthase, KR: β -ketoreductase, DH: dehydratase, ER: enoyl reductase.

1.2.1 Enoyl-acyl-carrier protein (ACP) reductases

The classical enoyl-ACP reductases (ENRs), referred to as FabI in most species, and InhA in *M. tuberculosis* and other members of the genus mycobacterium, display an essential component in the biosynthesis of FAs. As members of the short-chain dehydrogenase reductase (SDR) superfamily ENRs share a significantly conserved three-dimensional structure, although their sequence homology is relatively low, ranging from 15 – 30 % [58, 59]. A common feature is the central dinucleotide-binding site displaying a Rossmann fold with a central β -sheet composed of seven β -strands surrounded by 3 α -helices on each side. Additionally, ENRs contain a flexible substrate-binding loop (SBL), which may be either opened and disordered or ordered and more closed upon binding of the substrate during the catalytic cycle, shielding the acyl chain from the solvent (**Figure 1.2-II**). In its ordered state the SBL forms two α -helices ($\alpha 6$ and $\alpha 7$) on top of the active site, which is often observed in complexes with slow-binding inhibitors. In addition to their similar tertiary structure, all of these enzymes exist as homotetramers in their biologically active form [56, 60].

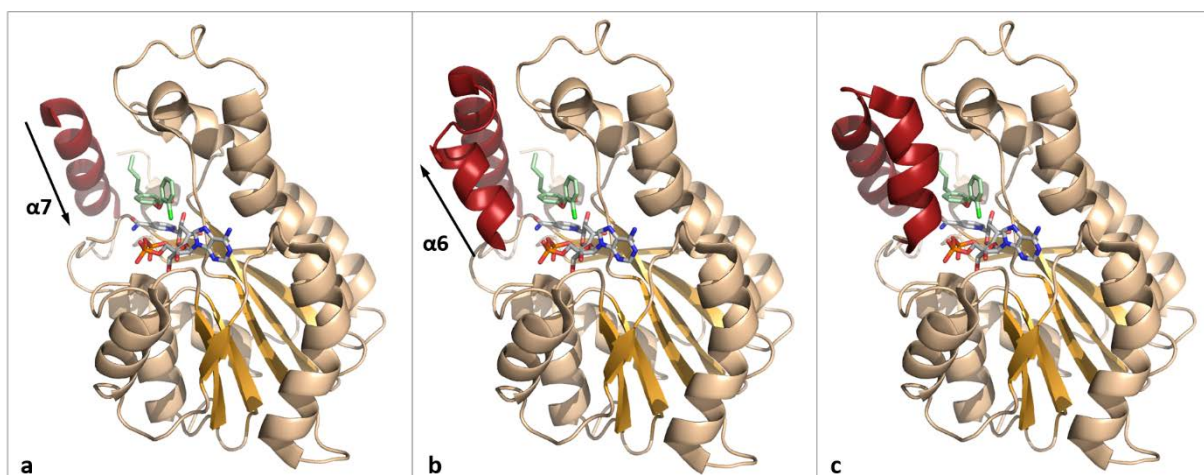


Figure 1.2-II: Three-dimensional structure of an ENR monomer using the example of InhA: The central β -sheet is coloured in light orange, the SBL is shown in red, displaying the disordered (**a**), open (**b**) and closed (**c**) conformation in the presence of the NAD^+ cofactor (grey) and an exemplary inhibitor (green).

ENRs are most commonly NADH or NADPH-dependent enzymes and catalyse the last and rate-limiting step in the elongation cycle of FAs. Within the active site of FabI-type ENRs there is a conserved SDR sequence motif containing **Y-X₆-K** (**Figure 1.2-IV, red diamonds**), in which tyrosine (Y156_{FabI} / Y158_{InhA}) displays the catalytically active proton donor or stabilises the reaction intermediate, and lysine (K163_{FabI} / K165_{InhA}) acts to stabilise cofactor binding through hydrogen-bond formation with the nicotinamide ribose [60, 61]. This sequence motif is part of the catalytic triad **Y/F – Y – K** found in the reductase-type of proteins in the SDR superfamily [62]. The reduction of the *trans*-2-enoyl substrate occurs through stereospecific transfer of the 4S-hydride from the cofactor to C3 of the unsaturated substrate [63]. The negatively charged oxygen at C1 of the enolate-intermediate is probably stabilised

via a hydrogen bond with the side-chain hydroxyl of Y156_{FabI} (Y158_{InhA}), or Y146_{FabI} (F149_{InhA}) [64] as discussed further below, and accepts a proton from the active-site tyrosine, followed by tautomerisation to yield the saturated product [56, 65] (**Figure 1.2-III (1)**). The proton abstracted from the catalytic tyrosine would subsequently be replenished through a proton wire comprising K163_{FabI} (K165_{InhA}), the ribose hydroxyls and a chain of ordered water molecules communicating with the solvent [56]. More recent studies propose that the active-site tyrosine rather functions to stabilise the negatively charged enolate intermediate via hydrogen-bonding interactions and instead, a proton is directly added to C2 from the solvent without a tautomerisation event taking place [10, 61, 66] (**Figure 1.2-III (2)**).

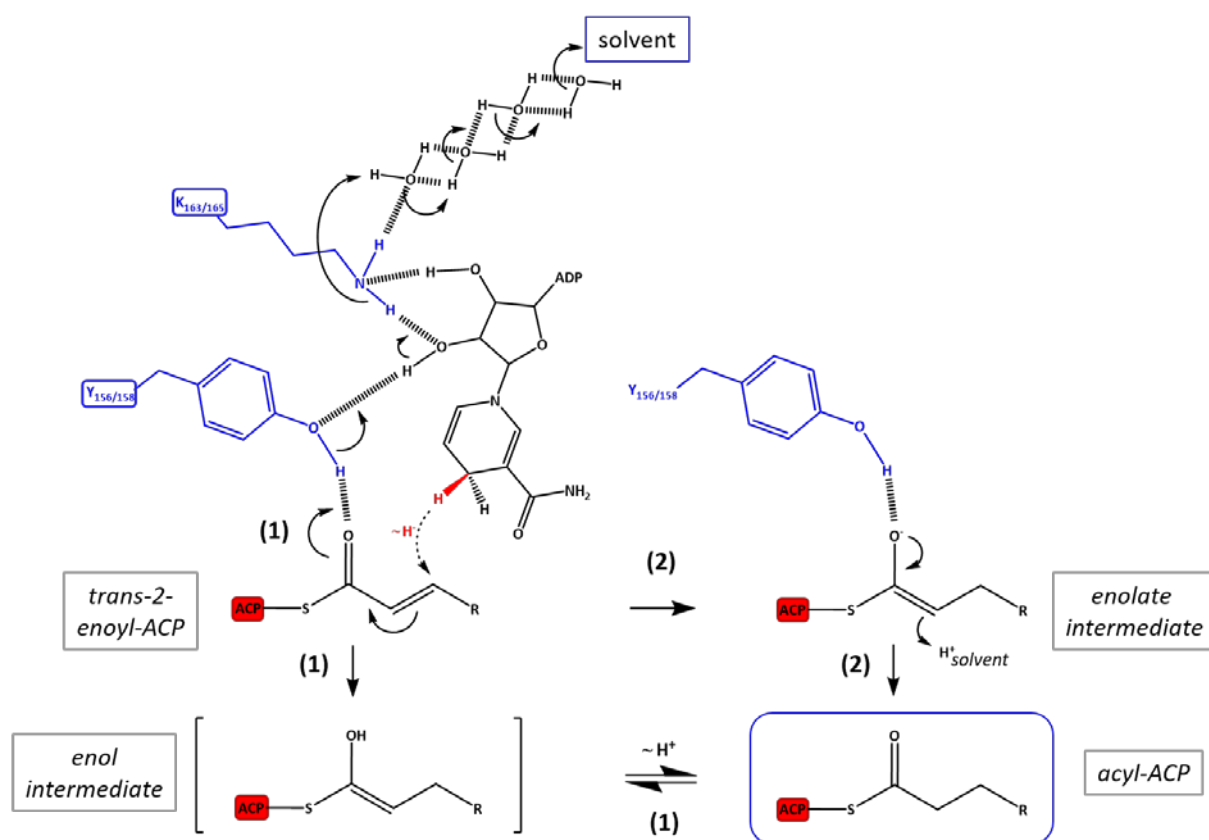


Figure 1.2-III: Proposed ER reaction mechanisms: Following hydride transfer from NAD(P)H, reaction (1) includes protonation of the enolate intermediate by Y156_{FabI}/Y158_{InhA} and a subsequent tautomerisation step; in mechanism (2) protonation occurs at the double bond through direct protonation from the solvent.

Some organisms, however, contain isoenzymes of FabI, either as their sole ENR or in addition to FabI. Known isoenzymes encompass FabK, FabL and FabV [67]. In contrast to FabI enzymes which form tetramers, FabV is present in its monomeric form in solution [68]; and whilst FabI, FabL and FabV, display a typical SDR fold, the architecture of FabK resembles a TIM-barrel structure and requires an FMN cofactor in addition to NADH [60]. In *Streptococcus pneumoniae* FabK is the only ENR present,

Introduction

conferring resistance to triclosan (TCL) and other FabI inhibitors [69], whereas *Bacillus subtilis* contains two ENRs, FabI and FabL [70].

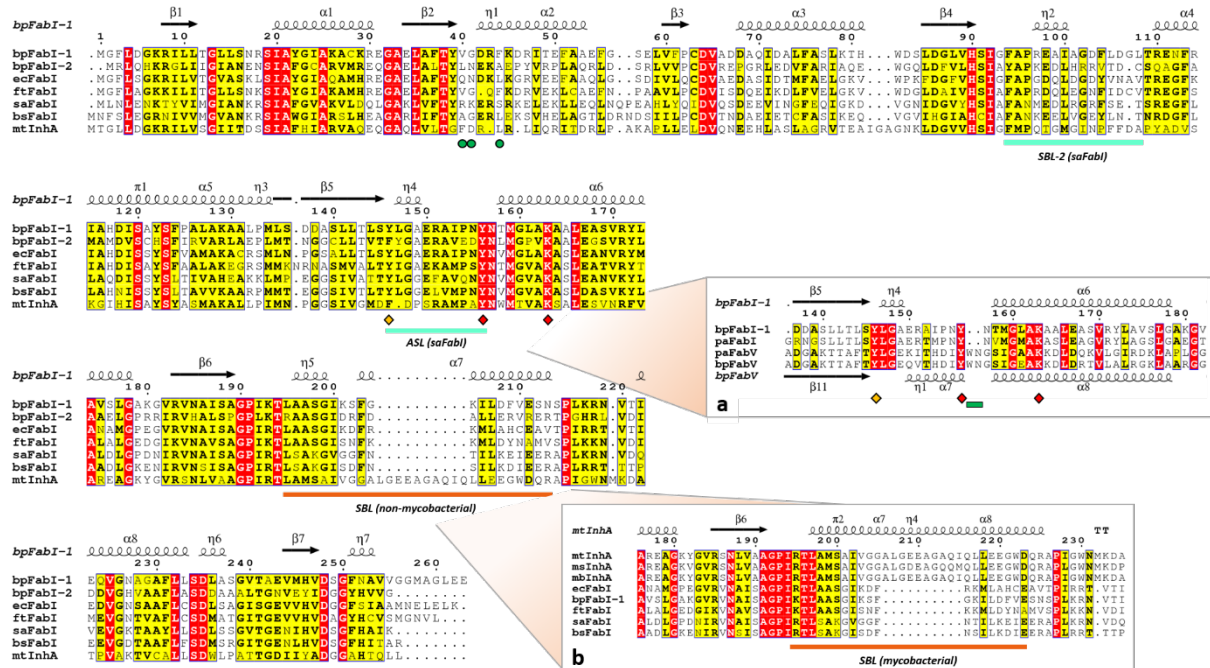


Figure 1.2-IV: Sequence alignment of different ENRs with secondary structures: Secondary structure elements are assigned for the reference structure displayed in the first line; identical residues are highlighted in red, similar residues are depicted in bold, black letters. The SDR catalytic triad is marked by red and orange diamonds; red diamonds refer to the Y-X₈-K motif. The SBL common to all FabI enzymes is underlined with an orange bar; cyan bars correspond to additional flexible loops in saFabI [71]. **Inset a** compares the FabI segment containing the catalytic triad with the corresponding sequence in FabV; the extension within the Y-X₈-K motif is assigned with a green bar. **Inset b** illustrates the insertion of 10 amino acids in the elongated SBL from mycobacteria. Abbreviations: bp: *Burkholderia pseudomallei*, ec: *Escherichia coli*, ft: *Francisella tularensis*, sa: *Staphylococcus aureus*, bs: *Bacillus subtilis*, mt: *Mycobacterium tuberculosis*, ms: *Mycobacterium smegmatis*, mb: *Mycobacterium bovis*, pa: *Pseudomonas aeruginosa*. The figure was prepared with ESPrnt 3.0 [72].

1.2.1.1 Special characteristics of InhA, the ENR of *M. tuberculosis*

InhA, the ENR of *M. tuberculosis*, fulfils a special role in the synthesis of FA derivatives, since it is part of the elongation of FAs required to build up mycolic acids (MAs) as essential components of the mycobacterial cell wall. MAs play a crucial role in the survival of mycobacteria, since the lipid composition of the cell wall determines its fluidity and allows adaptation of the organism to environmental conditions, but it also influences its virulence. Free MAs also promote biofilm formation.

In contrast to many other bacteria, the FAS-II system of *M. tuberculosis* including InhA, is only capable of extending long-chain FAs (C₁₂ – C₁₆), provided by the mycobacterial type-I FAS multienzyme complex, to very long-chain FAs with up to 56 carbon atoms [73-75]. These building blocks are then modified

with functional groups like methoxy or cyclopropane moieties to gain the so-called meromycolic chain. The subsequent condensation step involves the polyketide synthase 13 (PKS13) [76]. Here, one AMP-activated meromycolate is condensed with one carboxyacetyl-CoA, containing the α -branch, a saturated aliphatic FA chain of 24 – 26 carbon atoms [75] ; followed by reduction to form the final MA (**Figure 1.2-V**).

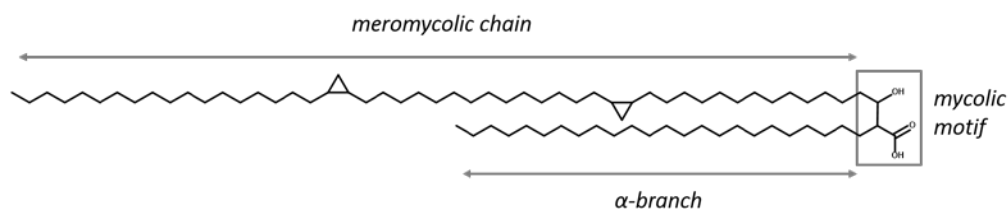


Figure 1.2-V: Architecture of MAs: The meromycolic chain and the α -branch are exemplary, the "mycolic motif" [76] is marked with a frame.

Due to the large substrates InhA has to accommodate, the hydrophobic cavity of its substrate-binding pocket has to be of an appropriate size. This is accounted for by a SBL which is increased in length by about ten amino acids in contrast to its homologous ENRs from other species (**Figure 1.2-IV, inset b**). Additionally, the substrate-binding pocket of InhA possesses high conformational flexibility and is able to assume distinct states with its hydrophobic-pocket residues F149, A198, M199, I202, and V203 [77], as well as Y158, oriented differently with respect to each other, as described by *Merget & Sotriffer* [78]. Also, α -helix 7 residues of the SBL including Q214, I215, L217, L218 and E219 are differently oriented depending on the bound substrate or inhibitor [7]. The high flexibility of the InhA substrate-binding pocket and extended length of the SBL seem to be essential to adjust to and to accommodate long and very long-chain FAs.

1.2.1.2 Diversity of ENRs in *B. pseudomallei*

B. pseudomallei possesses two *fabI* gene homologues, bpFabI-1 and -2, one on each of the two circular chromosomes [79]. Interestingly, only bpFabI-1 was found to display activity against acyl-ACP and acyl-CoA substrates present in the FAS-II biosynthesis pathway, whereas bpFabI-2 did not display any activity in the presence of these substrates and, additionally, was not transcriptionally active [67]. Recent studies clearly demonstrated the essentiality of bpFabI-1 for *in-vivo* growth of *B. pseudomallei*, thus rendering bpFabI-1 a clinically relevant target for the development of ENR inhibitors [80]. A comparison of the primary sequences of the active bpFabI-1 and inactive bpFabI-2 reveals slight disparities and an overall sequence identity of 41.4 % [67]. The most prominent difference is the substitution of the conserved Y146 among bacterial FabI enzymes by F146 as it is present in mycobacterial InhA proteins (**Figure 1.2-IV**). Nevertheless, bpFabI-2 was proven to be an NADH-

dependent enzyme and the substitution at position 146 might alter its specificity towards substrates other than the ones present in the FAS-II pathway, e.g. when adaptation to alternative growth conditions is necessary [67].

Unlike InhA and saFabI, bpFabI-1 is a representative of the “classical” bacterial ENRs with substrate specificity towards short-, medium- and long straight-chain FAs (SCFAs). The SBL of bpFabI-1 is about ten amino acids shorter than that of InhA, consisting of amino acids 195 – 213 (α -helices 6 and 7) similar to other FabI enzymes found in most bacterial species, and in contrast to saFabI it represents the only flexible region in bpFabI-1.

However, *B. pseudomallei* was found to harbour an additional ENR isoform, namely bpFabV, which is well conserved among various clinically relevant organisms such as *Vibrio cholerae*, *Yersinia pestis*, *Pseudomonas aeruginosa* and *Burkholderia* species [68, 81]. Similar to FabI enzymes, FabV belongs to the SDR family, although FabV proteins are significantly larger than FabIs and there is no remarkable sequence homology between both ENR types [81]. The active-site consensus sequence **Y-X₆-K** found in FabI enzymes is extended to **Y-X₈-K** in different FabV proteins [81] (**Figure 1.2-IV, inset a**). The increased size of bpFabV compared to bpFabI is due to an additional insertion between the two halves of the central β -sheet and a C-terminal extension of four α -helices; but notably the central Rossmann fold important for cofactor binding is a common feature of both enzymes. Interestingly, the SBL of bpFabV is covered by a β -hairpin formed by the inserted sequence, together with an N-terminal β -hairpin structure [82].

The presence of FabV might impart resistance to inhibitors targeting FabI enzymes and triclosan was shown to bind with low affinities to *V. cholerae*-, *B. mallei*- and *Y. pestis* FabV [68, 81, 82]. Nevertheless, in *B. pseudomallei* the presence of bpFabV does not seem to be a major determinant for *in-vivo* growth and virulence of the pathogen [80], but so far it is not clear whether bpFabV may function as an emergency response to maintain FA synthesis when bpFabI-1 is inhibited.

1.2.1.3 Special characteristics of saFabI, the ENR of *S. aureus*

The ENR of *S. aureus*, saFabI, harbours some significant differences compared to classical FabI enzymes from organisms like *Escherichia coli*, *Burkholderia pseudomallei* or *Francisella tularensis* [71]. One major difference is the presence of not only one SBL, comprising α -helices 6 and 7, but of two additional flexible regions, termed substrate-binding loop 2 (SBL-2) and active-site loop (ASL) [71]. These flexible regions are in close proximity to the classical SBL, flanking the substrate-binding pocket, and display a high degree of disorder or alternate positions when no cofactor and substrate or inhibitor is bound to the protein. This leads to a widened entrance of the active site compared to ENRs where

only the SBL is disordered prior to cofactor- and substrate-binding. However, although these regions are not disordered in the apo structure, also in ecFabI residues 95 – 115 and 152 – 156, which nearly correlate to the SBL-2 and ASL described in saFabI (residues 94 – 108 and 147 – 157, respectively) [71], were shown to possess enhanced mobility compared to the remaining domains of ecFabI, except the “classical” SBL [64].

SaFabI displays greater similarity to the respective *Bacillus subtilis* protein (bsFabI), which shows a preference for the catalytical conversion of BCFAs. Unlike many other bacteria, both staphylococci and bacilli contain a substantial amount of branched-chain FAs in their cell membrane [83], which is crucial for the regulation of membrane fluidity and their adaptation to changing environmental conditions. Accordingly, the biosynthesis machinery has to provide an enzyme, which can accommodate the more bulky BCFAs, which might explain the presence of the two additional flexible regions in saFabI.

Another interesting feature of saFabI is the altered cofactor specificity towards NADPH together with a positive cooperative binding of the cofactor [84]. Compared to most ENRs from other organisms, this seems to be a rather rare case among FabI enzymes [71, 84, 85]. The preference for NADPH can be explained by alterations in the primary sequence of saFabI, containing an RKXXS-motif that confers this cofactor specificity [71]. The positive charge of R40 and K41 enables binding of the additional phosphate moiety, a hydrogen bond with S44 further stabilises the interaction. Interestingly, any larger side chain at position 44 would clash with the 2'-PO₄ [71].

In contrast to the majority of ENRs, which form a tetramer in solution, saFabI again displays an exception to the rule. In the absence of cofactor and substrate or inhibitor, saFabI was found to be present in its dimeric form [71, 86] similar to observation made for the related FabL protein from *Bacillus cereus* [85]. It is hypothesised that the transition from the dimeric state to the tetrameric form upon cofactor and inhibitor binding is associated with the presence of the two additional flexible regions in saFabI [71], which have also been reported for bcFabL [85]. Binding of cofactor and inhibitor induces the formation of the active site and thus leads to an ordering of the previously disordered ASL and SBL-2. Since these regions are involved in the formation of the tetrameric interface, their ordering is a prerequisite for the establishment of dimer – dimer interactions.

1.2.2 The acyl-carrier protein (ACP) and substrate delivery

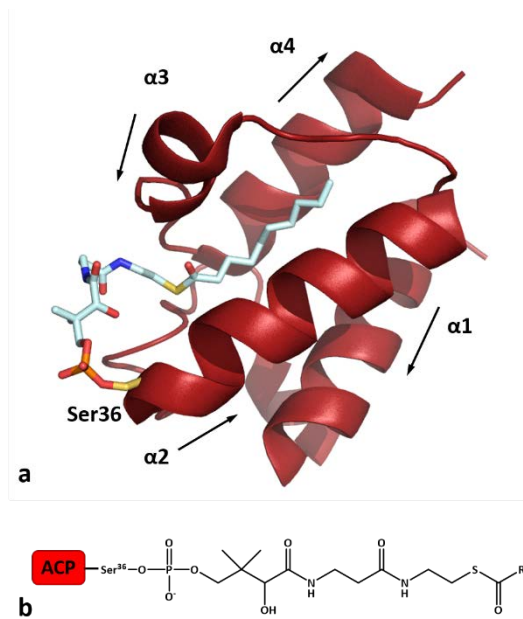


Figure 1.2-VI: (a) Overall structure of ecACP with the phosphopantetheine linker and an acyl chain (pale cyan) attached to Ser36 (yellow) (PDB: 2FAE); (b) Binding mode of the phosphopantetheine linker together with an acyl chain (R) attached via a thioester bond

ACP is one of the most abundant proteins in the cell with a fraction of 0.25 % of the total soluble protein in *E. coli* [56]. Due to its central role in many biosynthetic pathways involving the conversion of acyl intermediates, especially in the FAS and polyketide-synthesis (PKS) pathways, ACP possesses special properties to perform its task. Even at low primary sequence homology the overall tertiary structure of the relatively small (≈ 9 kDa), acidic and exclusively α -helical protein is conserved among many species [55], ranging from bacteria to plants to vertebrates. ACP consists of a four-helix bundle, of which three helices assume an almost parallel arrangement, whereas the shorter α -helix 3 lies almost perpendicular to the other three α -helices (Figure 1.2-VIa). For substrate transport and delivery ACP has to be converted from its *apo*-state into its activated *holo*-form through attachment of a 4'-phosphopantetheine prosthetic group from CoA. The phosphopantetheine arm, to which the acyl intermediates are attached via a thioester bond (Figure 1.2-VIb), is coupled to a specific serine residue located in a strictly conserved D-S-L-motif (Figure 1.2-VII, cyan stars). This motif is part of the C-terminus of α -helix 2; whereas the entire helix is referred to as “recognition helix”, which functions as “universal protein interaction domain” [87, 88]. Overall ACP is considered to be an acidic protein which is especially noteworthy for α -helix 2 that contains a large number of aspartates and glutamates in combination with hydrophobic residues. Amino acids D35, S36, L37, E41 and E47 (*S. aureus* numbering) of this helix are conserved within the ACP-protein family [88] (Figure 1.2-VII). The interconnecting loop between α -helix 2 and α -helix 3, as well as α -helix 3 itself might also participate in the recognition and binding of partner proteins [89, 90].

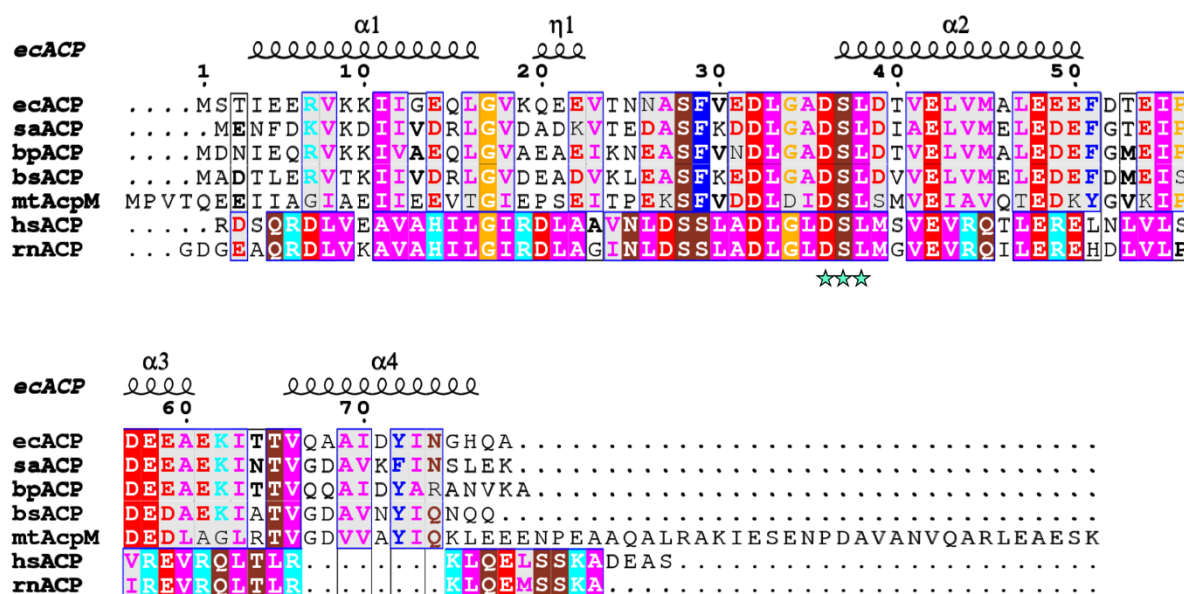


Figure 1.2-VII: Sequence alignment of bacterial and mammalian ACPs containing physicochemical properties and secondary structures: The sequence alignment of ACPs from all depicted organisms was overlaid with the physicochemical property colouring of singly aligned bacterial and mammalian ACPs to highlight differences. Secondary structure elements are assigned for the reference structure displayed in the first line; basic residues are highlighted in cyan, acidic residues in red, polar, non-charged residues in brown, hydrophobic residues in pink (A, V, L, I, M) or in orange (G, P) and aromatic residues in blue. The conserved DSL motif is marked by cyan stars. Abbreviations: bp: *Burkholderia pseudomallei*, ec: *Escherichia coli*, sa: *Staphylococcus aureus*, bs: *Bacillus subtilis*, mt: *Mycobacterium tuberculosis*, hs: *Homo sapiens*, rn: *Rattus norvegicus*. The figure was prepared with ESPript 3.0 [72]. Polar positive (H, K, R) or polar negative (D, E) residues are coloured cyan or red, respectively; polar neutral residues (S, T, N, Q) are depicted in brown, non-polar aliphatic residues (A, V, L, I, M) in pink, non-polar aromatic ones (F, W, Y) in blue, P and G in orange; and C in green. Coloured boxes with white characters represent strict identity, bold characters display similarity in a group and a blue frame indicates similarity across groups.

Since ACP has to deliver its bound substrates to a variety of enzymes, the established protein-protein interactions must have a transient character to avoid tight binding of ACP to one single substrate, which would otherwise slow down or disrupt the FAS II reaction cycle. The individual interaction partners of ACP do not share a defined ACP-binding motif in their primary structure [87, 88]. The ACP – FAS-II protein interaction is rather characterised by electrostatic contacts (salt bridges) between the negatively charged ACP surface and positively charged residues on the interaction partner's surface, which are complemented by additional hydrophobic interactions [64, 87-91]. Another important factor for the functionality of ACP is its highly dynamic nature, which is required to shield the acyl chain from the solvent during transport within the hydrophobic cavity surrounded by the four α -helices [92]. On the other hand, the acyl chain has to be extruded from the interior when it is presented to a partner enzyme. In order to rapidly switch between both conformational states and to accommodate variable lengths of acyl substrate, a high degree of flexibility is essential [55, 93].

Currently, there are two hypotheses of how ACP delivers the acyl chain to FabI, since there are two possibilities for a substrate to enter the active site – either through the minor or the major portal [66]. Experimental evidence from the structure of ecACP in complex with ecFabI, which was assessed by a combination of X-ray data and complementary computational modelling, suggests substrate delivery taking place through the minor portal [64]. In this scenario, the acidic residues D35, D38, E41, E48 of ecACP α -helix 2 interact with the basic residues K201, R204 and K205 on α -helix 7 of the SBL (referred to as “helix α 8” in [64]) in ecFabI (**Figure 1.2-VIII, “ACP 1”**). Additionally, residues of ecFabI α -helix 7 stabilise binding of the phosphopantetheine portion of the ACP substrate. Indeed, kinetic experiments reveal that substitutions of K201, R204 and K205 in ecFabI with either neutral (Ala) or oppositely charged (Glu) amino acids significantly impair catalytic activity towards ACP-coupled substrates [64]. Concerning the orientation of the substrate within the substrate-binding pocket delivered through the minor portal, together with mutational studies, it was also proposed that Y156 was not directly involved in catalysis and instead Y146 was the catalytically active residue. These findings are in stark contrast to the mechanism suggested by *Rozwarski et al.* [66] and *Schiebel et al.* [10]. However, in this first model the spatial arrangement of ACP only permits the binding of two molecules to the FabI tetramer at a time, which seems to be questionable in the light of metabolic efficiency.

A second model based on the analysis of the symmetry contacts, in which the parts of ACP that were resolved in the aforementioned structure are engaged, presumes that a neighbouring, symmetry-related FabI molecule is the actual interaction partner of ACP present in the unit cell [10, 11]. Hence, the relative orientation of ACP and FabI differs from the original model and the substrate would be delivered through the major portal. Here, residues of α -helix 2, the interconnecting loop and the N-terminus of α -helix 3 of ecACP interact with basic residues located on ecFabI α -helix 2 and on a loop between β -strand 1 and α -helix 1, surrounding the major portal. Interestingly, also residues K201, R204 and K205 on α -helix 7 of ecFabI, which were proven to be important for the interaction with ecACP would interact with the C-terminus of ecACP in this orientation (**Figure 1.2-VIII, “ACP 2”**). In this case, however, four ACP molecules could bind to the FabI tetramer and notably, insertion of the substrate through the major portal would substantiate the role of Y156 as the catalytically active residue. Nevertheless, experimental evidence of this interaction model could not be provided so far.

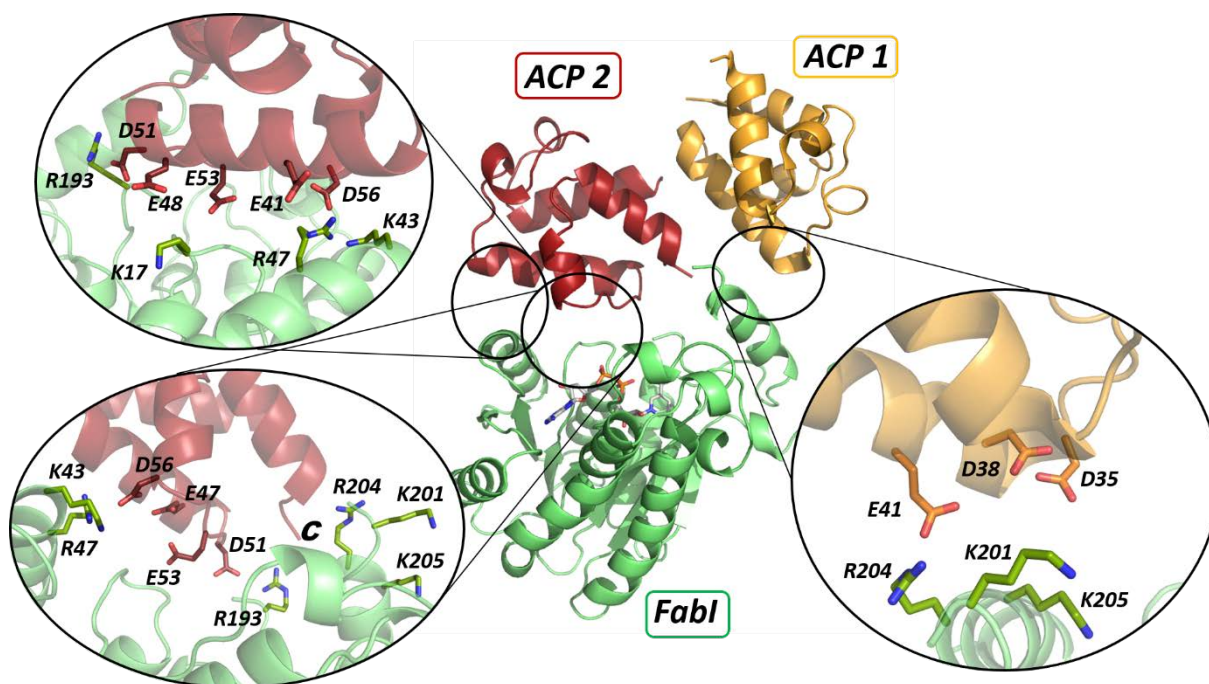


Figure 1.2-VIII: ACP-FabI interaction models: The position of ACP in complex with FabI proposed by Rafi et al. [64] is shown in orange (“ACP 1”) with residues in close contact with FabI displayed in a close-up view. The ACP position from the second model [10, 11] is depicted in red (“ACP 2”) and residues participating in the contact interface are shown in a close-up view with two distinct orientations. The FabI-ACP-1 model in this Figure was generated by superimposing *ecACP* (PDB: 2FAE) with the ACP fragments visible in the 2FHS complex leading to a model which couldn’t reconstruct all interactions reported in [64]. The FabI-ACP-2 model was generated as previously described [10, 11].

1.2.3 Essentiality in bacteria and implications for ENRs as valid drug targets

The FAS-II system is an essential basis for the viability of bacteria, since it is important for the synthesis of cell-wall and membrane components like long- and branched-chain FAs, as well as mycolic acids in mycobacteria. The integrity of the cell envelope is a major determinant of bacterial fitness and survival, since the composition of FAs – the ratio between saturated SCFAs and UFAs, or BCFAs – enables adaptation to altering environmental conditions, such as changes in temperature. Additionally, the cell membrane plays a major role in susceptibility of bacteria to small molecules like antibiotics, and mechanical, e.g. osmotic, strain [94].

Some gram-positive organisms like *Staphylococcus aureus*, *Streptococcus agalactiae* and *pneumoniae* have been reported to be capable of sequestering exogenous FAs from the host-blood serum to circumvent inhibition of their FAS-II pathway and thus, the role of FAS II as suitable drug target has been challenged [95]. These findings were confirmed for *S. agalactiae* and *S. pneumoniae*, which was attributed to different FAS-II regulation mechanisms between these organisms, as well as to the presence of the FabI isoenzyme FabK in streptococci; whereas *S. aureus* remained susceptible to FAS-II inhibition, even in the presence of exogenous FAs [96, 97]. Additionally, *S. aureus* depends on BCFAs

(\approx 55 – 65 % of total FAs) to maintain *in-vivo* fitness [98]. Even though humans contain high ratios of unsaturated linoleic (C18:2) and oleic (C18:1) acids, and the saturated palmitic (C16:0) and stearic acids (C18:0) [95], there is only a small amount (\approx 1 % of total FAs) of BCFAs present in the human blood serum [99]. Hence, it is not possible to draw a general conclusion about the validity of FAS II as drug target with respect to gram-positive bacteria. Importantly, there is no evidence, that gram-negative bacteria are able to compensate for an impaired FAS-II system by exploiting environmental FAs, although they incorporate exogenous FAs into their membrane phospholipids [100]. The essentiality of FAS II originates from the necessity of β -hydroxy FAs for the assembly of the lipid-A core structure, which provides the basic unit of outer-membrane lipopolysaccharides [100, 101].

As described earlier, the overall three-dimensional architectures of FAS I and II display remarkable differences with very low sequence identity between both systems [55]. Nevertheless, the order of the catalytic steps and the functional domains are conserved among all organisms [102] (**Figure 1.2-I**).

Especially in the light of drug development, it is an advantageous circumstance that in contrast to all the other functional subunits involved in the FAS-I and -II pathways, the fold of the ENR domain in the mammalian FAS (mFAS) significantly differs from its functional analogues of the bacterial FAS [102]. Whereas bacterial ENRs either belong to SDR (FabI, FabV, FabL) or TIM-barrel (FabK) proteins, the mFAS enoyl-ACP reductase (ER) domain is a member of the medium-chain dehydrogenase reductase (MDR) family [60], consisting of two subdomains: a nucleotide-binding and a substrate-binding domain [102]. Although the nucleotide-binding domain containing the Rossmann fold is structurally conserved between bacterial ENRs and mFAS ER there are clear differences in the active-site architecture as well as in the catalytically active residues (**Figure 1.2-IX**).

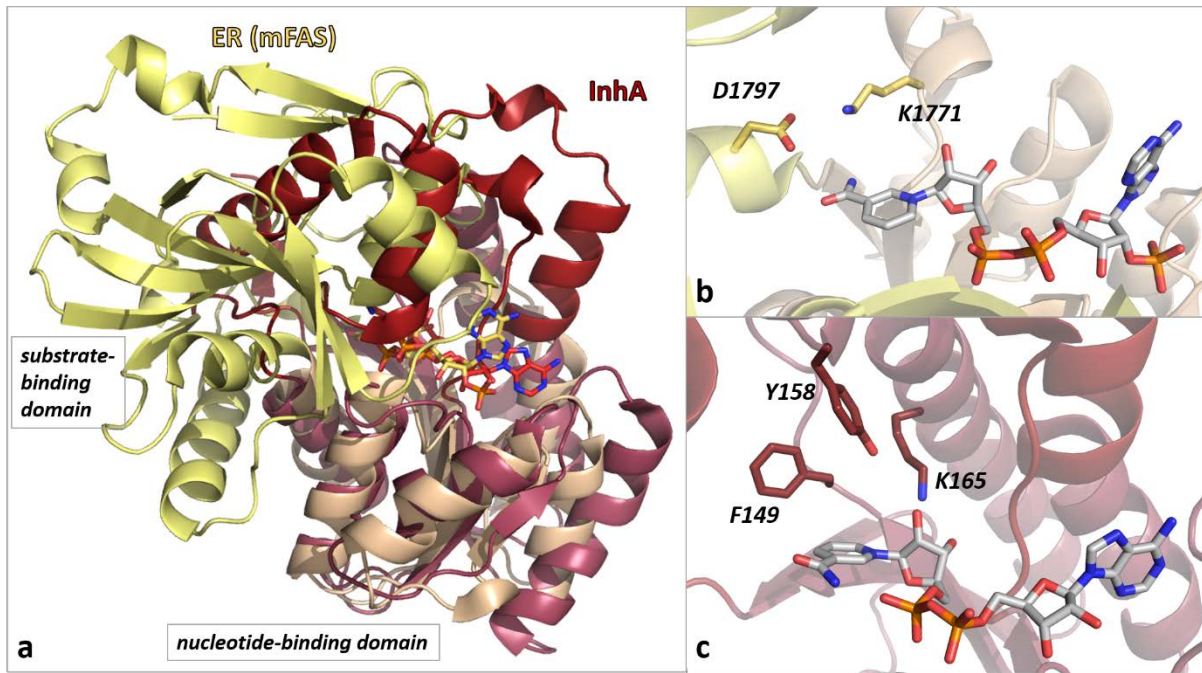


Figure 1.2-IX: Comparison of the mFAS-ER domain and the InhA enoyl-reductase protein: (a) Superposition of mFAS-ER (yellow/ wheat) and InhA (red/ raspberry) tertiary structures, where the nucleotide-binding domains (wheat and raspberry) superimpose well. (b) Putative catalytic residues in the mFAS-ER active site. (c) Catalytic triad of InhA. The NAD(P)⁺ cofactor is shown as grey sticks.

Not only concerning the ER domain of mFAS, but also with respect to ACP there are significant differences between the mammalian and the bacterial systems. Even though the overall tertiary structure comprising the four-helix bundle is similar in both, type-I and type-II ACPs [55], the surfaces involved in the interaction with the particular partner enzymes are notably distinct from each other. Whereas type-II ACP interacts via electrostatic contacts mediated by negatively charged residues, interactions in the mFAS system are predominantly of hydrophobic character with only few polar contacts and include shape complementarity between ACP and its cognate protein [103]. These differences in interaction patterns result in a less negative overall charge of mammalian type-I ACPs and an enhanced ratio of hydrophobic residues (Figure 1.2-vii).

1.3 Drug development and resistance emergence – an everlasting arms race

1.3.1 Mechanisms of antibiotic resistance in bacteria

The emergence of resistances against environmental antibacterial agents in bacteria is an ancient and natural phenomenon, originating in the competition for habitats and natural resources. Since the utilisation of antibiotics for human medicine, animal treatment or as growth-factor in intensive mass animal farming, and for other purposes, the evolutionary pressure for the emergence of antibiotic resistance has increased drastically [47]. Several mechanisms of resistance are known, which are

divided into three main categories: minimisation of the intracellular concentration of the antibiotic, thus preventing access to the target; modification of the target either by genetic mutation or post-translational modification, and inactivation of the antibiotic itself by hydrolysis or enzymatic modification. Overexpression of a drug target is commonly related to conferring resistance to certain antibiotic agents. However, this assumption cannot be generalised, since it does not apply to all mechanisms of drug action [104].

1.3.1.1 Minimisation of intracellular concentration

The prevention of access to the target can be achieved by reducing the permeability of the outer cell membrane in gram-negative bacteria, which prevents compounds from entering the cell or by increased efflux mediated through efflux pumps.

Hydrophilic antibiotics cross the outer membrane by diffusing through unspecific outer membrane porins [47]. To lower the permeability of the outer membrane integration of unspecific porins into the outer membrane is reduced or these porins are replaced by more selective outer-membrane proteins (Omps) (**Figure 1.3-I (1a)**). In *B. pseudomallei* as an example for gram-negative bacteria, the size-specific Omp38 pore displays enhanced permeability towards small antibiotic molecules, but prevents permeation of compounds with a molecular mass greater than $\approx 650 \text{ g}\cdot\text{mol}^{-1}$ through the membrane [105, 106].

Active efflux of antibiotic compounds is mediated by multidrug resistance (MDR) efflux pumps which are able to discharge a wide range of antibiotics from the cell (**Figure 1.3-I (1b)**). For instance, in *M. tuberculosis* resistance to azoles, clofazimine and bedaquiline is caused by overexpression of the multi-substrate efflux pump MmpL5, belonging to the family of resistance-nodulation-cell division (RND) proteins [107]. In *S. aureus* the multidrug efflux pump LmrS (lincomycin resistance protein of *Staphylococcus aureus*) is a putative promoter of resistance to different compounds such as lincomycin, linezolid and kanamycin [108]. Overexpression of efflux pumps genes is often induced by alterations in the regulatory network controlling their expression. Mutations in local repressor proteins, global transcription factors or intergenic sites may cause up- or down-regulation of the respective gene expression. Also response to environmental signals or, most commonly, direct binding of an effector molecule to a transcriptional repressor protein, which decreases the affinity of the repressor to its target DNA [47], increases efflux pump expression.

1.3.1.2 Target modification

Since most antibiotics bind to their targets with high specificity, a single change within the target structure may drastically reduce antibiotic binding, i.e. one single point mutation in the target gene can confer resistance to a specific compound (**Figure 1.3-I (2b)**). Another possibility to change the target is through transformation, i.e. uptake of DNA from the environment to acquire a gene encoding a homologue of the original target. A prominent example is the emergence of methicillin resistance in *S. aureus* by intake of the staphylococcal cassette chromosome *mec* (SCC*mec*) element, which contains the *mecA* gene. *MecA* encodes a β -lactam insensitive variant of the penicillin-binding proteins (PBP), PBP2a [109], which ensures cell wall biosynthesis despite the native PBPs being inhibited by methicillin.

Target protection by modification displays another effective method to prevent antibiotic binding and inhibition of vital functions in bacteria. Modification comprises the attachment of different chemical moieties like methyl groups or amino acids [110], thus altering the drug-binding site and preventing binding of antibiotics (**Figure 1.3-I (2a)**). For example, antibiotic action targeting the ribosomal RNA (rRNA) can be impaired by methylation of rRNA in many bacterial species. In *M. tuberculosis* Rv1694, the product of the *tlyA* gene, possesses methyltransferase activity towards 16S rRNA of the ribosomal 30S subunit and is involved in resistance to the macrocyclic peptide agent capreomycin [111, 112].

1.3.1.3 Inactivation of the antibiotic agent

In bacteria, a multitude of enzymes is capable for degrading or modifying antibiotics and thus restraining their inhibitory activity (**Figure 1.3-I (3a, b)**). As an example, shortly after the discovery of penicillin it was found that the β -lactamase penicillinase from pathogenic *E. coli* was able to hydrolyse penicillin [113]. Since then, many types of β -lactamases have evolved in both gram-positive and gram-negative bacteria, capable of hydrolysing or modifying a wide range of antibiotics like macrolides, β -lactams or aminoglycosides [47].

Many different chemical groups including acyl, phosphate, nucleotidyl and ribityl groups, are utilised to modify vulnerable sites on antibiotic molecules, thus leading to steric hindrance upon binding to the target. The most susceptible group of compounds are aminoglycosides, since they contain a large number of exposed hydroxyl and amino groups. Aminoglycoside modifications are conducted by three main classes of aminoglycoside-modifying enzymes: acetyltransferases, phosphotransferases and nucleotidyltransferases [47]. For instance, in *S. aureus* phosphorylation of hydroxyl-groups of several aminoglycosides is carried out by the broad-spectrum aminoglycoside phosphotransferase APH(3')-IIIa [114]; in *M. tuberculosis* the aminoglycoside 2'-N-acetyltransferase AAC(2')-Ic acetylates 2'-hydroxyl

or -amino groups of a wide range aminoglycosides [115], leading to impaired binding of the compounds to ribosomes.

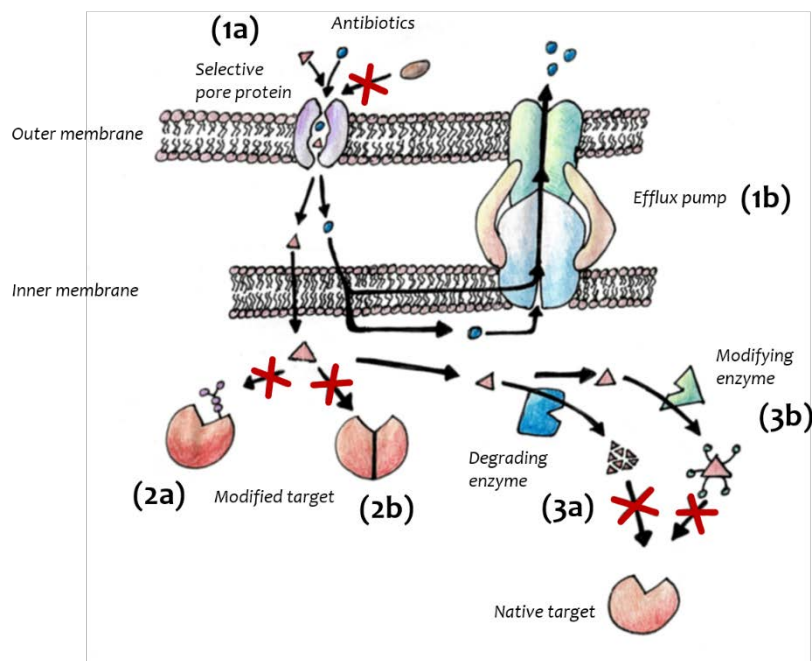


Figure 1.3-I: Mechanisms of antibiotic resistance in bacteria: (1) Minimisation of intracellular concentration; (2) Target modification; (3) Inactivation of the antibiotic agent

1.3.2 Examples of drugs targeting the bacterial ENR enzymes

There are two groups of ENR inhibitors based on their characteristic to either form a covalent bond with the NAD(P)⁺ cofactor or to bind non-covalently to the binary enzyme – cofactor complex.

One group of covalent-adduct forming inhibitors of ENRs are diazaborines, which contain a 1,2-diazine ring with an additional boron as a third heteroatom and are fused to a second five- or six-membered ring (**Figure 1.3-IIb**). In the presence of the nucleotide cofactor the boron atom engages in a covalent bond with the 2'-hydroxyl group of the NAD⁺ ribose, thus forming a bisubstrate inhibitor, which is tightly bound to its target enzyme [116]. Thereby, the diazaborine occupies the position on top of the cofactor where the acyl substrate is normally located. The activity of diazaborines is almost exclusively confined to gram-negative organisms where they interfere with the biosynthesis of lipopolysaccharides [117, 118]. In addition to the covalent bond, diazaborines are engaged in non-covalent interactions, including π - π stacking with the cofactor as well as several hydrogen bonds, in particular the frequently observed hydrogen bond with the active-site tyrosine (Y156) established by the boron-hydroxyl group [116, 117].

A second example for a bisubstrate enzyme inhibitor is the TB-specific compound isoniazid (isonicotinylhydrazide = “INH”). Since INH is a prodrug, it has to be activated by the catalase-peroxidase enzyme KatG [119]. The resulting isonicotinyl radical reacts with the cofactor to form an INH-NAD adduct [120], which binds tightly to the enzyme and thus interferes with substrate binding and turnover (**Figure 1.3-IIa**).

In contrast to inhibitors, which interact with the binary ENR-cofactor complex via the formation of a covalent cofactor – inhibitor complex, the diphenyl-ether (DPE) based compound triclosan (TCL, **Figure 1.3-IIc**) does not form a covalent bond with the cofactor, but due to its interaction pattern it depends on the presence of the cofactor. TCL has been shown to be a slow-binding inhibitor with respect to *E. coli* FabI with high affinity in the picomolar range [121]. Its binding position is similar to that of the diazaborines, but a more closed conformation of α -helix 6 of the SBL has been observed in the TCL complex, which leads to extended interactions between the protein and the cofactor, and protein and inhibitor [122]. Additionally, key interactions reminiscent of diazaborine binding are maintained in the ecFabI-TCL structure, namely the extensive π - π stacking interactions with the nicotinamide portion of NAD⁺, as well as strong hydrogen-bonding interactions with Y156 and the 2'-hydroxyl group of the nicotinamide ribose [122]. Although TCL displays high affinity towards ecFabI, it is a less potent inhibitor of other ENR enzymes; e.g. inhibitory constants (K_i) for saFabI are in the low (≈ 5 nM) and for InhA in the high (≈ 200 nM) nanomolar range [62, 123, 124]. Thus, there have been several advances towards the development of inhibitors based on the DPE scaffold of the broad-spectrum compound TCL by insertion of different types of substituents at distinct positions [7, 125-127], and altered substitution patterns seem to promote specificity of TCL derivatives towards ENRs of specific organisms.

The discovery of 2- and 4-pyridones as antibacterial agents [128, 129] (**Figure 1.3-II d-e**), which share a series of similarities with the DPE class of inhibitors, concerning structural characteristics and binding behaviour, expands the possibilities for comparative studies on their inhibitory properties towards ENRs. Interestingly, the pyridone scaffold lacks the metabolically labile hydroxyl group present in DPEs, but unflatteringly displays rapid-reversible binding to ENR enzymes [130]. Nevertheless, recent achievements in developing potent pyridone inhibitors [128, 130] provide a basis for further research efforts in this field.

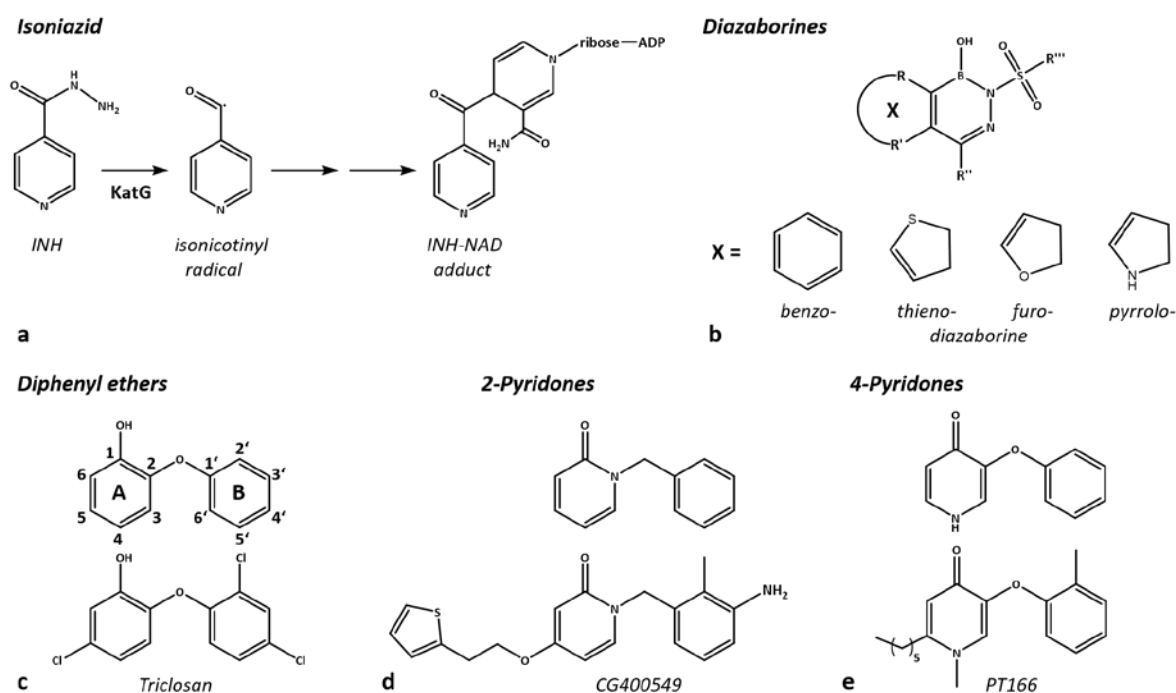


Figure 1.3-II: ENR inhibitors: (a, b) Covalent-adduct forming inhibitors; (c - d) Non-covalent inhibitors with the common scaffold given in the top position and an example below. A nomenclature example for the diaryl inhibitors is depicted for diphenyl ethers (c).

1.4 Research objective

During the course of this work, the interaction of ACP with ENR enzymes was intended to be characterised by macromolecular crystallography, since the identification of key residues crucial for protein-protein interaction would provide a basis for the design of novel inhibitors targeting the bacterial FAS-II pathway. Until now, there is only fragmentary evidence of the major protagonists available creating the interaction surface between ACP and the respective ENR interaction partner and two different models of how the substrate is delivered to the active site of the ENR enzyme [10, 64] leave room for speculation.

The characterization of the molecular determinants of the slow-binding mechanism of DPE inhibitors exhibiting an increased residence time on ENR enzymes was the second aim of this thesis. An interdisciplinary approach was pursued, which consisted of kinetic measurements, structural analysis and *in-vivo* assays. For this purpose, two different model systems, bpFabI and InhA, were employed and the kinetics of complex formation were investigated (*Tonge lab, Stony Brook, NY*) and rationalised by structural analyses. Insights from these experiments validated distinct combinations of substituents as well as novel substituents on the DPE scaffold to improve binding behaviour and bioavailability of

these compounds. Additionally, these findings provide a valuable basis for further optimisation and a valid model for drug design geared towards other ENR enzymes.

2 Materials and methods

2.1 Materials

2.1.1 Consumables

CHEMICALS

For the preparation of buffers and solutions analytical or better grade chemicals and ultrapure water from a TKA GenPure system were used.

Substance	CAS Number	Supplier
1,4-Bis-(maleimido)-butane (BMB)	28537-70-4	Thermo Scientific
1,8-Bis-(maleimido)-diethylene glycol (BM(PEG) ₂)	115597-84-7	Pierce
2-(N-morpholino)-ethanesulfonic acid (MES)	145224-94-8	Sigma®
2'-Deoxyadenosine 5'-triphosphate (dATP), sodium salt solution	1927-31-7	New England Biolabs
2'-Deoxycytidine 5'-triphosphate (dCTP), sodium salt solution	102783-51-7	New England Biolabs
2'-Deoxyguanosine 5'-triphosphate (dGTP), sodium salt solution	93919-41-6	New England Biolabs
2'-Deoxythymidine 5'-triphosphate (dTTP), sodium salt solution	18423-43-3	New England Biolabs
2-Methyl-2,4-pentanediol (MPD)	107-41-5	Fluka
Acetic acid	64-19-7	Carl Roth
Agarose NEEQ ultra quality	9012-36-6	Carl Roth
Ammonium persulfate (APS)	7727-54-0	Carl Roth
Ampicillin sodium salt	69-52-3	Carl Roth
Bis-(2-hydroxyethyl)-imino-tris-(hydroxymethyl)-methane (Bis-Tris)	6976-37-0	Carl Roth
Bis-(maleimido)-ethane (BMOE)	5132-30-9	Thermo Scientific
Bis-(maleimido)-hexane (BMH)	4856-87-5	Thermo Scientific
Bromphenol blue	115-39-9	Carl Roth
Cadaverin	462-94-2	Sigma-Aldrich
Coomassie Brilliant Blue G-250	6104-58-1	Carl Roth
Coomassie Brilliant Blue R-250	6104-59-2	Carl Roth
Crotonyl-/Butenoyl-Coenzyme A (CoA)	102680-35-3	Sigma®
Decanoyl-CoA	1264-57-9	Sigma®
Dimethyl sulfoxide (DMSO)	67-68-5	Carl Roth
Dithiothreitol (DTT)	3483-12-3	Carl Roth
Dodecenoyl-CoA	n/a	Tonge lab, Stony Brook, USA
Ethanol	64-17-5	Carl Roth
Ethylene glycol	107-21-1	Sigma-Aldrich

Materials and methods

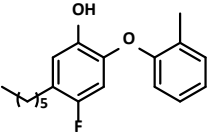
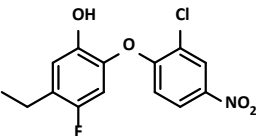
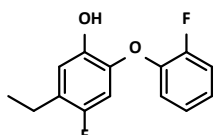
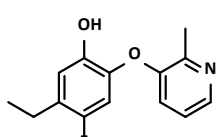
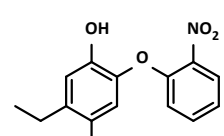
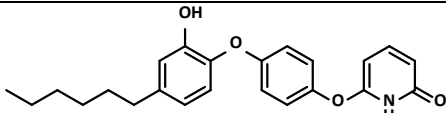
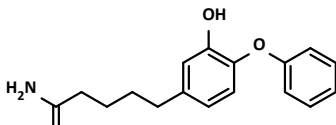
Ethylenediaminetetraacetic acid (EDTA)	60-00-4	Carl Roth
Formaldehyde	50-00-0	Sigma®
Glycerol	56-81-5	Carl Roth
Glycine	56-40-6	Carl Roth
Hexadienyl-N-CoA	n/a	Tonge lab, Stony Brook, USA
Hexadienyl-S-CoA	n/a	Tonge lab, Stony Brook, USA
Hydrochloric acid (HCl)	7647-01-0	Carl Roth
Imidazole	288-32-4	Carl Roth
Isopropyl-β-D-thiogalactopyranoside (IPTG)	367-93-1	Carl Roth
Kanamycin sulfate	25389-94-0	Carl Roth
Magnesium chloride hexahydrate	7791-18-6	Carl Roth
Malonyl-CoA	108347-84-8	Sigma®
Methanol	67-65-1	Carl Roth
Nicotinamide adenine dinucleotide (NAD ⁺ /H)	53-84-9 (ox.)/ 606-68-8 (red.)	Carl Roth
Nicotinamide adenine dinucleotide phosphate (NADP ⁺ /H)	24292-60-2 (ox.)/ 2646-71-1 (red.)	Carl Roth
Octanoyl-CoA	1264-52-4	Sigma®
Orange G	1936-15-8	Sigma-Aldrich
Piperazine-N,N'-bis-(2-ethanesulfonic acid) (PIPES)	5625-37-6	Carl Roth
Polyethylene glycol (PEG) 300	25322-68-3	Sigma-Aldrich
PEG 400	25322-68-3	Aldrich
PEG 550 monomethyl ether (PEG 550-MME)	9004-74-4	Aldrich
Potassium phosphate dibasic	7758-11-4	Sigma®
Silver nitrate (AgNO ₃)	7761-88-8	Sigma-Aldrich
Sodium acetate trihydrate	6131-90-4	Sigma-Aldrich
Sodium carbonate (Na ₂ CO ₃)	6132-02-1	Sigma-Aldrich
Sodium chloride (NaCl)	7647-14-5	Carl Roth
Sodium citrate tribasic dihydrate	6132-04-3	Sigma®
Sodium dodecyl sulfate	151-21-3	Carl Roth
Sodium hydroxide (NaOH)	1310-73-2	Carl Roth
Sodium phosphate monobasic	13472-35-0	Sigma®
Sodium thiosulfate (Na ₂ S ₂ O ₃)	7772-98-7	Sigma-Aldrich
SYPRO® Orange	n/a	Sigma-Aldrich
Tetrahydrofolic acid (THF)	135-16-0	ChemCruz
Tetramethylethylenediamin (TEMED)	110-18-9	Carl Roth

Tris-(2-carboxyethyl)-phosphine (TCEP)	51805-45-9	Carl Roth
Tris-(hydroxymethyl)-aminoethane (Tris)	77-86-1	Carl Roth
Urea	57-13-6	Carl Roth
Xylene cyanol	2650-17-1	Sigma-Aldrich

INHIBITORS

Table 2.1-I: Inhibitors used for crystallisation with different ENR enzymes

Inhibitor name	Structure	Crystallisation with	Synthesis
PT501		[InhA·NAD ⁺]	Tonge lab, Stony Brook, USA
PT504		[InhA·NAD ⁺]	Tonge lab, Stony Brook, USA
PT506		[InhA·NAD ⁺]	Tonge lab, Stony Brook, USA
PT511		[InhA·NAD ⁺]	Tonge lab, Stony Brook, USA
PT512		[InhA·NAD ⁺]	Tonge lab, Stony Brook, USA
PT514		[InhA·NAD ⁺]	Tonge lab, Stony Brook, USA
TCL		[bpFabI·NAD ⁺]	Fluka BioChemika
PT01		[bpFabI·NAD ⁺]	Tonge lab, Stony Brook, USA
PT02		[bpFabI·NAD ⁺]	Tonge lab, Stony Brook, USA
PT12		[bpFabI·NAD ⁺]	Tonge lab, Stony Brook, USA

PT401		[bpFabI·NAD ⁺]	Tonge lab, Stony Brook, USA
PT404		[bpFabI·NAD ⁺]	Tonge lab, Stony Brook, USA
PT405		[bpFabI·NAD ⁺]	Tonge lab, Stony Brook, USA
PT408		[bpFabI·NAD ⁺]	Tonge lab, Stony Brook, USA
PT412		[bpFabI·NAD ⁺]	Tonge lab, Stony Brook, USA
55JS		[InhA·NAD ⁺], [saFabI·NADP ⁺]	Dr. Reddy's Institute of Life Sciences, Hyderabad, India
101JS		[InhA·NAD ⁺], [saFabI·NADP ⁺]	Dr. Reddy's Institute of Life Sciences, Hyderabad, India

MANUFACTURED COMPOSITES

Designation	Type	Supplier
Bayer silicon grease medium viscosity	Silicon grease	Jena Bioscience
GC buffer	DNA polymerase reaction buffer	New England Biolabs
GeneRuler™ 1 kb DNA Ladder	DNA molecular-weight size marker	Thermo Fisher Scientific
GeneRuler™ 100 bp DNA Ladder	DNA molecular-weight size marker	Thermo Fisher Scientific
HF buffer	DNA polymerase reaction buffer	New England Biolabs
Lysogeny broth (LB) medium (Lennox)	Standard <i>E. coli</i> culture medium	Carl Roth
Midori green Advance DNA stain	DNA stain	Biozym Scientific
NEBuffer™ 2, NEBuffer™ 2.1	Restriction endonuclease reaction buffer	New England Biolabs
PageRuler™ Plus Prestained Protein Ladder	Protein molecular-weight size marker	Thermo Fisher Scientific

Materials and methods

PageRuler™ Prestained Protein Ladder	Protein molecular-weight size marker	Thermo Fisher Scientific
Rotiphorese® Gel 30 (37.5:1)	30 % acrylamide/bisacrylamide solution	Carl Roth
Rotiphorese® Gel 40 (29:1)	40 % acrylamide/bisacrylamide solution	Carl Roth
T4 DNA Ligase Reaction Buffer	DNA ligase reaction buffer	New England Biolabs

KITS

Designation	Purpose	Supplier
BCA Protein Assay Kit	Assay for determination of protein concentration	Novagen
NucleoSpin® Gel and PCR Clean-up kit	Extraction of DNA fragments from agarose gels, purification of PCR products	MACHEREY-NAGEL
NucleoSpin® Plasmid	Isolation of plasmid DNA from <i>E. coli</i> cells	MACHEREY-NAGEL
PCT™ Pre-Crystallization Test	Selection of appropriate protein concentrations for crystallisation screens	Hampton Research

ENZYMES

Name	Type	Supplier
ACP synthase (AcpS)	4'-Phosphopantetheinyl transferase	New England Biolabs
Bovine Serum Albumin (BSA)	Carrier protein	New England Biolabs
DNase I	Desoxyribonuclease	Invitrogen
DpnI	Restriction endonuclease	Stratagene
Phusion®	High-Fidelity DNA Polymerase	New England Biolabs
RecA	Single-stranded DNA-binding protein	New England Biolabs
T4 DNA polymerase	DNA polymerase	New England Biolabs
T4 Polynucleotide kinase (T4 PNK)	Polynucleotide kinase	New England Biolabs
TEV protease	Tobacco Etch Virus (TEV) cysteine protease	In-house production

DISPOSABLE LABWARE

The disposable labware used in this thesis is listed below, except for basic, interchangeable laboratory items such as reaction tubes and weighing dishes.

Type	Model	Supplier
24-well hanging-drop crystallisation plate	Crystalgen SuperClear™ Plate	Jena Bioscience
96-well sitting-drop crystallisation plate	Crystalquick™ 1 square well, flat bottom, low profile	Greiner Bio-One
96-well thin-wall PCR plate	Microplate 96 well, PP, for PCR	Greiner Bio-One
Centrifugal concentrator	Amicon® Ultra-0.5, -4 and -15	Millipore
Centrifugal concentrator	Vivaspin 500; 6 and 20	Sartorius
Cuvette	Rotilabo®-single-use cells, 1.6 ml	Carl Roth
Cuvette	UV-Cuvette micro, 70 µl	Brand
Cover slides	22 mm circular cover slides, siliconised	Jena Bioscience
Dialysis cassette	Slide-A-Lyzer	Thermo Scientific
Dialysis membrane	Spectra/Por®	Spectrum Laboratories
Optical quality sealing foil	VIEWseal™	Greiner Bio-One

SCREENS

Name	Description	Supplier
Additive Screen™	Optimisation screen, compound screen	Hampton Research
BMOE-BMB Finescreen	Crystallisation screen, optimisation of primary conditions	<i>Self-designed*</i>
Crystal Power	Crystallisation screen, optimisation of primary conditions	<i>Self-designed*</i>
Crystal Screen, Crystal Screen 2	Crystallisation screen, primary sparse matrix screen	Hampton Research
Crystal Shower	Crystallisation screen, optimisation of primary conditions	<i>Self-designed*</i>
HD-N-Ib Finescreen I – III	Crystallisation screen, optimisation of primary conditions	<i>Self-designed*</i>
HD-N-Ib Superfinescreen	Crystallisation screen, optimisation of primary conditions	<i>Self-designed*</i>
HD-N-saACP-saFabI Finescreen I & II	Crystallisation screen, optimisation of primary conditions	<i>Self-designed*</i>
Index	Crystallisation screen, primary diverse reagent screen	Hampton Research
JCSG+	Crystallisation screen, primary sparse matrix screen	Molecular Dimensions

Optimix™ 3	Crystallisation screen, primary sparse matrix screen	Fluidigm
Optimix™ PEG	Crystallisation screen, primary sparse matrix screen	Fluidigm
PEGs Suite, PEGs II Suite	Crystallisation screen, primary diverse reagent screen	Qiagen
pH Clear Suite, pH Clear II Suite	Crystallisation screen, primary diverse reagent screen	Qiagen
Protein Complex Suite	Crystallisation screen, primary sparse matrix screen	Qiagen
Silver Bullets Bio™	Optimisation screen, compound screen	Hampton Research
Thermofluor Advance	Optimisation screen, systematic salt screen	Based on Ericsson et al., 2006*
Thermofluor Standard	Optimisation screen, systematic buffer screen	Based on Ericsson et al., 2006*
Wizard 1+2, Wizard 3+4	Crystallisation screen, primary sparse matrix screen	Emerald BioSystems

* Compositions are given in the **Appendix, page XXV**.

PRIMERS

Primers were synthesised by Sigma-Aldrich®.

5'-3' sequence	Direction	Template (variant)
CAACGGCCACCAGGCGGATCCGAATTCGAGCTCCG	fw	ecACP (frame shift correction)
CGGAGCTCGAATTCGGATCCGCCTGGTGGCCGTTG	rv	ecACP (frame shift correction)
GATGATTAGGCGCTTGCTCACTTGATATCGC	fw	saACP (D35C)
GCGATATCAAGTGAGCAAGCGCCTAAATCATC	rv	saACP (D35C)
GGCGCTGACTGTCTTGATATCGC	fw	saACP (S36C)
GCGATATCAAGACAGTCAGCGCC	rv	saACP (S36C)
GCGCTGACTCACTTGATATCGCTTGTAGTAATGGAATTAG	fw	saACP (E41C)
CTAATTCCATTACTAAACAAGCGATATCAAGTGAGTCAGCGC	rv	saACP (E41C)
GTAATGGAATTATGTGACGAGTTTGGTACTGAAATCCC	fw	saACP (E47C)
GGGATTCAGTACCAAACCTCGTCACATAATCCATTAC	rv	saACP (E47C)
GGGAATCGCTAATTGCCGTAGTATTGCTTTTG	fw	saFabI (K17C)
CAAAGCAATACTACGGCAATTAGCGATTCCC	rv	saFabI (K17C)

Materials and methods

CGTAGCCGTAAAGAGCTTGAATGTTTATTAGAACAATTAATC	fw	saFabI (K50C)
GATTTAATTGTTCTAATAAACATTCAAGCTCTTTACGGCTACG	rv	saFabI (K50C)
CAGCTGGTCCAATCTGTACATTAAGTGCAAAGG	fw	saFabI (R194C)
CCTTTTGCACCTAATGTACAGATTGGACCAGCTG	rv	saFabI (R194C)
CAAACTTCTGTCATCATG	fw	saFabI (Y9S)
GATTCCCATGATGACAGAAGTTTTG	rv, SLIC	saFabI (Y9S)
GTATTTACTTCCCGTAAAGAAC	fw	saFabI (Y39S)
GTTCTTTACGGGAAGTAAATAC	rv	saFabI (Y39S)
CGCACTTATCTCAAATTG	fw	saFabI (Y63S)
CAATTTGAGATAAGTGCG	rv	saFabI (Y63S)
CATTAGTTCTTCTCATTAAC	fw	saFabI (Y123S)
GCTCAAGACATTAGTTCTTCTCATTAAC	fw, SLIC	saFabI (Y123S)
GTTAATGAGGAAGAACTAATG	rv	saFabI (Y123S)
CAACAACATCTTTAGGTGG	fw	saFabI (Y147S)
GTTGCAACAACATCTTTAGGTGG	fw, SLIC	saFabI (Y147S)
CCACCTAAAGATGTTGTTG	rv	saFabI (Y147S)
GCAAATGTTAAACAGTTAGCATTAGAC	fw	saFabI (Y173Q)
GTCTAATGCTAACTGTTAACATTTGC	rv	saFabI (Y173Q)
<u>saACP-ecFabI-I</u>		
GTTTAACTTTAAGAAGGAGATATACATATGGTGGAATTTTCGATAAAG	fw, SLIC	pET-23b_saACP
CTTTATCGAAATTTTCCACCATATGTATATCTCCTTCTTAAAGTTAAAC	rv, SLIC	pET-23b_saACP
GCCGCCGTTGCCGCTGCCGCTGCCGCCGTTGCCGCCGCTCGAGTTTTT CAAG	rv, SLIC	saACP_Linkers-I
GGCGGCAACGGCGGCAGCGGCAGCGGCAACGGCGGCATGGGTTTTCTT TCCGG	fw, SLIC	ecFabI_Linkers-I
<u>saACP-ecFabI-II</u>		
GCCGTTGCCGCTGCCGCTGCCGCCGCTGCCGTTGCCCTCGAGTTTCAGTT CGAGTTC	rv, SLIC	ecFabI_Linkers-II
GGCAACGGCAGCGGCGGCAGCGGCAGCGGCAACGGCATGGTGAAAA TTTCGATAAAG	fw, SLIC	saACP_Linkers-II
GTCTTGAAAACTCGAGCGCCACCACCACCACC	fw, SLIC	saACP_His-pET-23b
GTGGTGGTGGTGGTGGTGGCGCTCGAGTTTTTCAAG	rv, SLIC	saACP_His-pET-23b
<u>saACP-saFabI-I</u>		
CTTTATTTTCAGGGCGCCATGGTGGAATTTTCGATAAAG	fw, SLIC	saACP_His
CTTTATCGAAATTTTCCACCATGGCGCCCTGAAAATAAAG	rv, SLIC	saACP_His
GCCACGGCCGCCAGAGCCGCCGTTGCCGCCGCTCGAGTTTTTCAAG	rv, SLIC	saACP_Linkers-Ia
GCCGCCACGGCCGCCAGAGCCGCCGTTGCCGCCGCTCGAGTTTTTCAAG	rv, SLIC	saACP_Linkers-Ib

Materials and methods

GCCACCACGACCACCAGAGTTACCACCAGAACCACCGTTACCACCGCGCT CGAGTTTTTCAAG	rv, SLIC	saACP_Linkers-Ib-15 ₁
GCCAGAACCACGACCACCAGAACCACCAGAAGAACCACCGTTACCACCGCGC TCGAGTTTTTCAAG	rv, SLIC	saACP_Linkers-Ib-15 ₂
GCCACCACGACCACCGTTACCACCGTTACCACCGTTACCACCAGAACCAC CGTTACCACCGCGCTCGAGTTTTTCAAG	rv, SLIC	saACP_Linkers-Ib-20 ₁
GGCAACGGCGGCTCTGGCGGCGCCGTGGCATGGTAAATCTTGAAAAC AAAAC	fw, SLIC	saFabI_Linkers-Ia
GGCAACGGCGGCTCTGGCGGCGCCGTGGCGGCATGGTAAATCTTGAAAAC AAAAC	fw, SLIC	saFabI_Linkers-Ib
GGTGGTAACGGTGGTTCTGGTGGTAACTCTGGTGGTCGTGGTGGCATGG TAAATCTTGAAAACAAAAC	fw, SLIC	saFabI_Linkers-Ib-15 ₁
GGTAACGGTGGTTCTTCTGGTGGTTCTGGTGGTCGTGGTTCTGGCATGG TAAATCTTGAAAACAAAAC	fw, SLIC	saFabI_Linkers-Ib-15 ₂
GGTGGTAACGGTGGTTCTGGTGGTAACTGGTGGTAACTGGTGGTAACTGGT GGTCGTGGTGGCATGGTAAATCTTGAAAACAAAAC	fw, SLIC	saFabI_Linkers-Ib-20 ₁
<u>saACP-saFabI-II</u>		
GTCTTGAAAACCTCGAGCGCTAAGAGCACCACCACCACCAC	fw, SLIC	saACP_pETM-11
GTGGTGGTGGTGGTGGTCTTAGCGCTCGAGTTTTTCAAGAC	rv, SLIC	saACP_pETM-11
GGCAACGGCGGCTCTGGCTCTGGCGGCACCGCGGCATGGTGGAAAAT TTCGATAAAG	fw, SLIC	saACP_Linkers-IIa
GGCGGCAACGGCTCTGGCGGCTCTGGCGGCTCTGGCATGGTGGAAAATT TCGATAAAG	fw, SLIC	saACP_Linkers-IIb
GCCGCCGGTGCCGCCAGAGCCAGAGCCGCCGTTGCCTTAATTGCGTGG AATCCG	rv, SLIC	saFabI_Linkers-IIa
GCCAGAGCCGCCAGAGCCGCCAGAGCCGTTGCCGCTTAATTGCGTGG AATCCG	rv, SLIC	saFabI_Linkers-IIb

PLASMIDS

In the following table, pre-existing plasmids containing proteins used in this work or as basis to create mutants or fusion constructs are listed. A list of plasmids with varying inserts from the given ones generated in the course of this work is provided in the **Appendix, page LIV**.

Table 2.1-II: Plasmids used for protein expression and construct design

Vector	Insert	Resistance*	Specifications	Origin
pET-15b	InhA	Ampicillin	T7 promoter/ terminator,	<i>Sylvia Luckner</i>

Materials and methods

			N-terminal His-Tag/ thrombin cleavage site	
pET-23b	saACP, ecACP, ecFabl	Ampicillin	T7 promoter/ terminator, N-terminal T7-Tag, C-terminal His-Tag	<i>Johannes Schiebel;</i> <i>ecACP: Tonge lab,</i> <i>Stony Brook, USA</i>
pET-29b(+)	sfp	Kanamycin	T7 promoter/ terminator, N-terminal S-Tag/ thrombin cleavage site, C-terminal His-Tag	<i>Johannes Schiebel</i>
pETM-11	saFabl	Kanamycin	T7 promoter/ terminator, N-terminal His-Tag/ TEV- cleavage site, C-terminal His-Tag	<i>Johannes Schiebel</i>

* Antibiotic concentrations used for selection: ampicillin: 100 $\mu\text{g} \cdot \text{ml}^{-1}$, kanamycin: 50 $\mu\text{g} \cdot \text{ml}^{-1}$

ESCHERICHIA COLI STRAINS

Application	Strain	Genotype	Supplier
Plasmid amplification	DH5 α	F ⁻ $\phi 80lacZ\Delta M15 \Delta(lacZYA-argF)U169 recA1 endA1 hsdR17(r_k^- m_k^+) phoA supE44 thi-1 gyrA96 relA1 \lambda^-$	Invitrogen
	XL1-Blue	$recA1 endA1 gyrA96 thi-1 hsdR17 supE44 relA1 lac$ [F ⁻ <i>proAB lacI</i> ^q $\Delta M15$ Tn10 (Tet ^r)]	Stratagene
Protein expression	BL21 (DE3)	F ⁻ <i>ompT hsdS_B(r_B⁻ m_B⁻) gal dcm</i> (DE3)	Novagen
	BL21-CodonPlus [®] (DE3)-RIL	B F ⁻ <i>ompT hsdS(r_B⁻ m_B⁻) dcm⁺ Tet^r gal λ(DE3) endA Hte [argU ileY leuW Cam^r]</i>	Stratagene
	BL21 (DE3) pLysS	B F ⁻ <i>dcm ompT hsdS(r_B⁻ m_B⁻) gal λ(DE3)</i> [pLysS Cam ^r]	Novagen

2.1.2 Equipment

INSTRUMENTS

Type	Model	Supplier
Agarose gel electrophoresis system (DNA)	Mini-Sub [®] Cell GT System	Bio-Rad Laboratories
Autoclave	Systec V-150	Systec
Balance, analytical	XS 105 DR	Mettler-Toledo
Balance	XS 6002S DR	Mettler-Toledo
Cell disruption system	M-110P	Microfluidics
Centrifuge	Avanti J-26 XP	Beckman Coulter

Centrifuge	Avanti J-HC	Beckman Coulter
Centrifuge	Centrifuge 5415 D	Eppendorf
Centrifuge	Centrifuge 5415 R	Eppendorf
Crystallography: cryo-loop	CryoLoop	Hampton Research
Crystallography: sample holder	CrystalCap™ Magnetic	Hampton Research
Crystallography: sample vial	CryoVial	Hampton Research
Crystallography: handling tool	CrystalWand™ Magnetic	Hampton Research
Crystallography: storage pucks	SPINE Puck	Jena Bioscience
FPLC system	ÄKTA avant 25	GE Healthcare
FPLC system	ÄKTA pure 25	GE Healthcare
FPLC system	ÄKTApurifier	GE Healthcare
Heating block	Rotilabo®-Block-Heater H250	Carl Roth
Incubator shaker	ISF1-X	Kühner
Incubator shaker	LT-X	Kühner
Infrared imager	Odyssey	LI-COR
Lighting panel	2 E	Carl Roth
Liquid handling robot	Honeybee 963	Digilab
Liquid handling robot	Lissy 2002	Zinsser
Magnetic stirrer	MR 3002	Heidolph Instruments
Magnetic stirrer	MR Hei-Standard	Heidolph Instruments
Microscope	STEMI 2000-C	ZEISS
Microscope	SteREO Discovery.V12	ZEISS
Microscope camera	AxioCam MRc	ZEISS
Microscope light source	KL 2500 LCD	ZEISS
Microscope light source	CL 1500 Eco	ZEISS
MALS detector	DAWN® 8 + HELEOS® II	Wyatt Technology
pH-meter	pH-meter	SCHOTT
Polyacrylamide gel electrophoresis system	Mini-PROTEAN system	Bio-Rad Laboratories
Power supply	PowerPack™ Basic	Bio-Rad Laboratories
PCR-cycler	Mastercycler® EPgradient S	Eppendorf
Real-time (RT) PCR cycler	Mx3005P	Agilent Technologies
Refractometer	Optilab T-rEX	Wyatt Technology
Robotic sealing unit for microplates	RoboSeal	HJ-BIOANALYTIC
Rocker	Duomax 1030	Heidolph Instruments
Rocker	Gyro Mini	Labnet
Rotor assembly (4 x 2250 ml)	JS-5.0	Beckman Coulter
Rotor assembly (8 x 50 ml)	JA-25.50	Beckman Coulter
Sonicator	Labsonic® M	Sartorius

Spectrophotometer	BioPhotometer	Eppendorf
Spectrophotometer	NanoDrop ND 1000	Peqlab
Thermomixer	Thermomixer comfort	Eppendorf
Thermomixer	MHR 20	HLC BioTech
Ultrapure water system	TKA GenPure	Thermo Fisher Scientific
Ultrasonic bath sonicator	Sonorex RK 255 H	BANDELIN electronic
UV-illumination table	Electronic UV Transilluminator	Ultra Lum
UV imaging system	Gel Doc™ XR System	Bio-Rad Laboratories
Vortex mixer	Vortex-Genie 2	Scientific Industries
X-ray cryosystem	X-Stream™ 2000	Rigaku
X-ray detector	R-AXIS HTC	Rigaku
X-ray generator	MicroMax™-007 HF	Rigaku
X-ray optics	VariMax™	Rigaku

CHROMATOGRAPHY COLUMNS AND MEDIA

<i>Designation</i>	<i>Type</i>	<i>Supplier</i>
Econo-Column® 2.5 x 20 cm	Column body, low pressure	Bio-Rad Laboratories
HiLoad™ 16/60 Superdex™ 200	Preparative SEC FPLC column	GE Healthcare
HiLoad™ 26/60 Superdex™ 200	Preparative SEC FPLC column	GE Healthcare
HiPrep™ DEAE FF 16/10	High-capacity AIEX FPLC column	GE Healthcare
HiTrap™ FF crude	Immobilised metal-ion affinity chromatography FPLC column	GE Healthcare
HiTrap™ Blue HP	Dye-ligand affinity chromatography FPLC column	GE Healthcare
MonoQ™ 10/100 GL	High-resolution AIEX FPLC column	GE Healthcare
MonoQ™ 5/50 GL	High-resolution AIEX FPLC column	GE Healthcare
Protino® Ni-IDA	Immobilised metal-ion affinity chromatography resin	MACHEREY-NAGEL
Protino® Ni-TED	Immobilised metal-ion affinity chromatography resin	MACHEREY-NAGEL
Superdex™ 200 10/300 GL	Analytical SEC FPLC column	GE Healthcare
Superdex™ 75 10/300 GL	Analytical SEC FPLC column	GE Healthcare

2.1.3 Software

COMPUTER PROGRAMS

Program	Description	Supplier/Reference
<i>adxv</i>	Visualisation of X-ray diffraction images	Andrew Arvai (http://www.scripps.edu/tainer/arvai/adxv.html)
<i>AIMLESS</i>	Scaling and merging of diffraction data	Evans & Murshudov, 2013
<i>ALBULA VIEWER</i>	Visualisation of X-ray diffraction images	DECTRIS
<i>Apache</i>	Spreadsheet software	Apache Software Foundation
<i>OpenOffice™ Calc</i>		
<i>Astra VI</i>	MALS detector and refractometer control; MALS data collection and analysis	Wyatt
<i>AxioVision</i>	Microscopy image recording software	ZEISS
<i>CCP4</i>	Software suite for macromolecular X-ray structure determination	Winn et al., 2004
<i>CCP4i</i>	Graphical interface to <i>CCP4</i>	Potterton et al., 2003
<i>ChemDraw</i>	Chemical structure-drawing program	PerkinElmer
<i>Clustal Omega</i>	Biosequence analysis; multiple sequence alignment	Sievers & Higgins, 2014
<i>Coot</i>	Model-building software, X-ray crystallography	Emsley et al., 2010
<i>CrystalClear</i>	X-ray data collection and basic processing	Rigaku
<i>d*TREK</i>	Processing of X-ray diffraction images from two-dimensional position sensitive detectors	Rigaku
<i>DSSP</i>	Secondary structure assignment calculated from coordinate files	Touw et al., 2015
<i>ESPrpt</i>	Graphical illustration of sequence and secondary structure similarities from aligned sequences	Robert & Gouet, 2014
<i>ExPASy</i>		
<i>ProtParam tool</i>	Computation of physical and chemical properties of proteins	Artimo et al., 2012
<i>ExPASy Translate tool</i>	Translation tool of nucleotide sequences to protein sequences	Artimo et al., 2012
<i>GENtle</i>	Plasmid map database management; analysis and <i>in silico</i> editing of DNA sequences	Magnus Manske, University of Cologne (http://gentle.magnusmanske.de/)
<i>iMOSFLM</i>	Graphical interface to <i>MOSFLM</i>	Battye et al., 2011

Materials and methods

<i>Microsoft Excel</i>	Spreadsheet software	Microsoft Corporation
<i>MolProbity</i>	Geometric evaluation of macromolecular structure models	Chen et al., 2010
<i>MOSFLM</i>	Processing of diffraction images	Leslie, 2006
<i>ODYSSEY</i>	Infrared imaging software	LI-COR
<i>PHASER</i>	Phasing software	McCoy et al., 2007
<i>Phenix</i>	Software suite for macromolecular X-ray structure determination	Adams et al., 2010
<i>Phyre2</i>	Biosequence analysis; protein 3D-structure prediction	Kelley et al., 2015
<i>POINTLESS</i>	Space-group determination	Evans, 2005
<i>POVME</i>	Tool for binding-pocket volume determination	Durrant et al., 2011
<i>PRODRG2</i>	Small-molecule topology generator	Schüttelkopf & van Aalten, 2004
<i>PyMOL</i>	3-dimensional visualisation and graphical illustration software	Schrödinger
<i>Quantity One</i> [®]	UV imaging system control; UV image recording and analysis	BioRad
<i>REFMAC</i>	Macromolecular structure refinement	Murshudov et al., 1997
<i>SCALA</i>	Scaling and merging of diffraction data	
<i>ThermoFluor Script</i>	<i>Excel</i> script for thermofluor data analysis	SGC, Oxford
<i>UNICORN</i>	FPLC instrument control; recording, analysis and management of chromatograms	GE Healthcare
<i>XDS</i>	Processing and scaling of diffraction images	Kabsch, 2010

DATABASES

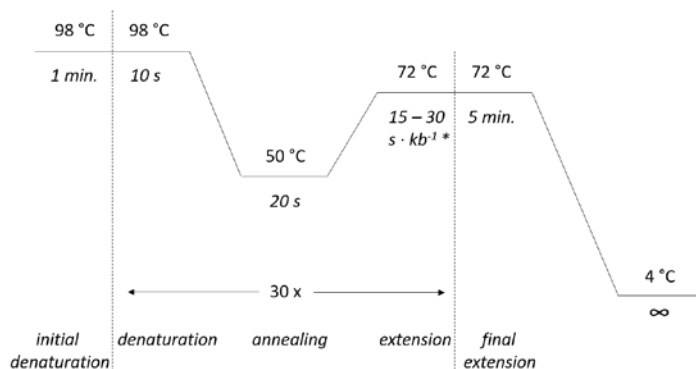
Database	Content	Web address	Reference
<i>PDB</i>	Structural data of biological macromolecules	www.rcsb.org	Berman et al., 2000
<i>PubMed</i>	Biomedical literature	www.ncbi.nlm.nih.gov/pubmed	National Center for Biotechnology Information (NCBI)
<i>UniProt</i>	Protein sequences	www.uniprot.org	UniProt Consortium, 2015

2.2 Methods

2.2.1 Molecular biology

MOLECULAR CLONING

The cloning process implies the introduction of a deoxyribonucleic acid (DNA) fragment with certain properties, e.g. a sequence encoding a distinct protein, into a vector and its amplification. For the assembly of recombinant DNA molecules the sequence- and ligation-independent cloning (SLIC) [131] technique was applied. Fragments with suitable overhangs were created using primers containing a region complementary to the DNA sequence of the fragment to be amplified and the respective homologous overhang for recombination with the target vector or another fragment. In case of the fusion constructs, one primer pair each contained overhangs composed of the sequence of the linker region to be introduced. Fragment amplification was conducted by the polymerase chain reaction (PCR) using the Phusion®-DNA polymerase. The reaction mix contained the supplied HF or GC buffer, 10 ng of template DNA, 0.5 µM forward and reverse primer each, 0.2 mM of each dNTP (dATP, dCTP, dGTP, dTTP) and 1 U of Phusion®-DNA polymerase. The PCR protocol contained the following steps, which were adjusted to the respective amplification reaction in terms of annealing temperature and elongation time, depending on the length and GC content of the primers used, as well as on the length of the fragments to be amplified:



* Phusion®-specific turnover

The PCR products were analysed and purified utilising a preparative agarose gel (*page 41*) followed by extraction from the gel using the NucleoSpin® Gel and PCR Clean-up kit according to the instructions of the manufacturer.

Subsequent ligation was preceded by T4-DNA polymerase digestion of the fragments to create single-stranded overhangs. The DNA was incubated with 0.3 U·µl⁻¹ T4-DNA polymerase in NEBuffer 2

containing $0.2 \mu\text{g}\cdot\mu\text{l}^{-1}$ BSA for 45 min at room temperature. The reaction was stopped by the addition of 1 mM dCTP and the fragments were combined using a 3 – 5-fold molar excess of insert over vector for annealing in T4-DNA ligase reaction buffer. Afterwards, the reaction mixtures were either submitted to temperature annealing, which comprised incubation for 5 min at $75 \text{ }^{\circ}\text{C}$, followed by 10 min at $25 \text{ }^{\circ}\text{C}$; or to ligation by adding $1 \text{ ng}\cdot\mu\text{l}^{-1}$ RecA and incubation for 30 min at room temperature. Reaction products were then used for transformation of competent *E. coli* DH5 α - or XL1-Blue cells. Verification of amplified recombinant plasmids by sequencing was carried out by Seqlab (Göttingen, Germany) or Eurofins Genomics (Ebersberg, Germany).

MUTAGENESIS

Point mutations were introduced by amplification of the DNA plasmid containing the gene of interest utilising complementary forward and reverse primers in one single PCR step as described on *page 40*. The primers contained the appropriate nucleotide variation to generate a single amino-acid substitution within the target protein. The PCR products were incubated with $0.1 - 0.2 \text{ U}\cdot\mu\text{l}^{-1}$ DpnI for 1.5 – 3 h or overnight at $37 \text{ }^{\circ}\text{C}$ to digest parental DNA. Competent cells were transformed with the linearised DNA containing the point mutation (*page 42*).

To generate variants containing manifold substitutions or fusion constructs, overlap-extension PCR [132, 133] was employed. First, fragments containing a single point mutation or fragments of the single components of a fusion construct were created with overhangs complementary to the future neighbouring fragments introduced by the specific primers. The target vector was linearised yielding overhangs complementary to the ends of the fragment to be inserted. In subsequent PCR reactions the fragments were combined via their complementary overlaps and amplified using their flanking primers. Any reaction contained supplied HF or GC buffer, $0.5 \mu\text{M}$ forward and reverse primer each, 0.2 mM of each dNTP (dATP, dCTP, dGTP, dTTP), 1 U of Phusion[®]-DNA polymerase and 25 ng of each of the two fragments to be combined and the PCR was conducted as described above (*page 40*). After each PCR step the products were separated and purified by agarose-gel electrophoresis and subsequent gel extraction as described below.

SEPARATION OF DNA-PCR PRODUCTS BY AGAROSE-GEL ELECTROPHORESIS

For the separation of the different DNA molecules agarose gels were prepared by dissolving 1 % (w/v) NEEO ultra quality agarose in TAE buffer. The mixture was heated until it started boiling and panned to dissolve the agarose completely. After short settling $4 \mu\text{l}$ Midori green Advance DNA stain per 50 ml volume was added to the solution, which then was cast using the Mini-Sub[®] Cell GT gel chamber and after hardening submerged in TAE buffer within the electrophoresis chamber. DNA samples were mixed 6:1 with DNA loading buffer and loaded onto the gel. To determine the size of the DNA

fragments a pre-mixed DNA ladder was added to one of the slots. Electrophoretic separation was performed at 100 V for 30 min and subsequently, DNA was detected exposing the gel to UV light. The fragments of interest were cut out and extracted from the gel slices using the NucleoSpin® Gel and PCR Clean-up kit following the manufacturer's instructions.

TAE buffer	40 mM Tris/HCl, pH 8.0, 20 mM acetic acid, 1 mM EDTA
DNA loading buffer	10 mM Tris/HCl, pH 7.6, 0.03 % (w/v) bromphenol blue, 0.03 % (w/v) xylene cyanol, 60 % (v/v) glycerol, 60 mM EDTA

TRANSFORMATION OF COMPETENT *E. COLI* CELLS

For plasmid amplification or to recombinantly express proteins in *E. coli*, the amplification- or expression host was transformed with the plasmid containing the DNA sequence encoding the protein of interest. 50 – 100 µl of thawed competent cells were first incubated with either half a volume of ligation reaction or 50 – 100 ng plasmid DNA on ice for 30 min. Afterwards, cells were exposed to elevated temperature (42 °C) for 60 s and instantly placed on ice for another 2 min. 0.5 – 1 ml of LB medium was added and cells were shaken for 60 – 90 min at 37 °C in a heating block. Subsequently, the cells were plated on LB agar containing the appropriate antibiotic for selection (**Table 2.1-II**). The plate was incubated overnight at 37 °C.

PRE-CULTURE PREPARATION AND PLASMID AMPLIFICATION

For pre-culture preparation or plasmid amplification one colony from the LB agar plate was added to 5 ml of LB medium supplemented with 50 µg · ml⁻¹ kanamycin or 100 µg · ml⁻¹ ampicillin (**Table 2.1-II**) and grown at 37 °C in an incubator shaker. The 5-ml pre-culture was added to 200 ml LB medium complemented with the respective antibiotic, which was either used for expression tests or further incubated for the purpose of large-scale protein expression.

Cells from the plasmid-amplification reaction were spun down for 10 min at 4 °C and 3220 x g and the supernatant was discarded. The plasmid DNA was isolated with the NucleoSpin® Plasmid kit following the instructions of the manufacturer.

EXPRESSION TESTS

Expression tests for generated variants or fusion constructs were usually conducted at two different temperatures (18 and 25 °C) in a small-scale expression setup. 200 ml LB medium containing the corresponding antibiotic were inoculated with 5 ml from a pre-culture of transformed cells. Cells were grown at 37 °C under constant shaking until an optical density at λ = 600 nm (OD₆₀₀) of 0.6 – 0.8 was reached. Protein expression was induced through addition of 0.5 – 1 mM IPTG and simultaneously, the

temperature was lowered to 18 or 25 °C. Samples of 40 ml each were taken 3, 6 and 18 – 20 and/or 22 – 24 h after induction, and were centrifuged for 10 min at 4 °C and 3220 x g. Pellets were resuspended in 500 µl of the corresponding lysis buffer and sonicated three times with 15 – 20 pulses each (cycle: 0.7 – 0.8, amplitude: 80 – 90 %). Afterwards the lysed cells were centrifuged for 30 min at 4 °C and 16 100 x g. The supernatant was separated from the pellet fraction, which was resuspended again in 500 µl lysis buffer. Both fractions were analysed by SDS-PAGE.

PROTEIN EXPRESSION

Large-scale expression was conducted similar to previously described expression tests, but at a volume of 2 l LB medium inoculated each with 40 ml of pre-culture resulting in an initial OD₆₀₀ of ≈ 0.05. After induction at an OD₆₀₀ of 0.6 – 0.8, cells were grown at 18, 20 or 25 °C under constant shaking and harvested after 4 – 6 h (InhA, sfp) or 18 – 22 h by centrifugation for 15 min at 4 °C and 5000 x g. Pellets were aliquoted and frozen at -80 °C.

2.2.2 Protein purification

All purification steps described below were conducted at 4 °C and protein samples were kept on ice during the entire purification procedure, unless treatment at different temperatures is explicitly stated.

AFFINITY CHROMATOGRAPHY

Except for ecACP, Ni²⁺-affinity chromatography was conducted as the first purification step for any protein described herein. 1 g of wet cell pellet was resuspended in 5 ml (wt-saACP + saACP-Cys mutants, sfp), 6 ml (wt-saFabI + saFabI-Cys mutants, saACP-saFabI fusion constructs + fusion-Cys mutants), 7 ml (saACP-ecFabI fusion construct), 8 ml (ecFabI) or 10 ml (InhA) lysis buffer (**Table 2.2-1**) and 1 U/ml DNase I. Afterwards the cells were lysed utilising a cell disruption system and applying a pressure of 1.5 kbar for two cycles of lysis followed by centrifugation for 1 h at 50 000 x g. The supernatant was then either incubated with Protino® Ni-TED resin (for purification of saFabI, ecFabI and sfp; 2 – 4 g Ni-TED per 6 g wet pellet, preequilibrated with lysis buffer) under constant inversion for 30 min, or loaded onto a 5 ml HisTrap™ FF crude column attached to a FPLC system (for purification of saACP, ecACP (2nd step), saACP-saFabI/ecFabI fusion constructs). The flow-through was released from the Ni-TED column by gravity flow, which was subsequently washed with 2 x 5 ml lysis buffer, 6 x 5 ml washing buffer and followed by fractionated elution with elution buffer volumes of 2 x 1 ml, 7 x 2 ml, 1 x 15 ml and 1 x 50 ml. For the FPLC-purification procedure either a linear gradient was applied, or a step-elution was conducted:

Protein	Elution technique	Column volume (CV)
saACP	Linear gradient (0 – 100 % B)	10
ecACP	Linear gradient (0 – 100 % B)	20
InhA	Linear gradient (0 – 100 % B)	20
saACP-saFabI/ecFabI fusion (initial purifications)	Linear gradient (0 – 100 % B) (buffer systems I & II (Table 2.2-I, Table 2.2-II))	10, 15, 20, 25
saACP-saFabI fusion (optimised protocol)	Step elution (buffer system II (Table 2.2-I, Table 2.2-II))	Step 1: 17 % B, 10 CV Step 2: 63 % B, 10 CV Step 3: 100 % B, 5 CV

All fractions were collected and analysed by SDS-PAGE (page 49). The eluate fractions containing the target protein were pooled and either concentrated and then centrifuged for 10 min at 3220 x g for subsequent size-exclusion chromatography (SEC), or dialysed in TEV-cleavage buffer (saFabI, page 46) or modification buffer (saACP, ecACP (Table 2.2-III)).

Table 2.2-I: Lysis-/Ni²⁺-binding buffers; Lysis- & DEAE-binding buffers*

Protein	Buffer composition
saFabI with His ₆ -tag*	50 mM Tris/HCl, pH 8.0, 500 mM NaCl
saFabI without His ₆ -tag*	50 mM Tris/HCl, pH 8.0, 200 mM NaCl, 5 % (v/v) glycerol
ecFabI	50 mM Tris/HCl, pH 8.0, 500 mM NaCl
InhA	20 mM Tris/HCl, pH 7.9, 500 mM NaCl, 5 mM imidazole
saACP*	20 mM Tris/HCl, pH 7.9, 500 mM NaCl, 5 mM imidazole
ecACP	25 mM MES/NaOH, pH 6.1*
	<i>Ni-binding buffer:</i> 25 mM MES/NaOH, pH 6.5, 500 mM NaCl, 5 mM imidazole
sfp	20 mM Tris/HCl, pH 8.0, 500 mM NaCl
saACP-saFabI fusion*	<i>Lysis I:</i> 25 mM Tris/HCl, pH 8.0, 500 mM NaCl, 5 mM imidazole <i>Lysis II:</i> 25 mM Na ₃ Citrate/HCl, pH 6.0, 500 mM NaCl, 5 mM imidazole
saACP-ecFabI fusion	20 mM Tris/HCl, pH 8.0, 500 mM NaCl, 5 mM imidazole

* Buffers for proteins containing Cys mutations were supplied with 0.5 mM TCEP or DTT

Table 2.2-II: Ni-affinity chromatography buffers

Protein	Buffer composition
saFabI with His₆-tag*	<i>Washing buffer:</i> 50 mM Tris/HCl, pH 8.0, 1 M NaCl <i>Elution buffer:</i> 50 mM Tris/HCl, pH 8.0, 500 mM NaCl, 250 mM imidazole
saFabI without His₆-tag*	<i>Washing buffer:</i> 50 mM Tris/HCl, pH 8.0, 500 mM NaCl, 5 % (v/v) glycerol <i>Elution buffer:</i> 50 mM Tris/HCl, pH 8.0, 200 mM NaCl, 250 mM imidazole, 5 % (v/v) glycerol
ecFabI	<i>Washing buffer:</i> 50 mM Tris/HCl, pH 8.0, 1 M NaCl <i>Elution buffer:</i> 50 mM Tris/HCl, pH 8.0, 500 mM NaCl, 250 mM imidazole
InhA	<i>Washing buffer:</i> 20 mM Tris/HCl, pH 7.9, 500 M NaCl, 45 mM imidazole <i>Elution buffer:</i> 20 mM Tris/HCl, pH 7.9, 500 mM NaCl, 500 mM imidazole
saACP*	<i>Washing buffer:</i> 20 mM Tris/HCl, pH 7.9, 500 mM NaCl, 40 mM imidazole <i>Elution buffer:</i> 20 mM Tris/HCl, pH 7.9, 500 mM NaCl, 500 mM imidazole
ecACP	<i>Washing buffer:</i> 25 mM MES/NaOH, pH 6.5, 500 mM NaCl, 30 mM imidazole <i>Elution buffer:</i> 25 mM MES/NaOH, pH 6.5, 500 mM NaCl, 500 mM imidazole
sfp	<i>Washing buffer:</i> 50 mM Tris/HCl, pH 8.0, 1 M NaCl <i>Elution buffer:</i> 50 mM Tris/HCl, pH 8.0, 500 mM NaCl, 250 mM imidazole
saACP-saFabI fusion*	<i>Washing buffer I:</i> 25 mM Tris/HCl, pH 8.0, 500 mM NaCl, 20 mM imidazole <i>Elution buffer I:</i> 25 mM Tris/HCl, pH 8.0, 500 mM NaCl, 400 mM imidazole <i>Washing buffer II:</i> 25 mM Na ₃ Citrate/HCl, pH 6.0, 500 mM NaCl, 20 mM imidazole <i>Elution buffer II:</i> 25 mM Na ₃ Citrate/HCl, pH 6.0, 500 mM NaCl, 400 mM imidazole (linear gradient) or 500 mM imidazole (step elution)
saACP-ecFabI fusion	<i>Washing buffer:</i> 20 mM Tris/HCl, pH 8.0, 500 mM NaCl, 30 mM imidazole <i>Elution buffer:</i> 20 mM Tris/HCl, pH 8.0, 500 mM NaCl, 800 mM imidazole

* Buffers for proteins containing Cys mutations were supplied with 0.5 mM TCEP or DTT

TEV CLEAVAGE

The total mass of saFabI in the pooled fractions from the affinity chromatography was determined using UV/Vis spectrophotometry at $\lambda = 280$ nm. To remove the His₆-tag, saFabI was incubated with TEV protease in a two-step procedure. In the first step, half of the mass of TEV protease, which would represent a TEV-to-saFabI mass ratio of 1:50, was added to the saFabI pool. The mixture was dialysed overnight at room temperature in 5 l of cleavage buffer containing 25 mM Tris/HCl, pH 8.0, 200 mM NaCl, 0.5 mM EDTA, 1 mM DTT. The second half of m_{TEV} was added the next day, followed by another 24 h of incubation to facilitate quantitative removal of the His₆-tag.

To remove non-cleaved saFabI and the His₆-tagged TEV protease, a second affinity-purification step was applied. The protein was loaded onto a HisTrapTM column equilibrated with size-exclusion chromatography (SEC) buffer (**Table 2.2-V**). Whereas the cleaved protein eluted in the flow-through and imidazole-free wash fractions, His₆-tagged components stayed bound to the resin and were removed from the column by a washing step of 10 CV with Ni-affinity elution buffer (

Table 2.2-II). Fractions containing cleaved saFabI were pooled and concentrated for subsequent SEC.

MODIFICATION OF ACP AND FUSION CONSTRUCTS WITH ACYL-COENZYME A (COA) SUBSTRATES

The protein concentration was determined using the BCA assay (for ACP, *page 49*), or via absorption at $\lambda = 280$ nm (fusion proteins). For the coupling reaction of an acyl substrate to the ACP (or -part of the fusion construct) the protein was concentrated or diluted in modification buffer to a concentration of 100 μ M (saACP or fusion construct) or 70 μ M (ecACP). 300 – 500 μ M (saACP or fusion construct) or 1.5 – 3-fold molar excess (ecACP) of acyl-CoA substrate was added; at low yields of saACP or fusion construct a 2 – 4-fold molar excess of substrate over [saACP] or [fusion construct] was used for modification. To initiate the reaction, sfp (saACP or fusion construct) or AcpS (ecACP) at a concentration of 3 μ M (sfp for 100 μ M saACP or fusion construct), 0.3 – 1 μ M (sfp for [saACP]/[fusion construct] \ll 100 μ M) or 2.5 μ M (AcpS) was added and the mixture incubated at 37 °C for 3 h (saACP or fusion construct) or at 30 °C for 1 h (ecACP) under gentle agitation.

Samples were taken at time point t_0 , at the end of the reaction and optional in 30 min or 1 h intervals between the start and the endpoint, immediately placed on ice and mixed 5:1 with CSGE-loading buffer. The modification efficiency was monitored using conformation-sensitive gel electrophoresis (CSGE, *page 50*).

Table 2.2-III: Modification buffers

Protein	Buffer composition
saACP	“D”: 75 mM Tris/HCl, pH 7.5, 10 mM MgCl ₂
	“I”: 20 mM Tris/HCl, pH 8.0, 10 mM MgCl ₂ , 30 mM NaCl
	“T4”: 70 mM Tris/HCl, pH 7.5, 10 mM MgCl ₂ , 5 mM TCEP + T4 PNK (0.04 – 0.08 U·μl ⁻¹)
ecACP	50 mM Tris/HCl, pH 7.5, 10 mM MgCl ₂ , 1 mM DTT
saACP-saFabI/ecFabI fusion	“D + urea”: 75 mM Tris/HCl, pH 7.5, 10 mM MgCl ₂ , 50 mM CO(NH ₂) ₂

ANION-EXCHANGE CHROMATOGRAPHY

Anion-exchange chromatography was utilised to separate modified and unmodified species of ACP or saACP-saFabI fusion constructs. This purification step was carried out using a Mono Q[®] 5/50 GL or 10/100 GL attached to an FPLC system. At first, a long, shallow gradient was applied over 20 – 40 CV from 0 – 100 % elution buffer. Later, optimised protocols were applied for modified saACP with gradients from 25 – 30 % elution buffer over 15 CV or 25 – 35 % elution buffer over 20 CV. The fractions were collected and analysed by both, SDS-PAGE and CSGE, and the eluate containing the modified protein was pooled and concentrated for subsequent SEC.

For an initial purification step of ecACP, the weak anion-exchange HiPrep[™] DEAE FF 16/10 column was used. Prior to the application of the lysate, the column was equilibrated with binding buffer, followed by a washing step with the same and elution via a linear gradient of 20 CV from 0 – 100 % elution buffer (**Table 2.2-IV**). The fractions were collected, analysed by SDS-PAGE (*page 49*) and eluate fractions containing the target protein were pooled and submitted to Ni-affinity chromatography (*page 43*).

Table 2.2-IV: Anion-exchange chromatography buffers

Protein	Buffer composition
saACP*	<i>Binding buffer</i> : 20 mM Tris/HCl, pH 8.0, 50 mM NaCl
	<i>Elution buffer</i> : 20 mM Tris/HCl, pH 8.0, 1 M NaCl
	<i>Binding buffer (DEAE & MonoQ)</i> : 25 mM MES/NaOH, pH 6.1
ecACP	<i>Elution buffer (DEAE)</i> : 25 mM MES/NaOH, pH 6.1, 850 mM NaCl
	<i>Elution buffer (MonoQ)</i> : 25 mM MES/NaOH, pH 6.1, 1 M NaCl
saACP-saFabI fusion	<i>Binding buffer I</i> : 20 mM Tris/HCl, pH 8.0, 50 mM NaCl

	<i>Elution buffer I:</i> 20 mM Tris/HCl, pH 8.0, 1 M NaCl
	<i>Binding buffer II:</i> 25 mM Na ₃ Citrate/HCl, pH 6.5, 50 mM NaCl
	<i>Elution buffer II:</i> 25 mM Na ₃ Citrate/HCl, pH 6.5, 1 M NaCl
saACP-ecFabI fusion	<i>Binding buffer:</i> 20 mM Tris/HCl, pH 8.0, 50 mM NaCl
	<i>Elution buffer:</i> 20 mM Tris/HCl, pH 8.0, 1 M NaCl

* Buffers for proteins containing Cys mutations were supplied with 0.5 mM TCEP or DTT

PREPARATIVE SIZE-EXCLUSION CHROMATOGRAPHY (SEC)

SEC was used as a final polishing step of protein purification. Proteins obtained from earlier purification steps were concentrated to less than 5 % of the column volume and centrifuged for 10 min at 4 °C and 3220 x g. The sample was applied to the SEC column, which was attached to an FPLC system and equilibrated with the respective SEC buffer (**Table 2.2-V**). Isocratic elution was performed over 1.2 CV, the fractions were collected and analysed by SDS-PAGE (*page 49*) and fractions containing pure target protein were pooled and concentrated. The final concentration was determined using UV/Vis spectrophotometry at $\lambda = 280$ nm, or at $\lambda = 562$ when the BCA assay was employed for ACP. Aliquots were shock-frozen in liquid nitrogen and stored at -80 °C.

Table 2.2-V: Size-exclusion chromatography buffers

Protein	Buffer composition
saFabI with His₆-tag*	20 mM Na ₃ Citrate/HCl, pH 5.6, 250 mM NaCl, 1 mM EDTA
saFabI without His₆-tag*	25 mM Tris/HCl, pH 8.0, 200 mM NaCl
ecFabI	20 mM PIPES/NaOH, pH 7.5, 200 mM NaCl, 1 mM EDTA
InhA	20 mM PIPES/NaOH, pH 6.8, 150 mM NaCl
saACP*	20 mM Tris/HCl, pH 7.0, 150 mM NaCl, 1 mM EDTA
ecACP	25 mM MES/NaOH, pH 6.1, 100 mM NaCl
sfp	10 mM Tris/HCl, pH 7.5, 150 mM NaCl, 1 mM EDTA, 10 % (v/v) glycerol
saACP-saFabI fusion*	<i>SEC I:</i> 25 mM Tris/HCl, pH 7.5, 200 mM NaCl, 1 mM EDTA <i>SEC II:</i> 20 mM Na ₃ Citrate/HCl, pH 5.6, 250 mM NaCl, 1 mM EDTA
saACP-ecFabI fusion	20 mM Tris/HCl, pH 7.5, 200 mM NaCl, 1 mM EDTA

* Buffers for proteins containing Cys mutations were supplied with 0.5 mM TCEP or DTT, where TCEP is the better alternative when subsequent modification or crosslinking experiments shall be conducted.

DYE-LIGAND AFFINITY CHROMATOGRAPHY

The dye-ligand affinity chromatography was employed as a special strategy in an attempt to separate modified, cross-linked fusion protein from non-modified and/or non-crosslinked protein. The preceding crosslinking reaction was applied to a 1 ml HiTrap™ Blue HP column, which was connected to an FPLC system and pre-equilibrated with *Binding buffer*. A salt-gradient elution from 0 – 100 % elution buffer over 10 CV was performed and fractions were collected and analysed by SDS-PAGE.

<i>Binding buffer</i>	20 mM Tris/HCl, pH 8.0
<i>Elution buffer</i>	20 mM Tris/HCl, pH 8.0, 2 M NaCl

2.2.3 Biochemical and biophysical characterisation

DETERMINATION OF PROTEIN CONCENTRATIONS USING UV/VIS SPECTROPHOTOMETRY

The concentration of a purified protein was determined by measuring the UV absorbance of the protein using the NanoDrop ND 1000 UV/Vis spectrophotometer. A UV/Vis spectrum ranging from 220 nm – 350 nm was recorded for the respective protein, corrected by the absorption proportion of the buffer solution. The protein concentration was calculated from the absorption at $\lambda = 280$ nm, implying the molar extinction coefficient of the protein. The molar extinction coefficient was derived from the protein's primary sequence using the *ExPASy ProtParam* tool. For proteins containing no or a low percentage of aromatic amino acids, the following method was utilised to determine their concentration.

DETERMINATION OF PROTEIN CONCENTRATIONS USING THE BICINCHONIC ACID (BCA) ASSAY

The concentrations of proteins, especially ACPs, showing weak absorption at 280 nm were determined using the BCA assay. For calibration, a standard curve was generated using BSA concentrations of 0.025, 0.125, 0.25, 0.50, 0.75, 1.00, 1.50 and 2.00 mg·ml⁻¹. Therefore, BSA was diluted in a working solution to a volume of 5 μ l each. 100 μ l of the working solution were added to each standard, as well as to 5 μ l of each sample, and mixed by up-and-down pipetting. The aliquots were then incubated for 30 min at 37 °C in a heating block. Subsequently, absorptions of the standards were recorded at the BioPhotometer spectrophotometer from the lowest to the highest concentration at $\lambda = 562$ nm with the working solution as blank value. The calibration curve was saved and the samples were measured accordingly.

PROTEIN SEPARATION BY SODIUM DODECYL SULFATE POLYACRYLAMIDE GEL ELECTROPHORESIS (SDS-PAGE)

Depending on the size of the protein, the percentage of polyacrylamide (PAA) in the separating gel varied between 15 % and 18 %. Gels were prepared by first casting the separating gel and after

complete polymerisation adding the stacking gel on top. Protein samples were mixed 5:1 with SDS-PAGE loading buffer and denatured at 95 °C for 5 – 10 min in a heating block. The protein samples and a molecular weight marker were loaded into the slots of the gel, which had been previously placed in an electrophoresis chamber filled with SDS-PAGE running buffer. A voltage of 180 V was applied and electrophoretic separation of proteins depending on their molecular weight was performed for 60 – 80 min.

The gels were stained either by incubation in Coomassie R-250 staining solution for 20 min, followed by destaining in destaining solution; or boiled three times with water and subsequently heated with Coomassie G-250 staining solution and incubated for 10 – 15 min, followed by destaining in water.

Stacking gel	5 % acrylamide/bisacrylamide mix (37.5:1), 125 mM Tris/HCl, pH 6.8, 0.1 % (w/v) SDS, freshly added: 0.1 % (w/v) APS, 0.1 % (v/v) TEMED
Separating gel	12 – 18 % acrylamide/bisacrylamide mix (37.5:1), 250 mM Tris/HCl, pH 8.8, 0.1 % (w/v) SDS, freshly added: 0.1 % (w/v) APS, 0.04 % (v/v) TEMED
SDS-PAGE loading buffer	250 mM Tris/HCl, pH 6.8, 0.5 M DTT, 0.5 % (w/v) bromphenol blue, 10 % (w/v) SDS, 50 % (v/v) glycerol
SDS-PAGE running buffer	25 mM Tris, 192 mM glycine, 0.1 % (w/v) SDS
Coomassie R-250 staining solution	0.1 – 0.5 % (w/v) Coomassie R-250, 50 % (v/v) methanol, 10 % (v/v) acetic acid
Coomassie G-250 staining solution	0.008 % (w/v) Coomassie G-250, 35 mM HCl
Destaining solution	10 % (v/v) ethanol, 5 % (v/v) acetic acid

PROTEIN SEPARATION BY CONFORMATION-SENSITIVE GEL ELECTROPHORESIS (CSGE)

The separation of proteins using the CSGE methods allows the detection of proteins according to their conformation. In case of ACP, slightly unfolding conditions induced by the presence of urea within the gel, loading and running buffer enables the detection of acyl modifications. Depending on the urea concentration different acyl-ACPs can be separated by their acyl chain length and degree of chain saturation. ACPs attached to shorter acyl chains separate at lower urea concentrations, whereas longer-chain acyl-ACPs separate at higher urea concentrations [134].

Gels were cast as described above. The protein samples were mixed 5:1 with CSGE-loading buffer and stored on ice until they were loaded onto the gel. The electrophoresis and staining procedures were similar to that described for an SDS-PAGE.

Stacking gel	5 % acrylamide/bisacrylamide mix (29:1), 125 mM Tris/HCl, pH 6.8, 500 mM urea, freshly added: 0.1 % (w/v) APS, 0.1 % (v/v) TEMED
---------------------	--

Separating gel	12 – 18 % acrylamide/bisacrylamide mix (29:1), 375 mM Tris/HCl, pH 8.8, 500 mM urea, freshly added: 0.1 % (w/v) APS, 0.04 % (v/v) TEMED
CSGE loading buffer	250 mM Tris/HCl, pH 6.8, 0.5 % (w/v) bromphenol blue, 250 mM urea, 50 % (v/v) glycerol
CSGE running buffer	25 mM Tris, 192 mM glycine

PROTEIN SEPARATION BY NATIVE PAGE

Gels for native PAGE were cast in one piece from a 5 % PAA solution. The gels were set into an electrophoresis chamber filled with running buffer and pre-equilibrated to 4 °C. Protein samples were mixed 6:1 with loading buffer, kept on ice and loaded into the slots of the gel in the cold room. Electrophoresis was performed for 1 – 2 h at 4 °C applying a voltage of 80 V. The gels were stained with Coomassie R-250.

Gel composition I (basic)	5 % acrylamide/bisacrylamide mix (37.5:1), 375 mM Tris/HCl, pH 8.0, freshly added: 0.1 % (w/v) APS, 0.1 % (v/v) TEMED
Gel composition II (acidic)	5 % acrylamide/bisacrylamide mix (37.5:1), 375 mM Na ₃ Citrate/NaOH, pH 5.6, freshly added: 0.1 % (w/v) APS, 0.1 % (v/v) TEMED
Native-PAGE loading buffer	0.01 % (w/v) Orange G, 60 % (v/v) glycerol
Native-PAGE running buffer I (basic, TAE)	40 mM Tris/HCl, pH 8.0, 20 mM acetic acid, 1 mM EDTA
Native-PAGE running buffer II (acidic)	40 mM Na-acetate/acetic acid, pH 5.6, 1 mM EDTA

SILVER STAINING

For a more sensitive detection of proteins in a gel, e.g. when protein crystals were submitted to SDS-PAGE, silver staining was applied. Gels were fixed for ≥ 1 h, afterwards rinsed with water and washed three times for 20 min in 50 % (v/v) ethanol. Subsequently, the gels were incubated for 1 min in sensitiser and washed three times for 20 s with water. The thus prepared gels were transferred to the AgNO₃ solution for 20 min and washed again three times for 20 s with water. Afterwards, developer solution was applied and the gels were incubated until sufficient staining was achieved. The reaction was stopped by the addition of 1 % acetic acid, followed by several washing steps with the same.

Fixer	50 % (v/v) methanol, 10 % (v/v) acetic acid
Sensitiser	0.02 % (w/v) Na ₂ S ₂ O ₃
AgNO₃ solution	0.2 % (w/v) AgNO ₃ , freshly added: 0.075 % (v/v) formaldehyde
Developer	6 % (w/v) Na ₂ CO ₃ , freshly added: 0.05 % (v/v) formaldehyde

DETERMINATION OF THERMAL PROTEIN STABILITY USING THERMOFLUOR ANALYSIS

To identify optimal buffer conditions that may enhance the thermal stability of the fusion constructs, different buffer conditions from the ThermoFluor Standard screen were tested followed by the ThermoFluor Advance array, containing the aforementioned buffer conditions in combination with different salt concentrations for further improvement. Each buffer condition contained 0.5 mg·ml⁻¹ protein and 5x SYPRO® Orange fluorescence dye. Controls were composed of SEC-II buffer alone (**Table 2.2-V**), SEC-II buffer plus the fluorescence dye, and protein in SEC-II buffer without the fluorescence dye.

To investigate the cofactor-binding ability of the fusion constructs, a plate containing a serial 1:2 dilution of NADPH in the respective SEC-II buffer was set up. The protein concentration was kept constant in all conditions at either 1 µM or 5 µM and the cofactor concentration ranged from 100-fold molar excess over protein to $\approx \frac{1}{20}$ of the respective protein concentration. Controls were set up in SEC-II buffer and included the highest NADPH concentration used throughout the assay with and without the fluorescence dye, fluorescence dye alone, and fluorescence dye with the protein at both concentrations tested.

ANALYTICAL SIZE-EXCLUSION CHROMATOGRAPHY

For analytical SEC the Superdex® 200 10/300 GL column attached to the FPLC system was used and pre-equilibrated with the appropriate SEC buffer at 4°C. FabI-protein samples were prepared by incubating the respective enzyme with NAD(P)⁺/H on ice for \approx 30 min. For single-protein analysis, the protein was centrifuged for 10 min at 16 100 x g at 4 °C and then applied to the column. To analyse ACP-FabI complexes, ACP was added to the FabI-cofactor mixture after incubation, the proteins were incubated together for another 60 min and centrifuged. Different molar ratios of [ACP:FabI] were tested including 2:1, 1:1 and 1:2, and different buffer conditions applied as well (*see table below*). Separation was conducted over 1.2 CV and the fractions were analysed by SDS PAGE.

Buffer	saACP	saFabI	ecFabI	bpFabI	ftFabI	[saACP· saFabI]	[saACP· ecFabI]
20 mM Na ₃ Citrate/ NaOH, pH 5.5, 200 or 250 mM NaCl, 1 mM EDTA	x	x	x	x	x	x	x
20 mM Tris/HCl, pH 7.0, 150 mM NaCl, 1 mM EDTA	-	-	x	-	-	-	x

"x": tested; "-" : not tested

MOLECULAR WEIGHT DETERMINATION BY MULTI-ANGLE LIGHT SCATTERING (MALS)

MALS analyses were performed at room temperature, comprising analytical SEC via an appropriate column attached to an ÄKTApurifier 10, coupled to a MALS detector and a refractive index (RI) monitor. Protein samples were diluted to a concentration of 5 – 20 mg·ml⁻¹ with MALS buffer, or dialysed in the respective buffer. When cofactor and/or inhibitor were added (10- and 20-fold molar excess, respectively), the complex was incubated on ice for 1 – 2 h. Samples were centrifuged for 20 min at 16 100 x g and 4 °C and equilibrated to room temperature prior to application to the system. 100 µl of the protein sample were injected to the pre-equilibrated column and separated over 1.2 CV. Recorded light-scattering data were processed and analysed with the *AstraVI* software.

CHEMICAL PROTEIN-PROTEIN CROSSLINKING

Crosslinking of proteins was conducted following the instructions of the supplier. Different [ACP:FabI:cofactor:crosslinker]-ratios were tested as well as crosslinkers with different spacer-arm lengths for different pairs of cysteines. The reaction was conducted in crosslinking buffer, containing 20 mM Tris/HCl, pH 6.9, 150 mM NaCl, 10 mM EDTA and the mixture was incubated for 1 h at room temperature, except for an initial test where crosslinking was monitored over 2 h incubation time.

Prior to the reaction start, saFabI was incubated on ice for 30 min with either oxidised or reduced cofactor, depending on the nature of the ACP-coupled acyl substrate used in the particular reaction setup. In case of the saACP-saFabI-Ib double-cysteine mutant, the cofactor was added simultaneously with the crosslinking reagent. The reaction was quenched by placing the tube on ice and either the addition of 50 mM DTT and/or buffer exchange via spin concentration or application to a size exclusion column. The success of the reaction was validated by SDS-PAGE analysis.

saACP-saFabI cysteine pair	Tested ACP:FabI- ratios	Concentration range (μ M, for single protein component)	NADP ⁺ /H (molar excess over saFabI)	Crosslinker	
				Type (spacer-arm (\AA))	Molar excess
E41C-K17C	1:1,	10 – 100	5 – 10	BMB (10.9), BMH	2 – 3 ^a ,
	1:1.5			(13.0), BM(PEG) ₂ (14.7)	1 – 1.5 ^b
E47C-K17C	1:2,	5 – 40	10 – 100	BMB (10.9), BMH	1 – 3 ^a ,
	2:1			(13.0)	0.7 – 2 ^b
E47C-K17C*	1:1	100	20	BMB (10.9)	3 ^{a,b}
E41C-K50C	1:1	100	20	BMOE (8.0), BMB	6 ^a , 3 ^b
				(10.9)	

*saACP_E47C-saFabI_K17C-Ib fusion construct; a: molar excess of crosslinking agent over the protein component with the highest concentration in each reaction, b: molar excess of crosslinking agent over the sum of protein in each reaction

2.2.4 Protein crystallisation

PRE-CRYSTALLISATION TEST (PCT)

To estimate protein concentrations suitable for crystallisation setups, the Hampton Research PCT™ was used. Pre-crystallisation tests were conducted at room temperature in a 24-well hanging-drop format following the manufacturer's instruction. The reaction progress was monitored either after 30 min and/or 24 h.

PROTEIN PREPARATION

For the crystallisation of protein-inhibitor complexes, the protein was diluted to the target concentration in SEC buffer. The cofactor was added at 5 – 10-fold molar excess and the inhibitor, dissolved in DMSO, at 20 – 100-fold molar excess with respect to the protein concentration, and the complex was incubated on ice for 1 – 2 h. Afterwards, the mixture was centrifuged for 20 – 30 min at 16 100 x g and 4 °C.

The ACP-FabI complexes were either directly obtained from the SEC column, diluted in SEC buffer and centrifuged for 10 min at 16 100 x g and 4 °C, or were combined by mixing the single components in the respective SEC buffer prior to crystallisation. Prior to complex formation, FabI was incubated with the cofactor at 10 – 20 molar excess for 30 min on ice and ACP was added subsequently, followed by incubation for another 60 - 90 min on ice. In other cases, all components were mixed at the same time and stored on ice for 1 h. After incubation, the proteins were centrifuged for 10 min at 16 100 x g and 4 °C. Complexes were set up at ACP:FabI-ratios of 1:2, 1:1 and 2:1.

Some complexes obtained from a crosslinking experiment were either directly submitted to crystallisation, or buffer was exchanged first using a spin concentrator.

CRYSTALLISATION BY 96-WELL SITTING-DROP VAPOUR-DIFFUSION

The 96-well sitting-drop vapour-diffusion setup was mostly used for initial crystallisation tests, but also for optimising promising conditions identified during initial screening. Optimisation included the variation of conditions regarding salt-, precipitant-, additive- and protein concentrations or pH. Additionally, the 96-well format was used to prepare additive screens.

Screens were set up at room temperature in a 96-well crystallisation plate with a reservoir volume of 40 μ l and a sitting drop composed of 0.3 μ l protein solution and 0.3 μ l reservoir solution using the HoneyBee 963 crystallisation robot. When additive screens were performed, 45 μ l reservoir of a specific reservoir solution were added to each well, followed by 5 μ l of the different additive solutions. The drops were pipetted afterwards in the above described 0.3 μ l protein/0.3 reservoir μ l composition. The plates were sealed with adhesive film and stored at 20 °C.

CRYSTALLISATION BY 24-WELL HANGING-DROP VAPOUR-DIFFUSION

The 24-well hanging-drop technique was used when crystallisation conditions were known, when crystals from the 96-well format were to be improved with respect to their size or when crystallisation conditions were optimised in a smaller range. The setups were prepared by hand using a 24-well plate with a reservoir volume of 1 ml and drop volumes of 2 – 3 μ l. Protein-solution:reservoir compositions of the drops varied between ratios of 1:1, 1:2 and 2:1. Plates were either prepared at room temperature and stored at 20 °C, or in the cold room and stored at 4 °C. The drops were pipetted onto circular cover slides and placed upside-down on top of the reservoir, which was coated with silicon grease to seal the well.

SEEDING

Seeding was used to optimise crystals for X-ray diffraction measurements. For micro-seeding pre-existing crystals from earlier crystallisation setups were diluted in reservoir solution to a \approx 1:50 ratio and destroyed by sonication in an ultrasonic bath for 10 min. The solution was vortexed and dilutions of 1:100, 1:250, 1:500 and 1:1000 were prepared. 0.2 μ l of the seeding solution were added to drops of the crystallisation experiment, or seeds were transferred to the drop utilising a cat whisker.

DEHYDRATION OF CRYSTALS

To improve the diffraction quality of crystals by reducing their solvent content, dehydration with different low-molecular-weight PEGs and MPD was tested. Prior to freezing, crystals were transferred

from a drop containing the mother liquor to a series of drops containing the mother liquor plus increasing concentrations of small PEGs or MPD (5 – 25 % (v/v)), or increasing concentrations of the PEG already existing in the respective reservoir solution. Crystals were incubated in each drop for \approx 5 min and then transferred to the next one.

In another attempt, the existing crystallisation drop was transferred on top of a reservoir containing the initial crystallisation solution supplemented with 13.75 % (v/v) MPD. The drop was incubated overnight, followed by incubation for another 8 h over a reservoir with twice the preceding MPD concentration. The same procedure was also applied to crystals which were transferred to a fresh drop composed of the crystallisation condition and a low concentration (7.5 % (v/v)) of low-molecular-weight PEG or MPD.

HIGH-PRESSURE COOLING

To improve crystal diffraction and avoid potential damage of crystals by the addition of cryoprotectants freezing of crystals by applying high pressure during this process was pursued alternatively [135]. Single crystals were first transferred into a transparent, spoon-shaped Kapton[®] capillary, which had been previously filled with the respective mother liquor from the reservoir. Subsequently, the sample holders containing the crystals were transferred to a drop tube and fixed at the top of the tube with a magnet. The lower part of the pressurising tube was placed in liquid nitrogen at 77 K. The pressure in the tube was then raised in two steps to 200 MPa and the magnet was removed. This caused the sample holder to drop to the cold zone of the tube and induce crystal freezing. The pressure was released and the sample holder was taken out of the drop tube, mounted to a cap suitable for spine pucks and transferred to a cryo vial under liquid nitrogen. The experiment was conducted at the ESRF in Grenoble, France and kindly assisted by the local staff.

2.2.5 X-ray crystallography

Prior to the collection of diffraction images, crystals were cryoprotected and flash-frozen in liquid nitrogen or frozen at high pressure without cryoprotectant as described above. For cryoprotection, crystals were transferred with a cryo-loop from the original condition to a drop of the same composition plus an additional cryoprotectant. The cryo-solutions contained, for example, 5 – 40 % (v/v) ethylene glycol, 15 – 25 % (v/v) glycerol or elevated concentrations of a cryoprotecting agent already present in the condition.

DATA COLLECTION AND PROCESSING

To initially estimate the diffraction quality of a crystal, test images were collected at least at two different angles. Data sets of crystals with sufficient quality were collected according to the known or calculated space group based on initial processing utilising *XDS*, *MOSFLM* or *d*TREK*. The collection parameters either followed a suggested data collection plan, e.g. by the sample characterisation softwares *EDNA* (ESRF) or *CrystalClearTM* (in-house X-ray source), or were adjusted to other purposes and considered overall crystal quality (e.g. mosaicity, resolution, anisotropy). Pre-tests and data collection were carried out either using the in-house X-ray source or at synchrotron radiation facilities in Berlin (BESSY), Grenoble (ESRF) or Hamburg (DESY/EMBL). The following parameters were applied for data collection of herein described structures:

Collection parameter	Data sets				
	<i>[InhA·NAD⁺·PT501]</i>	<i>[InhA·NAD⁺·PT504]</i>	<i>[InhA·NAD⁺·PT506]</i>	<i>[InhA·NAD⁺·PT511], merged</i>	
	<i>DS1</i>	<i>DS2</i>			
Beamline	BESSY BL 14.1	BESSY BL 14.1	BESSY BL 14.1	EMBL BL P13	
Wavelength (Å)	0.91841	0.91841	0.91841	0.96725	
Detector	Dectris PILATUS 6M	Dectris PILATUS 6M	Dectris PILATUS 6M	Dectris PILATUS 6M-F	
Detector distance (mm)	525.84	476.51	371.19	481.34	
Number of images	1000	1800	1800	2000	2000
Oscillation (°)	0.1	0.1	0.1	0.1	0.1
Exposure time (s)	0.4	0.3	0.15	0.05	0.1

Collection parameter	Data sets				
	<i>[InhA·NAD⁺·PT512]</i>	<i>[InhA·NAD⁺·PT514]</i>	<i>[InhA·NAD⁺·55JS]</i>	<i>[bpFabI·NAD⁺·PT405]</i>	<i>[saFabI·NADP⁺·55JS]</i>
Beamline	BESSY BL 14.1	BESSY BL 14.1	BESSY BL 14.1	ESRF ID29	ESRF ID30
Wavelength (Å)	0.91841	0.91841	0.91841	0.97625	0.97625
Detector	Dectris PILATUS 6M	Dectris PILATUS 6M	Dectris PILATUS 6M	Dectris PILATUS3 6M	Dectris PILATUS3 6M
Detector distance (mm)	323.73	349.91	371.19	567.53	387.01
Number of images	1800	1800	1800	780	3600
Oscillation (°)	0.1	0.1	0.1	0.15	0.1
Exposure time (s)	0.3	0.3	0.5	0.02	0.02

Data indexing, integration and scaling was either conducted using *XDS* or the combination of *MOSFLM* and *SCALA* or *AIMLESS* from the *CCP4 program suite*.

STRUCTURE SOLUTION AND MODEL REFINEMENT

All structures were solved by molecular replacement (MR) using PDB entry 2X23 (InhA in complex with PT70), PDB entries 3EK2 (*apo*-bpFabI) and 4BKU (bpFabI-1 in complex with PT155), or 4BNH (saFabI in complex with PT04) as search models for InhA-, bpFabI- or saFabI structures, respectively. The searches were performed with *PHASER* and subsequent refinement cycles with *REFMAC* or *Phenix*, where 5 % of the reflections were set aside for cross-validation. *Coot* was used for model building.

3 Results

3.1 Purification and crystallisation of InhA

3.1.1 Purification of InhA

The initial application of cell lysate containing recombinantly expressed InhA to a Ni²⁺-affinity chromatography column already resulted in large amounts of highly pure protein (**Figure 3.1-I, left panel**).

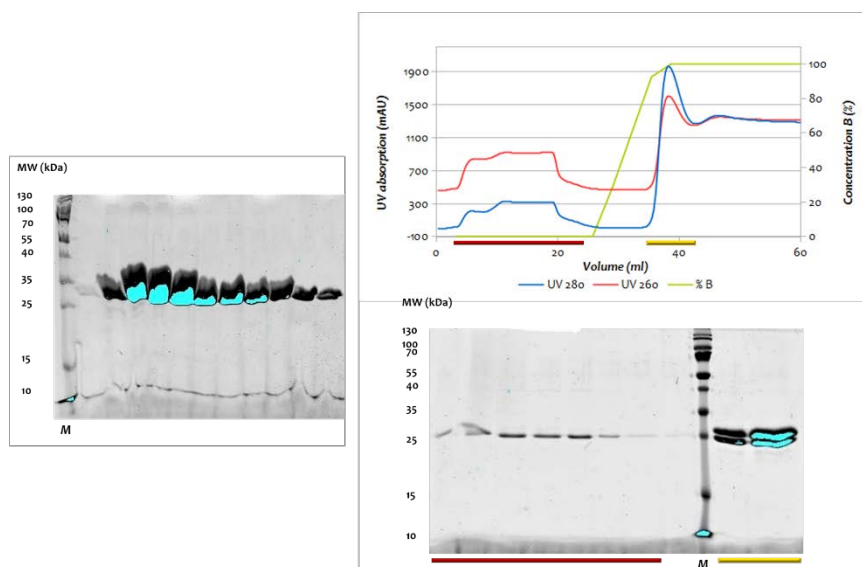


Figure 3.1-I: Protein obtained from Ni²⁺-affinity chromatography steps for non-cleaved (left panel) and thrombin-cleaved (right panel) InhA: The unbound fractions' peak (cleaved InhA) from the Ni²⁺-affinity column after thrombin-cleavage is indicated by a red bar, the Ni²⁺-bound InhA-elution fractions (non-cleaved InhA) are marked in yellow.

Subsequent thrombin cleavage as described previously [61] drastically reduced the amount of pure and cleaved protein and resulted in a large fraction of co-eluted cleaved and non-cleaved InhA. Even a second application of the pool containing both species to the affinity chromatography column did not lead to a satisfactory separation of both components (**Figure 3.1-I, right panel**). This is probably due to tetramer formation of InhA, irrespective of the presence or absence of a His₆-tag on single monomers. The presence of at least one His₆-tagged monomer can promote binding of an entire tetramer to the Ni²⁺-affinity column, hence resulting in the double band observed in fractions containing elevated imidazole concentrations. Consequently, the cleavage step was omitted from the purification protocol and a reasonable amount of pure protein was obtained from an initial Ni²⁺-affinity chromatography step, immediately followed by SEC (**Figure 3.1-II**).

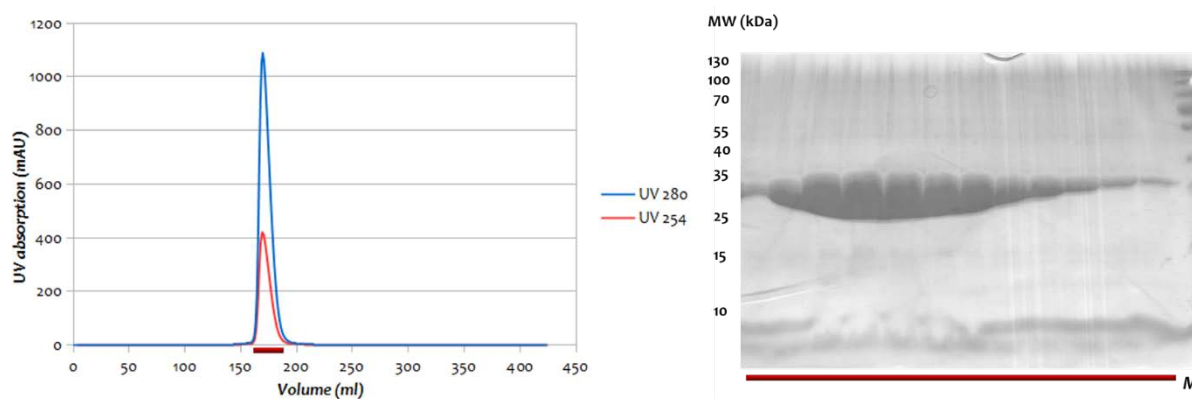


Figure 3.1-II: SEC elution profile and SDS-PAGE analysis of non-cleaved InhA: Peak fractions are marked with a red reference bar. This SEC result was obtained during the Master thesis work of Annica Pschibul.

3.1.2 Crystallisation of InhA

Initial 96-well screens, to identify appropriate crystallisation conditions for InhA containing the His₆-tag and to avoid the presence of DMSO in the crystallisation solution, yielded conditions different from those described earlier by *Silvia Luckner* [77].

Crystals of the ternary InhA-NAD⁺-inhibitor complexes were obtained from reservoir conditions containing either 2 – 3 M NaCl in combination with 100 mM Tris/HCl or Hepes buffer at a pH range between 7.0 and 9.0; or merely 1.6 – 3.5 M sodium acetate at pH 7.0. The crystals grew in various shapes comprising needles, plates or octahedrons at a protein concentration of 10 mg·ml⁻¹ (0.33 mM). The best data sets of the [InhA·NAD⁺·PT504] and [InhA·NAD⁺·PT512] complexes were collected from crystals grown in 1.6 M sodium acetate, pH 7.0, with a 5-fold molar excess of cofactor and a 50-fold molar excess of inhibitor relative to InhA. The [InhA·NAD⁺·PT506] complex crystallised at a sodium acetate concentration of 2.4 M with only a 20-fold molar excess of PT506. Crystals of the PT501- and PT514-complexes diffracted best when grown in 2.5 or 3 M sodium chloride and 100 mM Tris-HCl, pH 8.0 or 9.0, at a 10- or 5-fold molar excess of cofactor, respectively, and a 50-fold molar excess of inhibitor. The quality of the initial [InhA·NAD⁺·PT511] crystals was not sufficient for recording high resolution X-ray data. Hence, InhA-PT501 crystals were utilised for seeding to improve the PT511-complex crystals. Crystals displaying better diffraction properties were obtained in 2.6 M sodium acetate, pH 7.0, with a 10-fold molar excess of cofactor and a 20-fold molar excess of PT511 relative to InhA. For the [InhA·NAD⁺·55JS] complex the best data were collected from a crystal grown at a 5-fold molar excess of cofactor and a 20-fold molar excess of inhibitor over protein in 100 mM Tris/HCl, pH 8.4 and 3 M NaCl. The best data sets for the [InhA·NAD⁺·101JS] structure were collected from crystallisation conditions either containing 2.6 M sodium acetate, pH 7.0, or 100 mM Tris-HCl, pH 8.0

Results

and 2 M NaCl at a 10-fold molar excess of cofactor and a 50- or 20-fold molar excess of inhibitor, respectively.



Figure 3.1-III: Crystals of [InhA·NAD⁺·inhibitor] complexes: (a) [InhA·NAD⁺·PT501] grown in 100 mM Tris/HCl, pH 9.0, 2.5 M NaCl; (b) [InhA·NAD⁺·PT501] grown in 100 mM Hepes, pH 7.0, 3 M NaCl; (c) [InhA·NAD⁺·PT511] grown in 3.5 M sodium acetate, pH 7.0 with a 1:100 PT501-seeding solution

Results

Table 3.1-I: Data collection and refinement statistics of the ternary [InhA·NAD⁺·inhibitor] complexes

Data sets						
	[InhA·NAD ⁺ · PT501]	[InhA·NAD ⁺ · PT504]	[InhA·NAD ⁺ · PT506]	[InhA·NAD ⁺ · PT511]	[InhA·NAD ⁺ · PT512]	[InhA·NAD ⁺ · PT514]
Data collection						
Space group	P2 ₁ 22 ₁	I2	I4 ₁ 22	P2	P2	P2
Unit cell parameters						
a/b/c (Å)	91.92/ 130.36/ 176.36	87.92/ 92.78/ 180.43	90.66/ 90.66/ 182.88	88.22/ 92.45/ 181.20	87.59/ 92.23/ 180.53	88.04/ 92.30/ 181.16
α/β/γ (°)	90.00/ 90.00/ 90.00	90.00/ 97.26/ 90.00	90.00/ 90.00/ 90.00	90.00/ 96.45/ 90.00	90.00/ 96.05/ 90.00	90.00/ 96.45/ 90.00
Resolution (Å)*	46.30 - 2.80 (2.89 - 2.80)	46.58 - 2.60 (2.70 - 2.60)	45.72 - 1.95 (2.06 - 1.95)	45.01 - 2.60 (2.65 - 2.60)	58.33 - 2.00 (2.03 - 2.00)	47.08 - 2.00 (2.03 - 2.00)
Total reflections	195155	151789	369099	672176	442855	668106
Unique reflections	52514	43766	28237	89324	155047	184367
Completeness (%)*	99.5 (98.9)	98.6 (98.5)	100.0 (100.0)	100.0 (100.0)	80.3 (73.4)	99.8 (99.9)
Redundancy*	3.7 (3.9)	3.5 (3.6)	13.1 (12.8)	7.5 (7.5)	2.9 (2.9)	3.4 (3.5)
R_{merge} (%)*	14.9 (72.1)	14.1 (163.7)	12.5 (136.3)	19.3 (142.8)	10.3 (60.7)	9.6 (100.4)
R_{pim} (%)*	8.8 (41.9)	8.9 (100.5)	3.6 (39.6)	7.5 (55.4)	7.2 (41.3)	6.0 (62.0)
<I/σ(I)>*	9.1 (1.9)	7.9 (0.9)	14.6 (2.0)	8.2 (1.3)	6.4 (1.9)	9.6 (1.3)
CC(1/2) (%)*	98.9 (58.7)	99.4 (29.9)	99.9 (41.5)	99.5 (57.0)	98.8 (44.6)	99.7 (45.5)
Refinement						
Monomers in the AU	6	4	1	8	8	8
Total number of atoms	12674	8332	2306	16844	17729	17867
R_{cryst} (%)	20.60	21.07	16.36	19.12	20.50	15.50
R_{free} (%)	24.37	23.95	21.23	21.33	23.41	17.78

Results

r.m.s.d. from ideal						
Bond length (Å)	0.016	0.017	0.026	0.014	0.021	0.024
Bond angles (°)	1.665	1.983	2.393	1.661	2.110	2.255
Average B-values (Å ²) and (# of atoms)						
All atoms	38.4 (12674)	74.5 (8332)	46.1 (2306)	50.4 (16844)	25.6 (17729)	30.9 (17867)
Protein	38.8 (12007)	75.3 (7927)	46.2 (2063)	51.1 (15944)	26.9 (15913)	30.7 (15892)
NAD	33.9 (264)	59.8 (176)	36.5 (44)	38.8 (352)	14.8 (352)	23.4 (352)
Water	28.0 (224)	54.3 (133)	48.2 (174)	36.9 (324)	27.4 (1246)	36.3 (1402)
Inhibitor	35.7 (168)	61.8 (96)	34.4 (25)	39.4 (224)	15.7 (216)	23.4 (216)
Ramachandran plot (<i>MolProbity</i>)						
Favoured (%)	95.0	91.5	95.5	95.1	95.5	95.6
Allowed (%)	4.6	7.0	3.8	4.9	4.5	4.4
Outliers (%)	0.4	1.5	0.7	0.0	0.0	0.0
PDB code	<u>5UGS</u>	<u>5UGT</u>	<u>5UGU</u>	<u>5MTQ</u>	<u>5MTR</u>	<u>5MTP</u>

* Numbers in parentheses represent values from the highest-resolution shell.

$R_{\text{merge}} = \frac{\sum_{\text{hkl}} \sum_j |I_{\text{hkl}}(j) - [I_{\text{hkl}}]|}{\sum_{\text{hkl}} \sum_j I_{\text{hkl}}(j)}$, where $I_{\text{hkl}}(j)$ is the j^{th} measurement of the intensity of a reflection and $[I_{\text{hkl}}]$ is the weighted mean value of all measurements of I .

$R_{\text{cryst}} = \frac{\sum_{\text{hkl}} ||F_{\text{obs}}| - |F_{\text{calc}}||}{\sum_{\text{hkl}} |F_{\text{obs}}|}$, where F_{obs} and F_{calc} are the observed and calculated structure factors, respectively. $R_{\text{free}} = R_{\text{cryst}}$ for 5 % of the data randomly omitted from the refinement.

Table 3.1-II: Data collection and preliminary refinement statistics of the InhA-55JS complex**[InhA·NAD⁺·55JS]**

Data collection		Refinement	
Space group	P6 ₄ 22	Monomers in AU	1
Unit cell parameters		Total number of atoms	2410
a/b/c (Å)	95.52/ 95.52/ 128.37	R_{cryst} (%)	14.12
α/β/γ (°)	90.00/ 90.00/ 120.00	R_{free} (%)	18.43
Resolution (Å)*	47.76 – 2.01 (2.12 - 2.01)	r.m.s.d. from ideal	
Total reflections	453979	Bond length (Å)	0.023
Unique reflections	23730	Bond angles (°)	2.267
Completeness (%)*	100.0 (100.0)	Average B-values (Å²) and (# of atoms)	
Redundancy*	19.1 (19.4)	All atoms	16.9 (2410)
R_{merge} (%)*	17.7 (109.5)	Protein	14.7 (2047)
R_{pim} (%)*	4.1 (25.4)	NAD	18.0 (44)
<I/σ(I)>*	15.5 (2.9)	Water	31.7 (287)
CC(1/2) (%)*	99.8 (90.2)	Inhibitor	22.6 (28)

* Numbers in parentheses represent values from the highest-resolution shell.

$R_{\text{merge}} = \frac{\sum_{\text{hkl}} \sum_j |I_{\text{hkl}}(j) - [I_{\text{hkl}}]|}{\sum_{\text{hkl}} \sum_j I_{\text{hkl}}(j)}$, where $I_{\text{hkl}}(j)$ is the j^{th} measurement of the intensity of a reflection and $[I_{\text{hkl}}]$ is the weighted mean value of all measurements of I .

$R_{\text{cryst}} = \frac{\sum_{\text{hkl}} ||F_{\text{obs}}| - |F_{\text{calc}}||}{\sum_{\text{hkl}} |F_{\text{obs}}|}$, where F_{obs} and F_{calc} are the observed and calculated structure factors, respectively. $R_{\text{free}} = R_{\text{cryst}}$ for 5 % of the data randomly omitted from the refinement.

3.2 Purification and crystallisation of different FabI enzymes

3.2.1 Purification and crystallisation of ecFabI

PURIFICATION

E. coli FabI (ecFabI) was purified following a protocol established in the laboratory. The purification yielded high amounts of reasonably pure protein (≈ 23 mg from 4 l cell culture or 24 g wet cell pellet), which eluted in its tetrameric form from the SEC column (**Figure 3.2-I**).

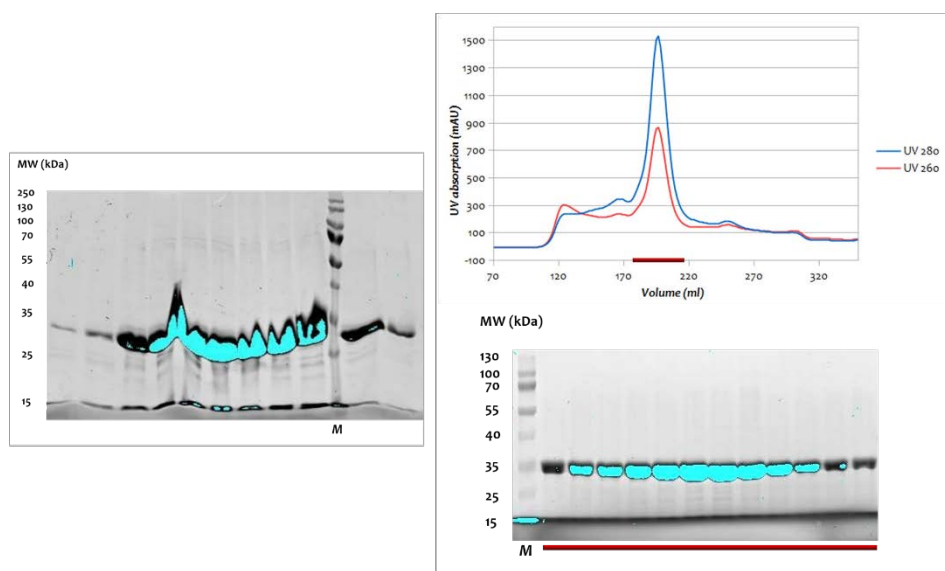


Figure 3.2-I: Purification of ecFabI: SDS-PAGE analysis of fractions obtained from Ni^{2+} -affinity chromatography (Ni-TED, left panel) and subsequent SEC (right panel). The red bar indicates the fractions from the SEC which were analysed by SDS-PAGE.

CRYSTALLISATION

The purified protein was used for the crystallisation of ecFabI in complex with the 4-pyridone inhibitor PT166, as it is described by *Schiebel and Chang, 2014* [130].

Various shapes of crystals were obtained at 13 and 15 $\text{mg}\cdot\text{ml}^{-1}$ (0.42 and 0.49 mM) ecFabI at different pH ranges. Crystals grew in reservoir conditions containing 0.1 M sodium citrate, pH 5.6, 0.2 M NH_4 acetate and 10 – 12 % (w/v) PEG 8000 or 8 – 28 % (w/v) PEG 3350; or in 0.1 M CAPS, pH 10.5, 0.2 M NH_4 acetate and 17 – 18 % (w/v) PEG 8000 or 24 – 30 % (w/v) PEG 3350. The best diffraction data were collected from a crystal grown in 0.1 M sodium citrate, pH 5.6, 0.2 M NH_4 acetate and 10 % (w/v) PEG 8000, containing a 10-fold molar excess of NADH and a 20-fold molar excess of PT166 over ecFabI.

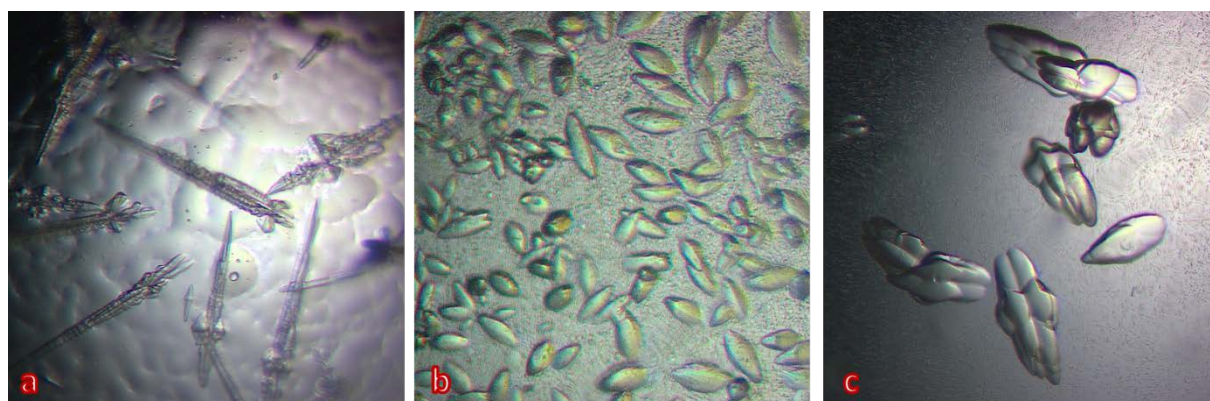


Figure 3.2-II: Crystals of [ecFabI-NADH-PT166] complexes: (a) 100 mM sodium citrate, pH 5.6, 0.2 M NH_4 acetate, 18 % (w/v) PEG 3350; (b) 100 mM CAPS, pH 10.5, 0.2 M NH_4 acetate, 30 % PEG 3350 (w/v); (c) 100 mM CAPS, pH 10.5, 0.2 M NH_4 acetate, 24 % (w/v) PEG 3350

3.2.2 Purification and crystallisation of saFabI

PURIFICATION

The purification of *S. aureus* FabI (saFabI) and its cysteine variants was conducted following an established protocol, which was derived from previously reported purification procedures [71, 136, 137]. Interestingly, during the SEC step from two different purifications in citrate buffer at pH 5.6 a different distribution of peaks was observed. In the second purification (**Figure 3.2-IIIb**) not only one peak at the elution volume of the tetramer with high absorption at $\lambda = 280$ nm as seen in an earlier purification (**Figure 3.2-IIIa**) was detected, but also an additional peak with low absorption at $\lambda = 280$ nm, but elevated absorption at $\lambda = 230$ nm at a higher elution volume, which might correspond to the dimeric form of saFabI. SDS-PAGE analysis revealed that the second (dimeric) peak contained reasonable amounts of saFabI and that these fractions contained less impurities than the ones from the first (tetrameric) peak. The reason why the second peak has been undiscovered so far, might originate from a neglect of UV-absorption detection at 230 nm during previous purifications. The higher content of impurities present in the first peak might contribute to the elevated absorption at $\lambda = 280$ nm, since saFabI itself generally exhibits moderate absorption at that wavelength. However, one difference between both purifications is that during the first purification the protein was dialysed in SEC buffer prior to application to the column. In contrast, for the second purification the sample was directly concentrated after the affinity step in Tris/HCl buffer at pH 8.0 and subjected to the SEC. It might be the case that the transition between the dimeric and tetrameric state had not fully taken place during the second purification. Nevertheless, SDS-PAGE analysis revealed that the small shoulder visible at higher elution volumes in the first purification chromatogram contains small amounts of saFabI as well and the peak asymmetry may be a sign for the presence of not only one single oligomeric species. This finding suggests that even at acidic pH saFabI is not exclusively present in its tetrameric state and exists in an – albeit strongly shifted towards the tetramer – equilibrium with its dimeric form, which may also apply to the fusion constructs as discussed in **Chapter 3.5.5**. Approximately 33 mg of pure protein were obtained from a 4 l cell culture (≈ 13 g wet cell pellet) from the tetrameric peak obtained during the first purification and a total amount of ≈ 73 mg saFabI were obtained from ≈ 14 g wet cell pellet (4 l cell culture) when both peaks from the second purification were pooled and concentrated separately.

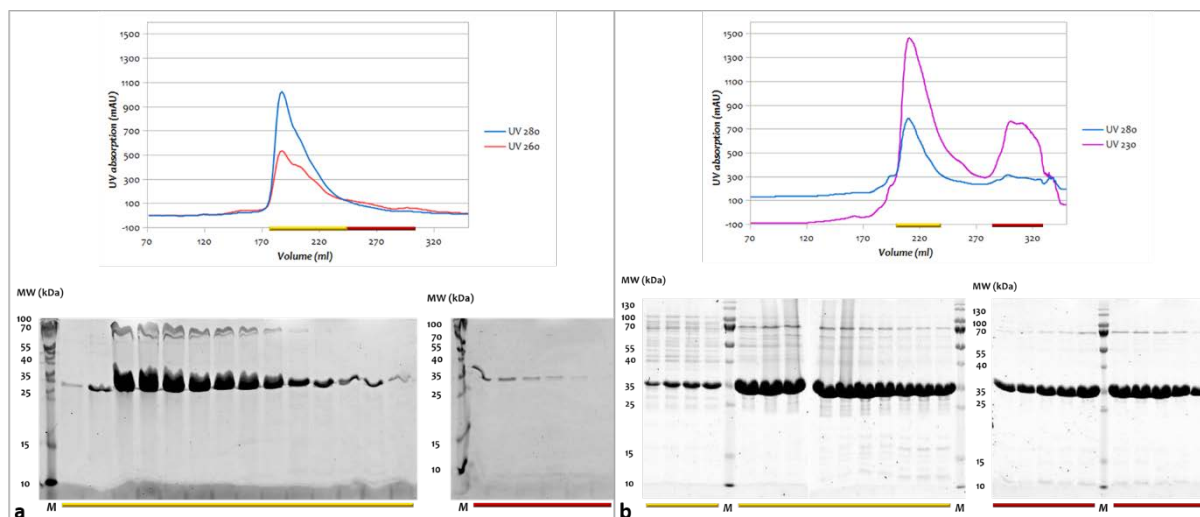


Figure 3.2-III: Elution profiles and SDS-PAGE analyses of SEC for saFabI: (a) Elution profile after preceding dialysis in SEC buffer; (b) Elution profile without previous dialysis; Fractions of the tetrameric peak are marked with a yellow, fractions from the putative dimeric peak are marked with a red reference bar.

CRYSTALLISATION

Crystals of saFabI in complex with different inhibitors displayed a platelet-like shape and only grew in very distinct reservoir conditions containing 100 mM Na/K-PO₄, pH 6.5 and 28 – 48 % (v/v) MPD (**Figure 3.2-IV**). The best diffraction data for [saFabI·NADP⁺·55JS] and [saFabI·NADP⁺·101JS] were obtained from crystals grown in 100 mM Na/K-PO₄, pH 6.5 and 35 or 48 % (v/v) MPD at a protein concentration of 0.42 mM (13 mg·ml⁻¹) or 0.48 mM (15 mg·ml⁻¹) and a molar protein : cofactor : inhibitor ratio of 1:10:50 or 1:10:20, respectively.



Figure 3.2-IV: Crystals of [saFabI·NADP⁺·inhibitor] complexes: (a) [saFabI·NADP⁺·55JS] grown in 100 mM Na/K-PO₄, pH 6.5 and 32 % (v/v) MPD; (b) [saFabI·NADP⁺·101JS] grown in 100 mM Na/K-PO₄, pH 6.5 and 48 % (v/v) MPD; (c) [saFabI·NADP⁺·101JS] grown in 100 mM Na/K-PO₄, pH 6.5 and 46 % (v/v) MPD

Table 3.2-I: Data collection and preliminary refinement statistics of the saFabi-55JS complex**[saFabi·NADP⁺·55JS]**

Data collection		Refinement	
Space group	P1	Monomers in the AU	8
Unit cell parameters		Total number of atoms	17147
a/b/c (Å)	90.35/ 94.56/ 94.78	R_{cryst} (%)	23.13
α/β/γ (°)	98.47/ 111.71/ 97.42	R_{free} (%)	25.95
Resolution (Å)*	49.55 – 1.96 (1.99 - 1.96)	r.m.s.d. from ideal	
Total reflections	696139	Bond length (Å)	0.021
Unique reflections	185831	Bond angles (°)	2.165
Completeness (%)*	91.6 (93.2)	Average B-values (Å²) and (# of atoms)	
Redundancy*	3.7 (3.8)	All atoms	19.5 (17147)
R_{merge} (%)*	16.3 (277.0)	Protein	17.8 (15805)
R_{pim} (%)*	9.7 (164.7)	NADP	31.8 (384)
<I/σ(I)>*	4.7 (0.4)	Water	40.8 (726)
CC(1/2) (%)*	99.4 (34.5)	Inhibitor	41.9 (224)

* Numbers in parentheses represent values from the highest-resolution shell.

$R_{\text{merge}} = \frac{\sum_{\text{hkl}} \sum_j |I_{\text{hkl}}(j) - [I_{\text{hkl}}]|}{\sum_{\text{hkl}} \sum_j I_{\text{hkl}}(j)}$, where $I_{\text{hkl}}(j)$ is the j^{th} measurement of the intensity of a reflection and $[I_{\text{hkl}}]$ is the weighted mean value of all measurements of I .

$R_{\text{cryst}} = \frac{\sum_{\text{hkl}} ||F_{\text{obs}}| - |F_{\text{calc}}||}{\sum_{\text{hkl}} |F_{\text{obs}}|}$, where F_{obs} and F_{calc} are the observed and calculated structure factors, respectively. $R_{\text{free}} = R_{\text{cryst}}$ for 5% of the data randomly omitted from the refinement.

3.3 Purification and modification of different ACP proteins

3.3.1 Purification and modification of saACP

SaACP was purified following the purification protocol established by Xu *et al.* [136]. Unmodified saACP could be obtained at an average amount of ≈ 5.4 mg per 10 g of wet cell pellet from the Ni²⁺-affinity purification step. However, during the subsequent modification process and separation by anion exchange chromatography, considerable amounts of protein were lost due to incomplete modification combined with insufficient separation of modified from unmodified protein during the anion-exchange step. Thus, optimisation trials for both steps were conducted.

MODIFICATION TESTS

During the modification reaction, *apo*-ACP is enzymatically converted to acyl-ACP by attaching a specific acyl substrate to a conserved serine residue of ACP. The acyl chain is coupled to the serine via a phosphopantetheine linker. Possible side reactions of the modification are the hydrolysis of the thioester bond between the phosphopantetheine and the acyl chain, leading to the presence of a *holo*-ACP species in the reaction mixture, which only contains the phosphopantetheine moiety. Modification assays in different buffers revealed that the best modification efficiency was achieved upon modification within the buffer composition ("*Buffer D*") previously suggested [136] (**Figure 3.3-1a**). Here, the endpoint of the reaction was already reached after 90 min and from this time point on no further conversion took place. In contrast, in "*Buffer I*" the reaction velocity was significantly slower and even after 5 h of incubation the conversion did not seem to be completed (**Figure 3.3-1b**). The "*T4 Buffer*" was introduced to shift the equilibrium by removing one of the products from the reaction and thereby increase the reaction velocity and efficiency. During the attachment of the acyl-phosphopantetheine moiety to saACP 3',5'-ADP is split off the acyl-CoA substrate, which in turn is a substrate of the T4-PNK enzyme and is decomposed to 5'-AMP and inorganic phosphate. Indeed, the reaction velocity was greater than the one for "*Buffer I*" and "*Buffer X*" and also the efficiency of the conversion was high, but it seems that the band located between the *apo* and acetyl-saACP is more prominent than in the other reactions (**Figure 3.3-1c**). "*Buffer X*" did not display any beneficial effect towards the reaction at all, since the velocity as well as the efficiency of conversion were least compared to the other reactions (**Figure 3.3-1d**).

In summary, "*Buffer D*" displays superior properties over the other buffer systems tested. The rapid conversion allows for shortened incubation times, once a proper modification protocol for a specific substrate is established. In "*Buffer I*" even greater amounts of *apo*-saACP might be converted to acetyl-ACP when the reaction time is prolonged. Nevertheless, longer incubation times also favour the cleavage of the acyl chain from saACP by hydrolysis of the thioester bond. This results in an increase of the band, which was visible in the middle between the *apo*- and the acyl-ACP bands in each modification reaction, probably representing *holo*-ACP. Hence, a compromise needs to be made between the reaction efficiency and incubation time to avoid decomposition of the acyl-ACP product. Modification efficiency also depends on the quality of the sfp used for each reaction and the incubation time might vary when using different batches of sfp.

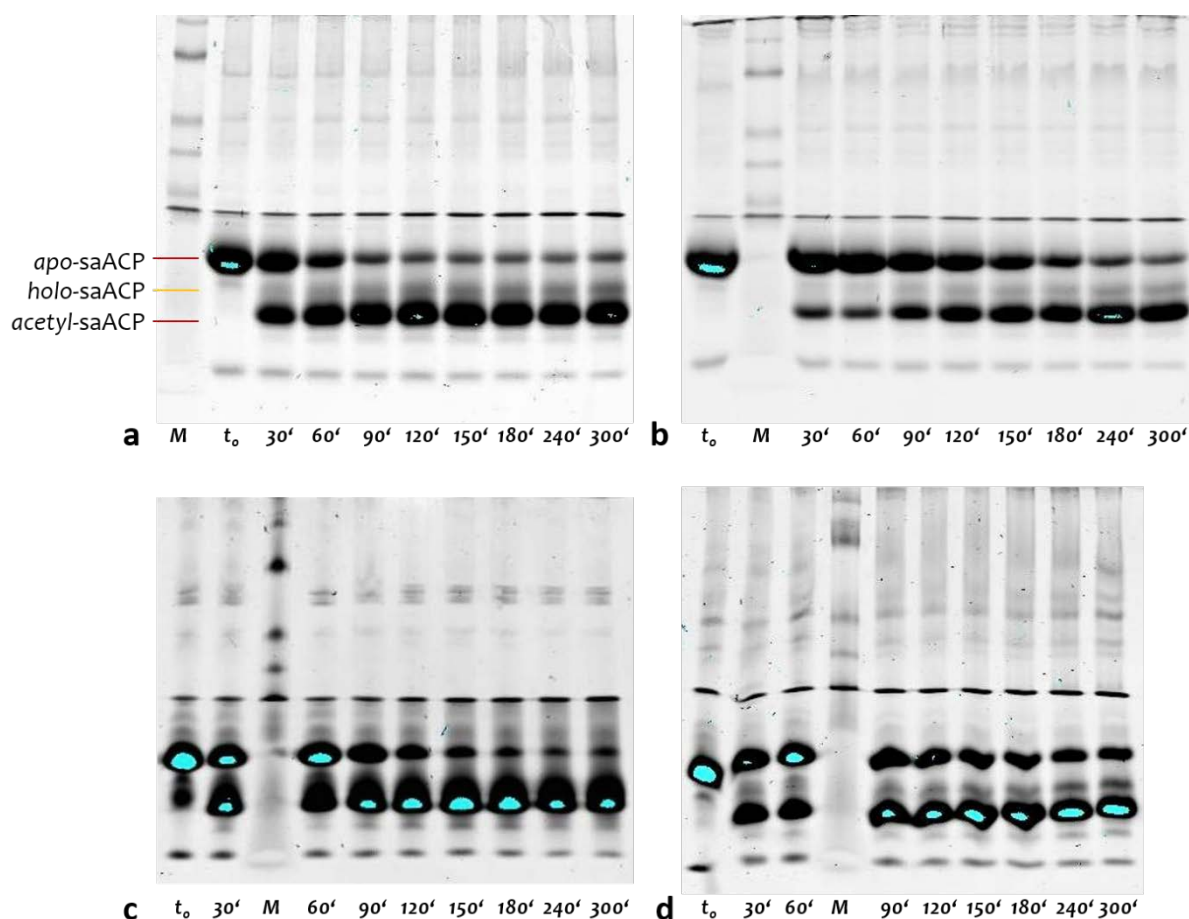


Figure 3.3-I: Modification trials for saACP with acetyl-CoA and sfp: The modification progress at 37 °C was monitored over 5 h. During the first three hours samples were taken each 30 min; afterwards samples were taken every 60 min. **(a)** 75 mM Tris/HCl, pH 7.5, 10 mM MgCl₂ ("Buffer D"); **(b)** 20 mM Tris/HCl, pH 8.0, 10 mM MgCl₂, 30 mM NaCl ("Buffer I"); **(c)** 70 mM Tris/HCl, pH 7.5, 10 mM MgCl₂, 5 mM TCEP, T4-PNK ("T4 Buffer"); **(d)** 25 mM Hepes, pH 7.4, 10 mM MgCl₂, 130 mM NaCl ("Buffer X")

OPTIMISATION OF THE YIELD FROM ANION-EXCHANGE CHROMATOGRAPHY

The analysis of the anion exchange chromatography revealed that next to fractions which contained either *apo* or acyl saACP, several fractions contained both, the *apo* and the acyl saACP even when a long and shallow gradient (35 CV) of increasing NaCl concentration was applied (**Figure 3.3-IIa**). After the evaluation of an initial purification, in the following described using the example of HD-N-saACP, the concentration of NaCl where a distinct acyl-ACP elutes from the column could be determined. Usually, *apo* and acyl-ACP eluted within the same peak displaying a gradient of an increasing proportion of modified ACP with increasing salt concentration. The elution procedure was then adapted in such a way that the concentration range crucial for the separation of *apo* and acyl-ACP was extended to 20 CV. **Figure 3.3-II** illustrates that a better separation of the main peaks I, II and III in the chromatogram was achieved and peak II, containing both ACP species was broadened when applying the optimised salt gradient. SDS analysis revealed a better separation of the modified and unmodified

ACP species, since within fractions of the initial purification, the portion of unmodified ACP in the mixed fractions was much more pronounced and only the last three fractions of the peak (**Figure 3.3-IIa, SDS gel**) contained pure HD-N-saACP or tolerable amounts of apo-saACP. In contrast, the optimised elution profile resulted in a larger number of fractions containing pure HD-N-saACP or only negligible amounts of apo-saACP and additionally, due to the better separation of peaks II and III, the very last fractions of peak II became usable for further applications (**Figure 3.3-IIb**).

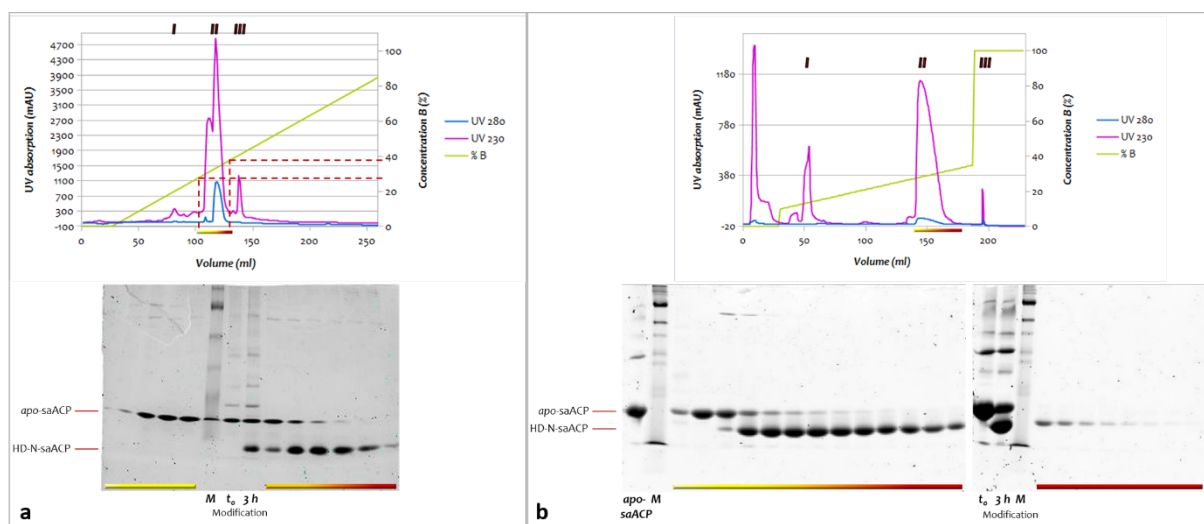


Figure 3.3-II: Optimised anion-exchange chromatography protocol for HD-N-saACP: (a) Initial separation of apo- and HD-N-saACP via anion-exchange chromatography using 35 CV of 0 – 100 % buffer B. Boundaries of NaCl concentrations at which saACP elutes are indicated by red, dashed lines. (b) Optimised salt gradient for the separation of apo- and HD-N-saACP using 20 CV from 10 – 35 % buffer B. The reference bar displays the proportions of apo- and HD-N-saACP, where higher concentrations of apo-saACP are indicated by a yellow and enhanced concentrations of HD-N-saACP are indicated by red colouring. The corresponding peaks from each elution are numbered.

The optimised elution could be applied to saACP modified with different acyl substrates purified in the course of this work, as well as to the saACP-cysteine variants. Nevertheless, optimal NaCl concentrations for separation varied with respect to the attached acyl chain. Thus, optimisation is necessary for each substrate, or a broader concentration range of NaCl must be covered when establishing a general standard purification protocol for any modification. To yield even larger amounts of HD-N-saACP it is possible to start the gradient at slightly higher concentrations of NaCl than applied for the exemplary purification described above, where a “buffer zone” was used to avoid elution of the target protein in the void volume.

3.3.2 Purification and modification of ecACP

EcACP was purified for the purpose of crystallisation trials with ecFabI, since saFabI is intrinsically more flexible compared to *E. coli* FabI and both proteins from the same organism may be necessary for proper complex formation.

Initially, ecACP was applied to a weak anion-exchange column and subsequent SDS-PAGE analysis of the different peaks revealed the presence of two putative ecACP bands within intersecting fractions of the elution. Nevertheless, a decrease of the higher-molecular weight species and an increase of the lower-molecular weight species was observed with rising salt concentrations (**Figure 3.3-IIIa**). A subsequent SEC step did not lead to a separation of both species due to their similar molecular weight. It might well be that one of the species is the native ecACP, since *E. coli* was used as expression host.

The purification protocol was therefore complemented with a Ni²⁺-affinity step succeeding the anion-exchange step, where the higher-molecular weight species was bound to the column, whereas the one with the lower molecular weight was eluted during the washing step (**Figure 3.3-IIIb**). The smaller protein might thus display native ecACP without a His-tag, whereas the larger protein could be identified to be the His-tagged ecACP. Although an affinity step was not described in former purification protocols [64], in this case it was necessary to obtain pure, recombinant protein. This step was important for subsequent modification steps, since native ecACP might be present as *holo* or acyl-ACP, resulting in an ACP sample containing several different acyl-ACP species, if both proteins were pooled after the anion-exchange step.

Results

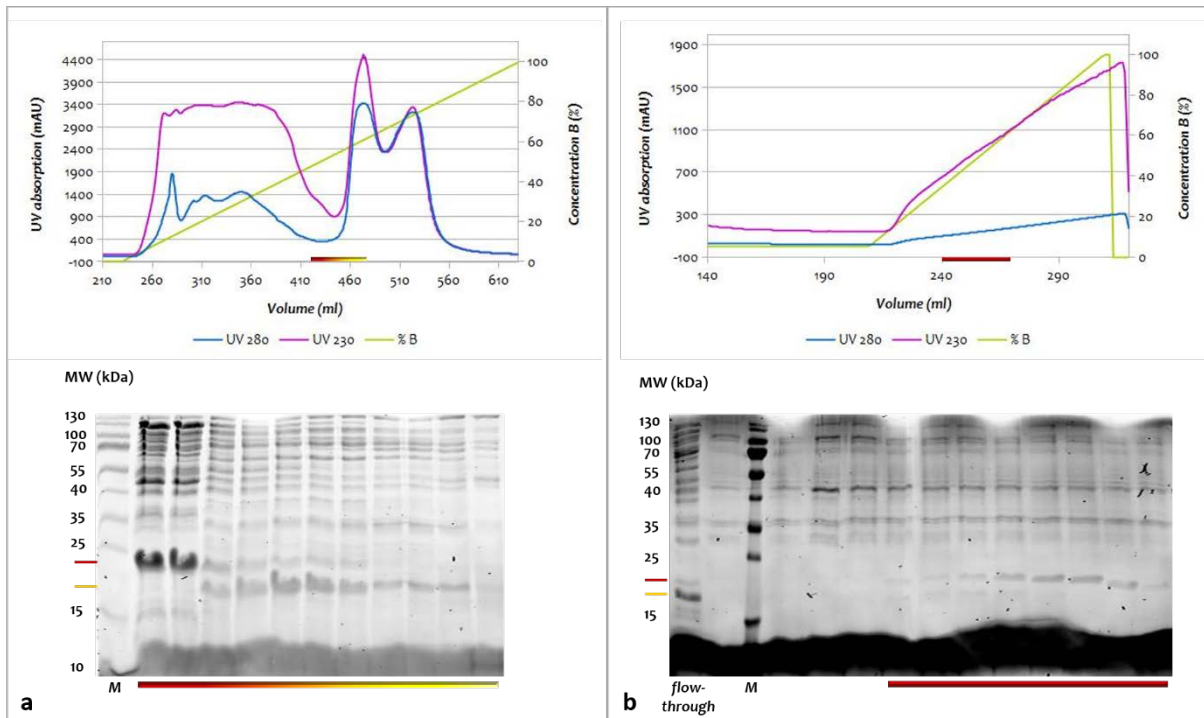


Figure 3.3-III: EcACP Purification: (a) Anion-exchange chromatography: The transition zone where both species are present is indicated by a reference bar. Red colouring displays an increased amount of His-tagged ecACP, whereas yellow colouring indicates the presence of the putative native ecACP. (b) Ni²⁺-affinity chromatography of ecACP: The lower-molecular weight species is primarily found in the flow-through.

Interestingly, CSGE analysis of a modification test did only display a weak band for unmodified ecACP already at time point zero and a prominent band at a position, where the modified species might be expected. The weak “*apo* band” seems to disappear totally towards the end of the modification process. Nevertheless, the comparison of the *apo*-ecACP sample with the reaction mixture revealed a clear difference in positions of the protein bands on the gel (Figure 3.3-IV). The faint band corresponding to *apo*-ecACP visible at the beginning of the reaction might be due to a very high activity of the AcpS enzyme used for modification. However, already the control sample of the presumably unmodified ecACP contains an additional band at the position of the putatively modified species. This might result from modification activity during protein expression in *E. coli* cells, since the target protein is a natural substrate for the enzymes present within the expression host.

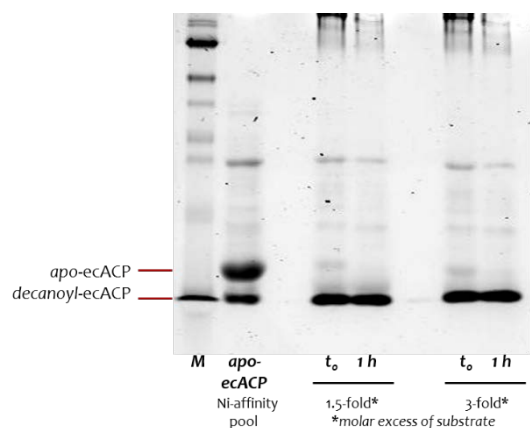


Figure 3.3-IV: Modification test for ecACP with decanoyl-CoA: The upper band probably represent the apo form of ecACP, whereas the lower band displays the modified fraction of ecACP or other, previously existing acylated species created by the expression host.

3.4 Investigation of complex formation between the single ACP and FabI components

3.4.1 Analytical size-exclusion chromatography (aSEC)

HD-N-saACP was analysed for complex formation in combination with different FabIs via analytical size-exclusion chromatography. Complex formation seemed to depend on different parameters, since HD-N-saACP by itself behaved differently on the aSEC column when eluted with different buffers. When Tris/HCl buffer was used for aSEC analysis, HD-N-saACP displayed a clear peak at an elution volume of ≈ 17 ml (**Figure 3.4-IIb**), whereas a high UV absorption at 230 nm was observed during the course of the entire elution when citrate buffer was used. However, very weak absorption peaks detected at $\lambda = 280$ nm indicated that the main HD-N-saACP peak shifted to a greater elution volume of ≈ 20 ml, supported by enhanced UV absorption at 260 nm (not shown), which was generally observed for HD-N-modified saACP (**Figure 3.4-Ib**). This elution profile was reproduced in a subsequent experiment. It is unclear why the absorption at $\lambda = 280$ nm was very low in both experiments. Both aSEC analyses were carried out using the same FPLC system and it is therefore possible that this was due to an intrinsic calibration error combined with a general weak absorption of saACP at that wavelength.

Taking these findings into consideration when comparing the elution profiles of the single proteins from the aSEC column with the ones from the complex, one might cautiously draw the conclusion that an interaction of HD-N-saACP with saFabI as well as with ecFabI took place in solution. In contrast, an interaction between HD-N-saACP and ftFabI could not be detected. The interaction experiment for HD-N-saACP with saFabI led to an additional peak at an elution volume of ≈ 17 ml compared to the elution volumes of the single components (**Figure 3.4-Ia, b**). SDS-PAGE analysis revealed that these fractions

indeed contained both proteins (**Figure 3.4-1c**). Considering the elution volume of the putative complex, the complex would contain one ACP and one FabI monomer, since the peaks at ≈ 13.5 and 16 ml correspond to the tetrameric and dimeric forms of saFabI, respectively, and the peak at ≈ 20 ml refers to saACP. Here, the single components as well as the complex were analysed in citrate buffer at pH 5.5.

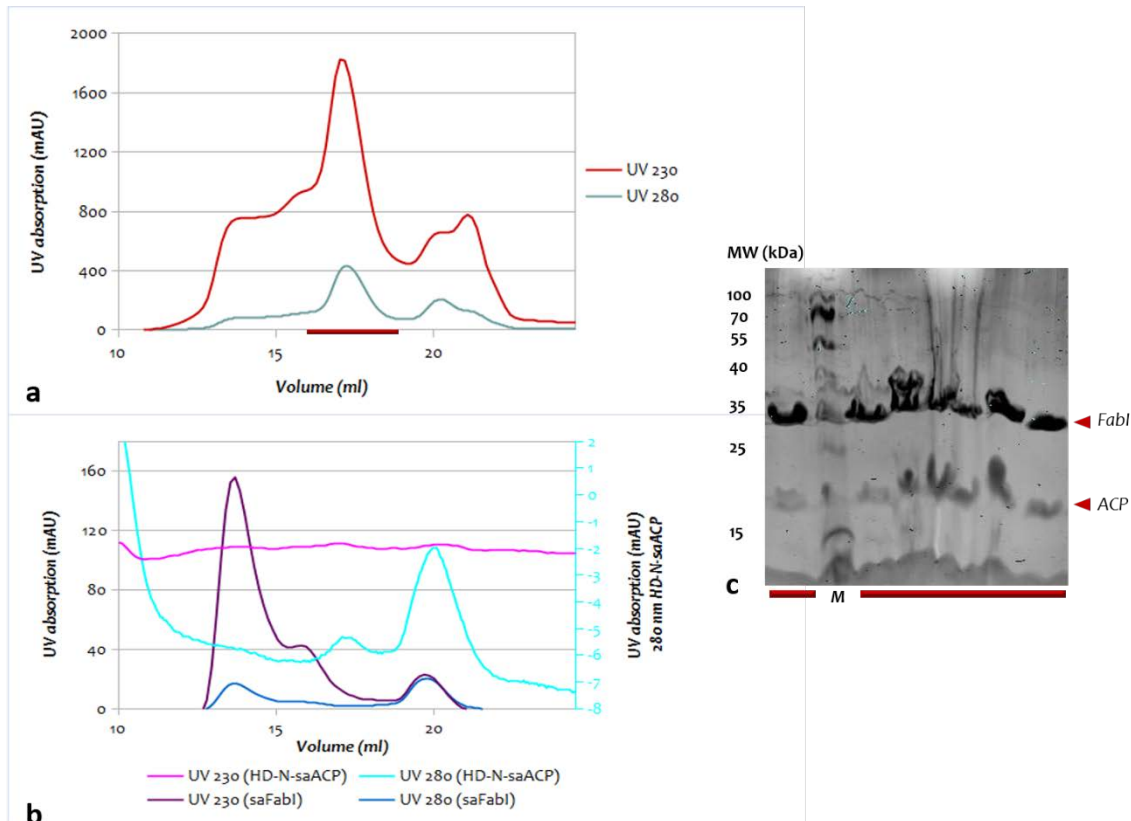


Figure 3.4-1: aSEC for complex formation of HD-N-saACP with saFabI: (a) Peaks observed for the assembled complex; **(b)** Peaks of the single proteins. The cyan scale on the right side is added to visualise the saACP peak at $\lambda = 280$ nm. **(c)** SDS-PAGE analysis of the peak fractions, which are indicated with a red reference bar in **(a)**. FabI and ACP bands are assigned by red arrowheads.

The best results for complex formation of HD-N-saACP with ecFabI were obtained in Tris/HCl buffer at pH 7.0, with the ecFabI tetramer peak being clearly shifted towards higher elution volumes (**Figure 3.4-1Ia, b**). This result suggests that the ecFabI tetramer might decompose to its monomeric form upon complex formation with HD-N-saACP. Nevertheless, a shoulder indicating the presence of a tetramer remains visible in the elution profile. Additionally, fractions of the shifted peak at a lower elution volume reveal the presence of an excess of ecFabI relative to HD-N-saACP, whereas fractions of the central peak contain a greater amount of HD-N-saACP at a higher elution volume. Only the fraction from the left half of the central peak, which seems to form a slight shoulder as well, shows an approximate stoichiometric ratio of both proteins (**Figure 3.4-1Ia, c; indicated by a red arrow**). It is

Results

possible that either the fractions containing the putative complex result from overlapping elution volumes of HD-N-saACP and ecFabI, or that the complex exists at different stoichiometric ratios. A different complex stoichiometry may be the consequence of the transient nature of the complex, which could be increased by the fact that both interaction partners originate from different organisms. However, the shift of the ecFabI peak suggests that an interaction between HD-N-saACP and ecFabI is likely to occur.

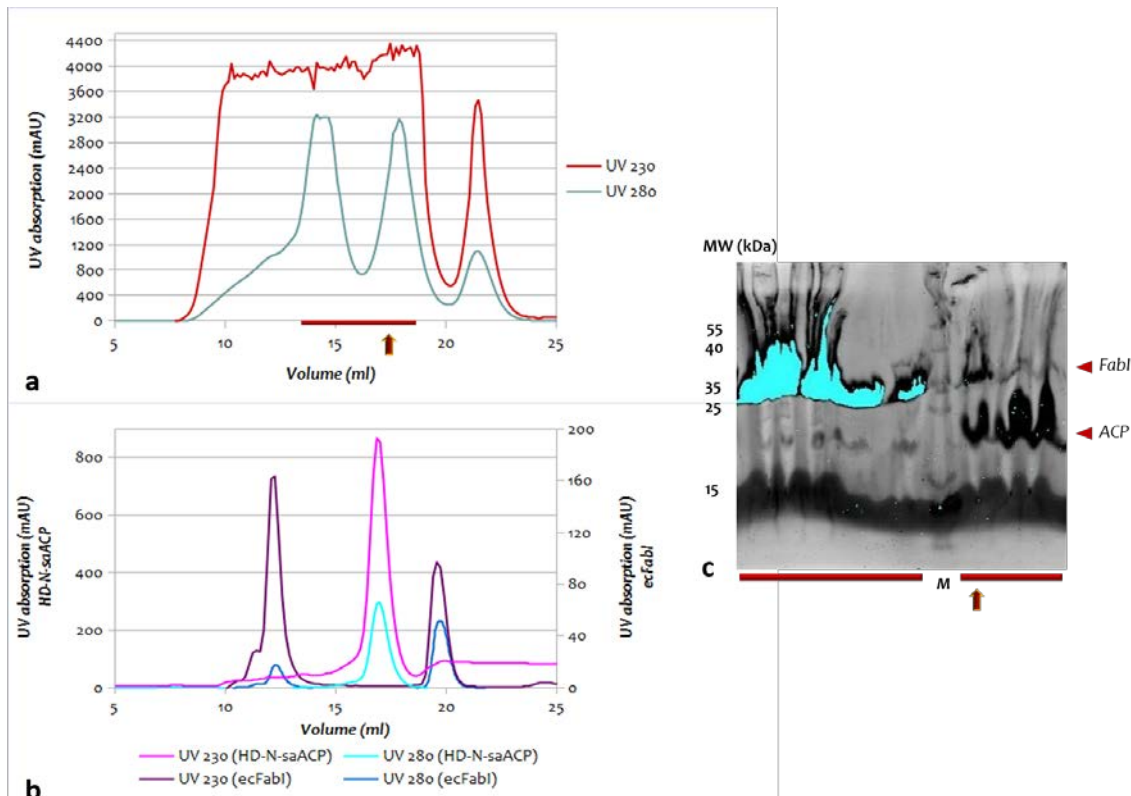


Figure 3.4-II: aSEC for complex formation of HD-N-saACP with ecFabI: (a) Peaks observed for the assembled complex; (b) Peaks of the single proteins. (c) SDS-PAGE analysis of the peak fractions, which are indicated with a red reference bar in (a). FabI and ACP bands are assigned by red arrowheads; the fraction containing an approximate stoichiometric ratio of ACP and FabI is indicated by a red arrow in (a) and (c).

The content of the peaks present at an elution volume of ≈ 20 ml in the aSEC analyses of both, the single saFabI and ecFabI proteins remains elusive, since SDS-PAGE did not reveal the presence of protein within these fractions and the peaks displayed enhanced absorption at $\lambda = 260$ nm (not shown). However, aSEC fractions from the HD-N-saACP – ecFabI complex at the same elution volume show faint bands corresponding to saACP, and fractions from the HD-N-saACP – saFabI experiment show a band, which can be assigned to saFabI, probably containing the monomer.

Interestingly, complex formation for both combinations described above could only be observed at relatively high protein concentrations and experiments conducted at lower protein concentrations did

not display the occurrence of additional peaks or peak shifts. This further supports the notion of the highly transient nature of the complex and the low affinity of both interaction partners towards each other. According to the elution volumes of the complex peaks, the formation of only a heterodimer composed of one ACP and one FabI molecule is observed during the aSEC experiments. This is surprising and contradicts the suggestion that substrate binding induces tetramer formation of saFabI [71] and that ENR enzymes exist as homotetramers in their biologically active form [56, 60]. However, it cannot be ruled out that the heterooctamer composed of four saACP and four FabI molecules is too large and exceeds the capacity of the column, although the calculated molecular weight should have been appropriate regarding the separating capacity. It is also possible that the heterooctamer falls apart during the separation procedure and cannot be purified via SEC.

3.4.2 Native PAGE analysis

Interestingly, also on a native PAA gel the HD-N-saACP – saFabI complex already analysed via aSEC in **Chapter 3.4.1** displayed a different behaviour compared to its single components and showed a downward shift compared to the saFabI band (**Figure 3.4-IIIa**). In another experiment, the single components including modified and unmodified saACP were compared to the fusion constructs. The band height of the fusion proteins might reflect the behaviour of the complex assembled from the single components, since the fusion construct should not be able to dissociate and thus mimic a stable saACP-saFabI complex. Indeed, the band seen for the assembly of HD-N-saACP with saFabI is almost at the same height as the bands of the fusion constructs. The fusion proteins, however, are located slightly more downwards compared to the complex from the single components, which might result from their inability to dissociate (**Figure 3.4-IIIb**). Another interesting aspect is that there is a difference when saFabI is present in complex with *apo*-saACP or with HD-N-saACP: When *apo*-saACP is present, two bands were observed one of which is located at the height of saFabI and the other one located at the position where the shifted band of the HD-N-saACP – saFabI complex is located (**Figure 3.4-IIIb, left**). This finding may indicate that saACP and saFabI also interact due to their surface complementarity when no acyl chain is attached to ACP, but complex formation is weaker since there is still a band representing “free” saFabI in the gel. Hence, the attachment of an acyl chain to saACP significantly strengthens the interaction, since in this case no band for saFabI was detected. The saFabI band cannot result from an excess of saFabI over saACP, since all samples contain \approx 3-fold molar excess of saACP relative to saFabI. Thus, saFabI should be fully incorporated when a stable complex is formed.

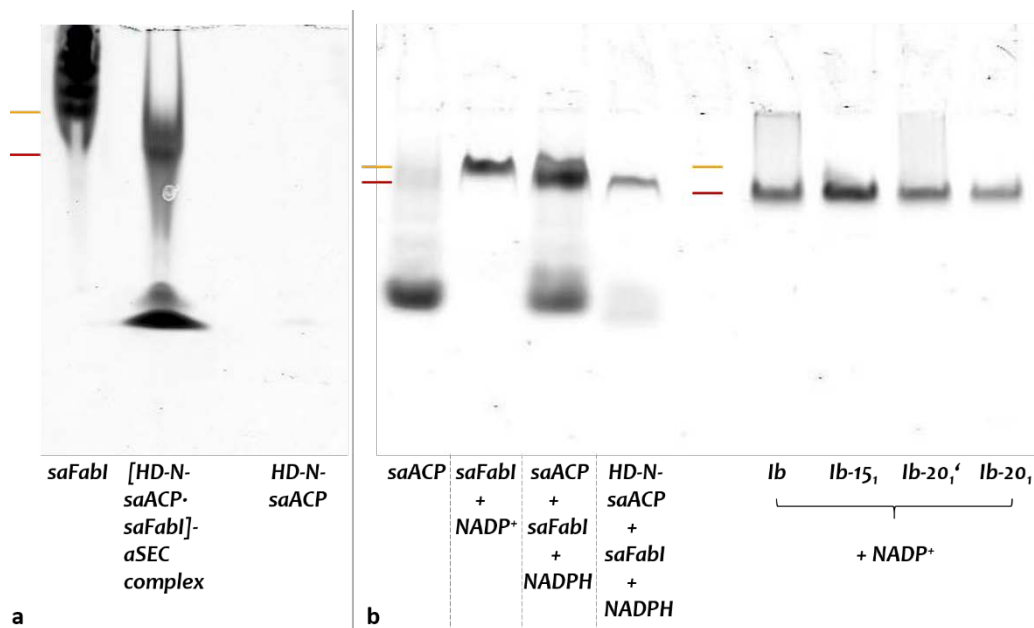


Figure 3.4-III: Native PAGE analysis of the saACP-saFabI complex, its single components and the fusion constructs: (a) Comparison of the single components with the HD-N-saACP – saFabI complex also analysed via aSEC. **(b)** Comparison of the single proteins with complexes containing modified and unmodified saACP and with the fusion constructs (Ib, Ib-15, Ib-20₁ and Ib-20). Shifts are indicated by red and orange bars, where orange marks initial positions of the single saFabI and red relates to shifted bands upon complex formation.

3.4.3 Crosslinking of saACP and saFabI cysteine variants

The cysteine variants of saACP and saFabI were created on the basis of the model described in **Chapter 1.2.2** [10]. Different pairs of amino acids with opposite charge located in close proximity on the putative interaction surface of saACP and saFabI were identified and virtually mutated to cysteines using *Coot*. For the choice of a crosslinking agent with an appropriate spacer length to connect both residues, possible rotamers of each pair of amino acids were considered and the shortest and longest possible distances between the respective residues were determined (**Figure 3.4-IV**). The most promising residue pairs for crosslinking were chosen to be the combination of E41C_{ACP} and K50C_{FabI}, and E47C_{ACP} and K17C_{FabI}, although crosslinking of E41C_{ACP} and K17C_{FabI} was tested as well to probe the possibility of crosslinking more distant entities. The combination of E47C_{ACP} and K50C_{FabI} did not seem to be too promising for crosslinking, since with increasing distance the likelihood of a crosslinking event decreases and in addition, the orientation of both residues towards each other did not appear to be extraordinarily favourable.

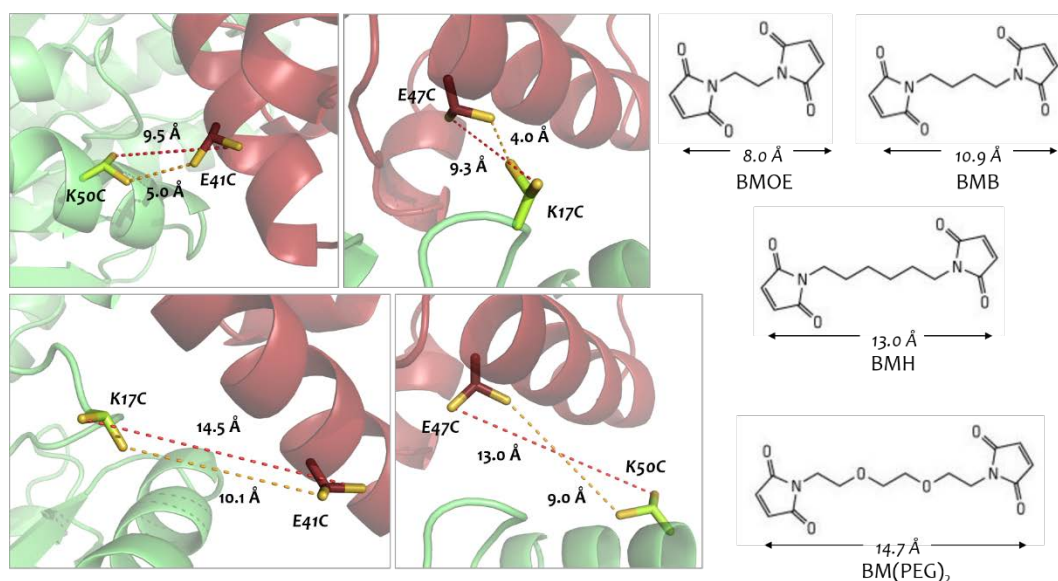


Figure 3.4-IV: Determination of distances between candidate pairs for crosslinking: Rotamers for both, the longest and shortest possible distances between two cysteine residues are shown as sticks. The longest distance is represented by a red, dashed line; the shortest distance is represented by an orange, dashed line. Green cartoons or sticks refer to FabI, red cartoons or sticks represent ACP.

Crosslinking tests for octanoyl-saACP_E41C with saFabI_K17C revealed the best crosslinking efficiency when the crosslinkers BMH or BM(PEG)₂ were utilised, resulting in reduced amounts of saFabI_K17C present in the reaction mixture, thus indicating a successful reaction (**Figure 3.4-V, left**). The crosslinking efficiency for BM(PEG)₂ is consistent with the fact that this crosslinker covers the longest as well as the shortest possible S-S distances predicted from the complex model. Interestingly, there is no obvious difference in crosslinking efficiency between BMH or BM(PEG)₂, although the spacer arm length of BMH does not account for the possibility of both residues assuming the longest possible distance to each other, suggesting that this might not occur at a high frequency. Crosslinking of HD-N-saACP_E41C with saFabI_K50C resulted in good yields for both crosslinkers, BMOE and BMB (**Figure 3.4-V, middle**), suggesting that non-optimal side-chain orientations for crosslinking occur more frequently for this pair of residues than for the saACP_E41C-saFabI_K17C pair of cysteines and thus a longer linker becomes necessary. When it was attempted to crosslink octanoyl-saACP_E47C with saFabI_K17C very low amounts of complex were obtained with either BMB or BMH and a strong saFabI_K17C band was observed when analysing the reaction mixture on an SDS gel (**Figure 3.4-V, right**). The reason for this result might be that crosslinking tests for octanoyl-saACP_E41C with saFabI_K17C and HD-N-saACP_E41C with saFabI_K50C were conducted at relatively high protein concentrations within a small reaction volume. In contrast, the crosslinking experiment for octanoyl-saACP_E47C with saFabI_K17C was performed using smaller amounts of protein within a larger volume of reaction buffer, since the reaction was conducted at a preparative scale. Thus, the probability of ACP and FabI to be in spatial proximity was decreased and

led to lesser crosslinking efficiency. The lower crosslinking rate may also result from inaccuracies in the model on the basis of which the crosslinking pairs were chosen. This hypothesis remains to be proven by further experiments. However, in general it seems to be advantageous to crosslink residues with the lowest distance towards each other, since the likelihood of a crosslinking event increases with decreasing distances of the crosslinking partners.

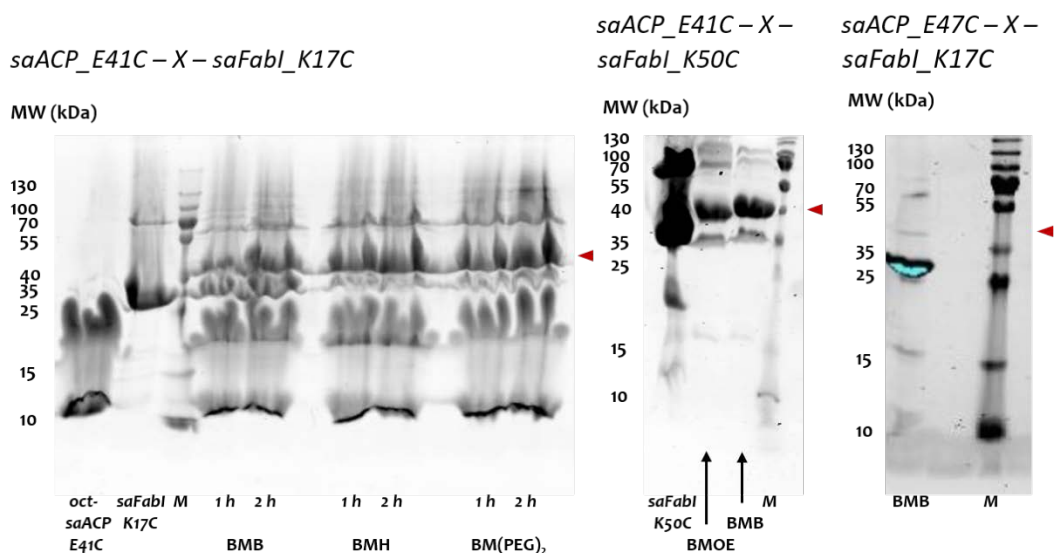


Figure 3.4-V: Examples of crosslinking tests for different pairs of saACP- and saFabI-Cys mutants: The standard reaction was conducted for 1 h at room temperature. The left panel indicates that efficiency is not increased by longer incubation time. The right panel shows a crosslinking reaction directly applied to a subsequent SEC step and thus was prepared in a higher reaction volume. The bands representing the crosslinked complex are indicated by a red arrowhead.

Unfortunately, further purification steps such as anion-exchange chromatography or SEC failed to separate the non-crosslinked, mostly saFabI proteins from the crosslinked complex. The SEC elution profile displayed two distinct peaks and upon SDS-PAGE analysis of the fractions it was observed that these resulted indeed from the separation of non-crosslinked saACP from the complex (**Figure 3.4-VI**). Nevertheless, single saFabI entities eluted in complex with the crosslinked components. A similar result was obtained from anion-exchange chromatography (data not shown). These results are again caused by the tetramer formation of saFabI and further purification steps so far only led to further material loss and not to an improvement in complex purity. Thus, the modification samples shown in **Figure 3.4-V (central panel)** were subjected to crystallisation setups, since the yield of crosslinked complex was remarkably high and could lead to the formation of crystalline structures despite the presence of some impurities.

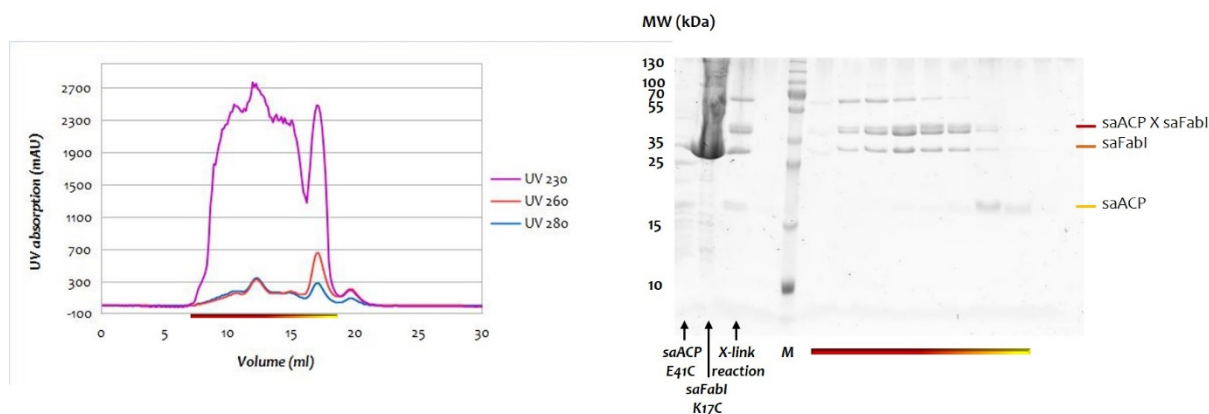


Figure 3.4-VI: aSEC for the HD-N-saACP_E41C-X-saFabl_K17C complex: The presence of single saACP is indicated by the yellow colouring of the reference bar; a red colouring represents the crosslinked complex together with non-crosslinked saFabl.

3.4.4 Crystallisation of ACP-Fabl complexes

Several crystallisation experiments were set up for crosslinked and non-crosslinked complexes with different acyl substrates attached to ACP. For non-crosslinked complexes, combinations of saACP, ecACP or AcpM in complex with saFabl, ecFabl or InhA were tested; not only containing both proteins from the same organism, but also from different species. Crystals of sufficient size for data collection and appropriate resolution for structure solution usually only contained the Fabl enzyme within the unit cell and were also obtained in crystallisation conditions characteristic for crystal formation of that specific ENR.

Some differing conditions were identified leading to small crystals, which did not display the characteristic shape of crystals usually formed by one of the enzymes present in the condition. Some of these crystals displayed weak diffraction. However, despite several optimisation attempts none of those conditions yielded crystals of sufficient quality for X-ray diffraction studies.

Complex	Crystallisation condition
	100 mM Tris/HCl, pH 8.0, 10 % (w/v) PEG 6000
	100 mM sodium acetate, pH 5.5, 150 mM (NH ₄) ₂ SO ₄ , 10 % (v/v) PEG 550-MME
	100 mM sodium acetate, pH 5.5, 200 mM (NH ₄) ₂ SO ₄ , 10 % (v/v) PEG 2000-MME
[HD-N-saACP-saFabl]	100 mM MES, pH 6.5, 100 mM sodium acetate, 20 - 30 % (w/v) PEG 2000-MME
	100 mM Na ₃ -Citrate, pH 4.0, 200 mM Na ₃ -Citrate, 20 % (w/v) PEG 3350
	100 mM sodium acetate, pH 4.6, 400 mM CaCl ₂ , 18 % (w/v) PEG 2000-MME
	100 mM BisTris, pH 5.5, 200 mM Li ₂ SO ₄ , 25 % (w/v) PEG 3350
	100 mM citric acid, pH 5.0, 1.6 M (NH ₄) ₂ SO ₄

Results

[HD-N-saACP·ecFabI]	100 mM BisTris, pH 6.0, 150 mM MgCl ₂ , 28 % (w/v) PEG 3350
[HD-S-saACP·ecFabI]	200 mM KF, 18 % (w/v) PEG 4000
[saACP_E41C X saFabI_K50C·PT176]	200 mM LiNO ₃ , 20 % PEG 3350
[octanoyl-saACP_E47C X saFabI_K17C]	100 mM MES, pH 5.5, 200 mM zinc acetate, 10 % (w/v) PEG 8000

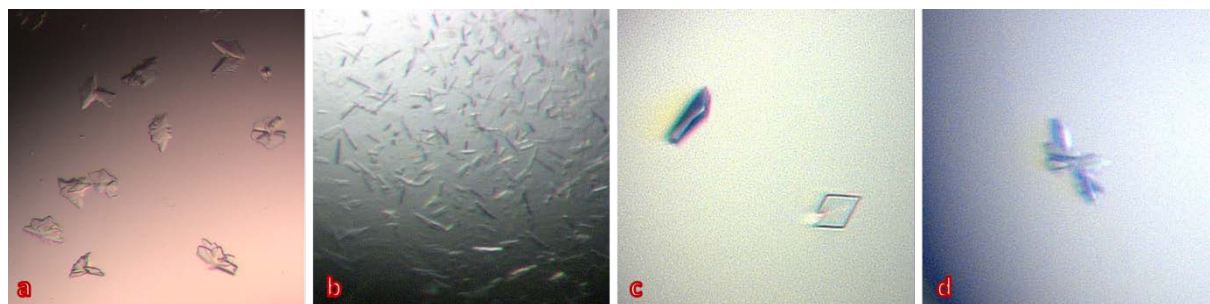


Figure 3.4-VII: Crystals of different ACP-FabI complexes: [HD-N-saACP-saFabI] in (a) 100 mM sodium acetate, pH 5.5, 200 mM (NH₄)₂SO₄, 10 % (v/v) PEG 2000-MME; (b) 100 mM MES, pH 6.5, 100 mM sodium acetate, 30 % (w/v) PEG 2000-MME with 1:500 seeding solution (prepared from a crystal obtained in 100 mM Na₃-Citrate, pH 4.0, 200 mM Na₃-Citrate, 20 % (w/v) PEG 3350); (c) 100 mM Na₃-Citrate, pH 4.0, 200 mM Na₃-Citrate, 20 % (w/v) PEG 3350 + Silver Bullets Bio additive screen, F11; (d) [HD-S-saACP-ecFabI] in 200 mM KF, 18 % (w/v) PEG 4000.

The crosslinking experiment for the HD-N-saACP_E41C – saFabI_K50C complex described in **Figure 3.4-V** led to large crystals in various conditions, preferably for the complex crosslinked with BMB (**Figure 3.4-VIII**). Considering the versatile composition of crystallisation conditions in which crystals were found it seemed unlikely that these crystals were composed of a certain component existing in a defined crystallisation condition. However, X-ray analysis revealed the presence of salt diffraction throughout all conditions, suggesting that the crystals originated from a substance already present in the protein mixture. During the purification procedure as well as the crosslinking step no salt other than NaCl was used. Hence, these crystals were most likely containing the crosslinking agent itself. To test this hypothesis, the buffer was exchanged to remove excess crosslinking agent. Afterwards, new crystallisation trials were performed and no crystals were observed, which confirmed the suspicion that the crystals were formed by the crosslinker.

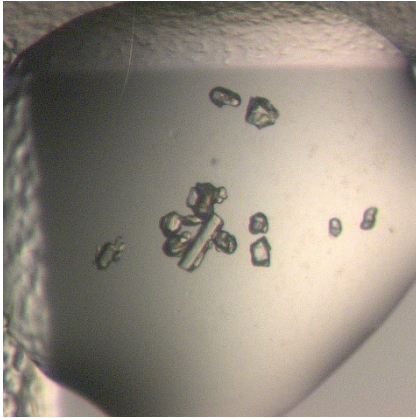


Figure 3.4-VIII: Crystals of [HD-N-saACP_E41C X saFabI_K50C-NADPH]: 100 mM sodium acetate, pH 4.6, 40 % (v/v) PEG 200

3.5 Investigation of different ACP-FabI fusion constructs

3.5.1 Construct design

Constructs were designed according to the ACP-FabI complex model described in **Chapter 1.2.2**. Close inspection of the distances between the different termini of the two subunits suggested a minimum linker length of 10 amino acids between the C-terminus of ACP and the N-terminus of FabI (consecutively referred to as “*construct I*”), and of at least 12 amino acids between the C-terminus of FabI and the N-terminus of ACP (consecutively referred to as “*construct II*”) to enable “native” protein-protein interactions as observed in the model. Linkers were designed to exhibit a high flexibility, but also complement charges present on the surfaces of ACP or FabI flanking the appendage of the linker. Thus, the linkers mostly contain small residues like Gly and Ser in their middle parts, combined with charged or polar residues like Asn, Arg or Thr which are more closely located towards their terminal sections (**Figure 3.5-I**). Since the behaviour of the linker regions in solution cannot be predicted, also longer linkers were tested to permit the fused proteins to adopt the optimal orientation with respect to each other upon interaction.

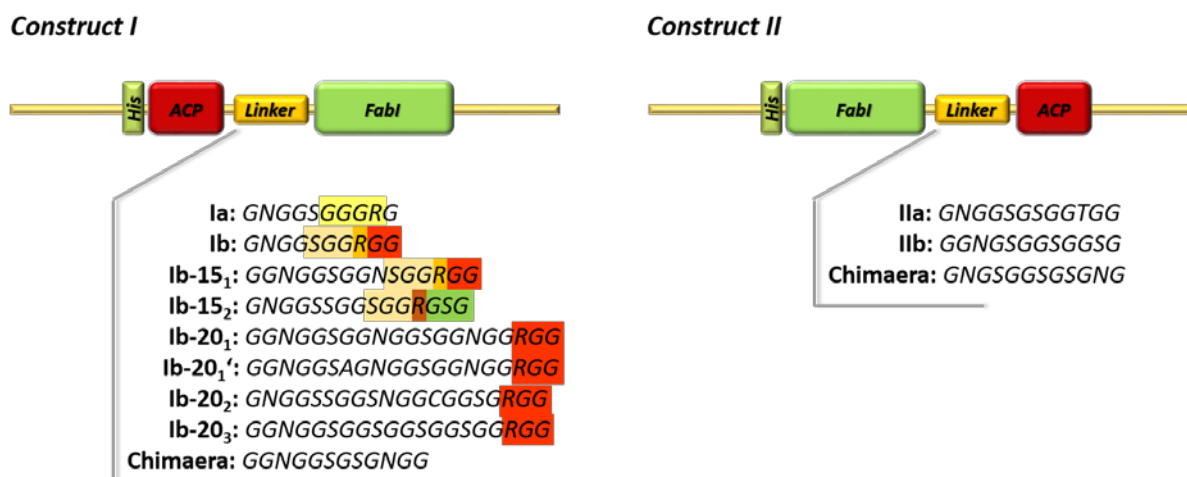


Figure 3.5-I: Architecture and linker compositions of different ACP-FabI fusion constructs: Numbered linkers refer to the saACP-saFabI fusion protein; “Chimaera” describes the saACP-ecFabI fusion construct. Special or common features of the respective linkers are highlighted.

3.5.2 Cloning and expression of fusion constructs

For both fusion proteins I and II, only *construct b* could be successfully cloned and expressed. Thus, to generate constructs with longer linker regions, *construct b* served as a template for linker design. The derived constructs *Ib-15₁* and *Ib-20₁* were successfully cloned and expressed. Interestingly, a single amino-acid substitution occurred when cloning *Ib-20₁*, resulting in *Ib-20₁'*, which contained an Ala instead of Gly at position 7 of the linker. Additionally, *construct Ib* provided the basis for the generation of the double-cysteine variants *Ib_E47C_{ACP}-K17C_{FabI}* and *Ib_E41C_{ACP}-K50C_{FabI}*, which were subjected to intramolecular crosslinking tests. From cloning attempts of the chimeric protein only recombinant DNA for *construct II* could be obtained followed by successful expression.

Expression in *E. coli* cells yielded sufficient amounts of protein at temperatures of 18, 22 or 25 °C, with *construct Ib* as well as the derived double-cysteine variants being expressed overnight. The best results for the chimeric protein were achieved by expression for 6 – 7 h (**Figure 3.5-II, upper right panel**). Interestingly, *constructs Ib-15₁* and *Ib-20₁'* displayed reduced stability and the tendency to migrate to the pellet fraction after elongated expression (**Figure 3.5-II**). Hence, upon expression of these constructs the cells were harvested after 5 – 7 h to avoid loss of protein. A general trend towards lower expression levels and enhanced vulnerability to aggregate was observed for fusion proteins containing longer linkers.

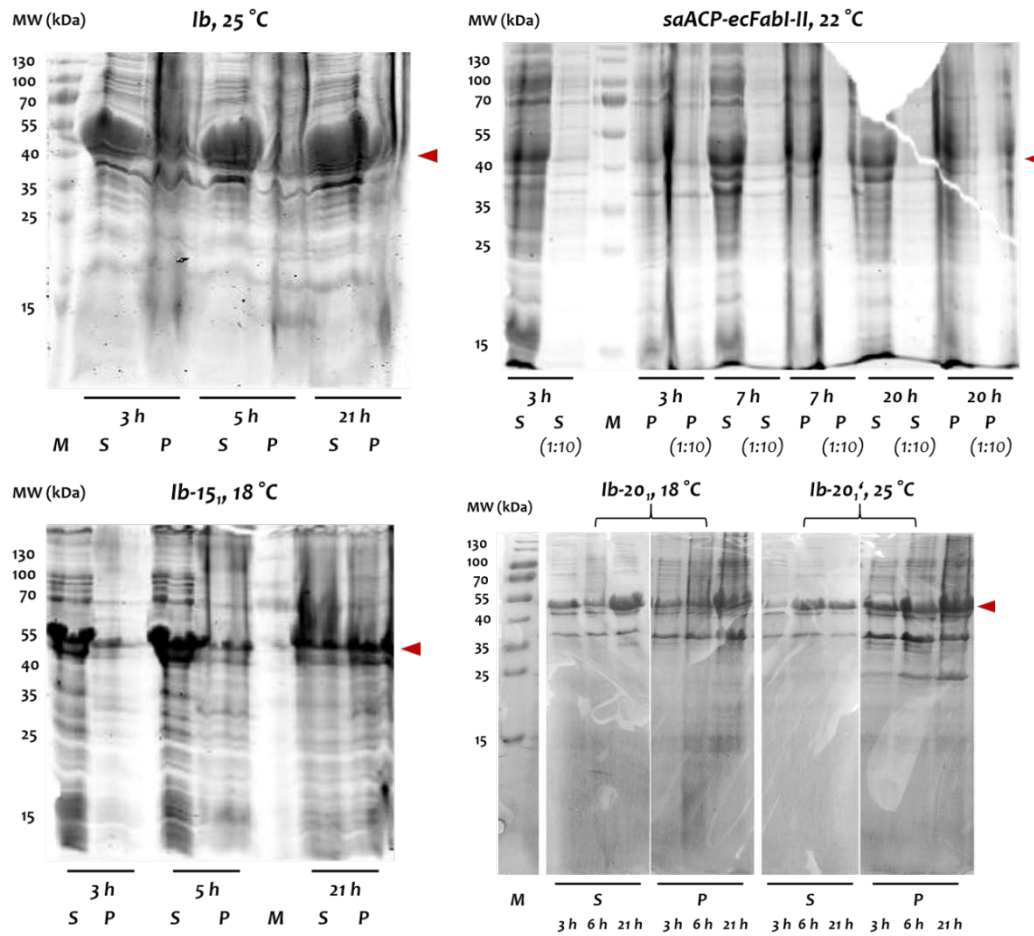


Figure 3.5-II: Expression tests of different fusion constructs: Expression of all constructs was conducted in *E. coli* BL 21 (DE3) cells, except for *Ib-20*₁' which was expressed in *E. coli* BL 21 (DE3)-RIL cells. The position of expressed protein is marked with an arrowhead; "S": supernatant, "P": pellet. The lower right panel is a result from the Bachelor thesis of Jonas Weinrich.

3.5.3 Purification of fusion constructs

PURIFICATION OF CONSTRUCT *IB* AND ITS DERIVATIVES

Construct Ib was initially purified using the Tris buffer system (Table 2.2-I – Table 2.2-V). Since Thermofluor analysis (Chapter 3.5.4) indicated higher stability in citrate buffer, the purification procedure was entirely changed to citrate as buffer substance (Table 2.2-I – Table 2.2-V). During the first purification step a second protein species of lower molecular weight became visible in the SDS gel, which could not be completely separated from the target protein, although the amount of this species decreased with rising imidazole concentrations (Figure 3.5-III).

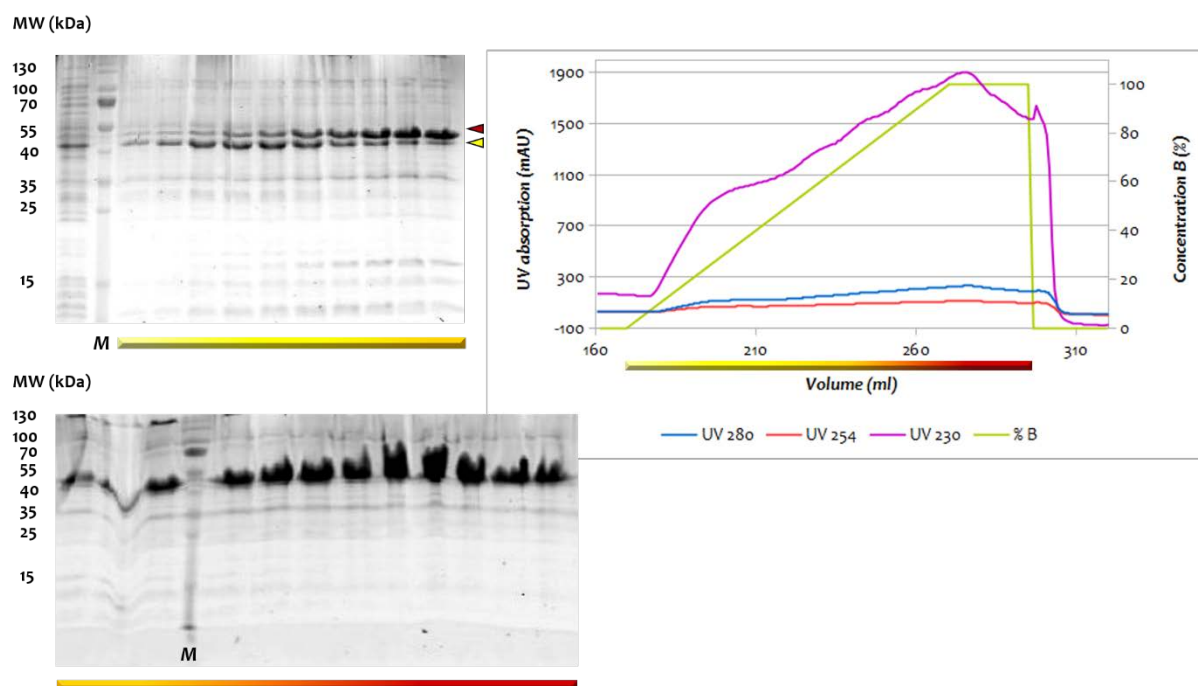


Figure 3.5-III: Elution profile of construct Ib from the Ni²⁺ affinity column: Increasing amounts of the higher molecular weight fraction of Ib are indicated by enhanced reddening of the reference bar. UV absorptions in the chromatogram at $\lambda = 280$, 254 and 230 are coloured blue, red and magenta, respectively. The concentration of imidazole-containing elution buffer (“% B”) is shown in green.

However, from the elution profile the putative imidazole threshold to remove the lower molecular-weight species could be estimated. In an optimised purification protocol the elution was carried out in a stepwise manner containing three steps of enhanced imidazole concentrations over several CVs. During the elution step with the lowest imidazole concentration (≈ 102 mM) the impurity could be eliminated quantitatively (**Figure 3.5-IV**) and the pure target protein eluted at concentrations of ≈ 322 and 500 mM imidazole. In the following SEC step *construct Ib* also showed higher stability and less contamination, when eluted with citrate buffer, which is indicated by the more narrow and more symmetrical elution peak. In contrast, the Tris purification contains a remarkable amount of low-molecular weight contaminant together with a band appearing at a molecular weight of ≈ 15 kDa on the SDS gel, which might be the ACP protein cleaved from the fusion construct (**Figure 3.5-Va**). The elution volume of *construct Ib* in Tris as well as in citrate buffer suggests the presence of a tetramer in solution.

Results

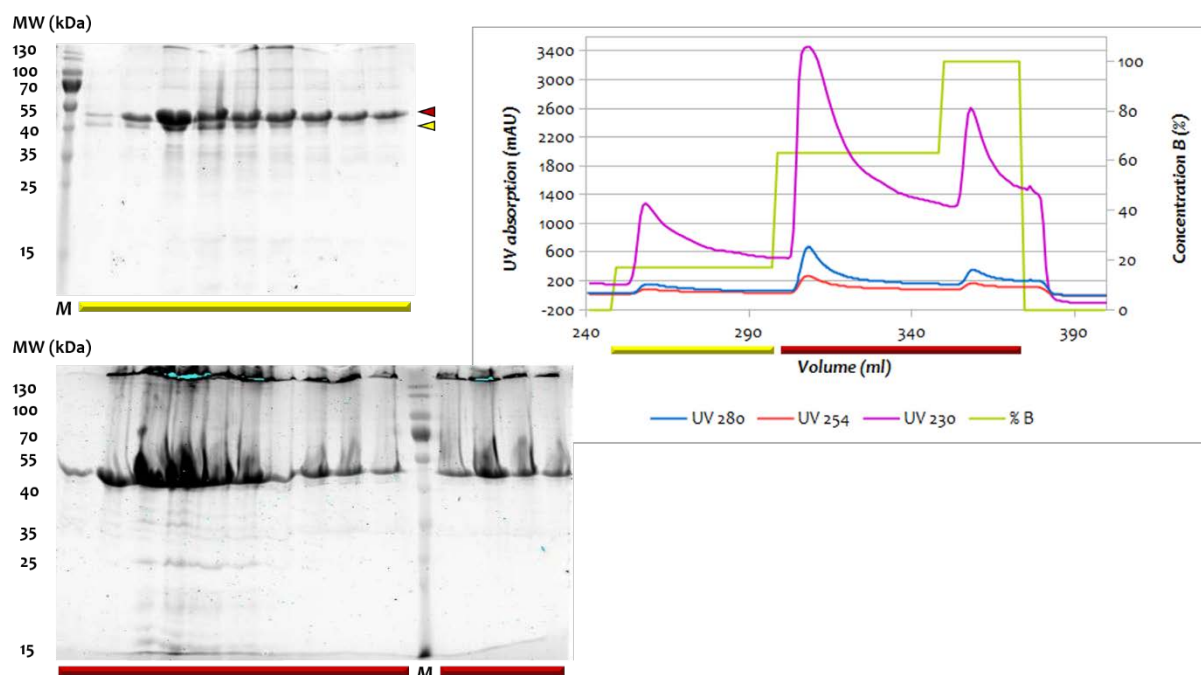


Figure 3.5-IV: Step-elution profile of construct *Ib* from the Ni^{2+} -affinity column: Fractions containing both species are assigned with a yellow, fractions containing pure *Ib* protein are assigned with a red reference bar. UV absorptions in the chromatogram at $\lambda = 280, 254$ and 230 are coloured blue, red and magenta, respectively. The concentration of imidazole-containing elution buffer (“% B”) is shown in green.

Although the same putative degradation product was also observed when purifying the *Ib-15₁* construct, step-purification was not necessary and the contamination could be removed by a linear gradient elution from the affinity column using citrate buffer. Interestingly, the protein peak from the subsequent SEC was observed at an unusual elution volume, which was located between the putative elution volumes of the dimeric or tetrameric forms (**Figure 3.5-Vb**). This unexpected elution behaviour might be caused by altered interactions, either between the linker regions, or between the ACP and the FabI subunits, since the elongated linker could allow an ACP portion of one fusion protein not only to interact with the FabI part directly attached to it, but also with a FabI portion from a neighbouring fusion protein.

Results

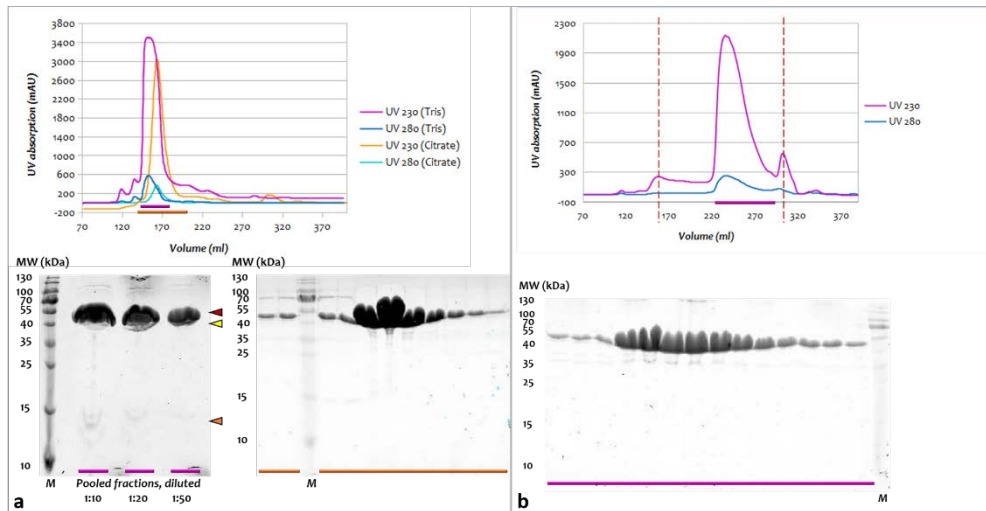


Figure 3.5-V: SEC chromatograms of *Ib* and *Ib-151*: (a) Comparison of SEC elution profiles of construct *Ib* in Tris and citrate buffer. The fusion construct is assigned by a red, the degradation product by a yellow triangle and the band resembling the putatively cleaved ACP part is indicated by an orange triangle. (b) SEC elution profile of *Ib-151* in citrate buffer. Probable elution volumes of the tetrameric or dimeric fractions are marked by red, dashed lines at V (tetramer) \approx 160 ml and V (dimer) \approx 300 ml. Elution fractions displayed on the SDS gels are indicated by a reference bar matching the colouring of the respective UV₂₃₀ absorption.

The citrate buffer system was directly applied to the purification of both, the *Ib-20₁* and the *Ib-20₁'* constructs. Interestingly, optimisation applying the step-elution procedure for the Ni²⁺-affinity column was only necessary for *construct Ib-20₁*, where the low molecular-weight species preferentially eluted at 116 mM imidazole and the pure protein was obtained at imidazole concentrations \approx 298 and 500 mM. In contrast, sufficient purity of *construct Ib-20₁'* could already be achieved when applying a linear gradient. The elution volume of both proteins from the SEC column indicates the presence of a tetramer. Although peaks from elution profiles of both constructs displayed an asymmetric shape and degradation bands are visible in the SDS gels in both cases, the *Ib-20₁* construct seems to be less stable compared to *Ib-20₁'* (**Figure 3.5-VIb**). The Ala mutation may thus prevent the linker region of *construct Ib-20₁'* to some extent from degradation.

The step-elution procedure together with the citrate-buffer system was also applied when purifying the *Ib_E47C_{ACP}-K17C_{FabI}* and *Ib_E41C_{ACP}-K50C_{FabI}* variants, resulting in sufficiently pure protein for *construct Ib_E47C_{ACP}-K17C_{FabI}*, whereas *construct Ib_E41C_{ACP}-K50C_{FabI}* contained a contamination also in eluate fractions from steps containing enhanced imidazole concentrations. This observation suggests that the combination of mutations at positions E41 of the saACP portion and K50 of the saFabI portion of the fusion construct impairs its stability although the linker region did not change with respect to *constructs Ib* and *Ib_E47C_{ACP}-K17C_{FabI}*. This is also reflected within the SEC elution profile of this construct, where an obvious asymmetry of the peak and an additional “shoulder” due to the

Results

probable degradation product can be observed (**Figure 3.5-VIa**). Both proteins exist in their tetrameric forms on the SEC column.

In general, elution profiles and SDS-PAGE analyses suggest that the contaminant is capable of interacting with the intact fusion protein, i.e. by forming tetramers; which causes the observed peak asymmetries and leads to the conclusion that the ACP part of the constructs is subject to degradation. This suspicion was further substantiated by the results obtained from MALS analyses (**Chapter 3.5.5**). Additionally, extended linker lengths resulted in enhanced susceptibility to degradation or decomposition of the fusion construct.

Due to their superior stability confirmed by Thermofluor measurements (**Chapter 3.5.4**), the *Ib* and *Ib_E47C_{ACP}-K17C_{FabI}* constructs both containing the shortest linker, were preferentially used for further studies.

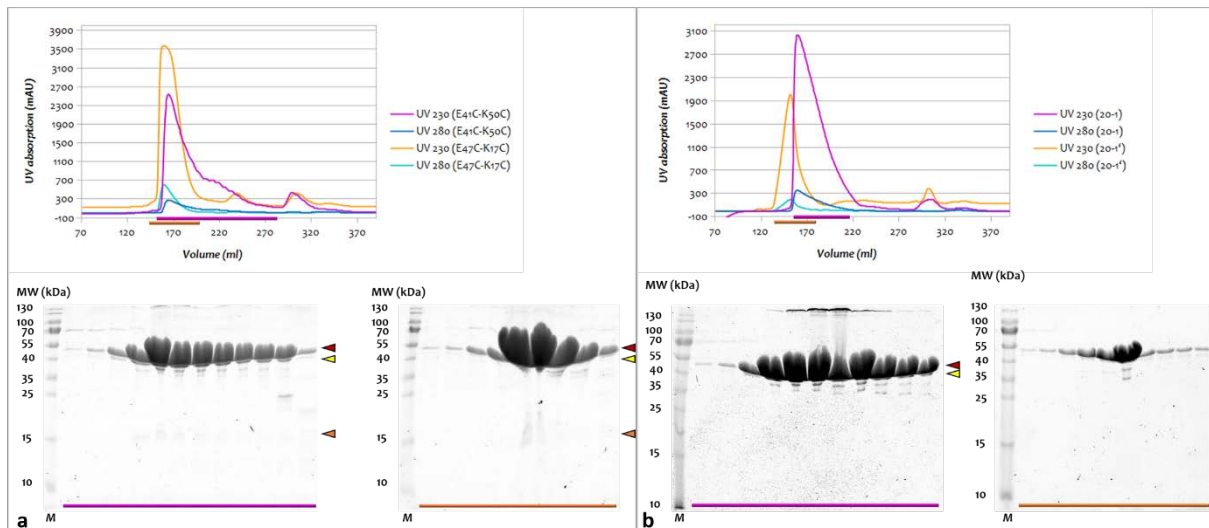


Figure 3.5-VI: SEC chromatograms of the *Ib*-cysteine double variants and *Ib* constructs with a 20-aa linker: (a) Comparison of SEC elution profiles of constructs *Ib_E41C-K50C* and *Ib_E47C-K17C* in citrate buffer. (b) SEC elution profile of *Ib-20₁* and *Ib-20₁'* in citrate buffer. The fusion construct is assigned by a red, the degradation product by a yellow triangle and the band resembling the putatively cleaved ACP protein is indicated by an orange triangle. Elution fractions displayed on the SDS gels are indicated by a reference bar matching the colouring of the respective UV₂₃₀ absorption.

PURIFICATION OF THE CHIMERIC SAACP-ECFABI-II CONSTRUCT

Although SDS analysis of the fractions from affinity chromatography revealed the presence of a lower-molecular weight band as well, the chromatogram showed a distinct elution peak for the chimeric fusion construct at $\approx 61 - 250$ mM imidazole (**Figure 3.5-VII, left panel**). The protein eluted in its tetrameric form from the SEC column in an asymmetric peak, suggesting the presence of different oligomeric species and including small amounts of the degradation product. The two adumbrated

“shoulders” at lower elution volumes also suggest higher-oligomer or aggregate formation (**Figure 3.5-VII, right panel**).

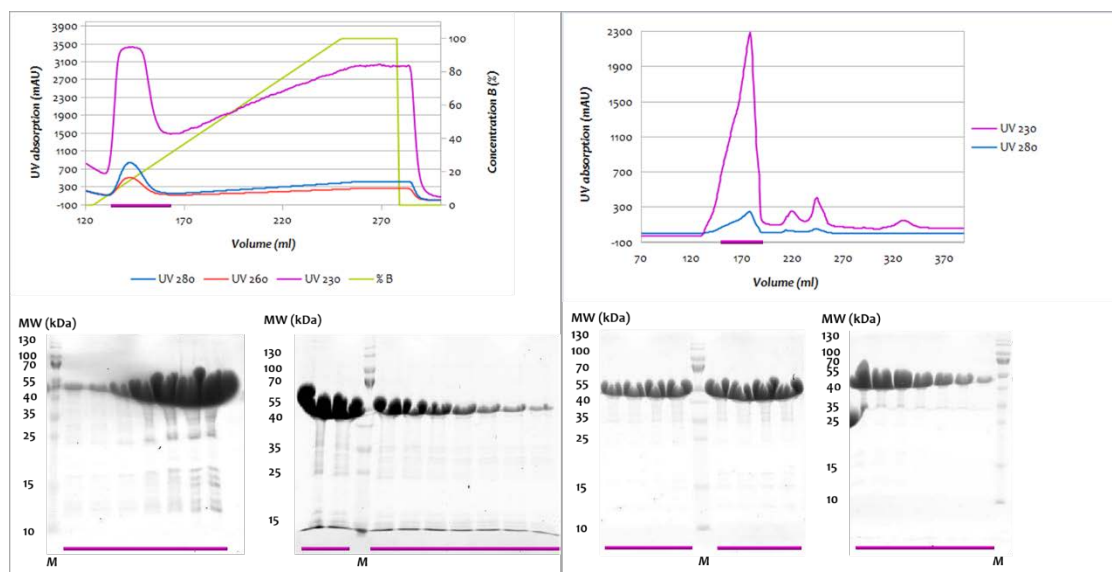


Figure 3.5-VII: Purification of the saACP-ecFabI-II construct: Chromatograms and SDS-PAGE from the affinity chromatography (left panel) and SEC (right panel). Elution fractions displayed on the SDS-PAGE are indicated by a reference bar matching the colouring of the respective UV₂₃₀ absorption.

3.5.4 Thermofluor analysis of selected fusion constructs

Earlier studies revealed that either Tris or citrate are the most suitable buffer substances for the purification of saFabI [11]. To test whether this finding is also true for saFabI with an attached ACP and to identify optimal buffer conditions for the fusion construct, Thermofluor analyses were carried out. Interestingly, constructs *Ib-15₁* and *Ib-20₁'* only displayed none or very weak fluorescence signals in the assay. With respect to *construct Ib-15₁*, this was not a surprising result since it already indicated diminished integrity on the SEC column (**Figure 3.5-Vb**). For *construct Ib-20₁'* the reason for the missing signal might be due to increased temperature sensitivity of the protein. During the SEC purification step, which was carried out at 4 °C, the protein did not display any peculiar properties (**Figure 3.5-VIb**). However, samples for the Thermofluor assay were prepared at room temperature and the measurement was conducted at room temperature with subsequent heating which could lead to impaired protein stability.

Thermofluor measurements of *constructs Ib* and *Ib-20₁* confirmed Tris and citrate as appropriate buffer substances, with citrate being superior compared to Tris. Citrate buffer without the addition of salt led to a similar stabilisation of the fusion constructs as Tris buffer containing the highest salt concentration (250 mM NaCl) tested in the assay. The addition of NaCl to the citrate buffer resulted in further

Results

stabilisation of the protein. Interestingly, none or only small differences in melting temperature could be observed when adding either 150 or 250 mM NaCl to both buffer solutions (**Figure 3.5-VIII**). Phosphate buffers, which are favoured for the crystallisation of saFabI, also led to reasonable stabilisation of the protein (data not shown).

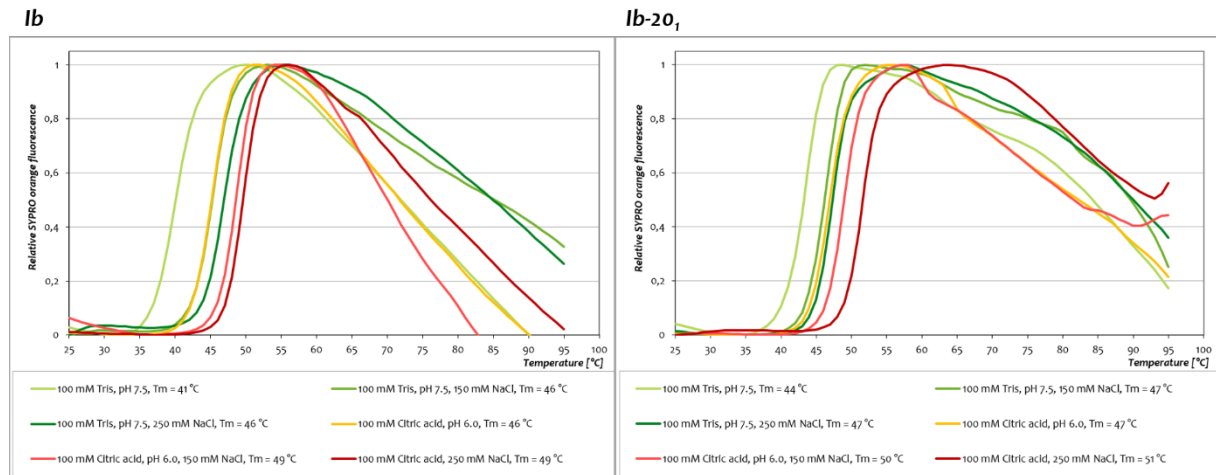


Figure 3.5-VIII: Thermofluor analyses of constructs *Ib* and *Ib-201*: Melting curves for Tris buffer are shown in green, curves for citrate in orange and different reds.

To test the ability of the fusion constructs used for further studies to bind NADPH, another Thermofluor assay was conducted. The protein was titrated with different cofactor concentrations, starting from a 100-fold excess with subsequent 2:1-dilutions. *Constructs Ib* and *Ib_E47C_{ACP}-K17C_{FabI}* revealed enhanced thermostability at increasing cofactor concentrations. *Construct Ib* displayed even at the lowest NADPH concentration a stabilising effect compared to the reference, where no cofactor was present. In contrast, the stability of the *Ib_E47C_{ACP}-K17C_{FabI}* construct without cofactor did not differ from samples containing low NADPH concentration and to observe a shift in the melting temperature, a 25-fold excess of cofactor was necessary. However, both constructs are capable of binding NADPH, although the affinity of cofactor to the double-cysteine mutant seems to be decreased.

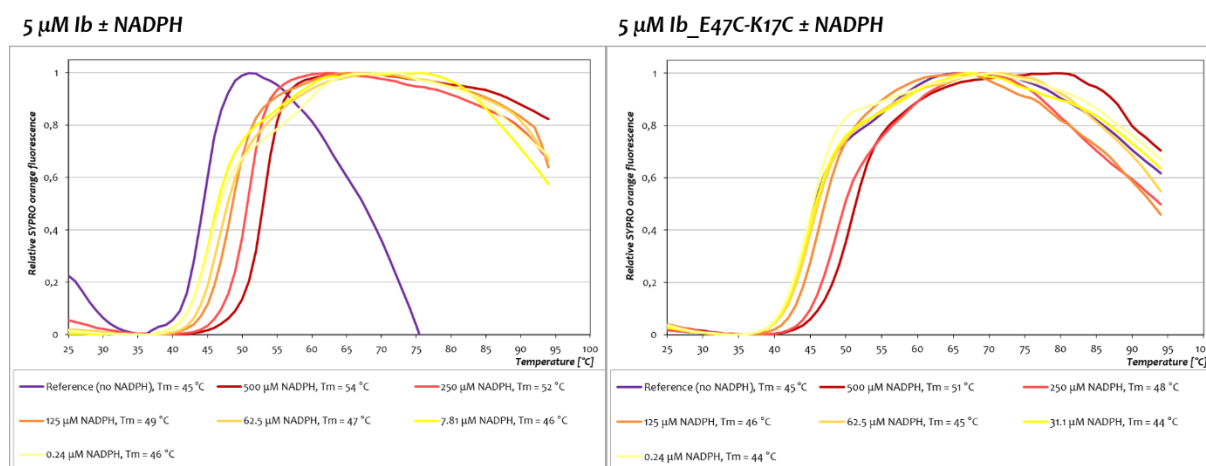


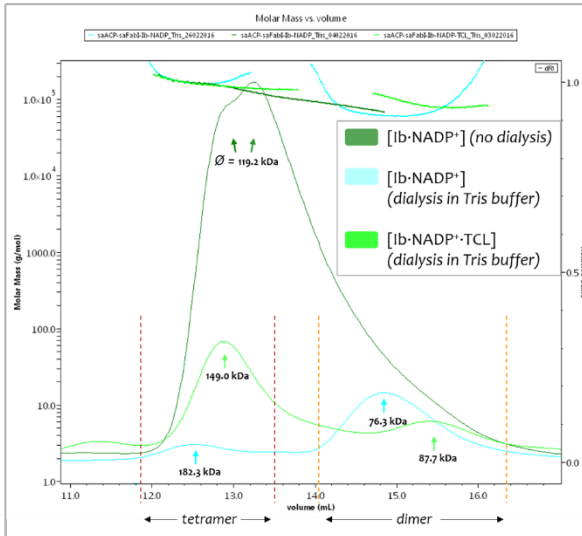
Figure 3.5-IX: Thermofluor analyses for constructs *Ib* and *Ib_E47C_{ACP}-K17C_{FabI}*: Increasing NADPH concentrations are indicated by increased reddening of the melting curves. Only the curves for the highest and lowest NADPH concentrations, and for the NADPH concentrations at which a shift in melting temperature (T_m) was observed, are shown. The reference sample lacking NADPH is displayed in violet.

3.5.5 MALS analysis of selected fusion constructs

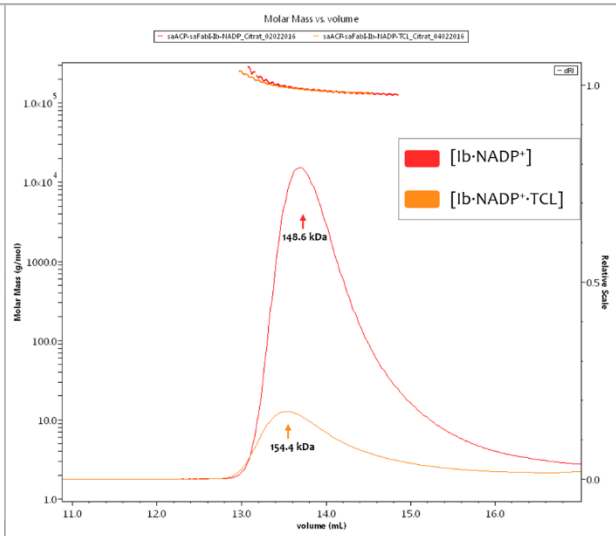
Fusion constructs that were found to be sufficiently stable were submitted to MALS analysis to obtain information with respect to their multimeric states in Tris and citrate buffer solutions as well as in the presence or absence of TCL.

Both, the *Ib* and the *Ib-20_I* constructs displayed the ability to form dimers or tetramers, which was previously reported to be a typical characteristic of saFabI [71]. In the absence of TCL with only cofactor bound, the fusion proteins were found to be present as dimers in Tris buffer at pH 8.2 or 8.5 (**Figure 3.5-X & Figure 3.5-XI, left panel**). In contrast, slightly acidic conditions, i.e. citrate buffer at pH 5.6 – 6.0, promote the formation of the tetramer even in the absence of TCL (**Figure 3.5-X & Figure 3.5-XI, right panel**). The results further suggested, that in acidic buffer conditions the addition of TCL further shifts the dimer-tetramer equilibrium towards the tetrameric state of the protein, since experimentally determined MWs in the presence of TCL are higher for both fusion constructs compared to MWs from measurements in citrate buffer without TCL.

Tris buffer



Citrate buffer

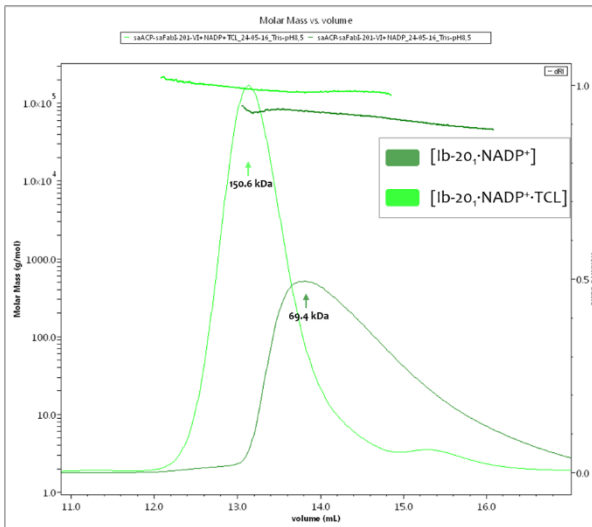


Calculated MW (protein only) for

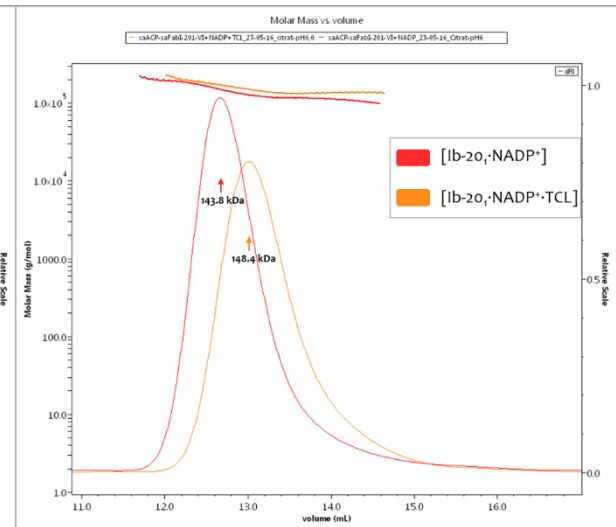
- Dimer = 81 881 Da
- Tetramer = 163 762 Da

Figure 3.5-X: MALS analysis for construct Ib in Tris or citrate buffer with or without TCL: The experimentally determined MW is assigned to each peak. Horizontal lines above the peaks indicate MW development throughout the analysis.

Tris buffer



Citrate buffer



Calculated MW (protein only) for

- Dimer = 83 209 Da
- Tetramer = 166 419 Da

Figure 3.5-XI: MALS analysis for construct Ib-20₁ in Tris or citrate buffer with or without TCL: The experimentally determined MW is assigned to each peak. Horizontal lines above the peaks indicate MW development throughout the analysis.

Interestingly, in most cases the molecular mass of the detected protein decreases within the elution peak, which confirms the assumption that either a dimer-tetramer equilibrium is present within the peak, or that the presence of degradation products causes the decrease in molecular weight, since the single FabL fragments are able to form tetramers with the intact fusion constructs as well; or a

combination of both. At the same time, higher discrepancies between calculated and experimentally determined MW can be observed for *construct Ib-20₁*, which may be the result of the prolonged linker region that might be more prone to degradation.

The presence of both, dimer and tetramer within one single peak could be demonstrated by simple changes in the protein preparation procedure: *Construct Ib*, which was previously purified and stored in citrate buffer was incubated in a first attempt with cofactor and subsequently applied to the MALS system, where the aSEC was conducted in Tris buffer at pH 8.2. A broad peak containing two local maxima was observed showing a constant molecular-weight decrease from lower to higher elution volumes (**Figure 3.5-X, left panel**). The same analysis was conducted with a protein sample, which was dialysed in Tris-aSEC buffer at pH 8.2 overnight prior to application to the MALS system and either incubated with cofactor only or with cofactor and TCL. An overlay of the three chromatograms clearly shows that within the non-dialysed sample a dimer-tetramer transition due to changing buffer condition is taking place directly on the aSEC column. Both, the dimer as well as the tetramer peak obtained from the following analyses fit into the volume of the single peak, which was observed in the first experiment. This explains the negative slope of the MW reference line and the fact that the experimentally determined MW of the entire peak quite precisely approximates the mean value calculated from both species. The altered peak intensities of dimeric and tetrameric fractions of *construct Ib* upon addition of TCL at basic pH clearly indicate that substrate- or inhibitor binding induces tetramer formation of the FabI part of the fusion protein. These findings also indicate the functional integrity of the fusion protein with respect to cofactor- and inhibitor binding as previously demonstrated by Thermofluor analysis (**Chapter 3.5.4**).

Another possibility for a molecular-weight decrease could be caused by an altered interaction pattern between monomers due to the length and flexibility of the linker, which may allow the ACP portion to interact with the saFabI part of a neighbouring fusion protein as well and lead to different oligomeric states of the fusion constructs. Nevertheless, the evidence that tetramer formation is possible upon the addition of TCL, rather suggests that the interaction of the monomeric fusion proteins amongst each other takes place via their FabI portions.

The decrease of the MW throughout a single peak on a SEC column might be a combination of a dimer-tetramer equilibrium on the one hand, which is shifted towards the tetrameric state upon TCL addition; and on the other hand, the presence of degradation products (most likely the saFabI portion) interacting with the intact fusion protein to form oligomers as well (**Figure 3.5-XII**).

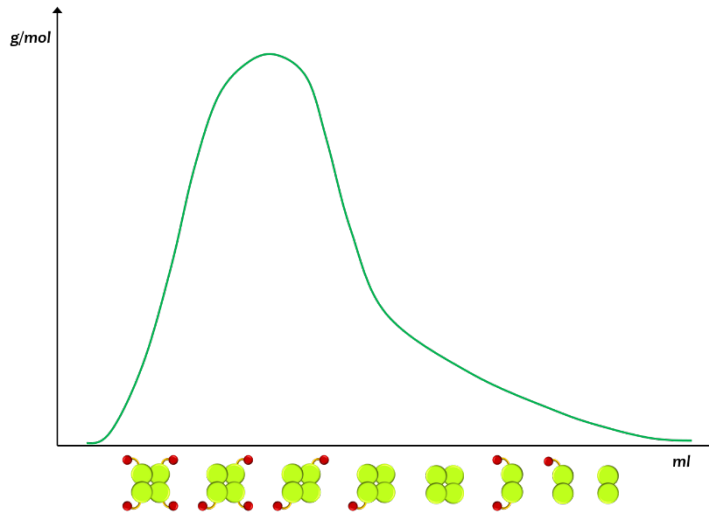


Figure 3.5-XII: Possible distribution of the tetrameric, dimeric and partially degraded fusion construct within a single peak observed during MALS analysis: The mass of the oligomeric fractions decreases at higher elution volumes. The FabI part is shown in green, the ACP portion is shown in red and the linker region is coloured orange.

3.5.6 Modification of fusion constructs

Fusion constructs were tested for their ability to be modified according to the modification protocol established for saACP.

MODIFICATION OF CONSTRUCT 1B

CSGE analysis of an initial modification test with octanoyl-CoA revealed the presence of a slight shift of one of the bands within the gel, suggesting that a conformational change due to the attachment of an acyl moiety to the fusion construct might have taken place (**Figure 3.5-XIII**). Additionally, since the ACP portion could be inaccessible in the context of the fusion construct due to possible interactions with the FabI part, the addition of different urea concentrations within the modification buffer was tested for beneficial effects on the modification. However, the presence of urea did not seem to have a major effect on modification efficiency. Interestingly, the protein bands on the CSGE gel faded at higher urea concentrations and eventually became invisible at urea concentrations of 0.5, 1.0 and 1.5 M urea.

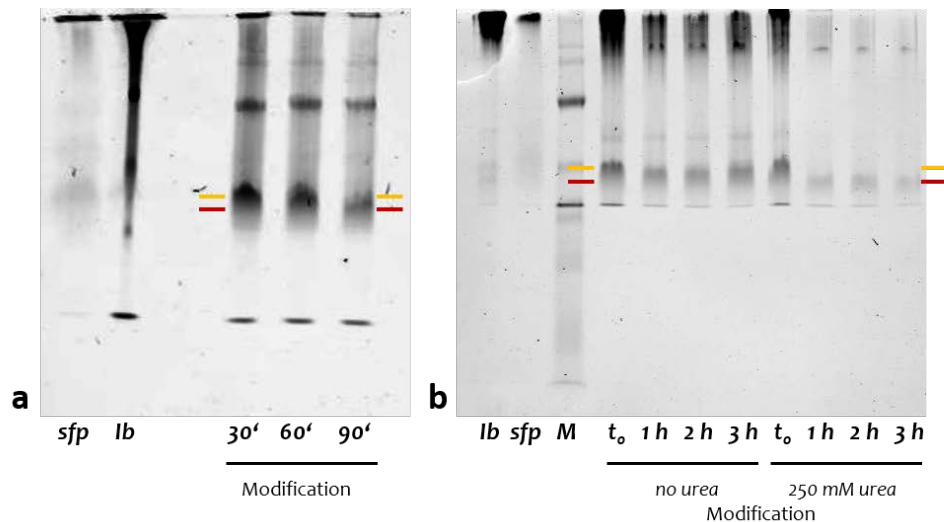


Figure 3.5-XIII: Modification tests of construct *Ib* with octanoyl-CoA: (a) Initial modification test; (b) Modification test in the presence of different urea concentrations; Gels with urea concentrations > 250 mM are not shown, since no bands were visible. The shift is illustrated by orange and red bars with orange bars indicating the initial position of the band and red bars indicating the final position adopted during the modification process.

Since modification of *construct Ib* seemed to be possible, the procedure was carried out at a larger scale using *hexadienyl-N-CoA* (HD-N-CoA) as the substrate for modification with subsequent separation of modified and unmodified fractions via anion exchange chromatography. The chromatogram from the elution with Tris buffer, pH 8.0 showed two major “landscapes” of peaks at different salt concentrations (**Figure 3.5-XIV, upper left**). The peaks at lower salt concentrations could be assigned to *sfp*, whereas the second cohort of peaks displayed bands of *construct Ib* in the SDS-PAGE analysis (**Figure 3.5-XIV, lower left**). Unfortunately, in the subsequent CSGE analysis of the *Ib* fractions the protein bands were very faint and difficult to analyse. Thus, the peak “landscape” was subdivided into several major peaks and transition zones (**Figure 3.5-XIV, upper right**), which were pooled and concentrated separately and then again analysed via CSGE. Here, clear bands could be detected where the second to last revealed a slight and the last fraction revealed a clear band shift (**Figure 3.5-XIV, lower right**), suggesting that the modified proteins elute at higher salt concentrations and the amount of modification increases throughout the peak “landscape”. Indeed, mass spectrometry analysis (*AG Schlosser, RVZ Würzburg; data not shown*) of pools *I* and *V* confirmed the presence of the modification in both fractions but a quantitative determination of the ratio of modified protein within each fraction was not possible. However, the band shift detected on the CSGE gel might represent an enhanced proportion of the modified target. Again, the mixture of modified and unmodified protein within the peaks may be the result of oligomer formation.

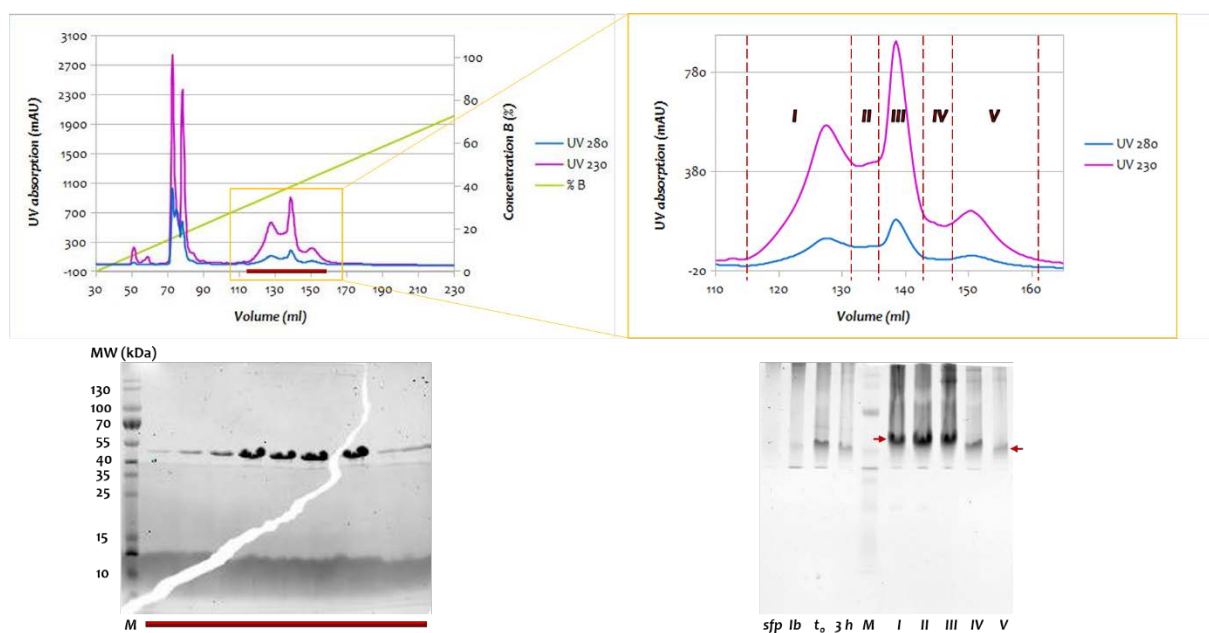


Figure 3.5-XIV: Elution profile and SDS/CSGE analyses of an anion-exchange chromatography of HD-N-Ib in Tris buffer: The entire anion-exchange chromatogram with the corresponding SDS-PAGE is shown on the left hand side, where the fractions containing construct Ib are marked with a red reference bar. The right hand side displays the magnification of the Ib peaks, the division of which into distinct pools is indicated by red, dashed lines. The corresponding CSGE gel is shown below. Fractions analysed by mass spectrometry are indicated with red arrows.

To remove high amounts of salt from *fraction V*, which seemed to be the most promising candidate for crystallisation trials and since the protein had previously been shown to be more stable in citrate buffer (**Chapter 3.5.4**), the buffer was exchanged to citrate via a spin concentrator. Unfortunately, the protein exhibited a high tendency to precipitate during this step, resulting in a decrease of total protein from initially $14.3 \text{ mg}\cdot\text{ml}^{-1}$ in $100 \mu\text{l}$ to $0.8 \text{ mg}\cdot\text{ml}^{-1}$ in the same volume. Nevertheless, crystallisation plates were set up for this fraction and also for *fraction IV* without a buffer exchange.

In a second modification experiment followed by anion-exchange chromatography, the fractions were dialysed into a Tris buffer containing reduced amounts of NaCl after the chromatography step. Retaining the same buffer significantly reduced the precipitation rate and crystallisation trials could be conducted at higher protein concentrations.

Another attempt for anion-exchange chromatography subsequent to the modification reaction was made using citrate buffer already during the chromatography step, resulting in a nearly similar elution profile as observed in Tris buffer. As described above, the “landscape” of peaks was subdivided into fractions, which were concentrated separately and subjected to crystallisation trials.

MODIFICATION OF CONSTRUCT *IB-20₁* AND SAACP-ECFABI-II

The *lb-20₁*-, *lb-20₁'*- as well as the chimeric fusion construct were tested for their ability to be modified using octanoyl-CoA as a substrate. CSGE analysis of the modification tests of constructs *lb-20₁*- and *lb-20₁'* did not display a significant shift of any of the protein bands. Nevertheless, two of the bands which might potentially correspond to the modified species observed in earlier modification trials of construct *lb* were sent to mass spectrometry analysis, where it was confirmed that no modification was present. Since the thioester bond of the substrate is susceptible to hydrolysis in a basic environment, the acyl chain may have been cleaved off. This could have happened either during the CSGE analysis, where the running buffer as well as the separating gel are of basic pH, or during sample preparation for mass spectrometry analysis, where the protein fragments are generated via digestion in basic conditions (*personal communication*). The fact, however, that the hexadienyl-N modification could be detected when coupled to construct *lb*, but acyl substrates containing a thioester bond instead of the carboxamide could not be detected or only in part, strongly suggests that this might be due to hydrolysis.

The chimeric protein was modified utilising similar conditions as the *lb* fusion constructs, since the ACP part is the same in all constructs. Modification tests at different urea concentrations up to 250 mM were conducted as well. Interestingly, no shift is observable within the 3-h course of the modification reaction. However, when the chimeric protein alone is compared with the reaction mixtures on the CSGE gel, a clear shift can be seen, as well as the disappearance of the lower band from the chimeric protein alone (**Figure 3.5-XV**). This might either be due to an extraordinary activity of *sfp*, resulting in almost complete substrate turnover right after the addition of the substrate to the reaction mix even before a sample is taken, or to the formation of a complex between the chimaera and *sfp*. The increased urea concentrations as present in the CSGE gel (500 mM) may result in the dissociation of protein complexes [138] and thus it seems unlikely that complex formation can be visualised in the CSGE gel. Nevertheless, in case of complex formation the actual stability of the complex is not known and thus it is not clear which urea concentration would be necessary to induce dissociation. Further experiments with gels containing different urea contents are required to provide insights regarding this putative complex formation.

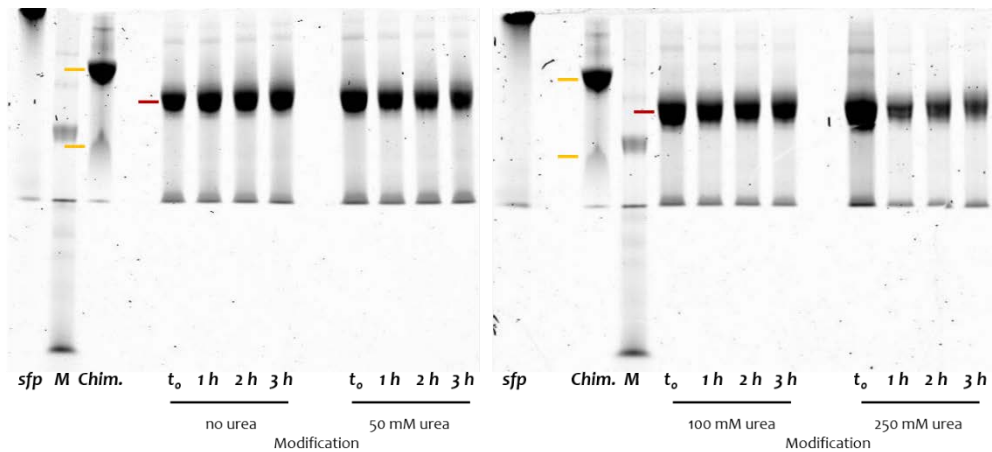


Figure 3.5-XV: Modification test for saACP-ecFabI-II ("Chim."): Initial bands of the fusion construct alone are marked by orange bars, the shifted band is assigned with a red bar.

MODIFICATION OF CONSTRUCT *lb_E47C_{ACP}-K17C_{FabI}*

For the purpose of subsequent intramolecular crosslinking (**Chapter 3.5.7**) the *lb_E47C_{ACP}-K17C_{FabI}* double-cysteine variant was tested for modification with crotonyl-CoA. Different urea concentrations up to 250 mM were applied, since previous modification tests for *construct lb* revealed that modification tests performed at higher amounts of urea cannot be evaluated. In contrast to *construct lb* a shift was observed for two adjacent protein bands in the CSGE gel, the intensity of which seems to vanish at increasing urea concentrations within the modification buffer (**Figure 3.5-XVI**). It is possible that the two shifting bands represent the oxidised and the reduced form of crotonyl-*lb*, since a conversion from crotonyl to butyryl-*lb* may be caused by the presence of cofactor in the reaction mixture. Interestingly, the shift is only detectable in 12 or 15 % CSGE gels, but not in 18 % CSGE gels.

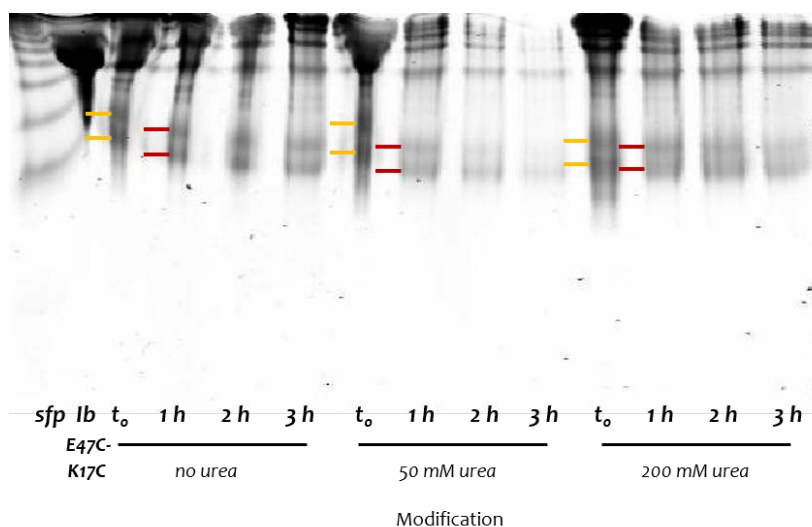


Figure 3.5-XVI: Modification tests of *Ib_E47C_{ACP}-K17C_{FabI}* with crotonyl-CoA at different urea concentrations: The shifts of the bands are indicated by orange and red bars with orange bars illustrating the initial position of the band and red bars highlighting the final position adopted during the modification process.

3.5.7 Intramolecular crosslinking of *Ib_E47C_{ACP}-K17C_{FabI}* – an initial attempt

Crystallisation trials and crystal diffraction analyses of *construct Ib* suggested a high disorder of the crystals resulting most likely from the high intrinsic flexibility of the fusion construct itself. Although the linker ensures that the ACP and the FabI parts are in close proximity to each other, its flexibility still permits the association and dissociation of both components via their interaction surface. Hence, it may be worthwhile to trap the associated state of both proteins through the introduction of an additional crosslinking site. Additionally, the interaction shall be inducible to trap the highest possible amount of protein during the association by adding the crosslinking reagent at a certain time point of the reaction (**Figure 3.5-XVII**).

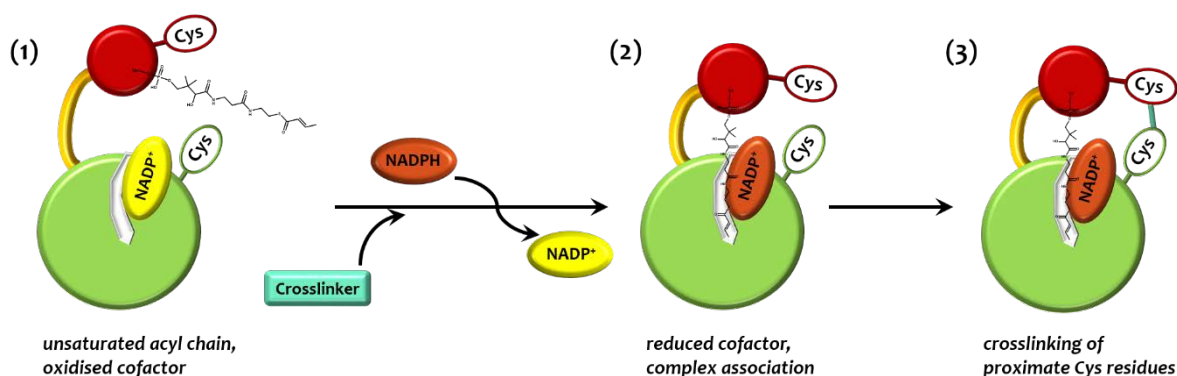


Figure 3.5-XVII: Proposed reaction scheme for intramolecular crosslinking of modified *Ib_E47C_{ACP}-K17C_{FabI}*: (1) In the initial state, NADP⁺ is bound to the modified protein. (2) Addition of NADPH replaces NADP⁺ in the active site and induces approximation of the cysteine residues. (3) In the presence of a crosslinker the interaction is trapped by crosslinking of the cysteines prior to the dissociation of the complex.

In a first step, the double-cysteine variant was pre-incubated with an excess of oxidised cofactor to remove traces of NADPH potentially present in the active site. This step ensures that upon subsequent modification with an unsaturated acyl substrate the same would not be immediately reduced (**Figure 3.5-XVII (1)**). The fusion construct was then modified with crotonyl-CoA and the reaction solution was applied to an anion-exchange column to separate modified from unmodified protein. The chromatogram did not reveal a rather distinct “landscape” as observed for HD-N-Ib, but a large peak containing adumbrated shoulders, which might result from the shorter acyl chain attached and from oligomer formation as described above. Unfortunately, the fractions were again difficult to analyse on the CSGE gel and required the subdivision of the peak into several pools as described above for *construct Ib* (**Figure 3.5-XVIII**).

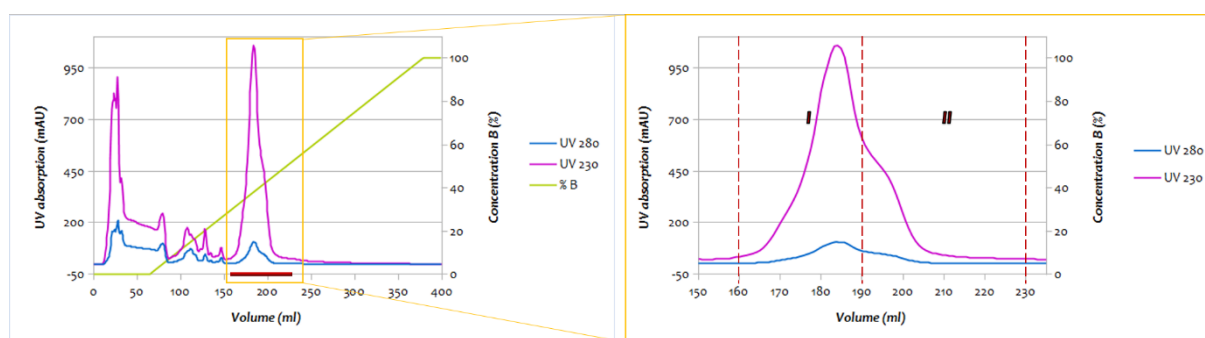


Figure 3.5-XVIII: Purification of intramolecularly crosslinked *cro-Ib_E47C_{ACP}-K17C_{FabI}*: The complete anion-exchange chromatogram prior to crosslinking is shown on the left, where the fractions containing *construct Ib_E47C_{ACP}-K17C_{FabI}* are marked with a red reference bar. On the right, the magnification of the peak and its division into distinct pools, which is indicated by red, dashed lines, is displayed.

The pools were dialysed in crosslinking buffer and BMB was used as crosslinking reagent. The crucial step to trap the associated complex was the induction of the ACP-FabI interaction by addition of the reduced cofactor and the simultaneous addition of crosslinker. Since the crosslinking reaction should not take place when the ACP and the FabI portions are not interacting, BMB was added first, immediately followed by addition of NADPH to induce the spatial approximation of ACP and FabI. The rationale of this step originates from the 1000-fold higher affinity of NADPH compared to NADP⁺ to saFabI [139], leading to a replacement of oxidised by reduced cofactor within the active site of the enzyme. Furthermore, the unsaturated substrate possesses a higher affinity to the NADPH-bound enzyme, which results in an enhanced interaction of the modified ACP with FabI within the fusion construct (**Figure 3.5-XVII (2)**). This complex is catalytically active and the substrate is quickly reduced, followed by rapid dissociation of acyl-modified ACP from FabI. Thus, immediate crosslinking is mandatory, since the cysteine residues that should be crosslinked are only in adequate proximity to each other, when the two protein moieties interact with each other (**Figure 3.5-XVII (3)**). The efficiency of the intramolecular crosslinking cannot be quantified by CSGE analysis, since the non-crosslinked

Results

protein might not only be present in its “open” form where there is no interaction between ACP and FabI, but also in the “closed” state where the ACP and FabI parts are interacting with each other, which would be the case for the crosslinked protein as well. On the other hand, an SDS gel could provide information about side reactions like intermolecular crosslinking between an ACP portion and a FabI part from a neighbouring fusion construct. It could be observed, that this reaction does not take place to a great extent (**Figure 3.5-XIX, left**), which confirms the assumption that interactions of fusion constructs with each other almost exclusively take place upon oligomer formation via the FabI portion as already discussed for the MALS experiments (*page 94*).

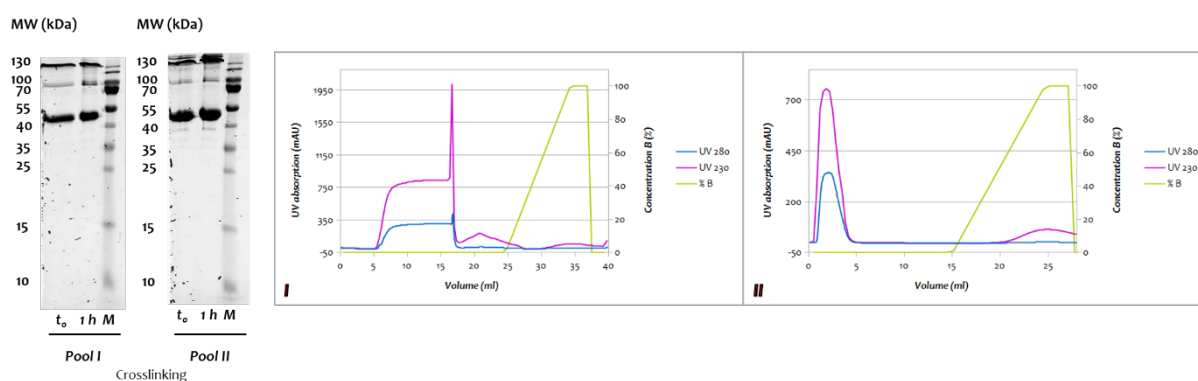


Figure 3.5-XIX: Evaluation of crosslinking and dye-ligand affinity-chromatography elution profiles: SDS analyses of the crosslinking reaction of both pools from the anion-exchange chromatography are shown on the left side. Elution profiles of both pools from the dye-ligand affinity column after crosslinking are displayed on the right side.

The subsequent purification step via dye-ligand affinity chromatography aimed to separate the “closed”, crosslinked species from the “open”, non-crosslinked one. The “open” form would be capable of binding to the column matrix, which mimics the cofactor, whereas in the “closed” form the cofactor-binding site is not accessible. The elution profiles of the fractions applied to the column displayed a large amount of protein, which did not bind to the matrix (**Figure 3.5-XIX, right**). This indicates that either the crosslinking efficiency was very high, that the affinity of the dye towards the cofactor-binding site was very low, or that the cofactor-binding site was not sufficiently accessible due to the presence of the ACP portion, which may hinder the binding to the matrix when interacting with FabI. Analysis by SDS-PAGE or CSGE would not provide any information about the amount of crosslinked protein due to the above-mentioned reasons. Nevertheless, crystallisation screens were set up for both pools. Since the protein fraction bound to the dye-ligand matrix was comparatively small, one might consider leaving this step out in future purification attempts.

3.5.8 Crystallisation of fusion constructs

Crystallisation trials for fusion constructs were set up utilizing unmodified proteins in the presence of cofactor and substrate, or from modified constructs as described in **Chapter 3.5.6**. Initially, very small crystals ($\approx 1 - 2 \mu\text{m}$) were obtained in different conditions and optimisation attempts were pursued utilising customised fine-screens and/or seeding. Initial crystals of both constructs, *lb* and *llb*, were either too small for submitting them to X-ray analyses, showed only weak spots or diffuse diffraction patterns; or were too labile to be collected and cryo-cooled prior to X-ray experiments (**Figure 3.5-XX**, **Figure 3.5-XXI**). The crystal quality could so far not be improved to gain suitable crystals for X-ray experiments.

Optimisation of crystallisation for *construct llb* was not further pursued, since the arrangement of the saACP and saFabI portions relative to each other in the context of the fusion protein may impair the ability of the saFabI part to form a tetramer and to properly bind an acyl substrate. The main reason for this inability to form a correct tetramer may also be due to the linker being located at the C-terminus of saFabI. The C-terminus of saFabI was found to be shorter compared to other ENRs, thereby permitting the expansion of the substrate-binding pocket for substrate binding [130]. Thus, the C-terminally attached ACP of this particular construct may result in a protein with altered oligomerisation and substrate-binding properties compared to the wild-type enzyme.

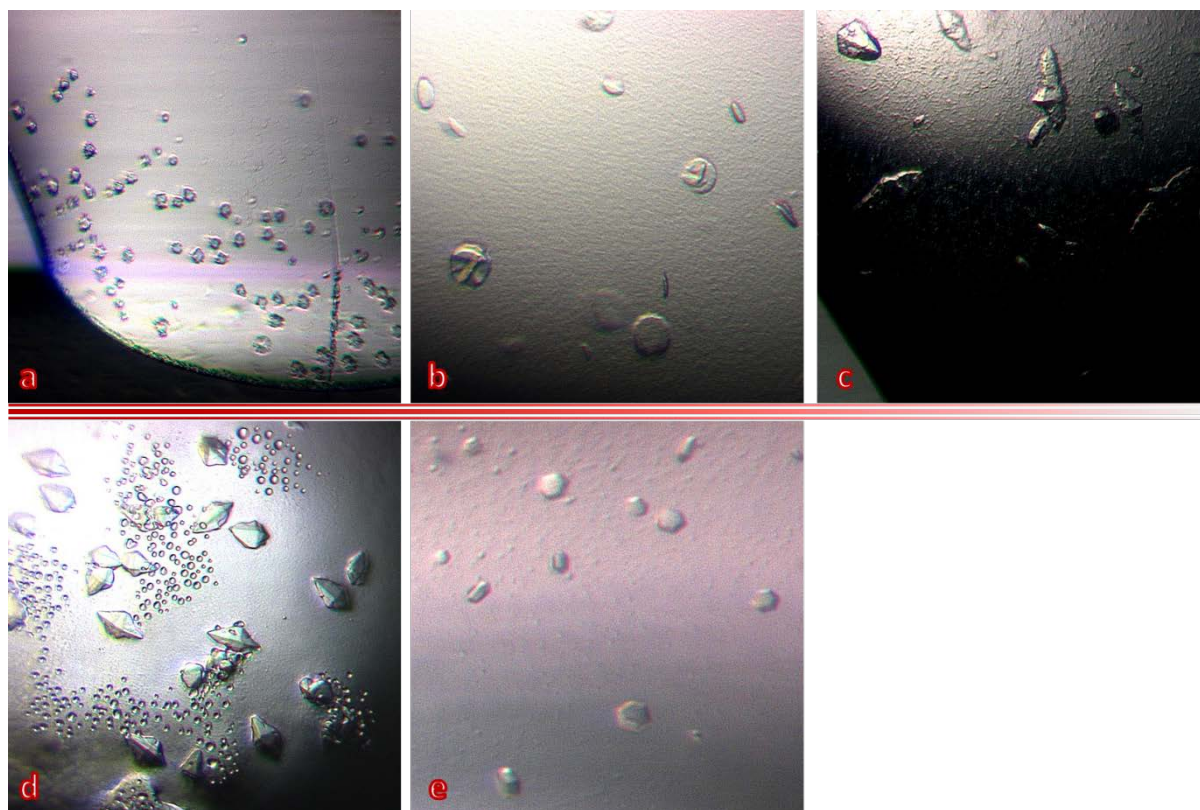


Figure 3.5-XX: Initial (a – c) and optimised (d, e) crystals of construct lb: lb + NADP⁺ + octanoyl-CoA grown in (a) 100 mM HEPES, pH 7.5, 500 mM Mg-formate; (b) 100 mM Tris/HCl, pH 8.5, 200 mM (NH₄)₂SO₄, 25 % (w/v) PEG 3350; (c) 100 mM

Results

glycyl-glycine, pH 8.5, 27 % (w/v) PEG 4000; **(d)** 100 mM glycyl-glycine, pH 8.5, 20 % (w/v) PEG 4000 with 1:50 seeding solution prepared from crystals in **(c)**; **(e)** [HD-N-Ib-NADPH] crystals grown in optimised conditions containing 100 mM Hepes, pH 7.5, 1.8 M $(\text{NH}_4)_2\text{SO}_4$, 40 % (v/v) MPD.

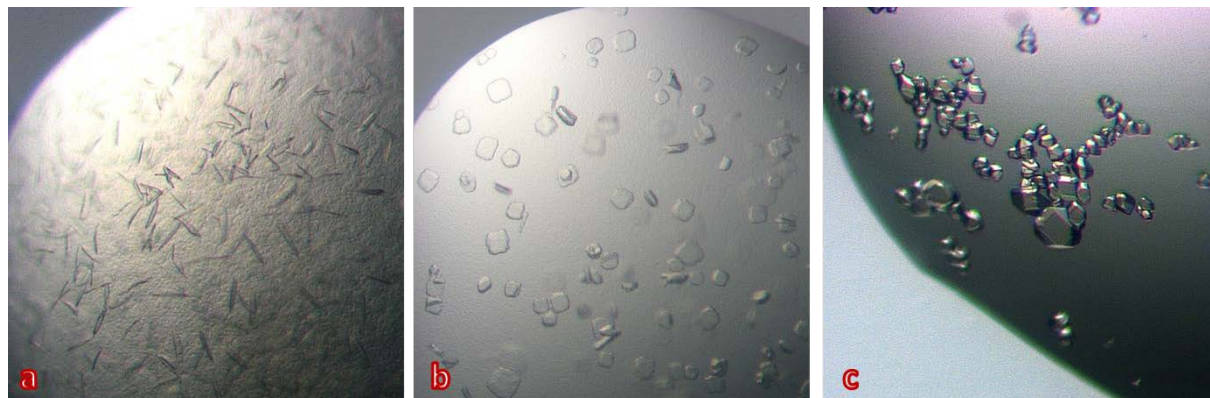


Figure 3.5-XXI: Initial crystals of construct IIb: IIb + NADP⁺ + octanoyl-CoA grown in **(a)** 100 mM Hepes, pH 7.5, 200 mM Li_2SO_4 , 25 % (w/v) PEG 3350; **(b)** 100 mM Hepes, pH 7.0, 150 mM $(\text{NH}_4)_2\text{SO}_4$, 20 % (w/v) PEG 4000; **(c)** 100 mM MES, pH 6.0, 1 M Na-/K-tartrate.

Interestingly, a crystallisation trial using a modification setup which was submitted to crystallisation without any further purification steps and hence still contained all components from the modification experiment, resulted in growth of large and well-shaped crystals in different crystallisation conditions after two days already (**Figure 3.5-XXII**). These crystals displayed protein spots at low-resolutions between $\approx 20 - 10 \text{ \AA}$ upon initial diffraction tests. Unfortunately, attempts to improve crystal quality including fine-screens, additive screens, crystallization at low temperature (4 °C), crystal seeding, diffraction experiments at ambient temperature using a humidity control device, dehydration experiments and high-pressure cooling [135] did not lead to crystals that diffracted to a resolution better than $\approx 8 \text{ \AA}$. In general, the best crystals were obtained from a condition containing 100 mM Hepes, pH 7.5 and 1 M sodium citrate, which was also used as the basic condition for the additive-screen preparation.

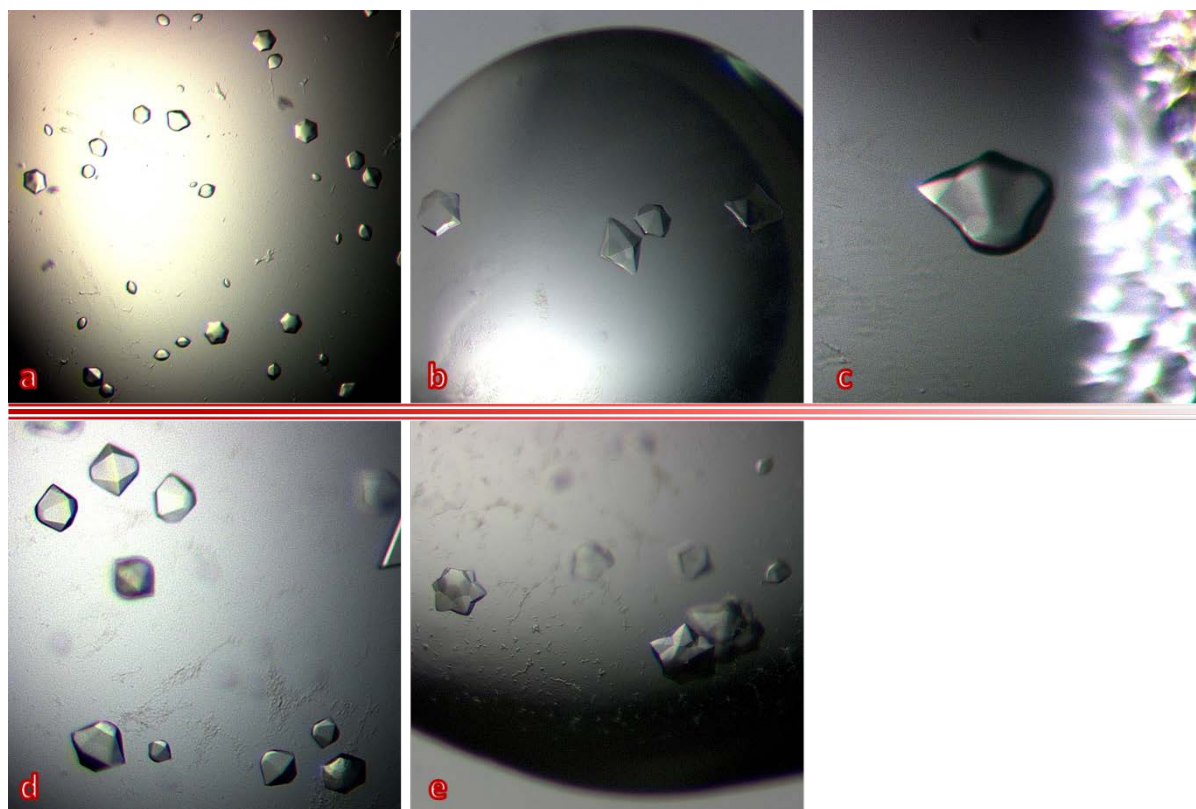


Figure 3.5-XXII: Initial (a – c) and optimised (d, e) crystals of construct *lb*: *lb* + NADP⁺ + octanoyl-CoA + *sfp* after 3 h of incubation at 37 °C in (a) 100 mM Hepes, pH 7.5, 1 M sodium citrate; (b) 1.2 M K₂HPO₄; (c) 100 mM Tris, pH 8.0, 1.2 M Na⁺/K⁺-tartrate; (d) 1.5 M K₂HPO₄ with 1:50 seeding solution prepared from (c); (e) 100 mM Ches, pH 9.25, 1 M sodium citrate with 1:100 seeding solution prepared from (c).

The low diffraction quality of these crystals is probably the result of a high degree of disorder within the crystal lattice, resulting from the flexibility of the ACP domain in addition to the flexible linker and could also be due to the intrinsic flexibility of saFabI itself. Of course, it may be argued that in addition to the fusion construct also the ACP synthase *sfp* is present in the crystallisation mixture. However, the amount of *sfp* is comparatively low ($\approx 3 \mu\text{M}$) in contrast to the fusion protein, which exists at a concentration of $\approx 250 \mu\text{M}$, and a slight band on a silver-stained SDS gel prepared from these crystals indicated the presence of the fusion protein (**Appendix, page LVI**). Since crystals were obtained in the presence of *sfp* and remaining amounts of the CoA substrate, it is possible that both or one of these “additives” benefit crystal formation and it might be worthwhile trying to vary the octanoyl-CoA as well as the *sfp* concentrations in subsequent crystallisation trials.

4 Rationalizing the Binding Kinetics for the Inhibition of the *Burkholderia pseudomallei* FabI Enoyl-ACP Reductase

This chapter is based on the following publication:

Neckles, C.* , Eltschkner, S.* , Cummings, J. E.* , Hirschbeck, M., Daryae, F., Bommineni, G. R., Zhang, Z., Spagnuolo, L., Yu, W., Davoodi, S., Slayden, R. A., Kisker, C., Tonge, P.J. (2017) *Rationalizing the Binding Kinetics for the Inhibition of the Burkholderia pseudomallei FabI Enoyl-ACP Reductase*. *Biochemistry* **56**, 1865-1878

Copyright:

Reproduced with permission from [6]. Copyright 2017 American Chemical Society.

Author contributions:

Neckles, C.: Enzyme kinetics

Eltchkner, S.: X-ray crystallography

Cummings, J. E.: Microbiology and animal infection model

Hirschbeck, M.: X-ray crystallography

Daryae, F.: Enzyme kinetics

Bommineni, G. R.: Synthesis of inhibitors

Zhang, Z.: Synthesis of inhibitors

Spagnuolo, L.: Synthesis of inhibitors

Yu, W.: Enzyme kinetics

Davoodi, S.: Enzyme kinetics

** These authors contributed equally*

Rationalizing the Binding Kinetics for the Inhibition of the *Burkholderia pseudomallei* FabI Enoyl-ACP Reductase

Carla Neckles,¹ Sandra Eltschkner,² Jason E. Cummings,³ Maria Hirschbeck,² Fereidoon Daryaei,¹

Gopal R. Bommineni,¹ Zhuo Zhang,¹ Lauren Spagnuolo,¹ Weixuan Yu,¹ Shabnam Davoodi,¹

Richard A. Slayden,³ Caroline Kisker,² and Peter J. Tonge,¹

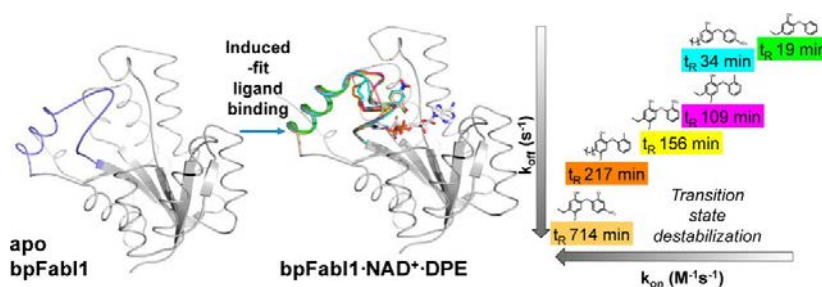
¹Institute for Chemical Biology and Drug Discovery, Department of Chemistry, Stony Brook University, Stony Brook, New York 11794, United States

²Rudolf Virchow Center for Experimental Biomedicine, Institute for Structural Biology, University of Würzburg, D-97080 Würzburg, Germany

³Rocky Mountain Regional Center of Excellence for Biodefense and Emerging Infectious Diseases Research and Department of Microbiology, Immunology and Pathology, Colorado State University, Fort Collins, Colorado 80523-0922, United States

4.1 Abstract

There is growing awareness of the link between drug–target residence time and *in vivo* drug activity, and there are increasing efforts to determine the molecular factors that



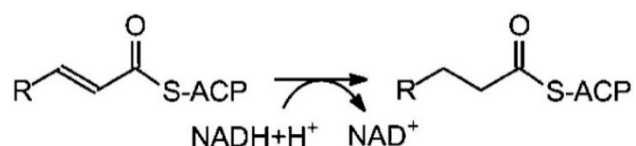
control the lifetime of a drug–target complex. Rational alterations in the drug–target residence time require knowledge of both the ground and transition states on the inhibition reaction coordinate, and we have determined the structure–kinetic relationship for 22 ethyl- or hexyl-substituted diphenyl ethers that are slow-binding inhibitors of bpFabI1, the enoyl-ACP reductase FabI1 from *Burkholderia pseudomallei*. Analysis of enzyme inhibition using a two-dimensional kinetic map demonstrates that the ethyl and hexyl diphenyl ethers fall into two distinct clusters. Modifications to the ethyl diphenyl ether B ring result in changes to both on and off rates, where residence times of up to ≈ 700 min (≈ 11 h) are achieved by either ground state stabilization (PT444) or transition state destabilization (slower on rate) (PT404). By contrast, modifications to the hexyl diphenyl ether B ring result in residence times of 300 min (≈ 5 h) through changes in only ground state stabilization (PT119). Structural analysis of nine enzyme:inhibitor complexes reveals that the variation in structure–kinetic relationships can be rationalized by structural rearrangements of bpFabI1 and subtle changes to the orientation of the inhibitor in the binding pocket. Finally, we demonstrate that three compounds with residence times on bpFabI1 from 118 min (≈ 2 h) to 670 min (≈ 11 h) have *in-vivo* efficacy in an acute *B. pseudomallei* murine infection model using the virulent *B. pseudomallei* strain Bp400.

4.2 Introduction

Melioidosis is a complex disease to treat because of its rapid progression and tendency to generate latent infections [140]. One of the most severe manifestations of this disease is melioidosis septic shock, which is often associated with pneumonia and bacterial dissemination to distant sites [25]. The etiologic agent of melioidosis is the Gram-negative soil-dwelling organism *Burkholderia pseudomallei*. While *B. pseudomallei* is susceptible to therapeutics such as ceftazidime, chloramphenicol, doxycycline, amoxicillin-clavulanate, trimethoprim-sulfamethoxazole, ureidopenicillins, and carbapenems, mortality is high because relapse often occurs [24, 32, 36]. Moreover, antibiotic resistance mechanisms have been identified in *B. pseudomallei*, including efflux from the cell, target mutation, target redundancy, exclusion from the cell, and enzymatic inactivation [106]. In addition, *B. pseudomallei* can potentially be used as a biowarfare agent and is thus now classified as a Tier 1 Biological Select Agent or Toxin (BSAT) by the Centers for Disease Control and Prevention (CDC) [36,

141]. Consequently, there is a need to develop chemotherapeutics that can be used to treat *B. pseudomallei* infections.

Enzymes in the bacterial fatty acid biosynthesis (FAS) pathway are attractive antimicrobial targets because this pathway produces metabolic precursors for the bacterial phospholipid membrane that are essential for Gram-positive and Gram-negative bacterial survival, and also because there are fundamental structural differences and low amino acid sequence identities between the mammalian FAS (FAS-I) and bacterial FAS (FAS-II) systems [100, 142]. In this regard, inhibitor discovery programs have focused primarily on the NAD(P)H-dependent enoyl-ACP reductase (ENR) that catalyzes the last reaction in the FAS-II elongation cycle and is targeted by antibacterial agents, including the diazaborines, triclosan, and isoniazid (**Scheme 4.2-1**) [4, 62, 116, 143, 144].



Scheme 4.2-1: Reaction Catalyzed by the Enoyl-ACP Reductase (ENR)

We have previously characterized the ENR isoforms FabI1, FabI2, and FabV in *B. pseudomallei* and demonstrated that FabI1 (herein bpFabI1) was the transcriptionally active and clinically relevant FabI isoform [67, 80, 145]. We also showed that diphenyl ethers, analogues of the broad-spectrum inhibitor triclosan (**Figure 4.2-1 B**), were potent low-nanomolar slow-binding inhibitors of bpFabI1 with antibacterial

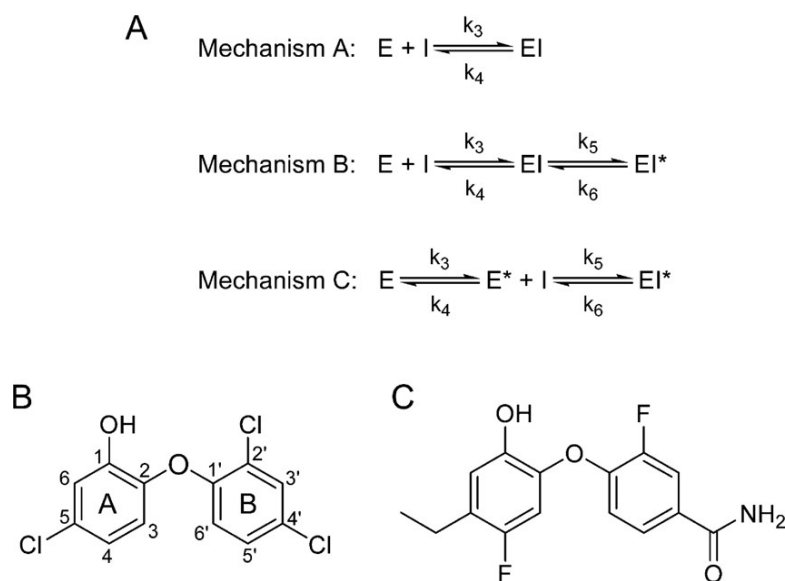


Figure 4.2-I: One- and two-step kinetic mechanisms for enzyme inhibition and slow-binding FabI inhibitors. (A) Three possible mechanisms (A–C) for slow-binding inhibition. (B) Triclosan is a broad-spectrum inhibitor that targets the FabI enoyl-ACP reductase. (C) FabI-specific inhibitor MUT056399 [125, 146, 147].

activity against *B. pseudomallei*. These diphenyl ethers were found to preferentially bind to the enzyme–NAD⁺ product complex, as observed for the inhibition of FabI enzymes from other species by similar analogues [62, 67, 77, 148]. In a second study, we confirmed that the inhibition of bpFabI1 with the diphenyl ether PT01 reduced bacterial burden and achieved efficacy in an acute *B. pseudomallei* murine model of infection [80].

Although we previously identified time-dependent diphenyl ether inhibitors of bpFabI1, we did not determine the precise mechanism of inhibition. Diphenyl ether inhibitors of the FabI enzymes from other pathogens follow either a one-step mechanism (**Figure 4.2-I, mechanism A**) or an induced-fit, two-steps slow-binding mechanism (**Figure 4.2-I, mechanism B**) [71, 77, 139, 149]. Because the inhibitor concentration is not constant *in vivo*, the rates of formation and breakdown of the enzyme–inhibitor complex are critical factors that may influence *in-vivo* efficacy [150]. Thus, there is a strong need to understand enzyme–inhibitor association and dissociation kinetics at the molecular level, so that this information can be used to optimize target engagement under fluctuating drug concentrations.

In this study, we performed an extensive analysis of bpFabI1-diphenyl ether binding kinetics and extended our structure–kinetic relationship (SKR) to include a potent antistaphylococcal clinical candidate developed by Mutabilis, MUT056399, which is a FabI-specific diphenyl ether inhibitor (**Figure 4.2-I C**) [125, 146]. Using kinetic and structural studies, we identified substituents on the inhibitor B ring that affect the transition and ground state energies on the inhibition reaction

coordinate. Using this information, we were able to increase the residence time of diphenyl ethers on bpFabI from 12 to \approx 700 min. Many of the diphenyl ethers in this study with a 5-ethyl substituent had antibacterial activity in the virulent efflux-compromised *B. pseudomallei* strain Bp400, and three diphenyl ethers reduced the bacterial burden in an acute *B. pseudomallei* mouse model of infection.

4.3 Materials and Methods

4.3.1 Materials

Luria-Bertani (LB) Agar Miller and Mueller-Hinton broth were purchased from BD. BALB/c female mice were obtained from Charles River Laboratories. His-bind Ni²⁺-NTA resin was purchased from Invitrogen. Crotonyl coenzyme A (crot-CoA) was purchased from Sigma-Aldrich. MUT056399 was a kind gift from Anacor Pharmaceuticals. All other chemical reagents were obtained from Fisher.

4.3.2 Expression and Purification of bpFabI

An expression plasmid for the *B. pseudomallei* FabI enoyl-ACP reductase was available from previous studies, in which a His tag was encoded at the C-terminus of bpFabI [67]. Protein expression and purification for bpFabI were performed as previously reported [67, 145, 151]. The protein purity was verified by a 15 % sodium dodecyl sulfate–polyacrylamide gel electrophoresis gel, which indicated an apparent molecular weight of \approx 28 kDa. The concentration of bpFabI was spectrophotometrically determined using an extinction coefficient of 13490 M⁻¹ cm⁻¹. This value was calculated from the primary sequence of the protein using the ExpASy ProtParam tool.

4.3.3 Crystallization and Structure Determination of the bpFabI Ternary Inhibitor Complexes

Solutions of bpFabI (0.34–1.02 mM) were incubated on ice for 1 h with a 10-fold molar excess of cofactor and a 10–100-fold molar excess of inhibitor from a 100 mg/ml stock solution in DMSO (TCL, PT01, PT12, PT405, and PT412), resulting in a final DMSO content of \approx 5–15 %, or the inhibitor was directly added as a pure solid (PT02, PT401, PT404, and PT408). Subsequently, the protein solution was centrifuged for 20 min at 16000 x g and 4 °C. The [bpFabI·NAD⁺·inhibitor] complexes were then crystallized by hanging-drop vapor diffusion at 20 °C. Crystals of the [bpFabI·NAD⁺·PT12], [bpFabI·NAD⁺·PT404], [bpFabI·NAD⁺·PT405], and [bpFabI·NAD⁺·PT408] complexes were obtained in 0.1 M Bis-Tris-HCl (pH 6.5) and 20–30 % (v/v) PEG 400. The [bpFabI·NAD⁺·PT01], [bpFabI·NAD⁺·PT401], and [bpFabI·NAD⁺·PT412] crystals were obtained from 0.1 M Bis-Tris-HCl (pH 6.5) and 26–36 % (v/v) PEG 300 as the precipitant. Crystals of both the bpFabI–PT02 and triclosan (TCL) complexes grew in a mixture of 8 % (w/v) PEG 1000 and 8 % (w/v) PEG 8000. All crystals were transferred to a cryoprotectant containing the mother liquor with elevated PEG concentrations and 10–25 % glycerol.

Data sets were collected at beamline ID29 at the ESRF [152], at beamline MX 14.1 at the BESSY [153], or at an in-house X-ray facility. Data sets were integrated with XDS [154] or Mosflm [155] and scaled in Scala [156, 157] or Aimless [158]. Structures were determined by molecular replacement with Phaser [159] utilizing either the apo structure of bpFabI [Protein Data Bank (PDB) entry 3EK2] or the complex structure of bpFabI with PT155 (PDB entry 4BKU) as a search model. Models were initially revised and adapted in Coot [160] and subsequently refined using Refmac [161] or Phenix [162, 163]. Data collection and refinement statistics are listed in **Table 4.9-I**. Figures were prepared using PyMOL [164]. The structure factors and coordinates for apo bpFabI and the bpFabI-NAD⁺-inhibitor ternary complexes have been deposited in the PDB as entries 5I7E (apo), 5IFL (TCL), 5I7S (PT01), 5I7V (PT02), 5I8Z (PT12), 5I8W (PT401), 5I9L (PT404), 5I7F (PT405), 5I9M (PT408), and 5I9N (PT412).

4.3.4 Synthesis of Diphenyl Ethers

Diphenyl ether compounds PT04, PT12, PT70, PT91, PT113, PT119, PT403, PT404, PT411, PT412, PT417, and PT443 were available from former studies, and PT405 was synthesized as previously described [77, 125, 139, 151, 165, 166]. PT400, PT401, PT406, PT407, PT408, PT409, and PT444 were synthesized as described in the *Supporting Information*.

4.3.5 Inhibition Kinetics

Slow-onset inhibition kinetics were monitored at 340 nm on a Cary 100 spectrophotometer (Varian) at 25 °C in 30 mM PIPES buffer (pH 8.0) containing 150 mM NaCl and 1.0 mM EDTA. The reactions were initiated by the addition of enzyme (8 nM) to a mixture containing glycerol [8 % (v/v)], bovine serum albumin (0.1 mg/ml), DMSO [2 % (v/v)], crot-CoA (750 μM), NADH (250 μM), NAD⁺ (200 μM), and inhibitor (0–8000 nM). All reactions were monitored until the steady state was reached, indicated by the linearity of the progress curve. Low enzyme and high substrate concentrations ensured substrate depletion would not significantly affect the reaction rates, such that in the absence of inhibitor, the progress curves were linear over a period of 30 min [121, 139, 167]. Data were globally fit to the Morrison and Walsh integrated rate equation (**eq 1**) [168].

$$A_t = A_0 - v_s t - (v_i - v_s) \times \frac{1 - e^{-k_{obs}t}}{k_{obs}} \quad (1)$$

where A_t and A_0 are the absorbance at time t and time zero, respectively, v_i and v_s are the initial and steady state velocities, respectively, and k_{obs} is the observed pseudo-first-order rate constant for the approach to steady state. The inhibition dissociation constant (K_i^{app}) for a one-step slow-binding model (**Figure 1, mechanism A**) was subsequently obtained from **eqs 2 and 3** where $v_i = v_0$.

$$v_s = \frac{v_0}{1 + \frac{[I]}{K_i^{app}}} \quad (2)$$

$$k_{obs} = k_4 \times \frac{v_0}{v_s} \quad (3)$$

Inhibition dissociation constants (K_i^{app} and K_i^{*app}) for a two-step slow-binding model (**Figure 4.2-I, mechanism B**) were subsequently obtained from eqs 4–6.

$$v_s = \frac{v_0}{1 + \frac{[I]}{K_i^{*app}}} \quad (4)$$

$$v_i = \frac{v_0}{1 + \frac{[I]}{K_i^{app}}} \quad (5)$$

$$k_{obs} = k_6 \times \frac{v_i}{v_s} \quad (6)$$

Parameters v_0 and $[I]$ are the uninhibited reaction velocity and the inhibitor concentration, respectively. The reverse rate constant for enzyme inhibition is k_4 for a one-step model, and the rate constant for conversion of EI^* to EI is k_6 for the two-step model. Parameter k_4 or k_6 is thought to be the rate-limiting step for recovery of the active enzyme, and thus, the residence time of the inhibitor on the enzyme (t_R) is the reciprocal of k_4 or k_6 .

4.3.6 Minimum Inhibitory Concentration (MIC) Determination

B. pseudomallei 1026b (efflux-proficient) and *B. pseudomallei* Bp400 (1026b Δ [bpeAB-oprB] Δ [amrAB-oprA]) were grown to an OD_{600} of 0.6. Samples were then stored at -80°C in 10 % glycerol and used as standard bacterial stocks. For each analysis, bacteria were freshly prepared by growth from the standard stocks on Luria-Bertani (LB) Agar Miller plates for 48–72 h at 37°C . Bacteria recovered from the LB plates were inoculated in 10 ml of LB broth. Broth cultures were then incubated for 18 h at 37°C , diluted 1:100, and incubated for an additional 6 h at 37°C . Bacteria were further diluted to a concentration of 1×10^6 colony-forming units (CFU) per milliliter in cation-adjusted Mueller-Hinton broth (CAMHB), and 50 μl aliquots were added to each well in the test plate. For MIC determinations, compounds were added to a 96-well plate starting at 256 $\mu\text{g/ml}$ and serially diluted 1:2 until a final concentration of 0.125 $\mu\text{g/ml}$ in CAMHB was obtained. The plates were incubated at 37°C for 18 h, and the MIC was determined by the lowest inhibitor concentration to inhibit visible bacterial growth.

4.3.7 Evaluation of Efficacy in an Acute *B. pseudomallei* Mouse Model of Infection

Five- to six-week-old BALB/c female mice were challenged by intranasal infection with 5000 CFU/mouse of *B. pseudomallei* Bp400 (1026b Δ [amrAB-oprA] Δ [bpeAB-oprB]) [169]. Animals were anesthetized with a mixture of 100 mg of ketamine/kg and 10 mg of xylazine/kg delivered intraperitoneally. Bacteria were diluted in PBS to achieve an inoculum concentration of 2.5×10^5 CFU/ml. This inoculum was then delivered dropwise in alternating nostrils. Ceftazidime was formulated in PBS and test compounds in a lipid-based delivery system as previously described [145, 170]. Compounds were delivered intraperitoneally, b.i.d. (twice daily) starting at the time of infection. The number of viable bacteria in the lung and spleen was determined 60 h post-infection by plating serial 10- fold dilutions of homogenates on LB agar and incubation for 48 h at 37 °C. The bacterial burden was assessed, and the difference in group means was determined using a one-way analysis of variance (ANOVA) followed by Tukey's multiple-comparisons test. The significance was determined by a P value of < 0.05 .

4.4 Results

FabI was initially revealed to be a target for the broad-spectrum biocide triclosan by McMurry et al., who discovered that triclosan-resistant *Escherichia coli* strains had mutations in the *fabI* gene [5]. Shortly thereafter, Heath et al. demonstrated that 2-hydroxydiphenyl ethers, including triclosan, directly inhibited FabI enzyme activity [171], and triclosan was then shown to be a slow, tight-binding inhibitor of *E. coli* FabI (ecFabI), binding preferentially to the E-NAD⁺ complex ($K_i = 7$ pM) [4, 121, 122, 147, 172]. Subsequently, a number of groups, including our own, have synthesized series of diphenyl ether-based compounds to explore the structural determinants of FabI inhibition in *E. coli* [148, 173] and in other bacteria, such as *Plasmodium falciparum* [173], *Staphylococcus aureus* [136, 139, 174], *Mycobacterium tuberculosis* [77, 127, 175], and *Francisella tularensis* [126].

Previously, we demonstrated that the diphenyl ether class of compounds also inhibited the bpFabI1 homologue in *B. pseudomallei* and that selected compounds had nanomolar K_i values and displayed time-dependent enzyme inhibition [67, 145]. The bpFabI1 inhibitors were shown to have antibacterial activity against *B. pseudomallei* both *in vitro* (0.5–4 μ g/ml) and *in vivo*, consistent with the knowledge that bpFabI1 is essential [80]. In the work presented here, we have performed a detailed structure–kinetic analysis to identify substituents on the diphenyl ether skeleton that modulate time-dependent inhibition. This work has concentrated primarily on two compound series, one based on the Mutabilis clinical candidate with fluoro and ethyl substituents on the A ring and the second with a hexyl substituent on the A ring. We also report additional *in-vivo* efficacy studies with a subset of the diphenyl ethers.

Rationalizing the Binding Kinetics for the Inhibition of the *Burkholderia pseudomallei* FabI Enoyl-ACP Reductase

Table 4.4-I: Kinetic and Thermodynamic Parameters for Inhibitors of bpFabI^a

Compound	Structure	K_i^{app} (nM) ^b	k_3^{app} (M ⁻¹ s ⁻¹) ^c	k_4 (min ⁻¹) ^b	t_R (min) ^d	MIC (mg/L)	
						Bp400	Bp1026b
Triclosan		32 ± 0	3.25 × 10 ⁴	0.062 ± 0.001	16 ± 0	0.125	2
PT443		1 ± 0	1.42 × 10 ⁵	0.0085 ± 0	118 ± 0	16	128
<i>Derivatives with 5-ethyl substituents</i>							
MUT056399		405 ± 2	3.33 × 10 ³	0.081 ± 0	12 ± 0	16	>128
PT01		32 ± 1	2.82 × 10 ⁴	0.054 ± 0.002	19 ± 1	16	64
PT411		31 ± 0	2.80 × 10 ⁴	0.052 ± 0	19 ± 1	16	128
PT405		4 ± 0	1.67 × 10 ⁴	0.0040 ± 0	250 ± 1	16	>128
PT406		3 ± 0	1.56 × 10 ⁴	0.0028 ± 0.0001	357 ± 6	8	128
PT412		58 ± 2	1.83 × 10 ³	0.0064 ± 0.0003	156 ± 7	16	>128
PT407		156 ± 0	4.38 × 10 ³	0.041 ± 0	24 ± 0	8	128
PT403		32 ± 0	1.30 × 10 ⁴	0.025 ± 0	40 ± 0	16	>128
PT404		153 ± 0	1.53 × 10 ² ^e	0.0014 ± 0.0005 ^e	713 ± 25 ^e	4	>128
PT408		55 ± 0	2.78 × 10 ³	0.0092 ± 0.0001	109 ± 1	>128	>128
PT444		0.51 ± 0.01	4.90 × 10 ⁴	0.0015 ± 0	667 ± 9	8	128
PT409		44 ± 0	6.43 × 10 ³	0.017 ± 0	59 ± 0	16	128
<i>Derivatives with 5-hexyl substituents</i>							
PT04		138 ± 3	6.65 × 10 ³	0.055 ± 0	18 ± 0	>128	>128
PT113		105 ± 0	1.75 × 10 ³	0.011 ± 0	91 ± 0	>128	>128
PT91		25 ± 0	3.73 × 10 ³	0.0056 ± 0.0001	179 ± 2	>128	>128
PT119		15 ± 0	3.67 × 10 ³	0.0033 ± 0	303 ± 1	>128	>128
PT70		48 ± 0	2.57 × 10 ³	0.0074 ± 0	135 ± 1	>128	>128
PT12		158 ± 0	3.07 × 10 ³	0.029 ± 0	34 ± 0	>128	>128
PT400		1134 ± 5	7.05 × 10 ²	0.048 ± 0.001	21 ± 0	>128	>128
PT401		55 ± 1	1.39 × 10 ³	0.0046 ± 0.0001	217 ± 2	>128	>128
PT417		130 ± 2	8.85 × 10 ²	0.0069 ± 0.0001	145 ± 2	>128	>128

^aParameters were determined using 8 nM enzyme, 0.75 mM crotonyl-CoA, 0.25 mM NADH, and 0.20 mM NAD⁺ at fixed inhibitor concentrations (0–8 μ M). ^bAll data sets at fixed inhibitor concentrations were globally fit to **eq 1**. v_s and k_{obs} are defined by **eqs 2 and 3**, when $v_i = v_0$. ^cCalculated using the equation $k_3^{app} = k_4/K_i^{app}$. ^dCalculated using the equation $t_R = 1/k_4$. ^eValues reported using a direct dissociation method developed by Yu et al. [151]

4.4.1 Mechanism of Inhibition

The inhibition constants and kinetic parameters for 22 triclosan analogues are listed in **Table 4.4-I**. The progress curve data have been analyzed by **eq 1** to give values for k_{obs} , v_i , and v_s , which have subsequently been analyzed by **eqs 2 and 3**. All progress curves resulting from the inhibition studies displayed curvature characteristic of slow-binding kinetics (**Figure 4.4-I A**).

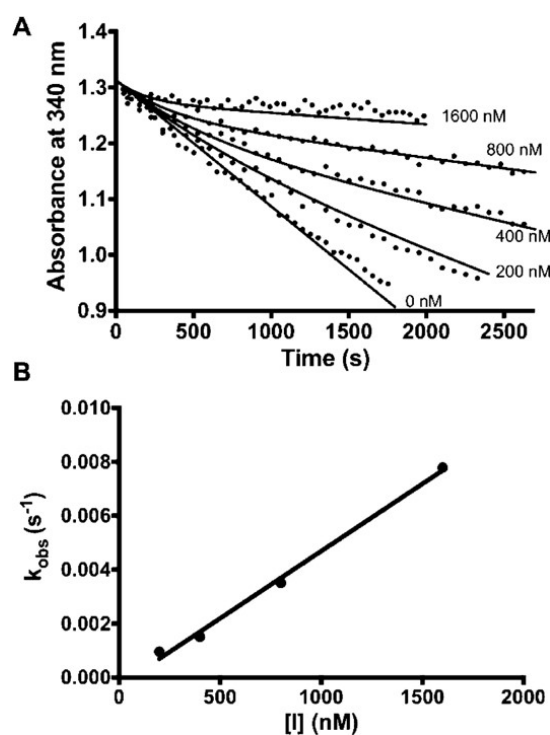


Figure 4.4-I: Representative data for the time-dependent inhibition of bpFabI1. (A) Progress curves for inhibition of bpFabI1 by PT12. The experimental data (\bullet) were globally fit to **eq 1** generating the solid lines ($R^2 = 0.98$). (B) Plot of the pseudo-first-order rate constant (k_{obs}) as a function of inhibitor concentration (\bullet). Curve fitting gave the solid line ($R^2 = 0.99$). Inhibition parameters for each compound are summarized in **Table 4.4-I**.

In principal, slow-onset inhibition can arise from one of three kinetic mechanisms (**Figure 4.2-I**) [168, 176, 177], a one-step model in which formation of the final EI inhibitor complex occurs slowly without any stable intermediate (**Figure 4.2-I, mechanism A**) and the induced-fit or conformational selection two-step models. For the induced-fit model, a slow conformational rearrangement occurs to form a more stable EI* complex after the rapid formation of EI (**Figure 4.2-I, mechanism B**). In contrast, the conformational selection model involves the slow interconversion of two forms of the enzyme, only

one of which is capable of binding the inhibitor (**Figure 4.2-I, mechanism C**). To determine the mechanism of slow-binding inhibition for this subset of diphenyl ethers, k_{obs} was plotted as a function of inhibitor concentration (**Figure 4.2-I B**). A positive linear fit was observed for all the compounds, which is typically a characteristic of a one-step mechanism, and the increasing k_{obs} at higher ligand concentrations unambiguously rules out the possibility of a conformational selection mechanism (**Figure 4.2-I, mechanism C**) [178]. We subsequently analyzed the inhibition data using both the one-step and two-step induced-fit models and found that all data sets fit globally to the one-step model (**Table 4.9-II**). In some cases, we obtained a better fit for the two-step model ($P < 0.0001$); however, $K_i^{\text{app}} \gg K_i^{*,\text{app}}$ by 15- to > 100 -fold with the exception of the values of PT411 and MUT056399 (6-fold). To further analyze the mechanism of inhibition, we solved the structures of nine enzyme:inhibitor complexes. As we show below, bpFabI inhibitor complexes can populate structures in which the substrate-binding loop (SBL) is either in an open or in a closed conformation. Such structural rearrangements have been observed previously for InhA, the FabI from *M. tuberculosis*, where there is clear evidence of a two-step binding mechanism (*mechanism B*) in which the open conformation is EI and the closed conformation is EI* [77, 149, 179]. Thus, our working hypothesis for bpFabI is that inhibition follows a special kind of two-step mechanism that is kinetically indistinguishable from the one-step mechanism, similar to saFabI [71, 139], in which the free energy of EI* is much lower than that of EI and the initial formation of EI cannot be detected at low inhibitor concentrations. Moreover, our results suggest that the detailed underlying mechanism of enzyme inhibition may be more complicated and suggest that the association and dissociation rates that are listed in **Table 4.4-I** can be considered macroscopic rate constants of a multistep process. Therefore, we give values for both the residence time ($1/k_4$) and the overall on rate (k_3) in **Table 4.4-I**, and we observe that the on rate can be used to formulate explicit structure–kinetic relationships for bpFabI inhibition.

4.4.2 Structure–Kinetic Analysis of bpFabI Inhibition

FLUOROETHYL A RING DIPHENYL ETHERS

MUT056399 is a diphenyl ether with potent activity toward several pathogens, including *S. aureus* [125, 146]. We first quantified the inhibition of bpFabI by MUT056399 and found that it had a K_i^{app} of 405 nM and a t_{R} of 12 min (**Table 4.4-I**). Compared to the inhibition of bpFabI by triclosan, MUT056399 binds significantly (≈ 13 -fold) less potently (K_i^{app} of 405 nM vs. 32 nM for triclosan), but with a t_{R} value that is only ≈ 1.3 -fold smaller (12 min vs. 16 min for triclosan), despite the significant differences in diphenyl ether substitution patterns for the two compounds: MUT056399 has both 4-F and 5-ethyl substituents on the A ring and 2'-F and 4'-amide substituents on the B ring, whereas triclosan has an A ring 5-Cl and B-ring 2'- and 4'-Cl substituents. We thus set out to evaluate the contributions of the

MUT056399 substituents to bpFabI binding and have analyzed enzyme inhibition by a series of ethyl diphenyl ethers with a variety of substitution patterns. PT01, which has only an ethyl substituent on the A ring, inhibits bpFabI with a K_i^{app} of 32 nM and a t_R of 19 min. Addition of a fluoro group to the A ring of PT01 results in PT411, in which the inhibition parameters K_i^{app} , k_3^{app} , and k_4 were unaffected. Addition of a 2'-F group to the B ring of PT411 gave PT405, which has a higher affinity ($K_i^{app} = 4$ nM) and longer residence time ($t_R = 250$ min). The B ring of PT411 was further modified to give PT406 (2'-Cl), PT412 (2'-NO₂), PT407 (4'-NO₂), PT403 (2'-Cl and 4'-NH₂), PT404 (2'-Cl and 4'-NO₂), and PT408 (methylpyridine ring). Compounds with the highest affinity contained less bulky or medium-sized substituents at the 2' position (i.e., fluoro or chloro). Also, the k_3^{app} was notably reduced by the addition of both 2' and 4' substituents to the B ring. Therefore, we conclude that retaining or slightly increasing the halogen size of the 2' substituent and replacing the 4'-amide substituent with a nitro group can increase the residence time of MUT056399 on bpFabI.

HEXYL A RING

Previously, we reported that the hexyl diphenyl ether PT70 was a slow tight-binding inhibitor of InhA, the FabI from *M. tuberculosis* [77]. To examine the ability of hexyl diphenyl ethers to inhibit bpFabI, we compared the binding of several analogues to the enzyme. This included PT04, which lacks substituents on the B ring, as well as PT113 (2'-F), PT91 (2'-Cl), PT119 (2'-CN), PT70 (2'-CH₃), and PT12 (4'-NO₂). We found that the compounds with the highest affinities had the lowest dissociation rates and little on rate variability. For example, the B ring cyano (PT119) has the longest residence time of ≈ 300 min and a K_i^{app} of 15 nM. This effect is also seen when the same substituent is added to PT01 ($t_R = 19$ min) to generate PT444 ($t_R \approx 670$ min).

We also compared the impact of introducing an A ring fluoro substituent into the hexyl-substituted diphenyl ethers. Examination of the data reveals that PT400 (empty B ring), PT401 (B ring 2'-CH₃), and PT417 (B ring 2'-Cl) have kinetic parameters for bpFabI inhibition different from those of the corresponding analogues that lack an A ring fluorine (PT04, PT70, and PT91). In general, the introduction of a fluoro group on the A ring led to slower association rates from 103 to 102 M⁻¹ s⁻¹. The slower association rate for PT400 led to a weaker affinity for bpFabI compared to that of PT04, yet the rate of dissociation was unaffected. Similarly, the dissociation rates for PT417 and PT91 were comparable, although the A ring fluoro substituent reduced the association rate and weakened the affinity for the enzyme. In contrast, the 2'-CH₃ group on the B ring compensated for the slower association rate, so that PT401 bound to the enzyme with an affinity similar to that of the parent compound. Therefore, we conclude that the A ring fluoro substituent plays a significant role in

governing enzyme affinity as well as the on rate for the hexyl-substituted diphenyl ethers; however, B ring modifications may offset the changes in binding resulting in comparable dissociation rates.

DIPHENYL ETHER KINETIC OPTIMIZATION

The overall association and dissociation kinetics for the ethyl and hexyl diphenyl ethers were analyzed using a two-dimensional (2D) kinetic map, in which the combinations of these rates that result in the same K_i values are represented as diagonal lines (**Figure 4.4-II**). Inhibitors with the highest affinity and longest residence time, such as PT444, are found in the bottom right quadrant (IV), having high association and low dissociation rate constants. However, it is also possible to obtain long residence times from less potent inhibitors such as PT404, by decreasing the association rate constant. Such compounds are found in the bottom left quadrant (III) of the plot with k_3 values ranging between 102 and 104 $M^{-1} s^{-1}$. These results reveal that we are able to moderately shift the on-rate kinetics of the analogues into the ideal “sweet spot” (103 and 105 $M^{-1} s^{-1}$) recently reported by Schoop and Dey to be the most attractive range for generating residence times of multiple hours without requiring subnanomolar affinity of the inhibitors for the enzyme [180].

Interestingly, the kinetic map revealed that the off-rate correlates better with the affinity for the hexyl-substituted diphenyl ethers, while the on rates remain almost constant. By contrast, a broader range of on-rates was observed for the ethyl-substituted diphenyl ethers. Both trends were observed regardless of whether the fluoro group was present on the A ring. These results indicate that an increase in residence time within a compound series can occur either by increase in affinity or by reduction in k_3 .

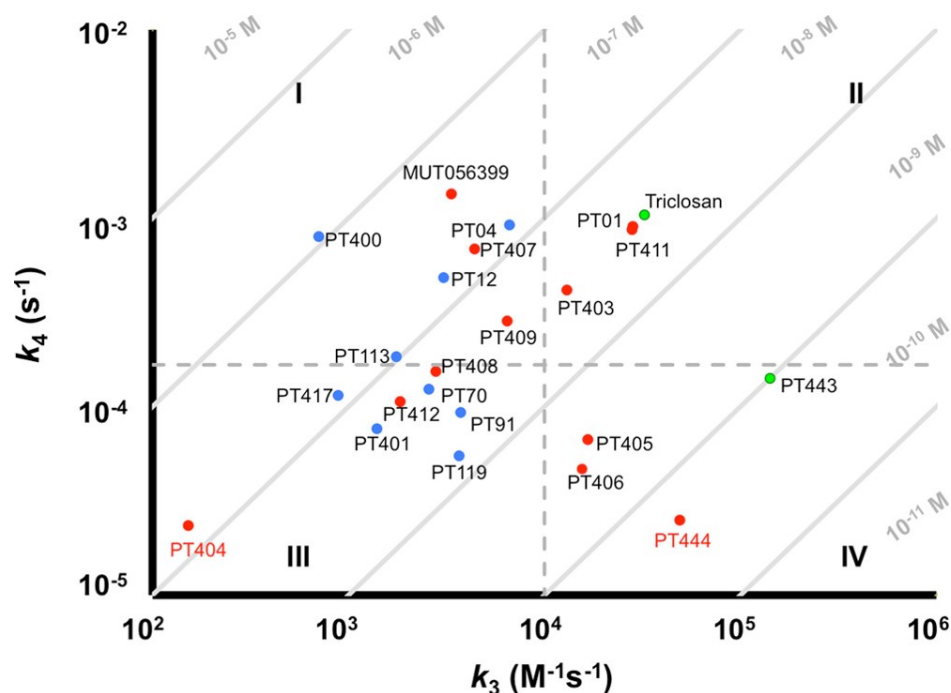


Figure 4.4-II: 2D kinetic map for the diphenyl ether inhibitors of bpFabI1. The 2D plot allows the structure–kinetic relationship (SKR) for bpFabI1 to be visualized. On-rate (k_3) and off-rate (k_4) data are plotted for the A ring ethyl (red) and hexyl (blue) diphenyl ethers. Combinations of k_3 and k_4 values that result in the same K_i value are represented as diagonal lines. PT443 and triclosan are colored green. The diphenyl ethers segregate into four distinct quadrants. Quadrant I: inhibitors with t_R values < 100 min and K_i values from 10^{-8} to 10^{-5} M. Quadrant II: inhibitors with t_R values < 100 min and K_i values from 10^{-10} to 10^{-7} M. Quadrant III: inhibitors with t_R values > 100 min and K_i values from 10^{-9} to 10^{-7} M. Quadrant IV: inhibitors with t_R values > 100 min and K_i values from 10^{-11} to 10^{-9} M.

4.4.3 Structural Elements and Key Residues Found in bpFabI1–Inhibitor Ternary Complexes

INDUCED-FIT LIGAND BINDING AND THE ROLE OF F203 IN INHIBITOR BINDING

In a search for a molecular understanding of enzyme inhibition, the structures of ternary inhibitor complexes of bpFabI1 [bpFabI1·NAD⁺·inhibitor] were determined for nine substituted diphenyl ethers as well as the apo-bpFabI1 structure. Structural studies revealed that α -helix 6 (residues T194–G199) of the bpFabI1 substrate-binding loop (SBL) becomes ordered and undergoes closure upon ligand binding. This loop is found in a similar closed conformation for all bpFabI1–inhibitor complexes, including those formed by triclosan (TCL), PT01, PT02, PT12, PT401, PT404, PT405, PT408, and PT412. In crystal structures containing more than one monomer in the asymmetric unit (e.g., PT02, PT405, PT408, and TCL), the inhibitor is present in each subunit and the corresponding SBL displays an identical conformation in all of the subunits. The closed conformation for all bpFabI1–inhibitor complexes is distinctly different from the open SBL conformation found in the apo-bpFabI1 structure and the recently published structure of 4-pyridone inhibitor PT155 in complex with bpFabI1 (PDB entry 4BKU)

[130] (**Figure 4.4-III A**). PT155 is a rapid reversible inhibitor of bpFabI1 displaying mixed inhibition with respect to *trans*-2-octenoyl-CoA ($K_i = 130$ nM, and $\alpha = 0.48$ (**Figure 4.9-I**)). Thus, these results are consistent with previous studies in which a closed SBL conformation has been observed for structures of ENRs from other bacteria in complex with slow-binding inhibitors [71, 77, 181-183].

F203 plays a key role in stabilizing the ternary inhibitor complexes of bpFabI1 for both rapid reversible and slow-binding inhibitors, in which its steric bulk may influence the open and closed SBL conformations. F203 was found to occupy the space in the *apo*-form of bpFabI1 where A197 of α -helix 6 in the inhibitor-bound (closed) form is located. Ligand binding causes a rotation of the ring plane of F203 toward L207, thus flanking the hydrophobic pocket to accommodate the 5-alkyl substituents. For the 4-F diphenyl ethers, potential C–H \cdots F halogen-bonding interactions can be observed between the 4-F substituent and the hydrogen of the aromatic system of F203 with $C_{\epsilon,F203}$ – $F_{C4,PT}$ distances ranging from ≈ 3.0 to 3.5 Å (**Figure 4.4-III B**). However, the interactions between F203 and the A ring display a larger hydrophobic component for inhibitors lacking a substituent at position 4, with $C_{\epsilon,F203}$ – $C4_{inhibitor}$ distances of ≈ 4 Å, and in which the side chain of F203 is slightly more oriented toward the interior of the substrate-binding pocket (**Figure 4.4-III C**). In contrast, the 4-CH₃ group of PT155 causes the ring plane of F203 to be perpendicular relative to the planes observed in the other [bpFabI·NAD⁺·inhibitor] structures, generating C–H \cdots π interaction distances of 3.4–4.1 Å from the center of the ring plane to the 4-CH₃ group of PT155 (**Figure 4.4-III D**). As a consequence, A197 is forced out of the binding pocket to avoid a steric clash with F203, leading to a more open SBL conformation when PT155 is bound. These results indicate that enzyme inhibition modulates the position of the SBL and provide direct insight into the structural changes that accompany the induced-fit slow-binding mechanism.

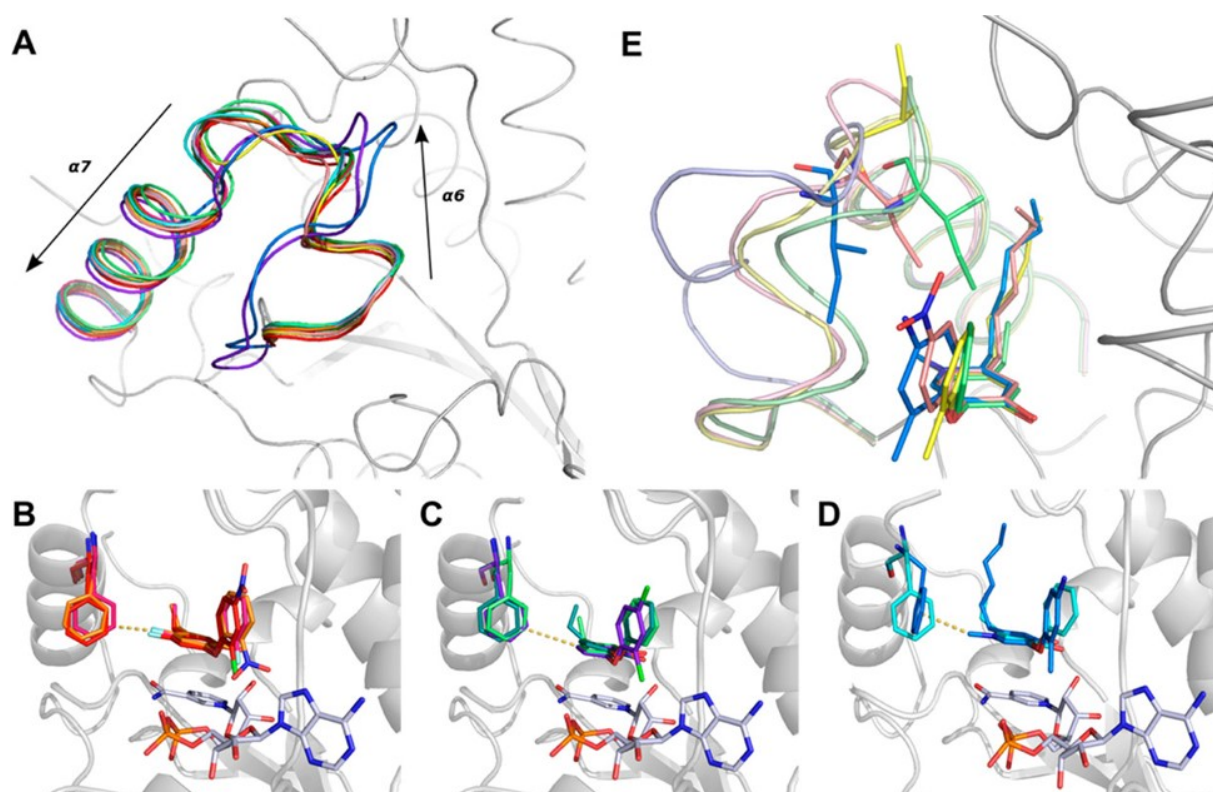


Figure 4.4-III: Substrate-binding loop conformations for the *bpFabI*–inhibitor ternary complexes. (A) The substrate-binding loop (SBL) of *bpFabI* forms a closed conformation in the diphenyl ether inhibitor-bound *bpFabI* complexes, while this loop is found in an open conformation in the apo-form (purple) and in the complex with rapid reversible 4-pyridone inhibitor PT155 (dark blue, PDB entry 4BKU). (B–D) Substituents at position 4 alter the interaction of the diphenyl ethers with residue F203. The 4-F groups of PT404 (red), PT405 (magenta), and PT412 (orange) participate in halogen-bonding interactions (B). Diphenyl ethers lacking a substituent at position 4, such as triclosan (purple), PT01 (light green), and PT02 (cyan), participate in van der Waals interactions (C). The presence of a 4-methyl substituent on PT155 (dark blue) leads to an approximate 90° flip of the aromatic ring plane of F203, which consequently engages in C–H \cdots π interactions with the methyl group. The steric requirements of the flipped residue result in A197 being pushed farther out of the binding pocket to avoid a steric clash, resulting in a more open SBL conformation compared to that of the PT02 (cyan) complex (D). The orientation of I200 is influenced by the chain length of the position 5 A ring acyl group, where longer chains require a slightly more open SBL conformation as shown in panel E for PT401 (yellow), PT155 (dark blue), and PT12 (light pink) complexes compared to the PT01 complex (light green). The loops in question are shown as colored cartoons. Interaction distances are represented by yellow dashes. Residues, inhibitors, and cofactors are shown as sticks.

FLEXIBILITY OF THE CLOSED SBL

The 2D kinetic plot indicates that ethyl-substituted diphenyl ethers have a range of on rates broader than that of the hexyl-substituted diphenyl ethers. To provide a structural basis for the modulation in on rate, we analyzed the precise conformation of the SBL in the enzyme:inhibitor complexes. Comparative analysis revealed that residues S198–K201, located in the loop between α -helix 6 and α -helix 7 of the SBL, have moved slightly farther from the substrate-binding pocket in the ternary PT12 and PT401 complexes, reaching a maximum C $_{\alpha}$ distance at the position of K201 of 1.9–4.1 Å, compared

to the other inhibitor structures. Because both inhibitors contain a 5-hexyl substituent on the inhibitor A ring, this movement is related to the spatial requirements to accommodate longer alkyl chains and I200 shifts out of the substrate-binding pocket by 1.8–3.0 Å (**Figure 4.4-III E**). This observation coincides with previous structural studies of ecFabI in complex with the 2-pyridone inhibitor, CG400549, in which I200 in ecFabI (corresponding to bpFabI1 position 200) was shown to restrict the available space for compounds containing large position 5 substituents [130]. Thus, longer alkyl (hexyl) chains require a slightly more open SBL conformation compared to inhibitors containing only a short alkyl (ethyl or propyl) substituent at this position. These results indicate a less flexible binding mode for the hexyl-substituted diphenyl ethers within the substrate-binding pocket, coinciding with the observed kinetic behavior of low on rate variability on the 2D kinetic map.

INTERACTION PATTERNS BETWEEN THE B RING SUBSTITUENTS AND THE SUBSTRATE-BINDING POCKET

Modifications on the B ring of diphenyl ethers may also result in changes to either the on- or off-rates, which can lead to long residence times by ground state stabilization or transition state destabilization. To explore structural elements that can help distinguish between these mechanisms, we evaluated the orientation of the diphenyl ether B ring and interaction patterns between the B ring substituents and the substrate-binding pocket. In general, the B ring of 4'-unsubstituted inhibitors forms van der Waals contacts with M159 and is oriented away from the SBL residues, with $C4'_{\text{inhibitor}}-C_{\alpha, A196}$ distances ranging from 5.7 to 6.2 Å (**Figure 4.4-IVA**). In contrast, the B ring planes for 4'-substituted inhibitors shift slightly closer to the side chains of the SBL residues (5.1–5.4 Å) to accommodate spatial requirements within the upper part of the substrate-binding pocket created by interactions between the SBL and residues F94 and A95. Taken together with the kinetic data, the movement of the B ring plane in the 4'-substituted inhibitor:enzyme complexes correlates with the slower on-rates and lower affinities for the ethyl-substituted diphenyl ethers (**Table 4.4-I**). Although the 4'-substituted inhibitors have affinities lower than those of the 4'-unsubstituted inhibitors, there are well-defined subtle differences in interaction patterns to stabilize inhibitor binding. For instance, the 4'-NO₂ group of PT404 may participate in a water-bridged hydrogen-bonding network with the side chain of R97 and the carbonyl of G93, and an even more extensive network can also be observed for PT12 (**Figure 4.4-IV B, C**). Because of this network, R97 can be oriented only toward the inhibitor, leading to a structure that resembles a lid on top of the binding pocket if the SBL is fully closed, whereas it would clash in the *apo*-state and ternary PT155 complex. These interactions of the 4'-NO₂ group may contribute significantly to the stabilization of inhibitor binding, and the structural elements provide insights into the observed kinetic behavior of slower on rates.

Compounds with substituents at position 2' display higher affinities for bpFabI1, unlike the 4'-substituted inhibitors, through favorable interactions with A196 of the bpFabI1 SBL. The orientations of the 2'-Cl substituents of PT404 and TCL are more likely to form favorable hydrophobic contacts with A196 of the SBL. Inhibitor PT405 (2'-F) assumes an orientation similar to that of the compounds with a 2'-Cl substituent, and because of its smaller van der Waals radius, it fills the cavity between SBL residue A196 and the opposing G93 to a lesser extent (**Figure 4.4-IV D, E**). However, the nature of the interaction between A196 and the 2'-F may differ compared to that of compounds with a 2'-Cl because the electronegativity of F is higher than that of Cl and the F-C_β distance in the PT405 structure ranges from 3.3 to 3.5 Å. Thus, the 2'-F group may have characteristics of a CH...F hydrogen bond in contrast to the rather hydrophobic nature that it would have with a 2'-Cl substituent. Nevertheless, a halogen group at position 2' is thermodynamically favorable with no significant change in the on-rate, as observed for PT411, PT405, and PT406, where K_i^{app} is reduced from 31 to 3 nM. In contrast, the nitro group of PT412 at position 2' is faced with a less advantageous, rather hydrophobic surrounding. Although a hydrogen bond with the 2'-OH group of the nicotinamide ribose can be formed by one of the oxygens from PT412, no hydrogen-bond donor from bpFabI1 is available in a favorable position (**Figure 4.4-IV F**). This structural observation coincides with kinetic data in which little to no difference in K_i^{app} was observed between PT411 and PT412 (31–59 nM); however, K_i^{app} can be significantly improved by replacement with a 2'-CN group as observed for PT443 and PT444 (0.5–1 nM). The interaction patterns that are observed between substituents at position 2' and bpFabI1 residues or NAD⁺ support ground state stabilization effects.

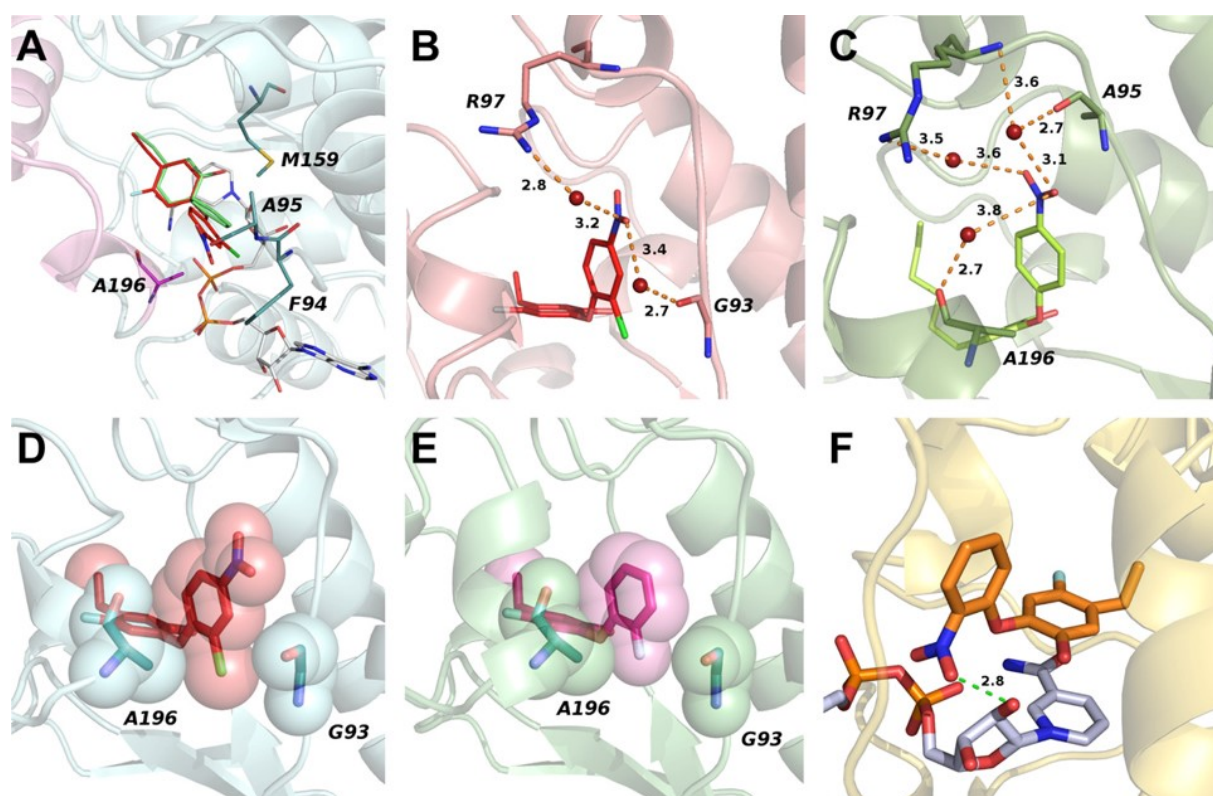


Figure 4.4-IV: Binding modes of different 2'- and/or 4'-substituted bpFabI inhibitors. (A) The B ring planes for the 4'-substituted inhibitors were compared with those for the 4'-unsubstituted inhibitors, here using the examples of PT01 (light green) and PT404 (red). For the 4'-substituted inhibitors, the B ring planes shift closer to the side chains of the SBL residues (magenta) in which the $C4'_{inhibitor}-C_{\alpha, A196}$ distances range from 5.1 to 5.4 Å. However, the range of $C4'_{inhibitor}-C_{\alpha, A196}$ distances increases (5.7–6.2 Å) for the B rings of 4'-unsubstituted inhibitors as the B rings establish van der Waals contacts with M159 (dark cyan). The 4'-NO₂ group may participate in a water-bridged hydrogen-bonding network with the side chain of R97 and the carbonyl of either G93, as observed for PT404 (B), or A95 for PT12 (C), which displays an additional water-bridged hydrogen-bond with the carbonyl of A196. (D–F) Substituents at position 2' can participate in both polar and nonpolar interactions. The 2'-Cl of PT404 (D, red space filling) fills a cavity between SBL residue A196 and the opposing G93, and this cavity is partially filled with a 2'-F substituent as observed for PT405 (E, magenta, space filling). (F) One of the oxygens from the 2'-NO₂ group of PT412 forms a hydrogen bond with the 2'-OH group of the nicotinamide ribose; there is no available hydrogen-bond donor from bpFabI to interact with the other oxygen. Interaction distances are represented by dashes, and residues, inhibitors, and cofactors are shown as sticks.

4.4.4 Most Diphenyl Ethers Displayed a Resistance Index against Bp400

The antimicrobial activity was evaluated for each compound against the efflux competent strain *B. pseudomallei* 1026b and the efflux mutant strain *B. pseudomallei* Bp400 (1026b $\Delta[bpeAB-oprB]$ $\Delta[amrAB-oprA]$) (Table 4.4-I). In general, the minimum inhibitory concentration (MIC) values for triclosan-based analogues ranged from 64 to > 128 mg/l in Bp1026b. These MIC values were at least 32–64-fold higher than that of triclosan (2 mg/l). In contrast, only compounds with 5-ethyl substituents

displayed improved antimicrobial activity against an efflux-compromised *B. pseudomallei* strain, ranging between 4 and 16 mg/l with an average resistance index of \approx 12-fold. PT404 had the maximal resistance index against Bp400 of 32-fold, and PT01 had the minimal resistance index against Bp400 of 4-fold. The MIC values for PT408 and all diphenyl ethers with 5-hexyl substituents remained $>$ 128 mg/l against Bp400.

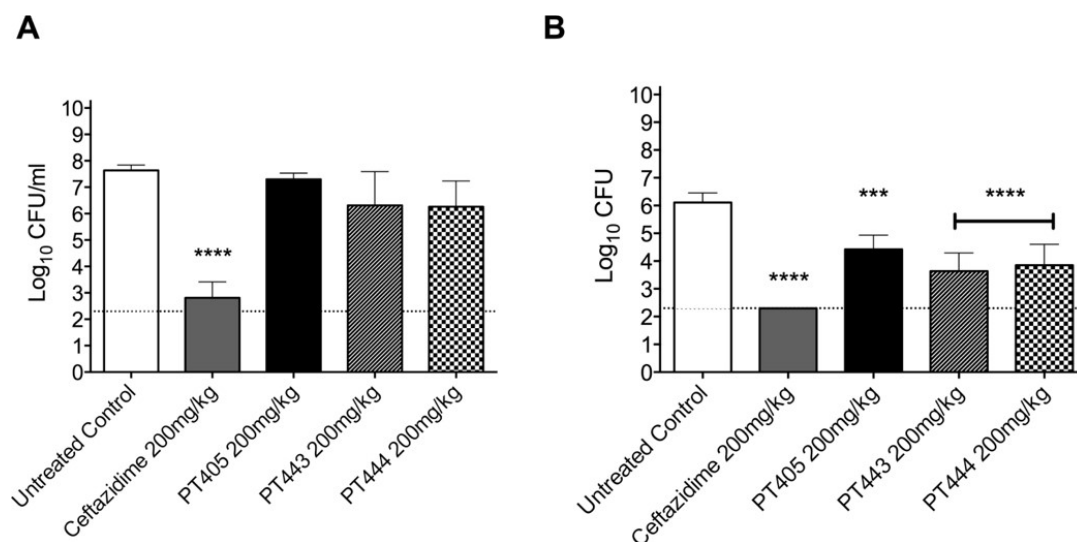


Figure 4.4-V: Bacterial burden in (A) mouse lung and (B) spleen 60 h post-infection. The mean of each group was plotted, and error bars indicate the standard deviation. Significance was determined by one-way ANOVA and Tukey's multiple-comparison post test ($***P < 0.001$; $****P < 0.0001$). The dotted line represents the limit of detection.

4.4.5 Selected Diphenyl Ethers Demonstrate *in-Vivo* Efficacy in an Acute *B. pseudomallei* Infection Animal Model

The efficacies of long residence time inhibitors PT443 ($t_r = 118$ min), PT405 ($t_r = 250$ min), and PT444 ($t_r = 670$ min) were evaluated in the acute *B. pseudomallei* animal model using the virulent *B. pseudomallei* strain Bp400 (**Figure 4.4-V**). Mice were challenged with 5000 CFU, and the bacterial burden was assessed 60 h post-infection in lung and spleen homogenate.

The efficacies of these compounds were measured against an untreated control group and a positive control treated with 200 mg of ceftazidime/kg. Tested compounds showed a significant decrease in bacterial burden in the spleen, which is used to determine efficacy in the acute model of disease because it provides information about disease progression and dissemination, both factors in disease relapse. All three inhibitors demonstrated efficacy better than those of previous generations of diphenyl ethers such as PT01, PT52, and PT68 that were found to reduce bacterial burden in the spleen between 1.1 and 1.4 log₁₀ CFU/ml [80, 145]. PT405 showed a modest improvement in reduction ($P <$

0.001) of 1.69 log₁₀ CFU/ml, and PT443 and PT444 significantly ($P < 0.001$) reduced the bacterial burden even more by factors of 2.48 and 2.26 log₁₀ CFU/ml, respectively.

4.5 Discussion

Previously, we demonstrated that diphenyl ether inhibitors of bpFabI1 had *in-vitro* and *in-vivo* antibacterial activity against *B. pseudomallei*, consistent with the observation that bpFabI1 was essential for bacterial growth [80, 145]. Although these initial studies revealed that some diphenyl ethers displayed slow-binding behavior, the mechanism of bpFabI1 inhibition was not reported at that time. Given the potential importance of both on- and off-rates for governing *in-vivo* drug pharmacology, we have now expanded our analysis of bpFabI1 inhibition in an attempt to provide a foundation for the rational optimization of drug–target kinetics in this system [178, 184, 185].

The diphenyl ethers generally bind to the E–NAD⁺–FabI product complex. In **Figure 4.5-I A**, we show the free energy profile of the binding reaction coordinate for the interaction of inhibitors with the bpFabI–NAD⁺ complex. This analysis allows us to distinguish ground and transition state contributions to the residence time observed for each compound. For the 5-ethyl-substituted diphenyl ethers, we can see that the residence time can be modulated by effects on the ground state, transition state, or both relative to PT01 (**Figure 4.5-I B**). Similarly, modulations were also observed for the ground and transition state contributions for each compound with a 5-hexyl substituent relative to PT04 (**Figure 4.5-I C**). In general, little to no difference in residence time was observed for compounds that exhibited transition and ground state destabilization to the same extent, such as MUT056399 and PT407 compared to PT01. In contrast, differential effects on the transition and ground states were observed for the other compounds, and their contributions to residence time were driven predominantly by either ground state destabilization, ground state stabilization, or transition state destabilization. Long residence times can therefore be rationalized by the improvement of affinity through ground state stabilization, as seen with compounds PT444 and PT119, or by transition state destabilization, as seen with compounds PT404 and PT417.

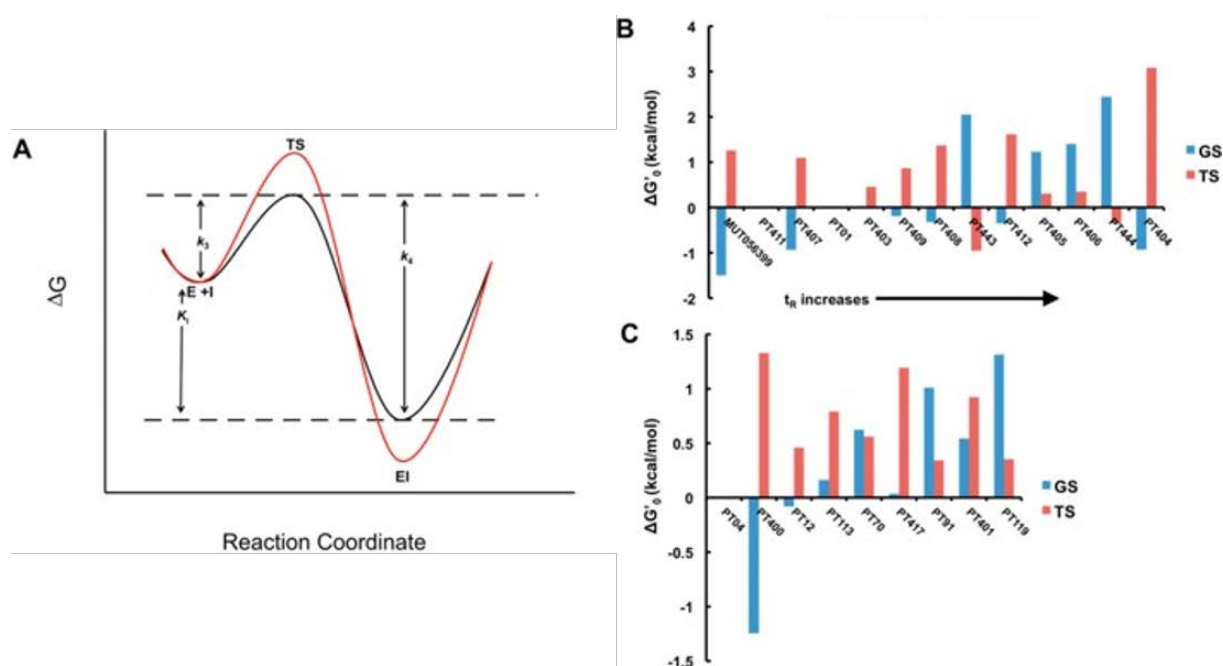


Figure 4.5-I: Free energy profile for bpFabI–diphenyl ether interactions. (A) The diphenyl ether inhibitors of bpFabI display a special case of the two-step induced-fit slow-binding mechanism that is kinetically indistinguishable from a one-step mechanism, and in which k_3 and k_4 define the overall apparent association and dissociation rate constants for the formation and dissociation of EI, respectively, and K_i is the dissociation constant of EI. A decrease in k_4 (increase in residence time) can occur either by an increase in barrier height [transition state (TS) destabilization] or by an increase in the stability of EI [ground state (GS) stabilization] (red line). To depict the relative contribution that changes in GS and TS stability make to the residence time of each inhibitor, we calculated the change in GS and TS free energy relative to either PT01 or PT04. For compound x , the change in GS free energy at 298 K is given by $\Delta G_{GS} = -RT \ln[K_{i(x)}/K_{i(PT01 \text{ or } PT04)}]$ and the change in TS free energy is given by $\Delta G_{TS} = -RT\{\ln[K_{i(PT01 \text{ or } PT04)}/K_{i(x)}] - \ln[k_{4(PT01 \text{ or } PT04)}/k_{4(x)}]\}$. (B) For the 5-ethyl-substituted diphenyl ethers, the change in free energy was calculated relative to PT01. (C) For the 5-hexyl-substituted diphenyl ethers, the change in free energy was calculated relative to PT04. GS contributions are colored blue, in which positive values indicate GS stabilization relative to the standard state and negative values indicate GS destabilization. TS contributions are colored red, in which positive values indicate TS destabilization and negative values indicate TS stabilization relative to the standard state.

Structural studies suggest that stabilization of the ground state can occur through the introduction of nonpolar substituents at position 2', which can interact with nonpolar amino acids near the SBL. For instance, the introduction of halogen groups at position 2' (2'-Cl, PT406 and PT91) can partially or completely fill a cavity between A196 and G93 (Figure 4.4-IV D, E). The replacement of the halogen group at this position with a nitrile (PT119, PT443, and PT444) may also stabilize the ground state, presumably because the 2'-CN substituent may form a hydrogen bond with the peptide backbone at position G93. Interestingly, although one of the oxygens from the 2'-NO₂ group found in PT409 and PT412 can form a hydrogen bond with the 2'-OH group of the nicotinamide ribose, there are no available hydrogen-bond donors from bpFabI to interact with the other oxygen from the NO₂ group

(**Figure 4.4-IV F**). Thus, this less-than-optimal interaction does not significantly affect the ground state compared to PT01, yet it results in a destabilization of the transition state plausibly because the 2'-NO₂ is positioned in a less favorable, hydrophobic environment. Moreover, replacement of the 2'-NO₂ with a 2'-CH₃ (PT70, PT401, and PT408) may complement this hydrophobic environment; however, the CH₃ group is still more sterically demanding than the favored small halogen groups, and thus, the transition state is destabilized.

While the substituents at position 2' may contribute to ground and transition state stabilization, substituents at position 4' predominantly alter the transition state. Structural studies revealed that the B ring planes for 4'-substituted inhibitors shift closer to the side chains of the SBL residues to accommodate spatial requirements within the upper part of the substrate-binding pocket created between the SBL and residues F94 and A95. These differences in the diphenyl ether skeleton are relevant to the B ring planes for PT12, PT403, and PT404, and such structural rearrangements may also result in a destabilization of the transition state.

Because k_3 is related to the difference in free energy between the ground and transition states on the binding coordinate, the evaluation of k_3 values can be used to improve our understanding of how transition state energies can be modulated to optimize residence time. The relationship between incremental changes to the diphenyl ether skeleton and its kinetic behavior was evaluated using a 2D kinetic map (**Figure 4.4-II**) [180, 186]. The 2D kinetic plot revealed that the overall improvement in residence time for the hexyl-substituted diphenyl ethers was achieved by an affinity gain, while there was a small variability in the corresponding on rates. This may be due to a lack of flexible binding modes for compounds with longer alkyl groups, in which hexyl diphenyl ethers require a slightly more open SBL conformation in the loop region between α -helices 6 and 7 compared to diphenyl ethers with shorter alkyl substituents at this position (**Figure 4.4-III A, E**). These results are also consistent with the observation that ethyl-substituted diphenyl ethers exhibited a broader range of on-rate variability, in which k_3 was a much more important contributor to residence time.

To provide a starting point for correlating drug-target kinetics with antibacterial activity, we determined the *in-vitro* activity of all compounds against wild-type *B. pseudomallei* and a pump mutant strain and analyzed the *in-vivo* efficacy of three compounds with significant residence times (PT405, PT443, and PT444) against efflux-compromised *B. pseudomallei* Bp400. While none of the hexyl diphenyl ethers demonstrated antibacterial activity toward either Bp400 or the efflux competent strain Bp1026b, all the ethyl-substituted analogues except PT408 had MIC values of 4–16 mg/l toward Bp400. The MIC values of the ethyl analogues increased to ≥ 128 mg/l for Bp1026b, demonstrating that they were efficiently effluxed by this strain of *B. pseudomallei*. In those cases in which circumvention of the

efflux pumps showed improved antibacterial activity, there was, however, no observable correlation between MIC values and residence time. This is not surprising because MIC values are obtained at a constant drug concentration whereas residence time is a kinetic parameter that is more likely to impact time-dependent antibacterial activity. We then analyzed the *in-vivo* efficacy of three compounds with measurable MIC values against Bp400 in an animal model of infection, and treatment with PT405, PT443, and PT444 was found to cause a 1.7–2.5 log₁₀ reduction of bacterial burden in the spleens of the infected animals. The observed efficacy is consistent with our previous reports for this series of compounds [80, 145], substantiating the importance of bpFabI as a clinically relevant molecular target for the development of novel agents to treat *B. pseudomallei* infection. Although PT405, PT443, and PT444 have residence times that range from 2 to 11 h at 25 °C, all had similar levels of activity in the animal model of infection. Thus, at this stage, it is not possible to draw any conclusions about the relationship between residence time and efficacy in this system. Future studies will aim to explore this relationship by determining the time-dependent *in-vivo* activity (*in-vivo* post-antibiotic effect) of selected compounds and including drug pharmacokinetics in models that relate time-dependent target engagement to drug activity [8, 187].

4.6 Associated Content

4.6.1 Supporting Information

The *Supporting Information* is available free of charge on the ACS Publications website at DOI: [10.1021/acs.biochem.6b01048](https://doi.org/10.1021/acs.biochem.6b01048).

4.7 Author Information

4.7.1 Corresponding Authors

*Department Microbiology, Immunology and Pathology, Colorado State University, Fort Collins, CO 80523.

E-mail: richard.slayden@colostate.edu. *Telephone:* (970) 491-2902. *Fax:* (970) 491-1815.

*Rudolf Virchow Center for Experimental Biomedicine, Institute for Structural Biology, University of Würzburg, D-97080 Würzburg, Germany.

Email: caroline.kisker@virchow.uni-wuerzburg.de. *Telephone:* +49 931 3180381.

*Department of Chemistry, Stony Brook University, Stony Brook, NY 11794-3400.

E-mail: peter.tonge@stonybrook.edu. *Telephone:* (631) 632-7907. *Fax:* (631) 632-7934.

ORCID

Peter J. Tonge: 0000-0003-1606-3471

4.7.2 Author Contributions

C.N., S.E., and J.E.C. contributed equally to this work.

4.7.3 Funding

This work was supported in part by the National Institutes of Health (Grants GM102864, AI044639, and AI070383 to P.J.T.) and by the Deutsche Forschungsgemeinschaft (Grants SFB630 and Forschungszentrum FZ82 to C.K.). C.N. was supported by the Chemical-Biology Interface Training Program grant (NIH T32GM092714) and SUNY LSAMP Bridge to the Doctorate (BD) Cohort at Stony Brook (National Science Foundation Grant HRD0929353). In addition, support was provided by the shared instrumentation grant, NIH/NCRR 1 S10 RR023680-1.

4.7.4 Notes

The authors declare no competing financial interest.

4.8 Acknowledgements

We thank the staff of BL 14.1 at BESSY II (Berlin, Germany) and ID29 of the ESRF (Grenoble, France) for technical support, along with Dr. Béla Ruzsicka from the Institute of Chemical Biology and Drug Discovery for mass spectroscopy instrumentation.

4.9 Supplemental Information

4.9.1 Supplemental Tables

Table 4.9-I: Data collection and refinement statistics of the *bpFabI*-NAD(H/*) inhibitor structures.

	<i>bpFabI apo</i>	<i>bpFabI PT02</i>	<i>bpFabI PT404</i>	<i>bpFabI PT01</i>	<i>bpFabI PT401</i>
Data collection					
Collection Source	ESRF ID 29	ESRF ID 23-2	ESRF ID 29	BESSY BL 14.1	Rigaku Micromax-007 HF

Rationalizing the Binding Kinetics for the Inhibition of the *Burkholderia pseudomallei* FabI Enoyl-ACP Reductase

Space group	I222	I222	I222	I222	I222
Unit cell parameters					
a /b/c (Å)	74.69 / 75.24 / 85.71	69.7 / 112.15 / 262.9	74.58 / 75.06 / 86.38	74.43 / 75.86 / 89.11	74.70 / 75.69 / 88.36
α/β/γ (°)	90.00 / 90.00 / 90.00	90.00 / 90.00 / 90.00	90.00 / 90.00 / 90.00	90.00 / 90.00 / 90.00	90.00 / 90.00 / 90.00
Resolution (Å)^a	37.62 - 1.65 (1.74 - 1.65)	43.98 - 2.60 (2.74 - 2.60)	43.19 - 1.80 (1.90 - 1.80)	31.28 - 1.60 (1.68 - 1.60)	28.74 - 1.63 (1.72 - 1.63)
Total reflections	125427	197779	160232	149473	120473
Unique reflections	28203	32230	22817	33816	29346
Completeness (%)^a	96.6 (98.3)	100 (100)	99.9 (99.9)	99.7 (99.3)	93.0 (88.4)
Redundancy^a	4.4 (4.3)	6.1 (6.2)	7.0 (6.7)	4.4 (4.3)	4.1 (4.1)
Rmerge (%)^a	6.1 (70.2)	21.6 (116.7)	7.2 (63.7)	9.6 (65.5)	6.3 (11.9)
Rpim (%)^a	3.0 (35.6)	9.6 (52)	3.0 (26.5)	5.1 (35.3)	3.5 (6.6)
<I/σ(I)>^a	13.1 (2.2)	9.0 (2.5)	15.4 (3.1)	11.2 (2.2)	15.9 (8.7)
Refinement					
Monomers in AU	1	3	1	1	1
Total number of atoms	2155	6046	2139	2320	2240
R_{cryst} (%)^b	15.85	22.12	17.50	15.21	16.26
R_{free} (%)^b	18.61	27.98	21.38	17.84	19.24
r.m.s.d. from ideal					
Bond length (Å)^b	0.006	0.008	0.006	0.007	0.006
Bond angles (°)^b	1.007	1.135	1.147	1.145	1.173
Average B-values (Å²) and (# of atoms)					

Rationalizing the Binding Kinetics for the Inhibition of the *Burkholderia pseudomallei* FabI Enoyl-ACP Reductase

All atoms	25.8 (2155)	84.1 (6046)	36.2 (2139)	11.3 (2320)	27.5 (2240)
Protein	24.5 (1935)	85.8 (5745)	35.7 (1915)	9.2 (1921)	26.0 (1912)
NAD(H)	---	60.3 (132)	38.0 (44)	6.1 (44)	27.0 (44)
Water	36.5 (220)	41.5 (118)	39.5 (153)	23.6 (339)	37.9 (262)
Inhibitor	---	63.9 (51)	42.3 (21)	8.3 (16)	33.7 (22)
Ramachandran plot (MolProbity)					
Favored (%)	98.1	95.8	97.3	97.7	95.7
Allowed (%)	1.9	4.2	2.7	2.3	4.3
Outliers (%)	0	0	0	0	0
<u>PDB code</u>	<u>5I7E</u>	<u>5I7V</u>	<u>5I9L</u>	<u>5I7S</u>	<u>5I8W</u>

Table 2.9-I continued: Data collection and refinement statistics of the *bpFabI*-NAD(H[±]) inhibitor structures.

Rationalizing the Binding Kinetics for the Inhibition of the *Burkholderia pseudomallei* FabI Enoyl-ACP Reductase

	<i>bpFabI</i> PT408	<i>bpFabI</i> PT12	<i>bpFabI</i> PT412	<i>bpFabI</i> TCL	<i>bpFabI</i> PT405
Data collection					
Collection Source	BESSY BL 14.1	Rigaku Micromax-007 HF	Rigaku Micromax-007 HF	BESSY BL 14.1	ESRF ID 29
Space group	I222	I222	I222	P1	I2
Unit cell parameters					
a /b/c (Å)	63.03/111.22 /260.70	74.55/75.91/ 89.67	72.6/74.7/ 96.75	70.4/99.9/ 139.9	138.4/109.8/ 269.8
$\alpha/\beta/\gamma$ (°)	90.00/90.00/ 90.00	90.00/90.00/ 90.00	90.00/90.00/ 90.00	82.87/89.20/ 78.13	90.00/104.51 /90.00
Resolution (Å)^a	47.21 – 2.25 (2.37 - 2.25)	28.97 - 1.62 (1.71 - 1.62)	59.11 – 2.51 (2.65 - 2.51)	51.39 - 2.60 (2.74 - 2.60)	48.99 - 2.70 (2.73 - 2.70)
Total reflections	321270	150403	43172	417582	241200
Unique reflections	48130	32015	8929	112071	101650
Completeness (%)^a	100 (100)	98.9 (99.8)	96.6 (94.1)	98.5 (97.9)	94.8 (95.7)
Redundancy^a	6.7 (6.3)	4.7 (4.3)	4.8 (4.8)	3.7 (3.8)	2.4 (2.4)
Rmerge (%)^a	9.2 (61.9)	3.7 (14.7)	12.0 (21.5)	10.6 (52.5)	10.1 (68.5)
Rpim (%)^a	3.9 (26.7)	1.9 (7.9)	6.1 (11.0)	6.4 (31.3)	7.7 (52.3)
$\langle I/\sigma(I) \rangle$^a	13.0 (3.0)	21.8 (7.5)	10.7 (6.4)	8.9 (3.2)	6.9 (1.4)
Refinement					
Monomers in AU	3	1	1	16	12
Total number of atoms	6225	2306	2112	31945	23949
R_{cryst} (%)^b	25.10	14.10	15.61	22.14	19.17
R_{free} (%)^b	28.08	16.27	21.52	26.24	22.30
r.m.s.d. from ideal					

Rationalizing the Binding Kinetics for the Inhibition of the Burkholderia pseudomallei FabI Enoyl-ACP Reductase

Bond lengths (Å)^b	0.008	0.021	0.007	0.003	0.005
Bond angles (°)^b	1.187	1.890	1.090	0.729	0.932
Average B-values (Å²) and (# of atoms)					
All atoms	54.7 (6225)	19.5 (2306)	34.2 (2112)	59.4 (31945)	53.9 (23949)
Protein	56.0 (5736)	17.5 (1917)	34.4 (1936)	59.7 (30400)	54.2 (22972)
NAD(H)	41.7 (132)	13.5 (44)	23.9 (44)	53.4 (704)	50.5 (528)
Water	37.2 (303)	31.8 (322)	35.1 (112)	46.0 (569)	35.4 (233)
Inhibitor	41.4 (54)	20.2 (23)	29.8 (20)	68.0 (272)	48.1 (216)
Ramachandran plot (MolProbity)					
Favored (%)	95.6	97.3	96.2	96.2	95.17
Allowed (%)	4.4	2.7	3.8	3.8	4.76
Outliers (%)	0	0	0	0	0.07
PDB code	<u>5I9M</u>	<u>5I8Z</u>	<u>5I9N</u>	<u>5IFL</u>	<u>5I7F</u>

^a Values in parentheses are for the highest-resolution shell.

^b Values derived from Phenix¹ refinement statistics.

$R_{merge} = \frac{\sum_{hkl} \sum_i |I_i - \langle I \rangle|}{\sum_{hkl} \sum_i \langle I \rangle}$ where I_i is the i th measurement and $\langle I \rangle$ is the weighted mean of all measurements of l .
 $R_{cryst} = \frac{\sum ||F_o| - |F_c||}{\sum |F_o|}$ where F_o and F_c are the observed and calculated structure factor amplitudes. R_{free} same as R_{cryst} for 5% of the data randomly omitted from refinement.²

Table 4.9-II: Inhibition of *bpFabI* by diphenyl ethers: Comparison of fits to equations 2-6.^a

Compound	Mechanism	Equation	Parameter values (\pm STD)	95 % Confidence Intervals ^b	Comparison of Fits Summary ^c
Triclosan	One-step	2-3	$v_0 = 2.2 \pm 0 \mu\text{M}/\text{min}$ $K_i^{\text{app}} = 32 \pm 0 \text{ nM}$ $k_4 = 0.062 \pm 0.001 \text{ min}^{-1}$	v_0 : 2.2 to 2.2 $\mu\text{M}/\text{min}$ K_i^{app} : 32 to 32 nM k_4 : 0.061 to 0.064 min^{-1}	Null hypothesis: one-step Alternative hypothesis: two-step P value: < 0.0001
	Two-step	4-6	$v_0 = 2.3 \pm 0 \mu\text{M}/\text{min}$ $K_i^{\text{app}} = 666 \pm 12 \text{ nM}$ $K_i^{*,\text{app}} = 19 \pm 0 \text{ nM}$ $k_6 = 0.032 \pm 0.001 \text{ min}^{-1}$	v_0 : 2.3 to 2.3 $\mu\text{M}/\text{min}$ K_i^{app} : 641 to 690 nM $K_i^{*,\text{app}}$: 19 to 20 nM k_6 : 0.031 to 0.034 min^{-1}	Conclusion (alpha = 0.05): reject null hypothesis Preferred model: two-step F (DFn, DFd): 4656 (1,40294)
PT443	One-step	2-3	$v_0 = 2.2 \pm 0 \mu\text{M}/\text{min}$ $K_i^{\text{app}} = 1.4 \pm 0 \text{ nM}$ $k_4 = 0.0085 \pm 0 \text{ min}^{-1}$	v_0 : 2.2 to 2.2 $\mu\text{M}/\text{min}$ K_i^{app} : 1.4 to 1.4 nM k_4 : 0.0084 to 0.0086 min^{-1}	Null hypothesis: one-step Alternative hypothesis: two-step P value: < 0.0001
	Two-step	4-6	$v_0 = 2.2 \pm 0 \mu\text{M}/\text{min}$ $K_i^{\text{app}} = 152 \pm 2 \text{ nM}$ $K_i^{*,\text{app}} = 1.2 \pm 0 \text{ nM}$ $k_6 = 0.0068 \pm 0 \text{ min}^{-1}$	v_0 : 2.2 to 2.2 $\mu\text{M}/\text{min}$ K_i^{app} : 148 to 155 nM $K_i^{*,\text{app}}$: 1.2 to 1.2 nM k_6 : 0.0067 to 0.0069 min^{-1}	Conclusion (alpha = 0.05): reject null hypothesis Preferred model: two-step F (DFn, DFd): 8424 (1,113451)
PT01	One-step	2-3	$v_0 = 0.54 \pm 0 \mu\text{M}/\text{min}$ $K_i^{\text{app}} = 32 \pm 1 \text{ nM}$ $k_4 = 0.054 \pm 0.002 \text{ min}^{-1}$	v_0 : 0.54 to 0.54 $\mu\text{M}/\text{min}$ K_i^{app} : 30 to 33 nM k_4 : 0.050 to 0.058 min^{-1}	Null hypothesis: one-step Alternative hypothesis: two-step P value: < 0.0001
	Two-step	4-6	$v_0 = 0.54 \pm 0 \mu\text{M}/\text{min}$ $K_i^{\text{app}} = 362 \pm 44 \text{ nM}$ $K_i^{*,\text{app}} = 23 \pm 2 \text{ nM}$ $k_6 = 0.029 \pm 0.004 \text{ min}^{-1}$	v_0 : 0.54 to 0.54 $\mu\text{M}/\text{min}$ K_i^{app} : 276 to 449 nM $K_i^{*,\text{app}}$: 19 to 27 nM k_6 : 0.022 to 0.037 min^{-1}	Conclusion (alpha = 0.05): reject null hypothesis Preferred model: two-step F (DFn, DFd): 73.24 (1,89239)
PT409	One-step	2-3	$v_0 = 2.0 \pm 0 \mu\text{M}/\text{min}$ $K_i^{\text{app}} = 44 \pm 0.1 \text{ nM}$ $k_4 = 0.017 \pm 0 \text{ min}^{-1}$	v_0 : 2.0 to 2.0 $\mu\text{M}/\text{min}$ K_i^{app} : 44 to 44 nM k_4 : 0.017 to 0.017 min^{-1}	Null hypothesis: one-step Alternative hypothesis: two-step P value: < 0.0001
	Two-step	4-6	$v_0 = 2.0 \pm 0 \mu\text{M}/\text{min}$ $K_i^{\text{app}} = 1591 \pm 32 \text{ nM}$ $K_i^{*,\text{app}} = 37 \pm 0.2 \text{ nM}$ $k_6 = 0.013 \pm 0 \text{ min}^{-1}$	v_0 : 2.0 to 2.0 $\mu\text{M}/\text{min}$ K_i^{app} : 1527 to 1654 nM $K_i^{*,\text{app}}$: 37 to 38 nM k_6 : 0.013 to 0.013 min^{-1}	Conclusion (alpha = 0.05): reject null hypothesis Preferred model: two-step F (DFn, DFd): 2946 (1,116295)
PT444	One-step	2-3	$v_0 = 2.3 \pm 0 \mu\text{M}/\text{min}$ $K_i^{\text{app}} = 0.51 \pm 0.01 \text{ nM}$ $k_4 = 0.0015 \pm 0 \text{ min}^{-1}$	v_0 : 2.3 to 2.3 $\mu\text{M}/\text{min}$ K_i^{app} : 0.50 to 0.52 nM k_4 : 0.0015 to 0.0016 min^{-1}	Null hypothesis: one-step Alternative hypothesis: two-step P value: — Conclusion: two-step is ambiguous

Rationalizing the Binding Kinetics for the Inhibition of the Burkholderia pseudomallei FabI Enoyl-ACP Reductase

Compound	Mechanism	Equation	Parameter values (\pm STD)	95 % Confidence Intervals ^b	Comparison of Fits Summary ^c
	Two-step	4-6	$v_0 = 2.3 \pm 0 \mu\text{M}/\text{min}$ $K_i^{\text{app}} = 912 \pm 32 \text{ nM}$ $K_i^{*,\text{app}} \approx 0.37 \text{ nM}$ $k_6 \approx 0.0011 \text{ min}^{-1}$	v_0 : 2.3 to 2.3 $\mu\text{M}/\text{min}$ K_i^{app} : 849 to 974 nM $K_i^{*,\text{app}}$: (Very wide) k_6 : (Very wide)	Preferred model: one-step F (DFn, DFd): —
PT411	One-step	2-3	$v_0 = 0.25 \pm 0 \mu\text{M}/\text{min}$ $K_i^{\text{app}} = 31 \pm 0.1 \text{ nM}$ $k_4 = 0.052 \pm 0 \text{ min}^{-1}$	v_0 : 0.25 to 0.25 $\mu\text{M}/\text{min}$ K_i^{app} : 31 to 32 nM k_4 : 0.051 to 0.053 min^{-1}	Null hypothesis: one-step Alternative hypothesis: two-step P value: < 0.0001
	Two-step	4-6	$v_0 = 0.25 \pm 0 \mu\text{M}/\text{min}$ $K_i^{\text{app}} = 169 \pm 4 \text{ nM}$ $K_i^{*,\text{app}} = 28 \pm 0 \text{ nM}$ $k_6 = 0.031 \pm 0.001 \text{ min}^{-1}$	v_0 : 0.25 to 0.25 $\mu\text{M}/\text{min}$ K_i^{app} : 161 to 176 nM $K_i^{*,\text{app}}$: 27 to 28 nM k_6 : 0.030 to 0.032 min^{-1}	Conclusion (alpha = 0.05): reject null hypothesis Preferred model: two-step F (DFn, DFd): 2449 (1,232779)
PT408	One-step	2-3	$v_0 = 2.2 \pm 0 \mu\text{M}/\text{min}$ $K_i^{\text{app}} = 55 \pm 0.3 \text{ nM}$ $k_4 = 0.009 \pm 0 \text{ min}^{-1}$	v_0 : 2.2 to 2.2 $\mu\text{M}/\text{min}$ K_i^{app} : 54 to 55 nM k_4 : 0.0090 to 0.0093 min^{-1}	Null hypothesis: one-step Alternative hypothesis: two-step P value: —
	Two-step	4-6	$v_0 = 2.2 \pm 0 \mu\text{M}/\text{min}$ $K_i^{\text{app}} > 100 \mu\text{M}$ $K_i^{*,\text{app}} = 54 \pm 0 \text{ nM}$ $k_6 = 0.0091 \pm 0.0001 \text{ min}^{-1}$	v_0 : 2.2 to 2.2 $\mu\text{M}/\text{min}$ K_i^{app} : (Very wide) $K_i^{*,\text{app}}$: 54 to 55 nM k_6 : 0.0089 to 0.0092 min^{-1}	Conclusion: two-step is ambiguous Preferred model: one-step F (DFn, DFd): —
PT405	One-step	2-3	$v_0 = 2.4 \pm 0 \mu\text{M}/\text{min}$ $K_i^{\text{app}} = 4.3 \pm 0.01 \text{ nM}$ $k_4 = 0.0040 \pm 0 \text{ min}^{-1}$	v_0 : 2.4 to 2.4 $\mu\text{M}/\text{min}$ K_i^{app} : 4.3 to 4.3 nM k_4 : 0.0040 to 0.0040 min^{-1}	Null hypothesis: one-step Alternative hypothesis: two-step P value: —
	Two-step	4-6	$v_0 = 2.4 \pm 0 \mu\text{M}/\text{min}$ $K_i^{\text{app}} > 100 \mu\text{M}$ $K_i^{*,\text{app}} = 4.3 \pm 0 \text{ nM}$ $k_6 = 0.0040 \pm 0 \text{ min}^{-1}$	v_0 : 2.4 to 2.4 $\mu\text{M}/\text{min}$ K_i^{app} : (Very wide) $K_i^{*,\text{app}}$: 4.3 to 4.3 nM k_6 : 0.0039 to 0.0040 min^{-1}	Conclusion: two-step is ambiguous Preferred model: one-step F (DFn, DFd): —
PT406	One-step	2-3	$v_0 = 2.5 \pm 0 \mu\text{M}/\text{min}$ $K_i^{\text{app}} = 3.3 \pm 0.1 \text{ nM}$ $k_4 = 0.0028 \pm 0 \text{ min}^{-1}$	v_0 : 2.5 to 2.5 $\mu\text{M}/\text{min}$ K_i^{app} : 3.2 to 3.4 nM k_4 : 0.0027 to 0.0030 min^{-1}	Null hypothesis: one-step Alternative hypothesis: two-step P value: —
	Two-step	4-6	$v_0 = 2.5 \pm 0 \mu\text{M}/\text{min}$ $K_i^{\text{app}} = 1847 \pm 60 \text{ nM}$ $K_i^{*,\text{app}} \approx 2.0 \text{ nM}$ $k_6 \approx 0.0017 \text{ min}^{-1}$	v_0 : 2.5 to 2.5 $\mu\text{M}/\text{min}$ K_i^{app} : 1728 to 1965 nM $K_i^{*,\text{app}}$: (Very wide) k_6 : (Very wide)	Conclusion: two-step is ambiguous Preferred model: one-step F (DFn, DFd): —
PT412	One-step	2-3	$v_0 = 0.37 \pm 0 \mu\text{M}/\text{min}$ $K_i^{\text{app}} = 58 \pm 2 \text{ nM}$	v_0 : 0.37 to 0.37 $\mu\text{M}/\text{min}$ K_i^{app} : 54 to 62 nM	Null hypothesis: one-step Alternative hypothesis: two-step

Rationalizing the Binding Kinetics for the Inhibition of the Burkholderia pseudomallei FabI Enoyl-ACP Reductase

Compound	Mechanism	Equation	Parameter values (\pm STD)	95 % Confidence Intervals ^b	Comparison of Fits Summary ^c
			$k_4 = 0.0064 \pm 0 \text{ min}^{-1}$	$k_4: 0.0059 \text{ to } 0.0070 \text{ min}^{-1}$	P value: — Conclusion: two-step is ambiguous
	Two-step	4-6	$v_0 = 0.37 \pm 0 \text{ }\mu\text{M/min}$ $K_i^{\text{app}} > 100 \text{ }\mu\text{M}$ $K_i^{*,\text{app}} = 57 \pm 3 \text{ nM}$ $k_6 = 0.0063 \pm 0.0004 \text{ min}^{-1}$	$v_0: 0.37 \text{ to } 0.37 \text{ }\mu\text{M/min}$ $K_i^{\text{app}}: (\text{Very wide})$ $K_i^{*,\text{app}}: 51 \text{ to } 63 \text{ nM}$ $k_6: 0.0055 \text{ to } 0.0071 \text{ min}^{-1}$	Preferred model: one-step F (DFn, DFd): —
PT407	One-step	2-3	$v_0 = 2.8 \pm 0 \text{ }\mu\text{M/min}$ $K_i^{\text{app}} = 156 \pm 0 \text{ nM}$ $k_4 = 0.041 \pm 0 \text{ min}^{-1}$	$v_0: 2.7 \text{ to } 2.8 \text{ }\mu\text{M/min}$ $K_i^{\text{app}}: 155 \text{ to } 157 \text{ nM}$ $k_4: 0.041 \text{ to } 0.041 \text{ min}^{-1}$	Null hypothesis: one-step Alternative hypothesis: two-step P value: —
	Two-step	4-6	$v_0 = 2.8 \pm 0 \text{ }\mu\text{M/min}$ $K_i^{\text{app}} > 100 \text{ }\mu\text{M}$ $K_i^{*,\text{app}} = 156 \pm 1 \text{ nM}$ $k_6 = 0.041 \pm 0 \text{ min}^{-1}$	$v_0: 2.7 \text{ to } 2.8 \text{ }\mu\text{M/min}$ $K_i^{\text{app}}: (\text{Very wide})$ $K_i^{*,\text{app}}: 154 \text{ to } 157 \text{ nM}$ $k_6: 0.040 \text{ to } 0.041 \text{ min}^{-1}$	Conclusion: two-step is ambiguous Preferred model: one-step F (DFn, DFd): —
PT403	One-step	2-3	$v_0 = 0.38 \pm 0 \text{ }\mu\text{M/min}$ $K_i^{\text{app}} = 32 \pm 0 \text{ nM}$ $k_4 = 0.025 \pm 0 \text{ min}^{-1}$	$v_0: 0.38 \text{ to } 0.38 \text{ }\mu\text{M/min}$ $K_i^{\text{app}}: 31 \text{ to } 32 \text{ nM}$ $k_4: 0.025 \text{ to } 0.025 \text{ min}^{-1}$	Null hypothesis: one-step Alternative hypothesis: two-step P value: < 0.0001
	Two-step	4-6	$v_0 = 0.38 \pm 0 \text{ }\mu\text{M/min}$ $K_i^{\text{app}} = 302 \pm 4 \text{ nM}$ $K_i^{*,\text{app}} = 20 \pm 0 \text{ nM}$ $k_6 = 0.011 \pm 0 \text{ min}^{-1}$	$v_0: 0.38 \text{ to } 0.38 \text{ }\mu\text{M/min}$ $K_i^{\text{app}}: 294 \text{ to } 310 \text{ nM}$ $K_i^{*,\text{app}}: 20 \text{ to } 21 \text{ nM}$ $k_6: 0.011 \text{ to } 0.012 \text{ min}^{-1}$	Conclusion (alpha = 0.05): reject null hypothesis Preferred model: two-step F (DFn, DFd): 5746 (1,238516)
PT404	One-step	2-3	$v_0 = 1.1 \pm 0 \text{ }\mu\text{M/min}$ $K_i^{\text{app}} = 153 \pm 0 \text{ nM}$ $k_4 = 0.0085 \pm 0 \text{ min}^{-1}$	$v_0: 1.1 \text{ to } 1.1 \text{ }\mu\text{M/min}$ $K_i^{\text{app}}: 152 \text{ to } 153 \text{ nM}$ $k_4: 0.0085 \text{ to } 0.0086 \text{ min}^{-1}$	Null hypothesis: one-step Alternative hypothesis: two-step P value: < 0.0001
	Two-step	4-6	$v_0 = 1.1 \pm 0 \text{ }\mu\text{M/min}$ $K_i^{\text{app}} = 6333 \pm 16 \text{ nM}$ $K_i^{*,\text{app}} = 74 \pm 0 \text{ nM}$ $k_6 = 0.0035 \pm 0 \text{ min}^{-1}$	$v_0: 1.1 \text{ to } 1.1 \text{ }\mu\text{M/min}$ $K_i^{\text{app}}: 6303 \text{ to } 6364 \text{ nM}$ $K_i^{*,\text{app}}: 73 \text{ to } 74 \text{ nM}$ $k_6: 0.0035 \text{ to } 0.0035 \text{ min}^{-1}$	Conclusion (alpha = 0.05): reject null hypothesis Preferred model: two-step F (DFn, DFd): 191818 (1,124878)
MUT056399	One-step	2-3	$v_0 = 0.53 \pm 0 \text{ }\mu\text{M/min}$ $K_i^{\text{app}} = 405 \pm 2 \text{ nM}$ $k_4 = 0.081 \pm 0 \text{ min}^{-1}$	$v_0: 0.53 \text{ to } 0.53 \text{ }\mu\text{M/min}$ $K_i^{\text{app}}: 402 \text{ to } 409 \text{ nM}$ $k_4: 0.079 \text{ to } 0.083 \text{ min}^{-1}$	Null hypothesis: one-step Alternative hypothesis: two-step P value: < 0.0001
	Two-step	4-6	$v_0 = 0.52 \pm 0 \text{ }\mu\text{M/min}$ $K_i^{\text{app}} = 2263 \pm 84 \text{ nM}$ $K_i^{*,\text{app}} = 359 \pm 4 \text{ nM}$ $k_6 = 0.051 \pm 0.002 \text{ min}^{-1}$	$v_0: 0.52 \text{ to } 0.52 \text{ }\mu\text{M/min}$ $K_i^{\text{app}}: 2098 \text{ to } 2427 \text{ nM}$ $K_i^{*,\text{app}}: 351 \text{ to } 367 \text{ nM}$ $k_6: 0.048 \text{ to } 0.054 \text{ min}^{-1}$	Conclusion (alpha = 0.05): reject null hypothesis Preferred model: two-step F (DFn, DFd): 894.7 (1,134845)

Rationalizing the Binding Kinetics for the Inhibition of the Burkholderia pseudomallei FabI Enoyl-ACP Reductase

Compound	Mechanism	Equation	Parameter values (\pm STD)	95 % Confidence Intervals ^b	Comparison of Fits Summary ^c
PT04	One-step	2-3	$v_0 = 0.24 \pm 0 \mu\text{M}/\text{min}$ $K_i^{\text{app}} = 138 \pm 3 \text{ nM}$ $k_4 = 0.055 \pm 0 \text{ min}^{-1}$	v_0 : 0.24 to 0.24 $\mu\text{M}/\text{min}$ K_i^{app} : 131 to 145 nM k_4 : 0.051 to 0.060 min^{-1}	Null hypothesis: one-step Alternative hypothesis: two-step P value: < 0.0001
	Two-step	4-6	$v_0 = 0.24 \pm 0 \mu\text{M}/\text{min}$ $K_i^{\text{app}} = 1274 \pm 131 \text{ nM}$ $K_i^{*,\text{app}} = 65 \pm 15 \text{ nM}$ $k_6 = 0.016 \pm 0.01 \text{ min}^{-1}$	v_0 : 0.24 to 0.24 $\mu\text{M}/\text{min}$ K_i^{app} : 1017 to 1531 nM $K_i^{*,\text{app}}$: 35 to 93 nM k_6 : 0.0065 to 0.025 min^{-1}	Conclusion (alpha = 0.05): reject null hypothesis Preferred model: two-step F (DFn, DFd): 88.23 (1,53540)
PT113	One-step	2-3	$v_0 = 2.0 \pm 0 \mu\text{M}/\text{min}$ $K_i^{\text{app}} = 105 \pm 0 \text{ nM}$ $k_4 = 0.011 \pm 0 \text{ min}^{-1}$	v_0 : 2.0 to 2.0 $\mu\text{M}/\text{min}$ K_i^{app} : 104 to 106 nM k_4 : 0.011 to 0.011 min^{-1}	Null hypothesis: one-step Alternative hypothesis: two-step P value: —
	Two-step	4-6	$v_0 = 2.0 \pm 0 \mu\text{M}/\text{min}$ $K_i^{\text{app}} > 100 \mu\text{M}$ $K_i^{*,\text{app}} = 104 \pm 1 \text{ nM}$ $k_6 = 0.011 \pm 0 \text{ min}^{-1}$	v_0 : 2.0 to 2.0 $\mu\text{M}/\text{min}$ K_i^{app} : (Very wide) $K_i^{*,\text{app}}$: 103 to 105 nM k_6 : 0.011 to 0.011 min^{-1}	Conclusion: two-step is ambiguous Preferred model: one-step F (DFn, DFd): —
PT91	One-step	2-3	$v_0 = 3.0 \pm 0 \mu\text{M}/\text{min}$ $K_i^{\text{app}} = 25 \pm 0.2 \text{ nM}$ $k_4 = 0.0056 \pm 0.0001 \text{ min}^{-1}$	v_0 : 2.9 to 3.0 $\mu\text{M}/\text{min}$ K_i^{app} : 25 to 26 nM k_4 : 0.0055 to 0.0058 min^{-1}	Null hypothesis: one-step Alternative hypothesis: two-step P value: —
	Two-step	4-6	$v_0 = 3.0 \pm 0 \mu\text{M}/\text{min}$ $K_i^{\text{app}} > 100 \mu\text{M}$ $K_i^{*,\text{app}} = 25 \pm 0 \text{ nM}$ $k_6 = 0.0056 \pm 0.0001 \text{ min}^{-1}$	v_0 : 2.9 to 3.0 $\mu\text{M}/\text{min}$ K_i^{app} : (Very wide) $K_i^{*,\text{app}}$: 25 to 26 nM k_6 : 0.0055 to 0.0058 min^{-1}	Conclusion: two-step is ambiguous Preferred model: one-step F (DFn, DFd): —
PT119	One-step	2-3	$v_0 = 2.4 \pm 0 \mu\text{M}/\text{min}$ $K_i^{\text{app}} = 15 \pm 0 \text{ nM}$ $k_4 = 0.0033 \pm 0 \text{ min}^{-1}$	v_0 : 2.4 to 2.4 $\mu\text{M}/\text{min}$ K_i^{app} : 15 to 15 nM k_4 : 0.0033 to 0.0033 min^{-1}	Null hypothesis: one-step Alternative hypothesis: two-step P value: —
	Two-step	4-6	$v_0 = 2.4 \pm 0 \mu\text{M}/\text{min}$ $K_i^{\text{app}} > 100 \mu\text{M}$ $K_i^{*,\text{app}} = 14 \pm 0 \text{ nM}$ $k_6 = 0.0033 \pm 0 \text{ min}^{-1}$	v_0 : 2.4 to 2.4 $\mu\text{M}/\text{min}$ K_i^{app} : (Very wide) $K_i^{*,\text{app}}$: 14 to 15 nM k_6 : 0.0032 to 0.0033 min^{-1}	Conclusion: two-step is ambiguous Preferred model: one-step F (DFn, DFd): —
PT70	One-step	2-3	$v_0 = 2.1 \pm 0 \mu\text{M}/\text{min}$ $K_i^{\text{app}} = 48 \pm 0 \text{ nM}$ $k_4 = 0.0074 \pm 0 \text{ min}^{-1}$	v_0 : 2.1 to 2.1 $\mu\text{M}/\text{min}$ K_i^{app} : 48 to 49 nM k_4 : 0.0073 to 0.0075 min^{-1}	Null hypothesis: one-step Alternative hypothesis: two-step P value: —
	Two-step	4-6	$v_0 = 2.1 \pm 0 \mu\text{M}/\text{min}$	v_0 : 2.1 to 2.1 $\mu\text{M}/\text{min}$	Conclusion: two-step is ambiguous Preferred model: one-step

Rationalizing the Binding Kinetics for the Inhibition of the *Burkholderia pseudomallei* FabI Enoyl-ACP Reductase

Compound	Mechanism	Equation	Parameter values (\pm STD)	95 % Confidence Intervals ^b	Comparison of Fits Summary ^c
PT12	One-step	2-3	$K_i^{app} > 100 \mu\text{M}$ $K_i^{*,app} = 48 \pm 0 \text{ nM}$ $k_6 = 0.0073 \pm 0 \text{ min}^{-1}$ $v_0 = 2.2 \pm 0 \mu\text{M}/\text{min}$ $K_i^{app} = 158 \pm 0 \text{ nM}$ $k_4 = 0.029 \pm 0 \text{ min}^{-1}$	K_i^{app} : (Very wide) $K_i^{*,app}$: 47 to 48 nM k_6 : 0.0072 to 0.0074 min^{-1} v_0 : 2.2 to 2.2 $\mu\text{M}/\text{min}$ K_i^{app} : 157 to 158 nM k_4 : 0.029 to 0.030 min^{-1}	F (DFn, DFd): — Null hypothesis: one-step Alternative hypothesis: two-step P value: — Conclusion: two-step is ambiguous Preferred model: one-step
	Two-step	4-6	$v_0 = 2.2 \pm 0 \mu\text{M}/\text{min}$ $K_i^{app} > 100 \mu\text{M}$ $K_i^{*,app} = 158 \pm 0 \text{ nM}$ $k_6 = 0.029 \pm 0 \text{ min}^{-1}$	v_0 : 2.2 to 2.2 $\mu\text{M}/\text{min}$ K_i^{app} : (Very wide) $K_i^{*,app}$: 157 to 158 nM k_6 : 0.028 to 0.029 min^{-1}	F (DFn, DFd): —
PT400	One-step	2-3	$v_0 = 2.2 \pm 0 \mu\text{M}/\text{min}$ $K_i^{app} = 1134 \pm 5 \text{ nM}$ $k_4 = 0.048 \pm 0.001 \text{ min}^{-1}$	v_0 : 2.2 to 2.2 $\mu\text{M}/\text{min}$ K_i^{app} : 1124 to 1145 nM k_4 : 0.047 to 0.050 min^{-1}	Null hypothesis: one-step Alternative hypothesis: two-step P value: —
	Two-step	4-6	$v_0 = 2.2 \pm 0 \mu\text{M}/\text{min}$ $K_i^{app} > 100 \mu\text{M}$ $K_i^{*,app} = 1144 \pm 5 \text{ nM}$ $k_6 = 0.048 \pm 0.001 \text{ min}^{-1}$	v_0 : 2.2 to 2.2 $\mu\text{M}/\text{min}$ K_i^{app} : (Very wide) $K_i^{*,app}$: 1133 to 1154 nM k_6 : 0.047 to 0.050 min^{-1}	Conclusion: two-step is ambiguous Preferred model: one-step F (DFn, DFd): —
PT401	One-step	2-3	$v_0 = 2.2 \pm 0 \mu\text{M}/\text{min}$ $K_i^{app} = 55 \pm 1 \text{ nM}$ $k_4 = 0.0046 \pm 0.0001 \text{ min}^{-1}$	v_0 : 2.2 to 2.2 $\mu\text{M}/\text{min}$ K_i^{app} : 54 to 56 nM k_4 : 0.0045 to 0.0047 min^{-1}	Null hypothesis: one-step Alternative hypothesis: two-step P value: —
	Two-step	4-6	$v_0 = 2.2 \pm 0 \mu\text{M}/\text{min}$ $K_i^{app} > 100 \mu\text{M}$ $K_i^{*,app} = 54 \pm 1 \text{ nM}$ $k_6 = 0.0044 \pm 0 \text{ min}^{-1}$	v_0 : 2.2 to 2.2 $\mu\text{M}/\text{min}$ K_i^{app} : (Very wide) $K_i^{*,app}$: 53 to 55 nM k_6 : 0.0043 to 0.0046 min^{-1}	Conclusion: two-step is ambiguous Preferred model: one-step F (DFn, DFd): —
PT417	One-step	2-3	$v_0 = 0.54 \pm 0 \mu\text{M}/\text{min}$ $K_i^{app} = 130 \pm 2 \text{ nM}$ $k_4 = 0.0069 \pm 0.0001 \text{ min}^{-1}$	v_0 : 0.54 to 0.54 $\mu\text{M}/\text{min}$ K_i^{app} : 125 to 134 nM k_4 : 0.0067 to 0.0072 min^{-1}	Null hypothesis: one-step Alternative hypothesis: two-step P value: < 0.0001
	Two-step	4-6	$v_0 = 0.54 \pm 0 \mu\text{M}/\text{min}$ $K_i^{app} = 10211 \pm 759 \text{ nM}$ $K_i^{*,app} = 89 \pm 4 \text{ nM}$ $k_6 = 0.0043 \pm 0.0003 \text{ min}^{-1}$	v_0 : 0.54 to 0.54 $\mu\text{M}/\text{min}$ K_i^{app} : 8723 to 11698 nM $K_i^{*,app}$: 80 to 97 nM k_6 : 0.0038 to 0.0048 min^{-1}	Conclusion (alpha = 0.05): reject null hypothesis Preferred model: two-step F (DFn, DFd): 199.7 (1,172398)

^aAll datasets were analyzed by comparing the fits of nonlinear regression models using the program GraphPad Prism version 6 (GraphPad Software, Inc., La Jolla, CA). Inhibition parameters for the one-step slow binding mechanism are summarized in **Table 1** for each inhibitor.

^b The 95 % confidence interval represents a range of values centered around the best-fit value for each parameter, in which one can be 95% certain that the calculated parameter is within the true mean of the population and evaluate the margin of errors as each parameter floats.

^c The one-step and induced-fit, two-step slow binding models were compared using the sum-of-squares F test. The F test compares the improvement of sum-of-squares versus the loss of degrees of freedom (DFn, DFd) and provides a calculated P value. As shown, all kinetic data globally fit to the one-step model and this model was the best fit for 13 compounds given that the values for K_i^{app} were much higher than K_i^{*app} . For the remaining 10 compounds, the two-step model provided a better fit of the data ($P < 0.0001$), which include triclosan, **PT443**, **PT01**, **PT409**, **PT411**, **PT403**, **PT404**, **MUT056399**, **PT04** and **PT417**. Given that is less likely for this diphenyl ether subset to switch kinetic mechanisms, it is possible that the calculated parameters for the one-step model represents the overall apparent association and dissociation rate constants between $E + I$ and EI^* , which is characteristic of a special case for a two-step slow binding mechanism. This hypothesis is supported by the rigorous characterization of structural rearrangements of bpFabI as described in the results section.

4.9.2 Supplemental Figures

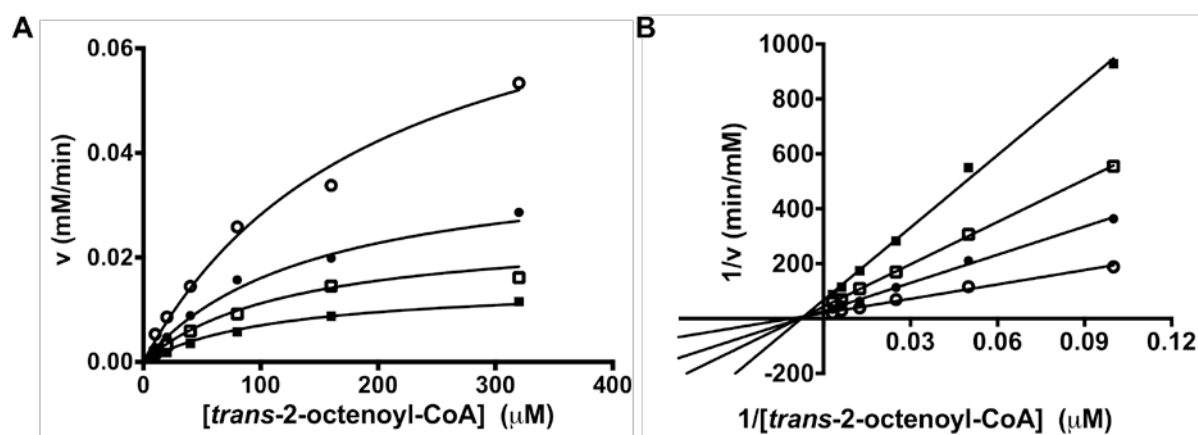


Figure 4.9-I: Inhibition plot for bpFabI. Assays were performed at 250 μM NADH and varying concentrations of trans-2-octenoyl-CoA at 0 (\circ), 75 (\bullet), 150 (\square) and 300 (\blacksquare) nM PT155. Data sets were analyzed by (A) non-linear regression analysis to mixed model inhibition and (B) linear regression to obtain double reciprocal plot using GraphPad Prism version 6 (GraphPad Software, Inc., La Jolla, CA). The inhibition kinetic parameters for bpFabI are $K_{M, \text{trans-2-octenoyl-CoA}} = 200 \pm 25 \mu\text{M}$, $V_{\text{Max}} = 0.084 \pm 0.006 \text{ mM/min}$, $K_i, \text{PT155}} = 134 \pm 35 \text{ nM}$, and $\alpha = 0.48 \pm 0.19$.

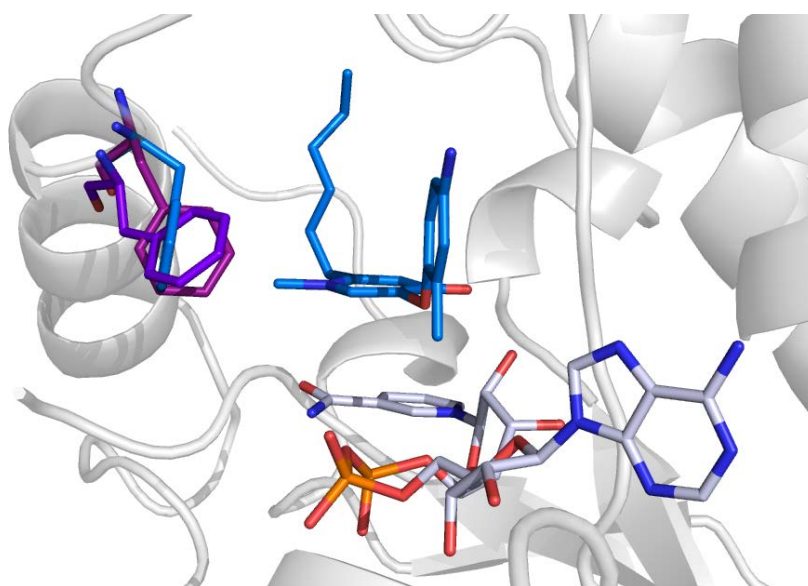


Figure 4.9-II: Orientation of F203 in bpFabI apo-structures compared to bpFabI in complex with PT155. The presence of a 4-methyl substituent on PT155 (blue) leads to an approximate perpendicular orientation of the aromatic ring plane of F203 compared to the apo-form of bpFabI observed in this study (purpleblue) as well as published in the PDB (3EK2, dark magenta).

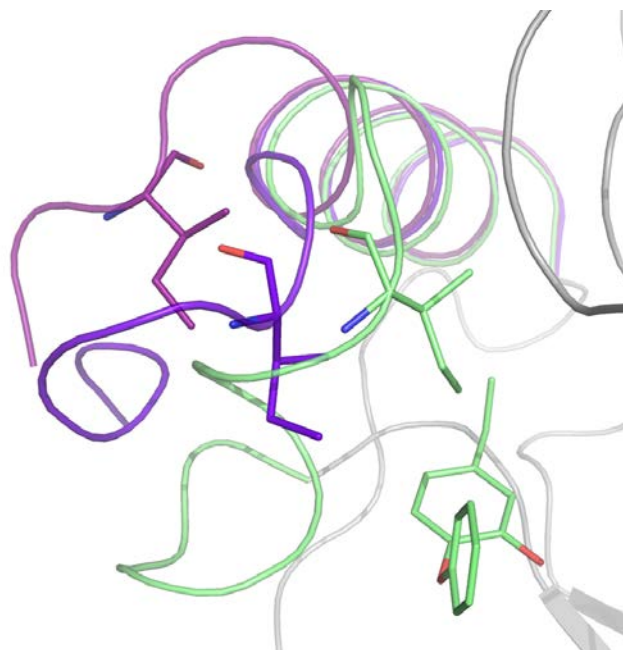


Figure 4.9-III: Orientation of I200 in bpFabI apo-structures. The orientation of I200 in the apo-structure considered in this study (purpleblue) differs from the conformation observed in PDB entry 3EK2 (monomer A, dark magenta). To illustrate the span width of possible conformations of I200, the position of I200 from the bpFabI-PT01 complex (green) is given. The discrepancy between both apo-forms may be the result of crystal packing effects: In the apo-structure of this study residues L195 – S198 are stabilized by a neighboring symmetry mate, whereas in 3EK2 crystal packing effects are less prominent, and crystal contacts with symmetry mates can only be observed for K201 – S202 of subunit A. In all four subunits of 3EK2 the SBL is not fully ordered (residues 193 – 197 are missing in monomer A, 194 – 202 in B, 195 – 201 in C and 194 – 201 in D), whereas the single subunit from this study's apo-form displays a fully ordered SBL.

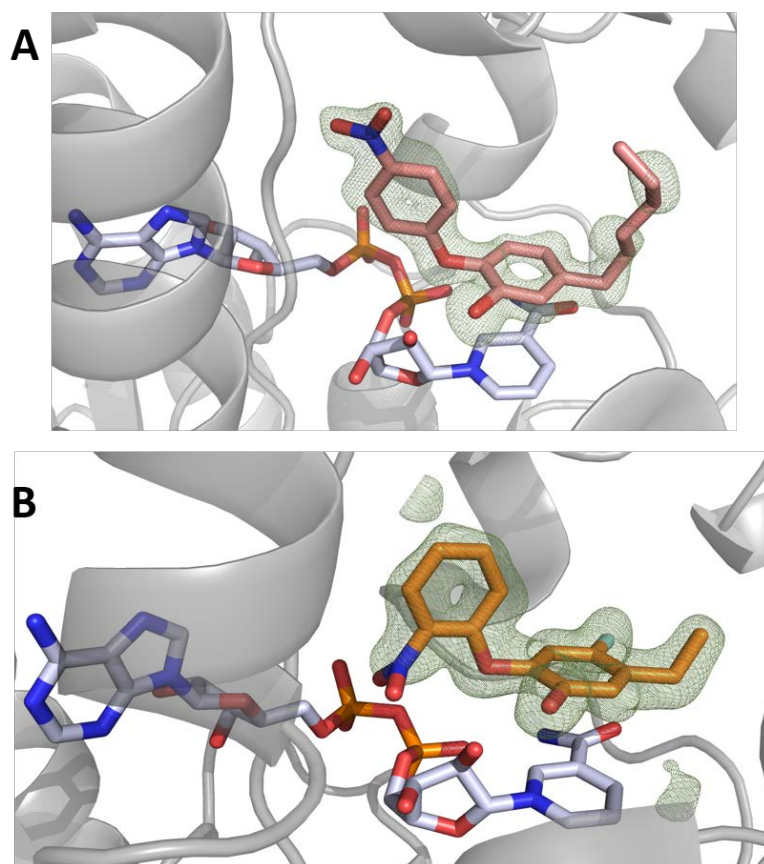


Figure 4.9-IV: Fo-Fc omit maps for PT12 (A) and PT412 (B) bound to bpFabI. As an example PT12 (A) and PT412 (B) Fo-Fc density maps (green mesh) were generated by omitting the respective inhibitor from the crystal structure and are shown at a contour level of 3.0 sigma.

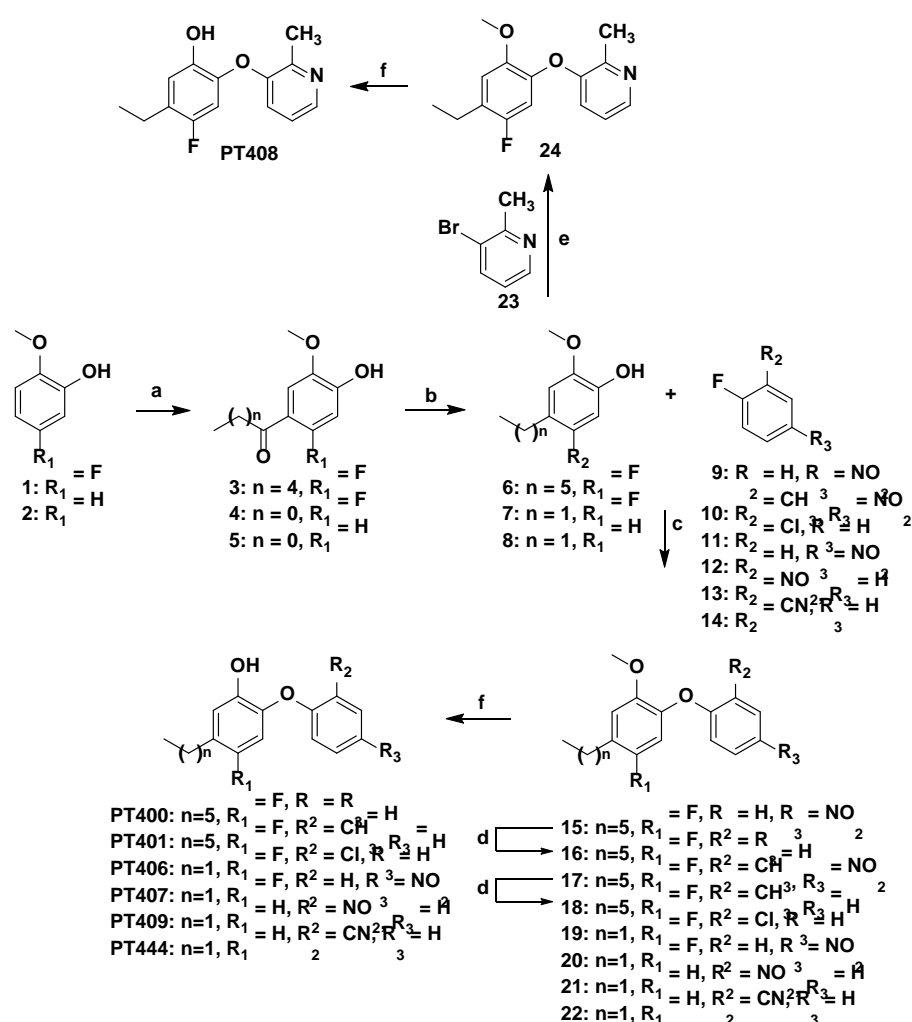
4.9.3 Supplemental Experimental Procedures

INHIBITION OF BPFAB1 BY PT155

Inhibition kinetics were performed on a Cary 100 Bio (Varian) spectrometer at 25 °C in 30 mM PIPES buffer pH 8.0 containing 150 mM NaCl and 1.0 mM EDTA. The reaction was initiated by the addition of enzyme (30 nM) and monitored by the oxidation of NADH to NAD⁺ at 340 nm ($\epsilon = 6,220 \text{ M}^{-1} \text{ cm}^{-1}$). The initial velocities were obtained as a function of *trans*-2-octenoyl-CoA (10 – 320 μM) at 250 μM NADH and fixed concentrations of PT155 (0, 75, 150, and 300 nM). Inhibition constants were determined by non-linear regression analysis for mixed inhibition model within the GraphPad Prism program and confirmed by a Lineweaver-Burk plot (version 6, GraphPad Software, Inc., La Jolla, CA).

SYNTHESIS OF DIPHENYL ETHER DERIVATIVES

Diphenyl ether derivatives were synthesized in a similar manner as previously reported (Scheme 4.9-I) [77, 148, 151, 165]. Friedel-Crafts acylation of **1** and **2** with the appropriate acid chlorides and in the presence of AlCl_3 led to formation of **3-5** after 3 days under reflux conditions. Then metal-catalyzed reduction of **3-5** with $\text{Zn}/\text{AcOH}/\text{HCl}$ was carried out to obtain **6-8** in 60-80 % yields. The phenols (**6-8**) were subsequently coupled with fluorobenzenes (**9-14**) or 3-bromo-2-methylpyridine (**23**), which afforded the corresponding coupled derivatives (**15, 17, 19-22, 24**). Compounds **16** and **18** were achieved by reduction of the nitrobenzenes (**15, 17**) to anilines and subsequent deamination with tert-butyl nitrate. Finally, demethylation of **16, 18, 19-22, and 24** using BBr_3 at low temperatures resulted in the targeted compounds (PT400, PT401, PT406-PT409, and PT444).



Scheme 4.9-I: Synthesis of diphenyl ether derivatives. Reagents and Conditions: a. AlCl_3 , hexanoyl chloride or acetyl chloride, DCE or DCA, reflux, 3 days, 60-80 %; b. Excess of Zn, conc HCl, AcOH, rt, 8 h, 75 %; c. K_2CO_3 , DMF, cat.18-crown-6 ether, 120 °C, 2 h, 96 %; d. Zn, NH_4Cl , MeOH/ H_2O , reflux, 1 h, then $t\text{-BuONO}_2$, DMF, 65 °C, overnight, 57 % (two steps); e. CuI, picolinic acid, K_3PO_4 , DMSO, 80 °C, 24 h, 75 %; f. BBr_3 , DCM, -78 °C to rt, overnight, 98 %.

General procedure I for the aromatic substitution reaction (for 15, 17, 19-22, 24): Different derivatives of the fluorobenzene or 3-bromo-2-methylpyridine (1.00 mmol), K_2CO_3 (3.00 mmol), and a catalytic amount of 18-crown-6 ether were added to a stirred solution of the corresponding phenol (1.00 mmol) in DMF (8 ml) at rt, and the solution was then heated to 120 °C for 3 h. After completion of the reaction, as shown by TLC, the reaction mixture was diluted with water (20 ml) and extracted with diethyl ether (2 x 20 ml). The organic layer was washed with brine (30 ml), dried over anhydrous Na_2SO_4 , and evaporated under vacuum. The crude product was purified by Flash chromatography to afford the substituted benzenes.

General procedure II for reduction of nitrobenzene to aniline (for 16, 18): To a stirred solution of the nitrobenzene (1.00 mmol) in methanol (7 ml) and water (1.5 ml) at rt. NH_4Cl (14.0 mmol) and Zn powder (11.0 mmol) were then added and the reaction mixture was refluxed for 1 h. The reaction mixture was monitored by TLC, and after completion, the reaction was cooled to rt and filtered, volatiles were removed by evaporation, and the aqueous solution was then extracted with EtOAc (2 x 20 ml). The organic layer was washed with water (20 ml), dried over Na_2SO_4 , and evaporated under vacuum. The crude product was subsequently purified by Flash chromatography to afford the corresponding anilines.

General procedure III for deamination of anilines (for 16, 18): To a stirred solution of amine (1.00 mmol) in DMF (8 ml), $t-BuONO_2$ (1.00 mmol) was added dropwise at 65 °C and stirred continuously at 65 °C overnight. The reaction mixture was cooled to rt, quenched with 2 N HCl and extracted with EtOAc (2 x 10 ml). The combined organic layer was washed with water (20 ml) and dried over Na_2SO_4 . Volatiles were removed by evaporation. The crude product was subsequently purified by Flash chromatography to afford the appropriate deaminated product.

General procedure IV for demethylation (for PT400-PT401, PT406-PT409, PT444): The methoxybenzene (0.627 mmol) was dissolved in dry CH_2Cl_2 (50 ml), and BBr_3 (0.94 ml, 2M in CH_2Cl_2 , 1.88 mmol) was added dropwise at -70 °C. The reaction was gradually warmed to rt and stirred for overnight. When TLC showed completion, the reaction was cooled to -40 °C and quenched with MeOH. The solution was dried in vacuo to give the crude product, which was purified by Flash chromatography to afford the corresponding demethylation product.

1-(2-fluoro-4-hydroxy-5-methoxyphenyl)hexan-1-one (3) [188]: To a solution of anhydrous aluminum chloride (3.0 mmol) in DCE (10 ml) cooled in ice under nitrogen, 3-fluorophenol (**1**) (1.0 mmol, neat) was added dropwise and followed by dropwise addition of hexanoyl chloride (3.0 mmol, neat). The ice bath was then removed and the reaction mixture refluxed for 3 days. After cooling to rt, the reaction

mixture was then poured onto ice water and extracted with EtOAc (2 x 50 ml). The extracts were washed with saturated aqueous NaCl solution (20 ml) and dried over MgSO₄, filtered and concentrated. The crude material was purified by Flash chromatography to afford the corresponding aryl ketone (**3**) as a white solid (Yield, 60 %). ¹H NMR (400 MHz, CDCl₃): δ 7.39 (d, *J* = 6.5 Hz, 1 H), 6.67 (d, *J* = 11.6 Hz, 1 H), 6.23 (br s, 1 H), 3.91 (s, 3 H), 2.94-2.90 (m, 2 H), 1.73-1.66 (m, 2 H), 1.36-1.32 (m, 4 H), 0.92-0.89 (m, 3 H). ¹³C NMR (100 MHz, CDCl₃): δ 194.7, 159.4, 156.9, 151.1, 151.0, 143.2, 117.0, 116.9, 110.75, 110.71, 103.1, 102.8, 56.3, 43.48, 43.40, 31.5, 23.94, 23.92, 22.53, 13.9. ¹⁹F NMR (400 MHz, CDCl₃) δ -113.56 (m). ESI-MS (*m/z*): calculated for C₁₃H₁₇FO₃ [M - H]- 239.1; found 239.0 [M - H].

1-(2-fluoro-4-hydroxy-5-methoxyphenyl)-ethanone (4): Compound **4** was obtained as a white solid from **1**, following the same procedure that was used to prepare **3** (Yield, 80 %). ¹H NMR (500 MHz, CDCl₃): δ 7.37 (d, *J* = 7.0 Hz, 1 H), 6.67 (d, *J* = 12.0 Hz, 1 H), 6.40 (s, 1 H), 3.90 (s, 3 H), 2.59 (d, *J* = 6.0 Hz, 3 H). ¹³C NMR (125 MHz, CDCl₃): δ 194.5, 159.8, 157.3, 151.5, 151.4, 143.2, 117.0, 116.8, 110.55, 110.54, 110.47, 110.43, 103.1, 102.8, 56.4, 56.3, 31.38, 31.30, 31.2. ¹⁹F NMR (300 MHz, CDCl₃) δ -113.64 (m). ESI-MS (*m/z*): calculated for C₉H₉FO₃ [M - H]- 183.1; found 183.0 (100) [M - H].

2-methoxy-4-acetylphenol (5): 10 ml solution of 500 mg (4.06 mmol) 2-methoxyphenol (**2**) and 1.6 g aluminum chloride in DCA was cooled to 0 °C. To the cooled solution, 960 mg (12.18 mmol) acetyl chloride was added dropwise. The reaction mixture was stirred under 0 °C for 1 h and then warmed to rt. The reaction was stirred under rt for 3 days. The solvent was evaporated. The residue was resuspended in water and extracted with DCM. The combined organic phase was dried over magnesium sulfate and evaporated under vacuum. The crude product was purified by Flash chromatography to yield compound **5**. ¹H NMR (400 MHz, CDCl₃): δ 7.52 - 7.59 (m, 2 H), 6.96 (d, *J* = 8.66 Hz, 1 H), 3.96 (s, 3 H), 2.57 (s, 3 H). ¹³C NMR (100 MHz, CDCl₃): δ 196.87, 150.44, 146.64, 130.22, 124.02, 113.79, 109.74, 56.08, 26.20.

5-fluoro-4-hexyl-2-methoxyphenol (6): To a stirred solution of aryl ketone (**3**) (1.0 mmol) and Zn powder (10 mmol) in AcOH (8 ml) in ice bath and was added excess of concentrated HCl (1 ml) dropwise. Ice bath was removed and stirred at rt for 2-8 h (if reaction was not completed, additional amount of Zn/conc. HCl were added). After completion of reaction, filtered and volatiles were evaporated with rotary evaporator. The residue was extracted with diethyl ether (2 x 15 ml) and combined organic phase were dried over MgSO₄, filtered and concentrated. The crude material was purified by Flash chromatography to afford the corresponding aryl alkane (**6**) as a colorless liquid (Yield, 75 %). ¹H NMR (400 MHz, CDCl₃): δ 6.65-6.63 (m, 2 H), 5.67 (s, 1 H), 3.85 (s, 3 H), 2.57-2.53 (m, 2 H), 1.57-1.34 (m, 2 H), 1.32-1.31 (m, 6 H), 0.90 (t, *J* = 6.8 Hz, 3 H). ¹³C NMR (100 MHz, CDCl₃): δ 156.3, 154.0, 144.2, 144.1,

142.6, 120.0, 119.8, 112.1, 112.0, 102.6, 102.3, 56.3, 31.6, 30.5, 28.9, 28.6, 22.5, 14.0. ESI-MS (m/z): calculated for $C_{13}H_{19}FO_2$ [M - H]⁻: 225.1; found 225.1 [M - H]⁻.

4-ethyl-5-fluoro-2-methoxyphenol (7): Compound **7** was obtained as a yellow liquid from **4**, following the same procedure that was used to prepare **6**. (Yield, 78 %). ¹H NMR (500 MHz, CDCl₃): δ 6.66-6.63 (m, 2 H), 5.70 (s, 1 H), 3.85 (s, 3 H), 2.62-2.56 (m, 2 H), 1.20 (t, $J = 7.2$ Hz, 1 H). ¹³C NMR (125 MHz, CDCl₃): δ 156.2, 153.8, 144.2, 144.1, 142.5, 121.3, 121.1, 111.5, 111.4, 102.6, 102.3, 56.3, 21.84, 21.82, 14.7. ESI-MS (m/z): calculated for $C_9H_{11}FO_2$ [M - H]⁻: 169.1; found 169.1 [M - H]⁻.

4-ethyl-2-methoxy-phenol (8): Compound **8** was obtained from **5**, following the same procedure that was used to prepare **6**. ¹H NMR (400 MHz, CDCl₃): δ 6.86 (d, $J = 8.16$ Hz, 1 H), 6.68 - 6.76 (m, 2 H), 3.91 (s, 3 H), 2.55 - 2.66 (m, 2 H), 1.24 (t, $J = 7.65$ Hz, 3 H). ESI-MS (m/z): calculated for $C_9H_{12}O_2$ [M - H]⁻: 151.1, found 151.1 for [M-H]⁻.

1-(5-fluoro-4-hexyl-2-methoxyphenoxy)-4-nitrobenzene (15): Compound **15** was obtained as a yellow solid from **6** and **9** using the general procedure I, and used without further purification or characterization (Yield, 96 %).

1-(5-fluoro-4-hexyl-2-methoxyphenoxy)benzene (16): Compound **16** was obtained as a colorless liquid from **15** using the general procedure II and III, and used without further purification or characterization (Yield, 57 %, two steps).

1-(5-fluoro-4-hexyl-2-methoxyphenoxy)-2-methyl-4-nitrobenzene (17): Compound **17** was obtained as a yellow solid from **6** and **10** using the general procedure I, and used without further purification or characterization (Yield, 95 %).

1-(5-fluoro-4-hexyl-2-methoxyphenoxy)-2-methylbenzene (18): Compound **18** was obtained as a colorless liquid from **17** using the general procedure II and III, and used without further purification or characterization (Yield, 57 %, two steps).

1-(2-chlorophenoxy)-4-ethyl-5-fluoro-2-methoxybenzene (19): Compound **19** was obtained as a colorless liquid from **7** and **11** using the general procedure I, and used without further purification or characterization.

1-ethyl-2-fluoro-5-methoxy-4-(4-nitrophenoxy)benzene (20): Compound **20** was obtained as a colorless liquid from **7** and **12** using the general procedure I, and used without further purification or characterization.

4-ethyl-2-methoxy-1-(2-nitrophenoxy)benzene (21): Compound **21** was obtained as a colorless liquid from **8** and **13** using the general procedure I, and used without further purification or characterization.

2-(4-ethyl-2-methoxyphenoxy)benzotrile (22): Compound **22** was obtained as a colorless liquid from **8** and **14** using the general procedure I, and used without further purification or characterization.

3-(4-ethyl-5-fluoro-2-methoxyphenoxy)-2-methylpyridine (24) [189]: An oven-dried flask was charged with a magnetic stirbar, copper(I) iodide (0.05 mmol, 5 mol %), picolinic acid **1** (0.10 mmol, 10 mol %), aryl halide (1.0 mmol), compound **7** (1.2 mmol), and K₃PO₄ (2.0 mmol). The flask was then evacuated and backfilled with argon, followed by dimethyl sulfoxide (2.0 ml) by syringe. The flask was placed in a preheated oil bath at 80 °C and the reaction mixture was stirred vigorously for 24 h. The reaction mixture was cooled to rt. Ethyl acetate (10 ml) and H₂O (2 ml) were added and the mixture was stirred. The organic layer was separated and the aqueous layer was extracted twice more with ethyl acetate (10 ml). The combined organic layer was dried over Na₂SO₄ and filtered through the pad of silica gel. The filtrate was concentrated, and the resulting residue was purified by Flash chromatography to afford the corresponding aryl alkane (**24**) as a solid (Yield, 75 %).

4-fluoro-5-hexyl-2-phenoxyphenol (PT400): Compound **PT400** was obtained as a colorless liquid from **16** using the general procedure IV (Yield, 98 %). ¹H NMR (400 MHz, CDCl₃): δ 7.35-7.31 (m, 2 H), 7.14-7.10 (m, 1 H), 7.02 (t, *J* = 6.8 Hz, 1 H), 6.85 (d, *J* = 8.0 Hz, 1 H), 6.57 (d, *J* = 8.0 Hz, 1 H), 5.49 (br s, 1 H), 2.57 (t, *J* = 7.6 Hz, 2 H), 1.62-1.58 (m, 2 H), 1.38-1.33 (m, 6 H), 0.91 (t, *J* = 6.8 Hz, 3 H). ¹³C NMR (125 MHz, CDCl₃): δ 156.4, 155.4, 153.0, 143.14, 143.11, 141.33, 141.23, 129.95, 129.90, 129.8, 125.6, 125.4, 123.88, 123.83, 123.7, 118.0, 117.9, 116.9, 116.87, 116.81, 106.2, 105.9, 31.6, 30.0, 28.9, 28.6, 28.4, 22.5, 14.0. ESI-MS (*m/z*): calculated for C₁₈H₂₁FO₂ [M-H]⁻ 287.2; found 287.1 [M-H]⁻.

2-(*o*-tolylloxy)-4-fluoro-5-hexylphenol (PT401): Compound **PT401** was obtained as a colorless liquid from **18** using the general procedure IV (Yield, 97 %). ¹H NMR (500 MHz, CDCl₃): δ 7.28-7.25 (m, 1 H), 7.18 (dd, *J* = 10.0, 5.0 Hz, 1 H), 7.10 (t, *J* = 10.0, 5.0 Hz, 1 H), 6.91 (d, *J* = 10.0 Hz, 1 H), 6.85 (d, *J* = 5.0 Hz, 1 H), 6.37 (d, *J* = 10.0 Hz, 1 H), 5.48 (br s, 1 H), 2.56 (t, *J* = 7.5 Hz, 2 H), 2.27 (s, 3 H), 1.62-1.58 (m, 2 H), 1.38-1.33 (m, 6 H), 0.91 (t, *J* = 7.5 Hz, 3 H). ¹³C NMR (125 MHz, CDCl₃): δ 154.3, 153.7, 142.2, 131.6, 129.4, 127.3, 124.6, 124.3, 124.2, 118.9, 116.5, 116.4, 104.2, 104.0, 31.6, 30.1, 28.9, 28.4, 22.5, 14.0. ESI-MS (*m/z*): calculated for C₁₉H₂₃FO₂ [M-H]⁻ 301.2; found 301.1 [M-H]⁻.

2-(2-chlorophenoxy)-5-ethyl-4-fluorophenol (PT406): Compound **PT406** was obtained as a light yellow liquid from **19** using the general procedure IV. ¹H NMR (400 MHz, CDCl₃): δ 7.49 (dd, *J* = 7.96, 1.60 Hz; 1 H); 7.27 (m; 1 H); 7.15 (td, *J* = 7.96, 1.56 Hz; 1 H); 7.05 (dd, *J* = 8.12, 1.52 Hz; 1 H); 6.89 (d, *J* = 7.32 Hz;

1 H); 6.47 (d, $J = 10.04$ Hz; 1 H); 2.62 (q, $J = 7.56$ Hz; 2 H); 1.23 (t, $J = 7.56$ Hz; 3H). ESI-MS (m/z): calculated for $C_{14}H_{12}ClFO_2$ [M-H]⁻ 265.6, 267.0; found 265.0, 267.0 [M-H]⁻.

5-ethyl-4-fluoro-2-(4-nitrophenoxy)phenol (PT407): Compound **PT407** was obtained as a light yellow liquid from **20** using the general procedure IV. ¹H NMR (400 MHz, CDCl₃): δ 8.26 (d, $J = 9.32$ Hz; 2 H); 7.1 (d, $J = 9.28$ Hz; 2 H); 6.94 (d, $J = 7.16$ Hz; 1 H); 7.72 (d, $J = 9.52$ Hz; 1 H); 2.67 (q, $J = 7.76$ Hz; 2 H); 1.27 (t, $J = 7.60$ Hz; 3 H). ESI-MS (m/z): calculated for $C_{14}H_{12}FNO_4$ [M-H]⁻ 276.1; found 276.1 [M-H]⁻.

2-(2-methylpyridin-3-yloxy)-5-ethyl-4-fluorophenol (PT408): Compound **PT408** was obtained as a colorless liquid, from **24** using the general procedure IV (Yield, 87 %). ¹H NMR (500 MHz, CDCl₃ and few drops of MeOH-*d*₄): δ 7.98 (d, $J = 5.0$ Hz, 1 H), 6.98-6.94 (m, 2 H), 6.69(d, $J = 7.0$ Hz, 1 H), 6.38 (d, $J = 10.5$ Hz, 1 H), 2.47-2.42 (m, 5H), 1.08 (t, $J = 7.5$ Hz, 3 H). ¹³C NMR (125 MHz, CDCl₃ and few drops of MeOH-*d*₄): δ 154.8, 152.1, 149.1, 144.0.6, 141.8, 140.3, 140.2, 127.3, 127.2, 123.3, 122.0, 117.09, 117.03, 107.2, 106.9, 21.2, 13.9. ESI-MS (m/z): calculated for $C_{14}H_{14}FNO_2$ [M-H]⁻ 246.1; found 246.1 [M-H]⁻.

5-ethyl-2-(2-nitrophenoxy)-phenol (PT409): Compound **PT409** was obtained as a colorless liquid, from **21** using the general procedure IV. ¹H NMR (400 MHz, CDCl₃-*d*): δ 7.92 (dd, $J = 8.16, 1.76$ Hz, 1 H), 7.45 - 7.56 (m, 1 H), 7.15 - 7.23 (m, 1 H), 7.09 (dd, $J = 8.41, 1.13$ Hz, 1 H), 6.98 (d, $J = 8.28$ Hz, 1 H), 6.94 (d, $J = 2.13$ Hz, 1 H), 6.75 (dd, $J = 8.16, 2.13$ Hz, 1 H), 2.60 - 2.68 (m, 2 H), 1.22 - 1.30 (m, 3 H). ESI-MS (m/z): calculated for $C_{14}H_{13}NO_4$ [M-H]⁻ 258.1; found 258.1 [M-H]⁻.

2-(4-ethyl-2-hydroxyphenoxy)-benzonitrile (PT444): Compound **PT444** was obtained as a yellow oil from **22** using the general procedure IV (Yield, 55 %). ¹H NMR (400 MHz, CDCl₃-*d*): δ 7.67 (dd, $J = 7.78, 1.68$ Hz, 1 H), 7.46 - 7.51 (m, 1 H), 7.15 (dt, $J = 7.63, 0.92$ Hz, 1 H), 6.94 (d, $J = 2.14$ Hz, 1 H), 6.90 (d, $J = 8.24$ Hz, 1 H), 6.88 (d, $J = 8.55$ Hz, 1 H), 6.75 (dd, $J = 8.24, 2.14$ Hz, 1 H), 2.64 (q, $J = 7.63$ Hz, 2 H), 1.22 - 1.28 (m, 3 H). ¹³C NMR (100 MHz, CDCl₃-*d*): δ 159.4, 147.4, 143.2, 139.3, 134.4, 133.9, 123.0, 120.4, 120.2, 116.5, 115.9, 115.8, 103.2, 28.4, 15.4. ESI-MS (m/z): calculated for $C_{15}H_{13}NO_2$ [M+H]⁺ 240.1; found 240.1 [M+H]⁺.

5 Structural characterisation of different ENR-inhibitor complexes and implications for future drug design

Contents and figures of **Chapters 5.1.1 and 5.1.2** have been partially adapted from the publication by Spagnuolo, Eltschkner, Yu et al. (2017) [7].

5.1 Binding characteristics of triazole-based DPE compounds to InhA

Diphenyl-ether inhibitors (DPE inhibitors) containing a triazole moiety in combination with different-sized cyclic alkyl substituents attached to the 5-position of the DPE scaffold were structurally characterised to elucidate the correlation between interaction patterns with the target enzyme InhA and the kinetic properties of these compounds. The triazole inhibitors were derived from the parental compounds PT70, PT91 and PT119 with respect to their 2'-substituents (**Figure 5.1-I**).

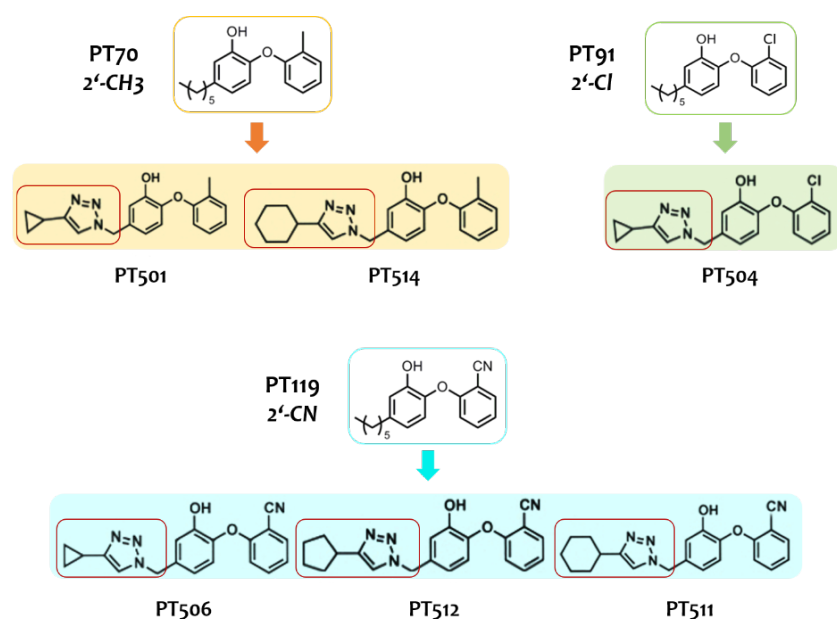


Figure 5.1-I: Parental DPE compounds and their triazole derivatives: Triazole moieties and their attached cycloalkyl groups are indicated by red boxes.

5.1.1 Structural comparison of different binding characteristics of PT91, PT119 and members of the PT500 series

Within all structurally examined ternary InhA-NAD⁺-inhibitor complexes the interactions known to be crucial for the binding of diphenyl ethers are maintained, consisting of π - π -stacking interactions between ring A and the nicotinamide ring of NAD⁺; accompanied by hydrogen bonds created by the 1-OH substituent of ring A with the hydroxyl group of Y158 as well as with the 2'-OH of the nicotinamide ribose. Ring B is embedded in a hydrophobic environment created by residues G96, F97, M98, M103, Y158 and M161, as well as by I202 belonging to the SBL of α -helix 6.

Interestingly, an additional hydrophobic contact with V203 can be observed in the subunits of the [InhA·NAD⁺·PT501], [InhA·NAD⁺·PT504], [InhA·NAD⁺·PT511], [InhA·NAD⁺·PT512] and [InhA·NAD⁺·PT514] structures, which possess a more closed SBL. Within these molecules, α -helix 6 closely resembles the conformational character of the [InhA·NAD⁺·PT91] ternary complex, which is proposed to represent conformational properties of the final EI* state of the InhA-inhibitor complex formation process. However, within monomers, which display a more open SBL conformation as well as in the [InhA·NAD⁺·PT506] complex, this region presents a higher similarity to the [InhA·NAD⁺·PT119] structure, leading to a reduced number of hydrophobic contacts with the diphenyl ether scaffold and excluding V203 from interacting with the compound. This difference in the interaction pattern between the SBL of InhA and the inhibitor is caused by a rotation of α 6 by approximately 100° resulting in a shift of residues A201 – V203 by one amino acid (**Figure 5.1-II a, b**).

Additionally, two alternative SBL conformations can be observed for InhA in complex with PT506, where V203 assumes a conformation, which completely differs from the orientations present in the other InhA-inhibitor structures. This conformation displays an even more disordered state of α 6, indicated by a $C_{\alpha,A}$ - $C_{\alpha,B}$ distance of 3.94 Å between the two positions of V203 in the two alternative orientations of the InhA-PT506 complex and are accompanied by a rotation of the residue of about 60° around the $C_{\beta,A}$ – $C_{\alpha,A/B}$ – $C_{\beta,B}$ angle. As a consequence, V203 is tilted further out of the binding pocket, suggesting that this conformation represents an intermediate state of the loop ordering mechanism of the PT506 inhibitor binding process (**Figure 5.1-IIc**).

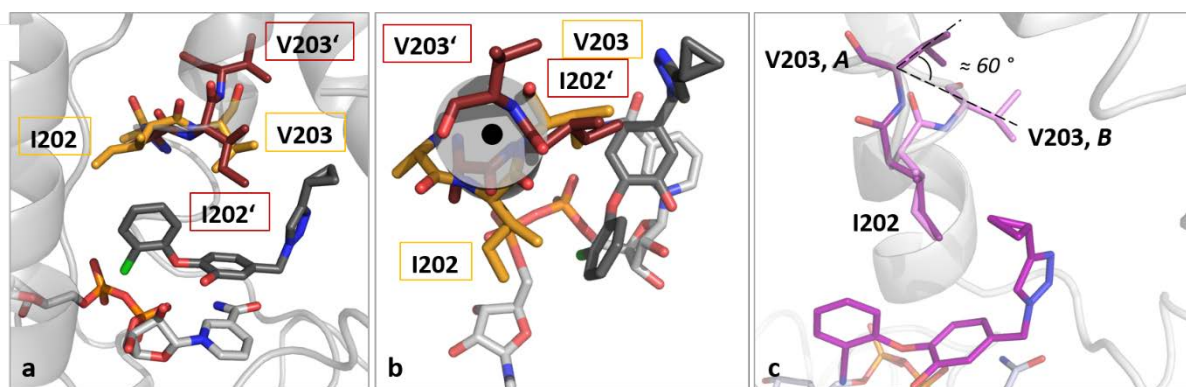


Figure 5.1-II: Conformations of key residues of α -helix 6 interacting with the inhibitor: Side view (a) and top view (b) of the A201 – V203 shift: The conformation of residues representing a more closed SBL is shown as orange sticks, the more open conformation is coloured red and indicated by a “’”. An exemplary inhibitor and the cofactor are displayed as grey sticks. (c) Additional intermediate opening state observed in the InhA-PT506 structure. The two alternative conformations of V203 are marked with A and B. The rotation angle is represented by dashed lines. Residues, inhibitor and cofactor are shown as sticks.

Considering the [InhA·NAD⁺·PT91] SBL conformation, including the typical orientation of residues A201 – V203 in α 6, as final EI* state, one can assume that the second most frequently occurring conformation of residues A201 – V203 represents an energetically elevated EI* state along the path towards the final EI* state of the inhibitor binding process, residing in a local energy minimum. This state is primarily observed for 2'-CN-substituted inhibitor complexes or subunits of 2'-Cl or 2'-methyl substituted InhA-inhibitor complexes containing a more open or partially disordered SBL and is characterised by a reduced contact interface between the inhibitor and α 6 of the protein. Instead, V203 now partially occupies the space within the hydrophobic cavity, which in the totally closed SBL state of [InhA·NAD⁺·PT91] would be claimed by I215 of α 7. To prevent clashes between these residues, I215 is directed closer towards the 5-substituent of the respective inhibitor, thus leading to a global rearrangement of the entire SBL in the PT506 and PT119 complex structures.

The 2'-substituent of the DPE inhibitors is accommodated in a mostly hydrophobic environment formed by G96, A198 as an integral part of α 6; but also the ribose pyrophosphate portion of the cofactor [7]. A comparison of the orientation of the 2'-substituents in different InhA-diphenyl ether complex structures reveals significant differences, particularly between the 2'-CN in contrast to the 2'-Cl and 2'-Me groups. Differences in the distances between the 2'-substituents and the position of the C _{β} of A198 reveal the most striking aspect when comparing the binding modes of altering substitution patterns at the 2'-position. The 2'-Cl substituents of PT91 and PT504 as well as the 2'-methyl groups of PT501 and PT514 tend to be oriented more towards A198, thereby forming close van-der-Waals contacts with the C _{β} of A198 (Figure 5.1-III a-c) [7]. Within monomers containing fully defined SBLs, van-der-Waals distances ranging from 3.2 Å (PT504) to 3.5 Å (PT91), and 3.2 Å to 3.5 Å among the

subunits of the InhA-PT501 complex structure can be observed. In contrast, the 2'-CN groups are oriented further away from A198 and located in closer proximity to G96, adopting a weak hydrogen-bonding distance to the backbone NH of G96, ranging from a minimum of 3.1 Å in the InhA-PT512 complex to a maximum of 3.6 Å for PT506 (**Figure 5.1-III d-f**) [7]. A closer approach to the backbone NH would also be accompanied by a reduced distance to the backbone carbonyl of G96, which would in turn lead to a repulsion between the two negatively charged entities and thus the formation of a stronger hydrogen-bond may not be feasible. The tilted arrangement of the 2'-CN group of a bound inhibitor in its final conformation permits the carbon atom of this group to approach C_β of A198 in a concerted action while decreasing the distance to NH_{G96}. This leads to an additional but weak van-der-Waals contact at a distance of ≈ 3.5 Å with C_β,_{A198} and thereby may be beneficial for SBL stability [7].

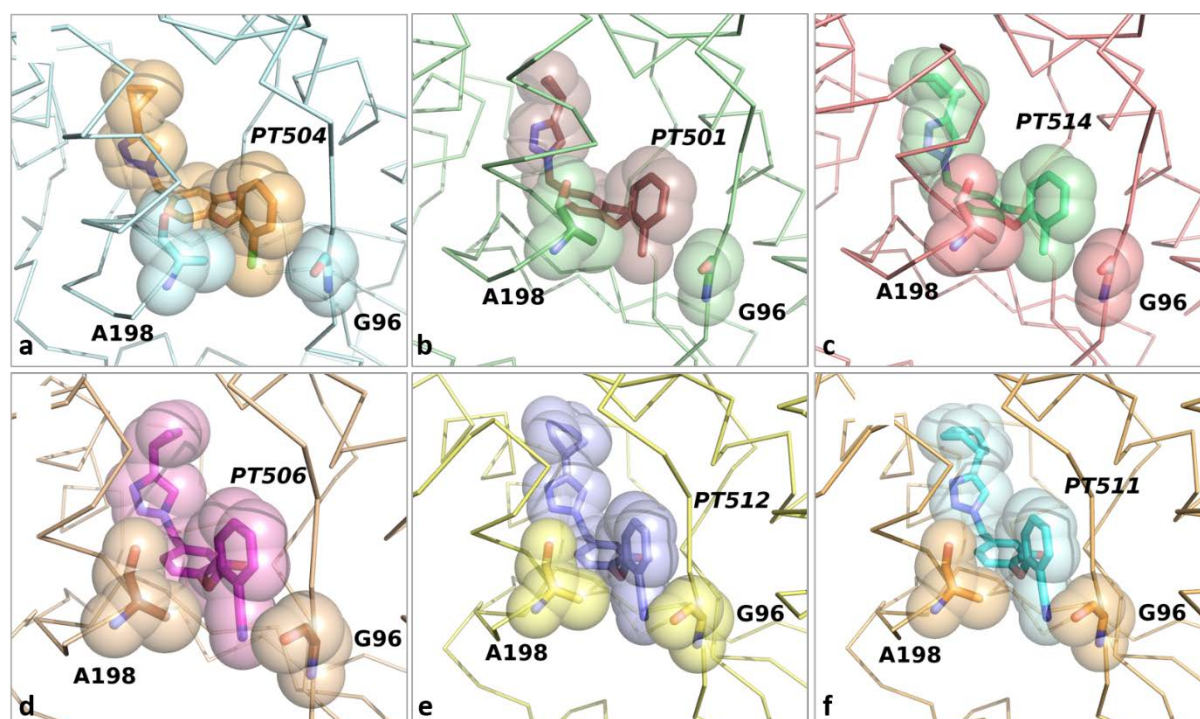


Figure 5.1-III: Interactions of the 2'-substituent with G96 and A198 in the InhA substrate-binding pocket: (a – c) Inhibitors containing a 2'-chloro or a 2'-methyl group; (d – e) Inhibitors containing a 2'-cyano group. The residue- and inhibitor scaffolds are shown as sticks. To illustrate van-der-Waals interactions, the atom radii of the residues and the inhibitors are displayed as spheres. Reproduced with permission from [7]. Copyright 2017 American Chemical Society.

The structural data therefore suggest that hydrophobic 2'-substituents, especially the smaller 2'-Cl group, are preferable in this position since they permit tight interaction with A198, which leads to a stabilisation of the SBL in a more closed state upon inhibitor binding. A more polar 2'-CN substituent instead, is faced with attractive as well as repulsive forces.

A striking difference between the precursor compounds PT91, PT119 and the novel inhibitors PT501 – PT514 is represented by the substituents in ring A at its 5-position with PT91 and PT119 possessing an overall hydrophobic hexyl substituent in contrast to a more bulky and not exclusively hydrophobic triazole moiety, supplemented by a cycloalkyl group in the new compounds. Due to this substitution pattern clear differences in the interactions with InhA can be observed, resulting in prolonged residence times of the inhibitors at their target enzyme.

While the hexyl substituents participate in van-der-Waals contacts with F149, M199, I202 or V203, and L218, the protein – inhibitor interactions of the 5-triazole substituted compounds are more extensive and show greater diversity regarding their chemical nature: The triazole ring is in close vicinity to the aromatic rings of Y158 and F149, as well as to M199 and I202 or V203, depending on the conformational state of $\alpha 6$ [7]. In most cases an additional hydrogen bond either with E219 or Q214 is formed. The size of the 5-cycloalkyl rings creates a large hydrophobic interaction surface with numerous residues of the substrate binding pocket including residues from $\alpha 6$ (I202 or V203) and $\alpha 7$ (I215, L217, L218) of the SBL [7]. In addition, the better space-filling properties of more bulky 5-substituents may further stabilise the protein-inhibitor complexes and lead to longer residence times.

Interestingly, some distinct differences in the interaction pattern between the different triazole-substituted compounds can be observed. Whereas E219 within the [InhA·NAD⁺·PT504] and [InhA·NAD⁺·PT506] complexes is located in close proximity to the 5-triazole substituent, forming a hydrogen bond at distances between 2.6 and 3.0 Å in the different monomers (**Figure 5.1-IVa**), the interaction with $\alpha 7$ of the SBL of InhA in complex with PT501, PT511, PT512 and PT514 is stabilised by a hydrogen bond formed between Q214 and the triazole moiety (**Figure 5.1-IVb**). Thus, a hydrogen-bonding interaction with Q214 seems to be only preferred in the presence of bulkier groups at the 5-position of ring A, or when combining a smaller cyclic group at the 5-position with a larger 2'-substituent like the methyl group of PT501. The larger van-der-Waals radius of the 2'-methyl group might result in an increased spatial requirement of this inhibitor, which impedes the hydrogen-bond formation of PT501 with E219 in contrast to PT504 and PT506 and causes a preference for an interaction with Q214.

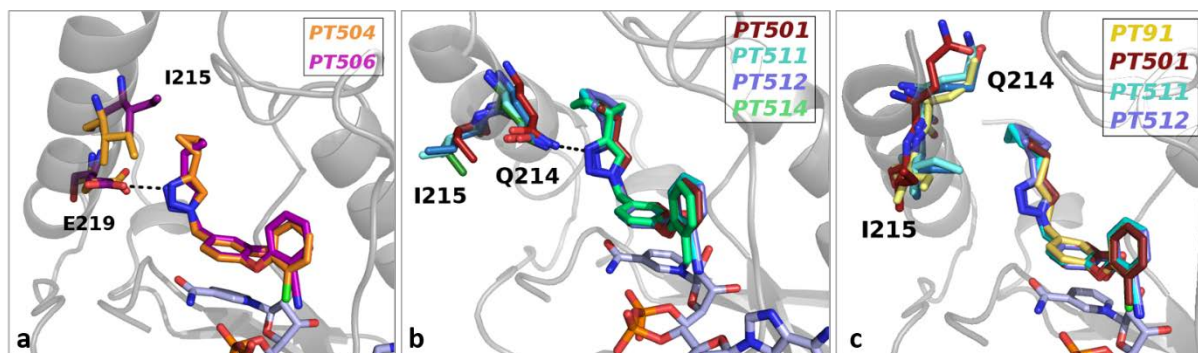


Figure 5.1-IV: Interaction of α -helix 7 with different 5-substituents: (a) Hydrogen-bonding interaction of PT504 (orange) and PT506 (magenta) with E219 and the inward-rotated I215; (b) Hydrogen-bonding interaction of PT501 (ruby), PT511 (cyan), PT512 (blue) and PT514 (green) with Q214, where I215 is directed away from the hydrophobic pocket; (c) Absence of the hydrogen bond with Q214 or E219 and inward rotation of I215: PT501 (ruby), PT511 (cyan) and PT512 (blue) compared to the PT91 conformation (yellow). Reproduced with permission from [7]. Copyright 2017 American Chemical Society.

However, there are some exceptions to these hydrogen-bonding interactions: In one of the monomers of the PT501, PT511 and PT512 structures an orientation of α -helix 7 can be observed which approximates the conformational state of the [InhA·NAD⁺·PT91] complex, where I215 is directed into the binding-pocket and occupies the position of Q214 within the hydrogen-bonded conformation (**Figure 5.1-IVc**).

An inward-rotation of I215 can also be observed within the [InhA·NAD⁺·PT504] and [InhA·NAD⁺·PT506] structures (**Figure 5.1-IVa**). In combination with the hydrogen-bond formed to E219 this might have a positive synergistic effect on the residence times of these inhibitors and seems to represent the energetically most favourable SBL conformation among the herein discussed InhA-inhibitor complexes [7]. However, this phenomenon only seems to be possible for the inhibitors PT504 and PT506 which possess a more flexible and less bulky cyclopropane substituent combined with a rather small 2'-chloro or -cyano group. The sufficient amount of space, which is still present within the substrate-binding pocket upon binding of PT504 or PT506, presumably creates a higher degree of rotational freedom for α 7 whereby E219 can reach into the substrate-binding pocket to form a hydrogen-bond and at the same time the side chain of I215 can be accommodated [7]. The solvent-shielded state of I215 might then also contribute to an entropic gain over the otherwise solvent-exposed conformation of I215.

To reach the inward-rotated conformation of I215 in InhA complexes with PT501, PT511 and PT512, a rotation of α 7 has to take place, where Q214 is moved upwards with respect to the substrate-binding pocket [7]. Along with this rotation Q214 would have to pass the free space between the inhibitor's 5-cycloalkyl moiety and either V203 or V207, depending on the closure state of α -helix 6 (**Figure 5.1-V**). Hence, the replacement of Q214 by I215 is only possible within certain borders concerning the

bulkiness of the 2'- and 5-substituents [7]. For the structure of InhA in complex with PT514 this inward-rotated state of I215 was not observed in any of the subunits, suggesting that the combination of a 2'-methyl group with a 5-cyclohexane ring might push the boundary of $\alpha 7$ rotation and reached the limit of a substituent size feasible for slow-onset inhibitors of InhA.

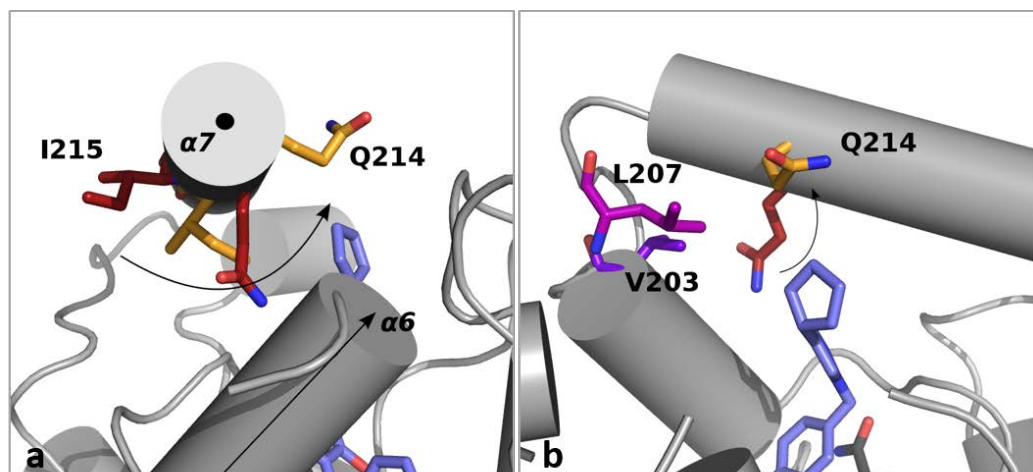


Figure 5.1-V: Proposed mechanism for α -helix 7 closure that prevents an inward rotation of I215 upon binding of inhibitors that reach a “steric demand” limit: (a) View along the rotation axis of α -helix 7 ($\alpha 7$) (depicted by a black dot); (b) View onto $\alpha 7$ perpendicular to the rotation axis. From the initial state (residues shown in red) Q214 has to pass the open space between the inhibitor’s 5-cycloalkyl moiety and either V203 (purple, representing a more open conformation of $\alpha 6$) or L207 (magenta, representing a more closed conformation of $\alpha 6$) to reach the final state (residues shown in orange) where I215 is oriented into the hydrophobic pocket. The course of rotation is depicted by an arrow; an exemplary inhibitor is shown in blue. Reproduced with permission from [7]. Copyright 2017 American Chemical Society.

Since PT514 displays a slightly longer residence time than PT511 and PT512, both assuming either the hydrogen-bonded or the “I215-in” states of SBL-closure, it could be envisioned that one of these conformations displays an energetically enhanced intermediate state during the process of SBL-ordering, from which the system might fall back more readily into the initial EI state even before the final EI* complex is formed.

Another interesting difference arises in the orientation of the triazole ring’s nitrogen portion of PT504 and PT506 compared to PT501, PT511, PT512 and PT514. A torsion angle of $\approx 40 - 60^\circ$ can be observed along the longitudinal axis of the ring plain. Due to this orientation, different interactions of the two groups of inhibitors with $\alpha 7$ can be observed. The different orientation modes of the triazole moieties may influence the orientation of the cycloalkyl groups or *vice versa*. The smaller cyclopropane rings of PT501, PT504 and PT506 possess a higher rotational freedom within the substrate-binding pocket and are thereby able to assume different orientations. This is illustrated by the orientation of the triazole ring of PT501, which differs in the presence and absence of hydrogen-bond formation with Q214. In

the absence of this interaction, the orientation of the ring resembles the orientation observed in the PT504 and PT506 complexes, whereas a different arrangement is observed in the presence of a hydrogen bond. In contrast, the cyclopentane and -hexane rings of PT511, PT512 and PT514, adopt one distinct orientation in all subunits within the substrate-binding pocket, creating an altered contact interface with $\alpha 7$.

5.1.2 Impacts of different substitution patterns on the kinetic behaviour of enzyme-inhibitor complexes

Kinetic measurements for the herein described inhibitors were conducted by members of the *Tonge laboratory, Stony Brook, NY*. In contrast to their parental compounds PT70, PT91 and PT119 the triazole derivatives display improved kinetic properties, resulting in superior residence time. The prolonged lifetime of the InhA-inhibitor complexes results from a transition-state destabilising effect of the triazole moiety, partially complemented by ground-state stabilisation. The extent of these effects depends on the combination of 2'- and 5-substituents attached to the DPE scaffold. For example, a 2'-CN substituent reduces the affinity of the respective compound to InhA and thus leads to slower on-rates during complex formation [7]. A decelerated onset behaviour likewise contributes to an extended residence time and this effect may result from the repulsive force between the cyano substituent and the backbone carbonyl-O of A96, which has to be overcome to reach the stable EI* state. The favourable van-der-Waals interaction of the less polar 2'-methyl or chloro groups with C β of A198 instead, may benefit SBL stability in the closed conformation and thus lead to a stabilisation of the final EI* state, which is accompanied by higher affinity and faster on-rates of the respective inhibitors to InhA [7]. The combination of a slower on-rate resulting from transition-state destabilisation and a faster off-rate of a 2'-CN substituted DPE analogue might result in a residence time similar to a 2'-methyl substituted DPE analogue, which exhibits a faster on-rate combined with a decreased dissociation rate, which results from a stabilisation of the ground state.

The different interactions established by the triazole and the adjacent cycloalkyl substituents additionally modulate the residence time of the inhibitor on InhA. The combination of the hydrogen bond between E219 and the triazole with a buried state of I215 leads to the greatest stabilising effect with respect to the final EI* state. In contrast, one of the two conformational states observed for PT501-, PT511- and PT512 complexes may represent an additional, local energy minimum along the reaction coordinate, which might provide additional stability during the transition from EI to EI*. In case of PT514 a steric bulk limit seems to be reached, since the size of the 2'- and 5-substituents does

not permit the necessary conformational change to rotate I215 into the binding pocket. Thus, the such increased energy required to overcome the steric clash during the transition state results in a remarkable decrease of the on-rate upon complex formation of PT514 with InhA. Interestingly, kinetic experiments utilising an inhibitor with a larger and more rigid 5-substituent, which exceeds this steric limit, reveal loss of slow-onset behaviour [7].

5.1.3 Comparison of inhibitor- and substrate binding to InhA

Comparing the PT504 and PT506 structures with InhA in complex with its C16-acyl substrate (PDB: 1BVR), reveals that $\alpha 7$ in the acyl substrate bound structure assumes a highly similar orientation as observed in the PT506 and PT504 complex structures. Accordingly, E219 within all three structures adopts a similar position, but in the substrate-bound complex its side chain together with Q216 is involved in hydrogen-bonding interactions with R195 located at the N-terminal end of $\alpha 6$. Within the [InhA·NAD⁺·PT506] complex the orientation of E219 slightly changes to benefit the hydrogen-bond formation with the triazole moiety of PT506, but still remains within long-range hydrogen-bonding distance to R195. In contrast, in the InhA-PT504 complex this stabilising interaction with the far N-terminal edge of the SBL cannot be observed and the side chain of E219 solely points towards the inhibitor's triazole group (**Figure 5.1-VIa**).

With respect to α -helix 7, the PT504 and PT506 inhibitors mimic a substrate bound-like state. In contrast, $\alpha 6$ of the substrate-bound complex displays a more open conformation compared to the inhibitor-bound InhA structures. This might be due to the different space occupied by the substrate within the binding pocket, since its U-shaped conformation results in the location of the “ ω -end” at the position which in the inhibitor complexes is occupied by amino acids A201 – V203. The substrate-bound state is also accompanied by the presence of a water molecule, which is coordinated by T196 and one phosphate oxygen of the NAD⁺ cofactor, creating a bridged hydrogen bond with the thioester sulfur of the fatty acid substrate [66]. In contrast, upon inhibitor binding this water is no longer present in the active site and is replaced by A198, which interacts with the inhibitor's 2'-substituent (**Figure 5.1-VI b, c**).

Thus, in the presence of an acyl substrate, specific hydrogen-bonding interactions between α -helices 6 and 7 of InhA are established to achieve a “self-stabilisation” of the SBL, which is complemented by a water-bridged hydrogen bond between α -helix 6 and the acyl substrate. Interestingly, inhibitor binding partially disrupts these interactions to benefit an altered hydrogen-bonding network

accompanied by an increased closure of the SBL, especially with respect to the conformation of α -helix 6.

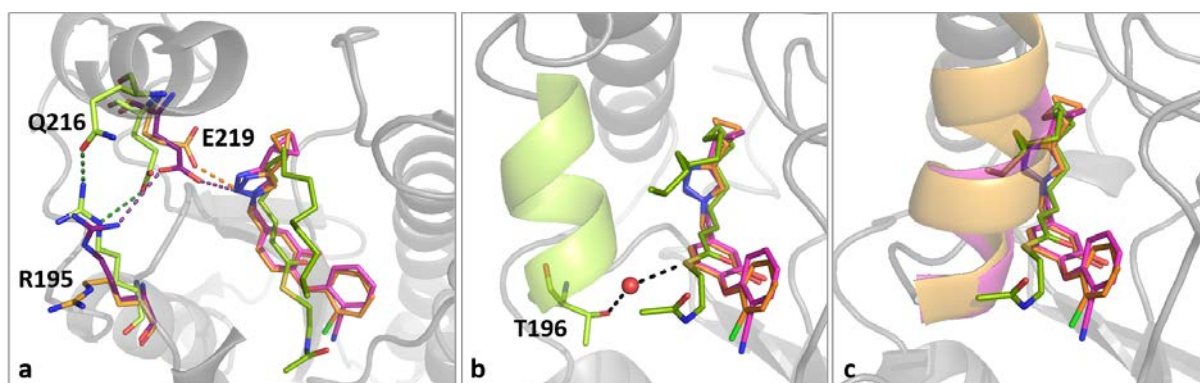


Figure 5.1-VI: Comparison of substrate-bound with inhibitor-bound conformation of the InhA SBL: (a) Hydrogen-bond network between residues of the SBL helices and between the SBL and the inhibitor; (b) Stabilising, water-bridged hydrogen bond between the more open conformation of α -helix 6 and the acyl substrate; (c) Closed conformation of α -helix 6 in complex with DPE inhibitors, which would clash with the “ ω -end” of a bound acyl substrate. Residues and helices belonging to the InhA-substrate complex as well as the substrate itself are shown in green. PT504 and PT506 with the corresponding residues and helices are depicted in orange and magenta, respectively. Hydrogen bonds in (a) are coloured according to the substrate or inhibitor; with hydrogen bonds of the C16-acyl, PT504 and PT506 complexes shown in green, orange and purple, respectively. Side chains of Q216 are directed away from R195 in the subunits containing an ordered SBL in the PT504 and PT506 structures, or their distance is significantly increased (to ≈ 3.5 Å); and they are thus omitted for clarity. Hydrogen bonds in (b) are displayed as black, dashed lines.

5.2 A novel type of DPE inhibitor displays binding to saFabI and InhA

A DPE inhibitor, which was initially designed to inhibit saFabI (“SKTS1” [8], herein referred to as 55JS) was investigated for complex formation with saFabI and InhA. This inhibitor contains an additional pyridone ring attached to ring B in *para* position with respect to the bridging ether between rings A and B (**Figure 5.2-I, central panel**). To the author’s knowledge, a rather bulky substituent at that position in the context of a DPE scaffold was so far not employed to target this area of the substrate-binding pocket. In contrast, the oxotetrahydronaphthyridine group of AFN-1252, a selective saFabI inhibitor [9, 190, 191], occupies this region upon binding to saFabI and forms hydrogen bonds with the backbone atoms of A97 [9] (**Figure 5.2-IV**). A previous study revealed favourable kinetic binding properties of 55JS to saFabI, including a highly prolonged residence time of almost 6 h at 37 °C compared to other saFabI inhibitors investigated in this work [8]. Crystal structures from both, saFabI and InhA with bound 55JS display the known interactions with the enzyme and the cofactor common to all DPE inhibitors (**Figure 5.2-I**).

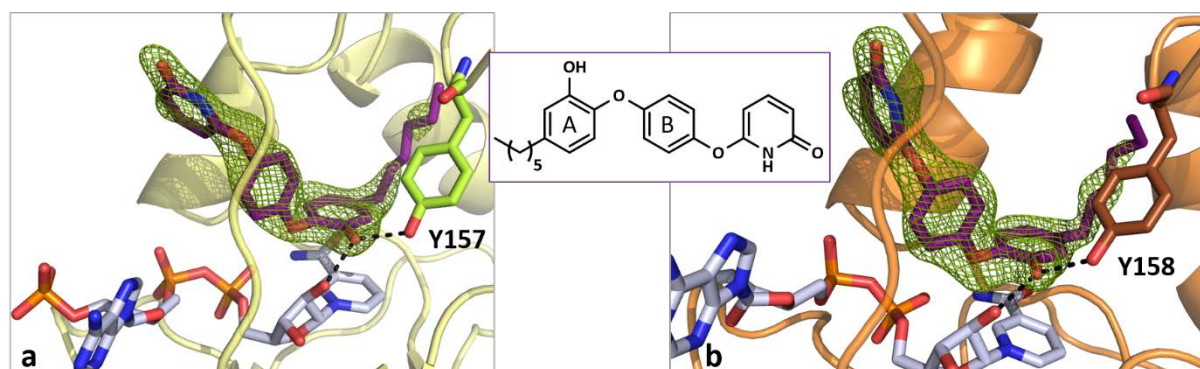


Figure 5.2-I: Common interactions of the DPE scaffold observed for 55JS complexes: 55JS (purple sticks) binds on top of the nicotinamide ring of NADP⁺ (saFabI, (a)) or NAD⁺ (InhA, (b)), shown in light blue stick representation. The green mesh indicates the initial difference electron density observed in the crystal structure at a σ -level of 3.0; black, dashed lines display hydrogen bonds. The inhibitor scaffold is shown in the central panel.

Novel interactions with saFabI, established by the additional pyridone ring observed in the crystal structure, confirm the proposed binding position of this substituent to saFabI [8] (**Figure 5.2-IIc**). These include hydrogen bonds with the backbone atoms of A97, which consist of interactions between the connecting ether-O of ring B and the pyridone ring with the peptide NH at a distance of ≈ 3.3 Å, and an interaction between the backbone carbonyl of A97 and the NH of the pyridone ring at ≈ 2.6 Å distance. A nearly parallel-displaced π -stacking interaction is established between the pyridone ring and the aromatic side chain of F96. An additional water-bridged hydrogen bond is created by the pyridone-carbonyl O with one of the side-chain carboxyl oxygens of E100. Interestingly, a bridging water molecule seems to be loosely coordinated between the two entities and is only observed within three of the eight subunits present in the asymmetric unit of the crystal structure. Two monomers display favourable interaction distances between the pyridine-carbonyl oxygen and the water molecule of ≈ 2.6 Å, and distances between the water molecule and the E100-side chain of $\approx 3.1 - 3.2$ Å. Within the third monomer containing the water molecule, distances are longer with a 55JS-carbonyl to water distance of 4.5 Å and a water-E100 distance of 3.6 Å. In one of the monomers an alternative conformation of the E100 side chain, pointing away from the inhibitor, predominates. Since this monomer in fact does not possess a directly neighbouring monomer, the conformation of E100 directed towards the inhibitor might partially be considered a packing artefact. However, within another monomer, which is also not in direct contact with another subunit, the side-chain conformation oriented towards the inhibitor is still present.

Interestingly, inhibitor binding is also observed to InhA, although the residence time of 55JS on InhA compared to saFabI is reduced to ≈ 5 h at 25 °C (*unpublished data; Tonge lab, Stony Brook*). This might result from an altered interaction pattern of the pyridone moiety with the protein compared to saFabI. Here, binding of the inhibitor in its pyridone- as well as in its tautomeric hydroxypyridine state is possible, but the hydroxypyridine tautomer is preferred with respect to the possible interaction patterns between the inhibitor and InhA. In its tautomeric state, the free electron pair of the nitrogen in the heterocycle establishes a weak hydrogen bond with the backbone NH of M98 (3.3 Å) and hence enables the protonated oxygen of the ring to interact tightly with the carbonyl-O of the M98 backbone by forming a hydrogen bond at a distance of 2.6 Å (**Figure 5.2-IIb**). Another hydrogen bond is created with the Q100 N ϵ at a distance of ≈ 3.2 Å. In the presence of the pyridone form of the inhibitor bound to InhA, interactions would be less favourable. The ether oxygen between ring B and the pyridone may form a hydrogen bond with the backbone NH of M98 at ≈ 3.4 Å, which is similar to the one observed in saFabI with A97 (≈ 3.3 Å). Additionally, the interaction with Q100 would still be established, but strong repulsive forces between the pyridone carbonyl and the backbone carbonyl of M98 would occur, since the distance between both oxygens is only 2.6 Å. An additional hydrogen bond between the pyridone NH and the backbone N of M98 or the backbone carbonyl-O of the latter is possible, but the distances of 3.3 and 3.1 Å, respectively, resulting in a rather weak character of these bonds, may hardly compensate the unfavourable distance between the two aforementioned oxygens (**Figure 5.2-IIa**). The parallel-displaced π -stacking interaction as seen in saFabI can also be observed in the InhA complex between the pyridone ring and the aromatic ring of F97.

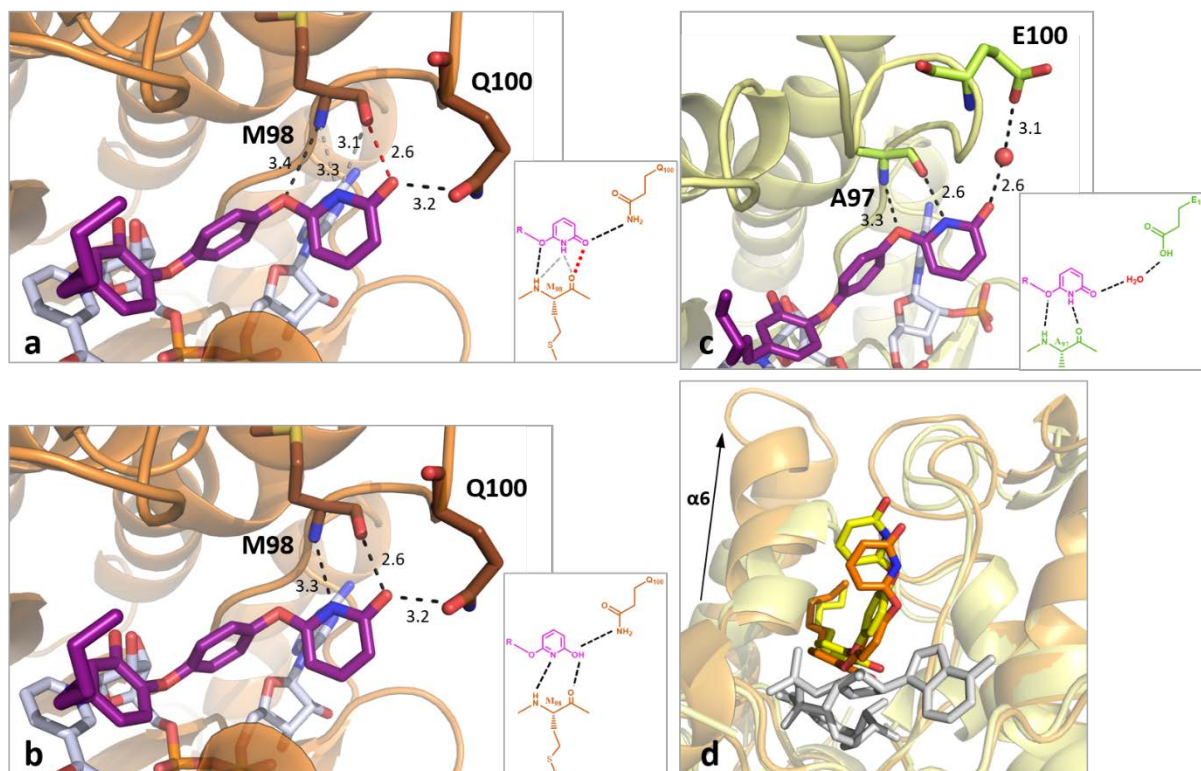


Figure 5.2-II: Positioning of the 55JS pyridone ring in the substrate-binding pocket of saFabI and InhA: (a) Interactions of the pyridone with the protein environment in InhA; (b) Interactions of the hydroxypyridine tautomer of 55JS with InhA; (c) Pyridone interactions with the saFabI protein; (d) Different accommodation of the pyridone ring of 55JS in saFabI (yellow) and InhA (orange). 55JS, the cofactor and interacting residues are displayed as sticks; hydrogen bonds are shown as black, dashed lines; alternative hydrogen bonds and repulsive interactions in (a) are coloured grey and red, respectively; in (d) only the NAD⁺ cofactor of InhA is shown. Schematic views of Interaction networks related to each binding mode of the pyridone are shown in smaller boxes.

Indeed, MD simulations confirm a preferred binding of the pyridone form to saFabI, which displays much weaker binding to InhA. In contrast, the hydroxypyridine tautomer is energetically favoured and establishes more stable interactions with M98 of InhA compared to the pyridone. Additional QM calculations for the inhibitor independently determined from the protein environment in vacuum or in solvent reveal a slight energetical preference of the tautomeric pyridone state (*unpublished data; Engels lab, Würzburg*). Thus, binding to InhA might be accompanied by increased constraints applied to the preferred tautomeric state of the inhibitor itself and may account for a less stable enzyme-inhibitor complex and shorter residence time.

The different size of the substrate-binding pockets of both enzymes causes a varying flexibility of the inhibitor in its bound state to both enzymes. Due to the longer SBL of InhA, especially α -helix 6, the pyridone moiety is buried to a larger extent than it is possible within the smaller substrate-binding pocket of saFabI (**Figure 5.2-II(d)**). Hence, the pyridone ring exhibits a much higher flexibility when

bound to saFabI than in its bound state to InhA as shown by MD simulations (*unpublished data; Engels lab, Würzburg*). This might also be the reason for the only intermittent presence of the bridging water molecule between the pyridone carbonyl-O and the side chain of E100 in the saFabI structure.

Despite the enhanced flexibility of the pyridone moiety of 55JS bound to saFabI compared to the InhA complex, the interactions seem to be favoured for saFabI binding, since the pyridone ring is present in its energetically favoured tautomeric state upon hydrogen-bond formation with the protein. In InhA, however, favourable interactions are established by the hydroxypyridine form of the inhibitor. Although the hydrogen-bonding distances are similar to the ones present in the saFabI complex, the preference for the pyridone form of 55JS provides the opportunity of repulsive interactions to occur. Thus, it might be worthwhile to modify this inhibitor when trying to target InhA to that effect that the carbonyl oxygen is exchanged by a proton donor, e.g. an amino- or hydroxyl group, whereas the position of the heteroatom in the ring may or may not be protonated. Another option would be to substitute the heteroatom within the aromatic ring as well. A heteroatom containing a free electron pair and thus acting as sole proton acceptor may establish the hydrogen bond to the backbone amine of M98 as it occurs in the hydroxypyridine form. Nevertheless, a hydrogen at that position may be donated to the free electron pair of the backbone nitrogen and in turn the hydrogen of the latter may establish another hydrogen bond with the ether bridge between ring B and the heterocycle. This would be the case if the pyridone was substituted by e.g. 2-aminoimidazole (**Figure 5.2-III d**) or a related heterocycle. The protonated nitrogen of the imidazole ring could enable the formation an additional hydrogen bond and provide three different possibilities for the arrangement of a hydrogen-bonding network with InhA. There is a tautomeric equilibrium between the two nitrogens of the imidazole ring and hence, the hydrogen can migrate between these atoms. Nevertheless, the potential hydrogen bond with the protein may benefit the location of the hydrogen atom at one distinct nitrogen. In contrast, heterocycles containing a non-protonated heteroatom would maintain the hydrogen bonds as observed for the hydroxypyridine form of 55JS as depicted in **Figure 5.2-III a-c**. However, derivatives **a – c (Figure 5.2-III)** should be less prone to tautomerisation. In fact, the lactol moiety (**Figure 5.2-III a**) is not even planar due to the loss of its aromatic character and possible conformers of the ring might or might not benefit adaptation to the architecture of the substrate-binding pocket. The iminopyran (**Figure 5.2-III b**) would be planar and less prone to tautomerisation in contrast to a hydroxypyran and thus more likely maintain the hydrogen-bond donor property of the nitrogen. The same is true for the 2-aminopyridine ring (**Figure 5.2-III c**), where even in the case of tautomerisation at least one hydrogen atom would always remain at the exocyclic nitrogen. The cyclic heteroatom would not contain

hydrogen-bond donor properties in examples **a – c** shown in **Figure 5.2-III**, although a tautomerisation of the 2-aminopyridine holds the potential to establish an additional hydrogen bond with the protein.

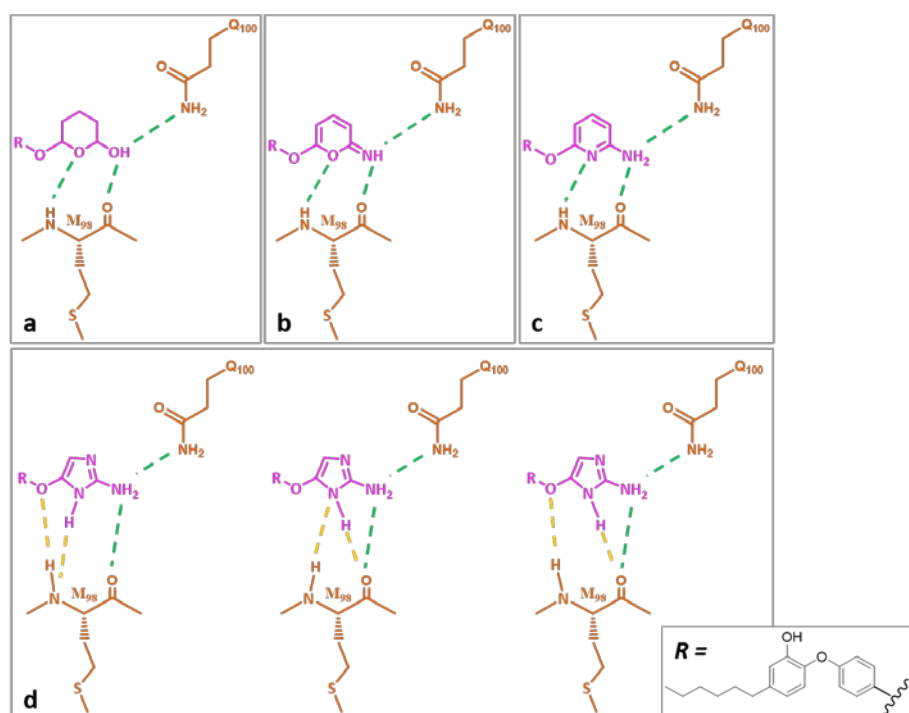


Figure 5.2-III: Possible alternatives for the pyridone substituent of 55JS to specifically target InhA: (a-c) Putative preferred hydrogen-bonding interactions established by a lactol- (**a**), iminopyran- (**b**) or aminopyridin- (**c**) ring; (**d**) Alternative orientations of an additional hydrogen bond established by a protonated heteroatom; Preferred hydrogen bonds are indicated by green, dashed lines, alternative hydrogen bonds are shown as orange, dashed lines.

The pyridone group attached to ring B of 55JS occupies the same region in saFabI, which is targeted by the AFN-1252 oxotetrahydronaphthyridine moiety. Interestingly, crystal structures of AFN-1252 in complex with ENRs from *E. coli* (PDB: 4JQC) and *B. pseudomallei* (PDB: 4RLH [192]) reveal similar binding of the inhibitor to these ENRs including two hydrogen bonds established between the fused heterocycles of the inhibitor and A95 in ecFabI and bpFabI. Thus, it is likely that also 55JS might be able to bind to other ENRs like ecFabI and bpFabI, since the additional area of the binding pocket addressed by 55JS has been shown to interact with AFN-1252 as well. Since, in contrast to InhA, the orientation of the backbone atoms and the amino-acid type is similar between saFabI, ecFabI and bpFabI, optimisation of the pyridone moiety might not even be necessary to achieve favourable binding properties. Additionally, in both ENR structures charged residues at a similar position as E100 in saFabI are present (D98 in ecFabI, E98 in bpFabI), which have the potential to establish a water-bridged hydrogen bond as observed in the saFabI-55JS complex (**Figure 5.2-IV**).

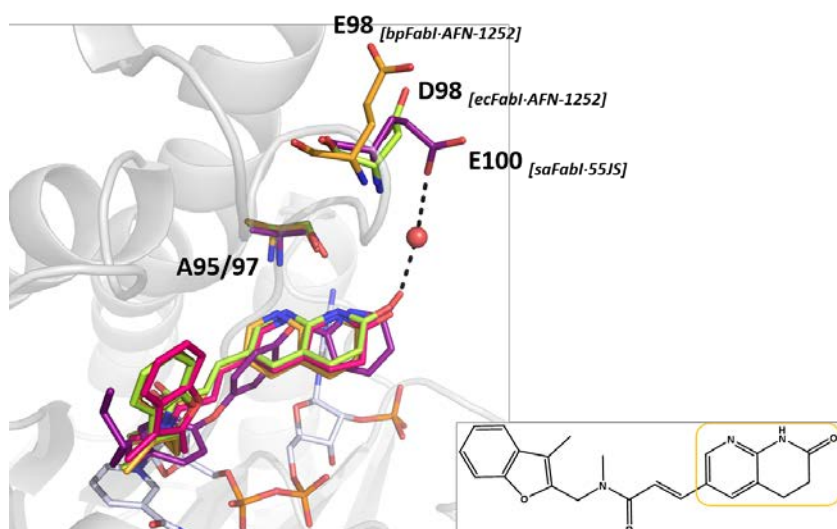


Figure 5.2-IV: Comparison of the binding mode of 55JS to saFabI with the interaction pattern of AFN-1252 to different ENR enzymes: Side chains important for interactions with the inhibitors are shown as sticks. Residues and the inhibitor of the bpFabI-AFN-1252 complex are coloured in orange, of the ecFabI-AFN-1252 complex in green and those of saFabI-55JS are coloured in purple. AFN-1252 from the saFabI structure is shown in magenta, the corresponding residues assume similar positions to those of the saFabI-55JS structure; a difference can be seen in the rotamer conformation of E100. The scaffold of AFN-1252 is shown in the lower right panel and the oxotetrahydronaphthyridine moiety is framed in orange.

Thus, 55JS displays a favourable scaffold to be optimised for binding to different ENR enzymes, for example by altering the hydrogen-bond donor pattern of the pyridone moiety to improve binding to InhA. A second starting point for optimisation may as well be provided by altering substituent properties at the 5-position of the DPE scaffold, e.g. by testing the effect of different acyl-chain lengths on saFabI, ecFabI and bpFabI inhibition. In case of InhA, attaching the previously described triazole substituents to that position may greatly affect binding properties of the inhibitor.

5.3 Implications for future drug design

5.3.1 Drug residence time and the importance of pharmacodynamic properties

After the model of drug-target residence time had been introduced about one decade ago [184, 193], the awareness to understand the kinetics of drug binding, which provides the opportunity to improve a drug's residence time on a specific target molecule, has risen significantly. Prolonged residence time (t_R) has been recognised as an important factor of a compound's clinical effectiveness *in vivo*, extending the duration of its pharmacodynamic activity, even when systemic concentrations have already been reduced through elimination routes [194]. Additionally, longer binding to target molecules reduces the risk of off-target mediated side-effects and leads to higher selectivity when dissociation from the target

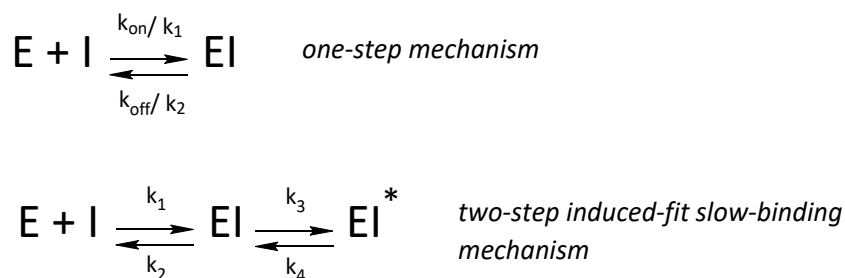
is slow in contrast to fast dissociation rates from potential anti-targets. Prolonged residence of drugs already bound to their target molecule might also attenuate some of the resistance mechanisms described in **Chapter 1.3.1**, particularly efflux from the cell as well as chemical modification or degradation. In addition, an enhanced residence time might allow a reduced dosing schedule during therapeutic applications.

The simplest description of a drug's affinity to a certain target is provided by determining the equilibrium dissociation constant K_d , which relates association (k_{on}) and dissociation rates (k_{off}) for a simple one-step binding mechanism (**Equation 5.3-I; Scheme 5.3-I, top**). The " K_d for inhibition" [176], which is the inhibitory constant K_i , is also measured under equilibrium conditions, but in the presence of a substrate of the target enzyme. In contrast to the IC_{50} value, which describes the inhibitor concentration leading to 50 % reduction in enzymatic activity under certain conditions, K_i is independent of substrate type and concentration for competitive inhibitors [176]. These thermodynamic descriptors, however, neglect the detailed kinetic parameters as well as the structural determinants underlying the drug – target interactions of a specific system [194]. Moreover, thermodynamic parameters are valid in equilibrium conditions of a closed (*in vitro*) system, but do not consider fluctuations in local drug concentrations as they occur in an open (*in vivo*) system [150, 184].

In contrast to one-step binding, high-affinity inhibition is often associated with a two-step induced-fit slow-binding mechanism (**Scheme 5.3-I, bottom**) in which the rapid formation of an initial enzyme – inhibitor complex is followed by a slow isomerization event. This second step leads to the formation of a final and more stable complex, which determines the overall drug – target interaction time [150]. The lifetime of a drug-target complex *in vivo* is predominantly dependent on the off-rate (k_{off}) [193], but yet is composed of both, on- (k_{on}) and off-rate. Hence, besides focussing on the achievement of slow off-rates to enhance the potency of an inhibitor, it is also worthwhile to consider changes in the on-rates. Although slower on-rates may lead to a decrease in thermodynamic affinity, they can make a significant contribution to prolong the lifetime of a drug-target complex [6, 7].

Equation 5.3-I:

$$K_d = \frac{[E] \cdot [I]}{[EI]} = \frac{k_{off}}{k_{on}}$$



Scheme 5.3-I: One-step binding and two-step induced-fit slow-binding mechanisms: For slow-onset binding the following assumption is made: $k_2 \gg k_3$ & k_4 , resulting in $k_{\text{off}} \approx k_4$ and $t_R = 1/k_4$. [184]

Extended drug-target residence time accompanied by kinetic selectivity has the potential to permit reduced dosing requirements and furthermore, a high selectivity decreases off-target interactions, which are usually facilitated by high systemic drug concentrations [187, 193]. Provided the residence time of a drug on its target surpasses its pharmacokinetic lifetime in the circulation, the selectivity can be very high, thus resulting in improved safety properties [193].

Limits to the concept of residence time are set by re-synthesis of the target enzymes, which has a considerable effect in rapidly proliferating organisms, where the dosing schedule will be dictated by the velocity of *de-novo* protein synthesis [184, 193]. For slowly growing species like *M. tuberculosis*, where the generation time is approximately 14 – 15 h [195], drug residence time is likely to be the major determinant of dosing intervals. This might still hold true for *B. pseudomallei*, where the intracellular growth rate was calculated to be ≈ 6 h [196]. However, in *S. aureus* for which the simulated *in-vivo* doubling time is only ≈ 1 h [197] and thus, the rate of protein synthesis is presumably greater than in *M. tuberculosis* and *B. pseudomallei*, the effect of long residence time inhibitors might be partially circumvented.

5.3.2 Molecular basis of residence-time modulation on enoyl-ACP reductases

In enzymes of the FabI class of enoyl-ACP reductases of bacteria like *Staphylococcus aureus*, *Burkholderia pseudomallei* and *Mycobacterium tuberculosis* – saFabI, bpFabI and InhA, respectively, inhibition kinetics are characterised by conformational changes of the SBL during a substrate- or inhibitor-binding event (**Figure 1.2-II**). Slow-onset inhibition can be described as a two-step induced-fit binding mechanism (**Scheme 5.3-I, bottom**) and is accompanied by the full ordering of the SBL [6, 7, 67, 78, 136, 149, 165, 179, 198], which is considered the rate-limiting step of DPE-binding kinetics on ENR enzymes [62]. In the first step, the rapid formation of an initial enzyme-inhibitor complex, EI, takes place, which displays a more open conformation of the SBL and is structurally similar to the

substrate-bound state during the catalytic cycle of the enzyme [7]. Subsequently, the system has to overcome an energy barrier, which is described by the complete closure of the SBL leading to the formation of the final and energetically lowest EI* state, where a maximum of favourable interactions between the enzyme and the inhibitor is reached (**Figure 5.3-I**).

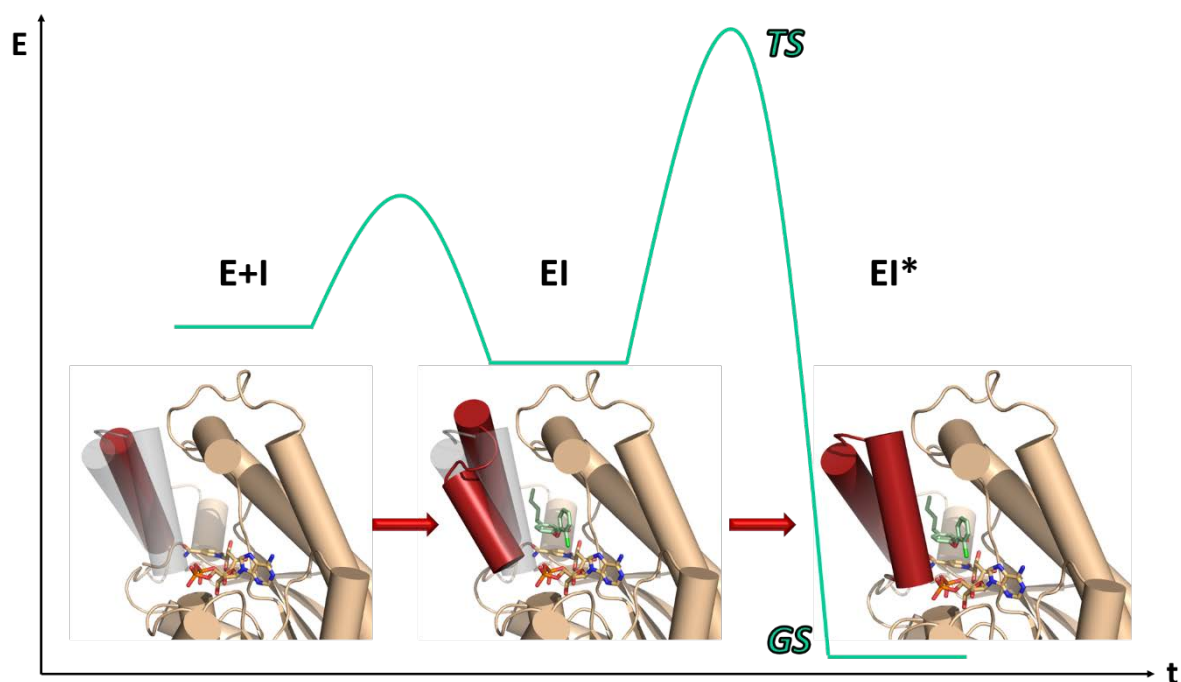


Figure 5.3-I: Energy diagram of the two-step binding mechanism of slow-onset inhibitors: The SBL-ordering process is illustrated using the example of *InhA*. The conformation of SBL-helices 6 and 7 is depicted as red cylinders, according to the state of the enzyme-inhibitor complex. A reference of the final, closed SBL is shown as grey cylindrical helices in the E+I and EI states. TS: transition state; GS: ground state

5.3.3 Impact of residence-time optimisation on pharmacokinetics of ENR inhibitors

Drug-elimination routes described in **Chapter 1.3.1**, especially the active elimination of compounds by specific efflux pumps as well as degradation mechanisms display a major problem for rapid-reversible inhibitors, but can be significantly reduced for compounds, which exhibit prolonged residence times at their targets. Once these compounds are bound to their targets, they are not available in their free form for an extended period and thus, drug elimination mechanisms remain ineffective. Additionally, even when the concentration of free compounds within the cell has decreased or the drug has already been removed from the system, the antibiotic activity may be maintained for an elongated time span. This so-called post-antibiotic effect (PAE) [187, 199], which is essentially promoted by the increased

residence time, may be even enhanced by the phenomenon of drug rebinding [200, 201], which in turn is highly influenced by the k_{on} rate [193].

Especially DPE compounds, which usually display broad-spectrum antibacterial activity [9], may strongly benefit from a prolonged residence time, since the phenol group of DPEs is metabolically labile and thus rather prone to enzymatical conversion like glucuronidation and sulfonation in the host liver [10]. A prolonged binding to the target enzyme might compensate for their lowered stability, since the free drug concentration within the cell is reduced and thus less available for efflux from the bacterial cell and subsequent degradation by the host metabolism or degradation mechanisms of the pathogen itself. In contrast, the more stable pyridones display rapid-reversible binding behaviour on ENR enzymes and thus may be eliminated from the cell by an efflux pump more readily. Therefore, it is important to understand the binding mechanisms, which underlie inhibitor binding to its specific target and the modulation of which dictates the effectiveness of a drug under non-equilibrium conditions.

DPE compounds represent a suitable tool to target ENR enzymes important in the FAS-II pathway and to optimise kinetic binding behaviour. The DPE scaffold can be modified according to the properties of the respective ENR; for example, altering substitution patterns at the 2'- and 5-position influences the stability of the ground and/or transition state during the two-step slow-onset binding process of a compound to InhA and thus affects its residence time [7]. A similar effect can be observed for DPE binding to bpFabI, where the nature of the 2'-substituent primarily influences the stability of both, the ground and transition state, and the substituent at the 4'-position primarily affects the transition state [6]. Consequently, the residence time can be maximised when both parameters are combined in a favourable manner, i.e. by destabilising the transition state to achieve a slower binding process together with a stabilisation of the ground state, which results in an increased affinity and a decelerated dissociation of the enzyme-inhibitor complex. Therefore, it is not sufficient to contemplate inhibitor affinity in an isolated way, since low affinity may be the result of slow-onset inhibitor binding and prolong the lifetime of a drug-target complex.

The 4'-position of the DPE scaffold, which is important for modulating binding properties on bpFabI [6], was employed to design the saFabI inhibitor 55JS to extend the number of favourable interactions between the inhibitor and the enzyme. This was achieved by attaching a bulky pyridone substituent to the DPE scaffold at that position. The region addressed by this ring is located at the entrance of the major portal, through which the substrate is presumably delivered for catalysis [10]. Interestingly, also in this structure and in the InhA-55JS complex, ring B of 55JS assumes a slightly tilted conformation as it is observed for bpFabI in complex with 4'-substituted inhibitors [6] to accommodate the additional

substituent within the substrate-binding pocket. Kinetic measurements revealed a long residence time of 345 min for 55JS on saFabI at 37 °C, which is superior compared to the values reported for the 4'-unsubstituted DPE compounds; as well as a prolonged PAE for 55JS compared to these inhibitors [8]. Interestingly, the ClogP value calculated for 55JS in its pyridone form (ClogP = 5.85), is only slightly better than that of e.g. PT119 (ClogP = 5.90 [7]), which was also examined in this study. The ClogP value of the hydroxypyridine state of 55JS (ClogP = 7.35) on the other hand, seems to be rather unfavourable.

Interestingly, this compound has been shown to bind to InhA as well and preliminary data reveal a favourable residence time of 55JS towards this enzyme. However, since the properties of the pyridone ring are optimised to target saFabI, minor changes applied to the 4'-heterocycle may bear the potential to improve binding to InhA. Considering structural homologies of saFabI with ENRs from other bacteria like *E. coli* and *B. pseudomallei*, this inhibitor should also be tested for its efficacy against these organisms. Structural data of ecFabI and bpFabI in complex with AFN-1252 [9] display a similar binding mode of this compound as observed in complex with saFabI for which the inhibitor was initially designed [8]. AFN-1252 targets the same area in the substrate binding pocket as the pyridone moiety of 55JS and interacts with a widely conserved alanine residue, which is substituted by Met in InhA. This residue has been shown to interact with several potent saFabI inhibitors like TCL and CG400549 [71, 130] and forms hydrogen bonds with the 55JS pyridone substituent as well. Thus, it is very likely that other ENRs may also be inhibited by 55JS.

In contrast to 55JS, ClogP values of the triazole substituted DPE compounds are significantly improved to 3.60 – 3.98 for PT70-, PT91- and PT119 triazole derivatives containing the 5-cyclopropyl substituents and to 4.20 – 4.90 for analogues containing larger cycloalkyl (pentyl-, hexyl-) moieties [7]. An improved ClogP value, reflecting a reduced lipophilicity, enhances the bioavailability of a compound [166]. Thus, it might be worthwhile to test triazole DPEs for their binding ability to other ENR enzymes than InhA. For example, the enhanced flexibility of the substrate-binding pocket of saFabI necessary to accommodate more bulky BCFAs, might also provide a sufficient amount of space for the triazole substituent. Additionally, the available space within the saFabI substrate-binding pocket is slightly increased [130] due to substitutions of I200 (ecFabI annotation), present in most ENRs (**Figure 5.4-I, bottom**), by a valine residue in saFabI, and of M206 by an isoleucine, which is present in other ENR enzymes as well. The favourable binding properties of CG400549 to saFabI [130], which contains a thiophene ring at its 5-position, further support the notion that saFabI fulfils the spatial requirements of the triazole ring as well. Indeed, a superposition of CG400549 and PT504 reveals that sufficient space to accommodate the bulky 5-substituent of PT504 is available. Unfortunately, the residues surrounding this moiety present in the CG400549 structure are exclusively hydrophobic and thus, no hydrogen

bond might be formed with the triazole ring as it is observed in the InhA structures [7] (**Figure 5.3-II**). Using the saFabI-CG400549 complex as a model for triazole-DPE binding, larger substituents than the cyclopropyl group at the 5-position would lead to steric clashes with the protein environment of the substrate-binding pocket. Either the size of larger alkyl rings generally exceeds the available space within the cavity, or conformational rearrangements might allow the accommodation of larger substituents.

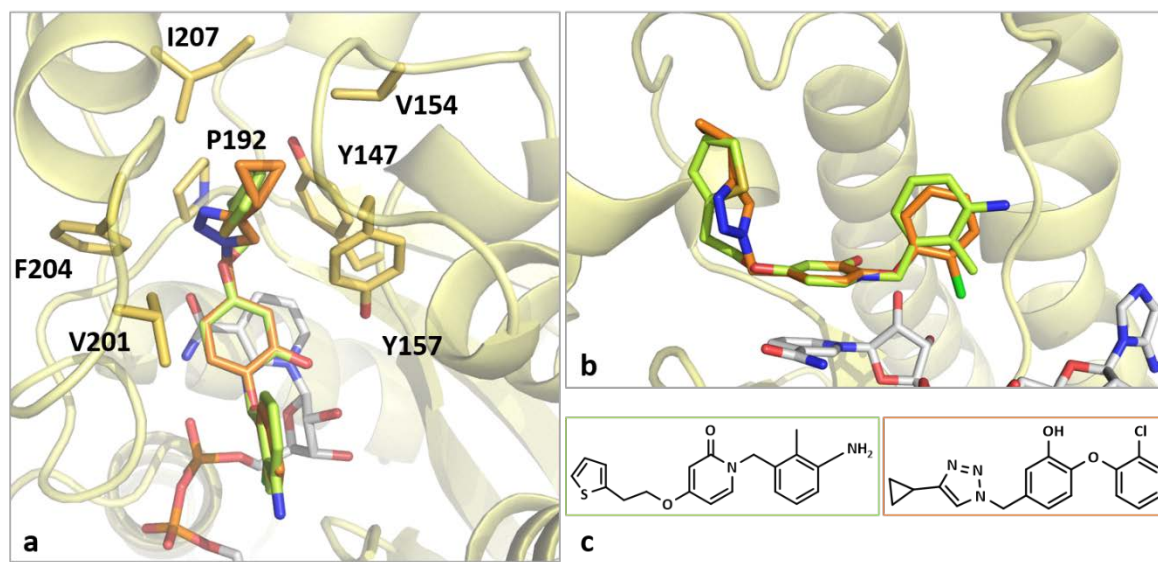


Figure 5.3-II: Overlay of CG400549 bound to saFabI (PDB: 4CV0, Monomer B) and PT504: (a) Top view including residues of the hydrophobic pocket of saFabI; **(b)** Side view of the aligned inhibitors; PT504 was arranged to best match the orientation of CG400549. **(c)** Schematic view of the inhibitor scaffolds of CG400549 (green box) and PT504 (orange box); Inhibitors, NADPH and residues flanking the hydrophobic pocket are represented as sticks. CG400549 is shown in green, PT504 in orange and NADPH in grey. The protein is displayed in yellow.

5.4 Lessons learned from the investigation of the ACP-FabI complex

The basic region consisting of K201, R204 and K205 as it is present in ecFabI is not entirely conserved in other FabI enzymes, or some basic residues present in this area are altered in their positions. None of the ENR enzymes except ecFabI included in the sequence alignment contains more than two basic residues in this region (**Figure 5.4-1c**). In saFabI basic residues in this area only comprise K199 and K209, which differ from the residues in ecFabI regarding their position and do not display a similar, clustered arrangement (**Figure 5.4-1a**). In the complex structure solved by Rafi *et al.* [64] K201, R204 and K205 from ecFabI are located in close proximity to ecACP. However, a superposition with saFabI in its *apo* form (PDB: 4ALN) or in complex with TCL (PDB: 4ALI) clearly indicates that K209 might participate in an interaction with ACP, whereas K199 is either absent in the *apo* structure or resides in close vicinity

to the ACP molecule located at the position suggested by *Schiebel et al.* [10]. In the bpFabI *apo* structure (PDB: 3EK2), containing a partially disordered SBL, K201 and K205 are present and located at the same position as in the ecFabI-ecACP complex from *Rafi et al.* [64] and *Schiebel et al.* [10], but R204 is replaced by a glycine residue in bpFabI (**Figure 5.4-1a**). Upon substrate binding the SBL would be expected to be locked in a certain, ordered conformation to shield the substrate from the solvent. Since residues K201 and K205 in both, ecFabI in complex with ecACP and bpFabI in the absence of ACP assume a similar orientation, this arrangement might represent a common arrangement of the SBL in the absence of substrate or inhibitor. Two interpretations could be derived from this analysis: Either this orientation represents a pre-ordered state which facilitates a rapid recognition between both interaction partners; or this SBL conformation correlates with a random, but frequently occurring state of the SBL in the *apo* form of the protein.

Interestingly, the ecFabI monomer suggested to interact with ecACP from the structure solved by *Rafi et al.* (PDB: 2FHS) [64] contains a fully ordered SBL, whereas the model from *Schiebel et al.* [10] displays a partially disordered SBL of the ecFabI monomer which is in contact with ecACP (**Figure 5.4-1b**). A superposition of the ecFabI molecules of both structures shows that the ordered SBL of ecFabI in the structure from *Rafi et al.* would clash with the ecACP molecule as it is positioned in the structure from *Schiebel et al.* Consequently, it remains unclear whether the presence of ecACP in the complex structure from *Rafi et al.* leads to an ordering of the SBL of ecFabI which is induced by a specific interaction with ecACP, or whether this is due to crystal packing effects. Additionally, the ordered conformation of the SBL in this structure is not compatible with the position ecACP assumes in the model suggested by *Schiebel et al.* Thus, either the position of ecACP in this model is not entirely correct, or the true conformation of the SBL upon interaction with ecACP is different, but not available due to the lack of appropriate data. The absence of both, the cofactor and the acyl substrate in the structure, suggests that the partially disordered conformation of the SBL probably better reflects the situation between the two interaction partners in this structure, and the information which can be deduced from these data.

Furthermore, the high degree of conservation in the primary sequence and the spatial arrangement of residues of the recognition helix α_2 of ACP contrasts with the absence of a strictly conserved amino-acid pattern between the area comprising K201 – K205 in ecFabI and the equivalent regions in other bacterial homologues. Hence, it is questionable whether this area plays a critical role for the interaction between ACP and FabI.

The design of a fusion protein consisting of saACP and saFabI connected by a flexible linker yielded protein, which could be expressed and purified and maintained its functionality with respect to cofactor binding within the active site of saFabI, as well as the ability to be modified at the saACP moiety. However, the efficiency of modification with an acyl substrate seems to be reduced compared to the single saACP protein and the separation of the modified from the unmodified fusion construct is hampered by tetramerization of the saFabI portion of the fusion protein. The ability to form tetramers provides further evidence towards the integrity of the fusion constructs, but is highly disadvantageous concerning the isolation of the desired species. Modification and separation may also be impaired by the transient interaction between the saACP and saFabI portions in solution, rendering the saACP less accessible for the 4'-phosphopantetheinyl transferase *sfp* for modification. Additionally, upon interaction of the modified saACP with saFabI, the acyl portion can no longer be utilised for separation by anion-exchange chromatography, which is usually employed to isolate modified saACP. Thus, inhomogeneity of the sample as well as a slight susceptibility to degradation combined with enhanced flexibility may impede the fusion construct to form well-ordered crystals. The approach of introducing an additional crosslink to trap the fusion construct upon the interaction between its two subunits (**Chapter 3.5.7**) may provide enhanced stability by impairing their dissociation and by decreasing the accessibility of the linker region concerning the cleavage of the latter. However, this approach requires further optimisation to obtain reasonable amounts of the protein in the desired conformation.

5.5 Conclusion

Although the uptake of exogenous FAs was suggested to circumvent FAS-II inhibition, endogenous FAs have been shown to be essential for many clinically relevant strains such as *E. coli*, *H. influenzae*, *F. tularensis* and *M. tuberculosis* [71, 96, 97, 202], which in addition do not contain isoenzymes to complement inhibited functionality of their ENR enzymes. Concerning *S. aureus* as a highly clinically relevant pathogen, it has been shown that there is no mechanism to down-regulate FAS-II gene expression by exogenous FAs [203] and FAs from the host-blood serum cannot compensate for the endogenously synthesised *anteiso*-15:0 FAs that modulate membrane fluidity in staphylococci [96].

Due to the diversity of FA patterns as well as the FabI enzymes in different bacteria, targeting FAS II implies the dedicated inhibition of proteins from one single pathogen, i.e. drug development to treat one specific disease [100]. However, this prerequisite offers the chance to develop highly effective

drugs with preferably minor side-effects, which is amongst others enabled by considering kinetic parameters such as residence time.

Although the basic catalytic steps in FAS II are conserved, some organisms use isoforms of the respective enzymes to carry out specific reactions [100]. Where isoenzymes of the drug target are present, e.g. the FabI isoenzymes FabV, FabK, FabL, one of which is present for example in *S. pneumoniae* and *V. cholerae* [68-70], it becomes necessary to develop inhibitors targeting these enzymes as well, or to target other key regulatory steps of the FAS-II system, e.g. enzymes performing the carboxylation or the condensation reaction [100], to effectively inhibit FA biosynthesis.

Inhibition of substrate delivery using an inhibitor, which abolishes the interaction between ACP and FabI, would provide new perspectives in drug development against FAS II and, in the case of compounds binding to the surface of ACP, would not be limited to FabI, but also affect potentially existing isoenzymes interacting with ACP.

6 Bibliography

1. Ehrlich P, *Anwendung und Wirkung von Salvarsan*. Deutsche medizinische Wochenschrift, 1910. **36**: p. 2437-2438.
2. Domagk G, *Ein Beitrag zur Chemotherapie der bakteriellen Infektionen*. Deutsche Medizinische Wochenschrift, 1935. **61**: p. 250-253.
3. Fleming A, *Penicillin*. British Medical Journal, 1941. **2**(4210): p. 386-386.
4. Levy CW, Roujeinikova A, Sedelnikova S, Baker PJ, Stuitje AR, Slabas AR, Rice DW and Rafferty JB, *Molecular basis of triclosan activity*. Nature, 1999. **398**(6726): p. 383-4.
5. McMurry LM, Oethinger M and Levy SB, *Triclosan targets lipid synthesis*. Nature, 1998. **394**(6693): p. 531-2.
6. Neckles C, Eltschkner S, Cummings JE, Hirschbeck M, Daryae F, Bommineni GR, Zhang Z, Spagnuolo L, Yu W, Davoodi S, Slayden RA, Kisker C and Tonge PJ, *Rationalizing the Binding Kinetics for the Inhibition of the Burkholderia pseudomallei FabI Enoyl-ACP Reductase*. Biochemistry, 2017. **56**(13): p. 1865-1878.
7. Spagnuolo LA, Eltschkner S, Yu W, Daryae F, Davoodi S, Knudson SE, Allen EK, Merino J, Pschibul A, Moree B, Thivalapill N, Truglio JJ, Salafsky J, Slayden RA, Kisker C and Tonge PJ, *Evaluating the Contribution of Transition-State Destabilization to Changes in the Residence Time of Triazole-Based InhA Inhibitors*. J Am Chem Soc, 2017. **139**(9): p. 3417-3429.
8. Daryae F, Chang A, Schiebel J, Lu Y, Zhang Z, Kapilashrami K, Walker SG, Kisker C, Sotriffer CA, Fisher SL and Tonge PJ, *Correlating Drug-Target Kinetics and In vivo Pharmacodynamics: Long Residence Time Inhibitors of the FabI Enoyl-ACP Reductase*. Chem Sci, 2016. **7**(9): p. 5945-5954.
9. Kaplan N, Albert M, Awrey D, Bardouniotis E, Berman J, Clarke T, Dorsey M, Hafkin B, Ramnauth J, Romanov V, Schmid MB, Thalakada R, Yethon J and Pauls HW, *Mode of action, in vitro activity, and in vivo efficacy of AFN-1252, a selective antistaphylococcal FabI inhibitor*. Antimicrob Agents Chemother, 2012. **56**(11): p. 5865-74.
10. Schiebel J, Chang A, Merget B, Bommineni GR, Yu W, Spagnuolo LA, Baxter MV, Tareilus M, Tonge PJ, Kisker C and Sotriffer CA, *An Ordered Water Channel in Staphylococcus aureus FabI: Unraveling the Mechanism of Substrate Recognition and Reduction*. Biochemistry, 2015. **54**(10): p. 1943-55.
11. Schiebel J, *Structure-Based Drug Design on Enzymes of the Fatty Acid Biosynthesis Pathway*. 2013, University of Wuerzburg: Wuerzburg.
12. World Health Organization., *Global tuberculosis report 2016*. 2016, Geneva: World Health Organization. 214 p.
13. Ernst JD, *The immunological life cycle of tuberculosis*. Nat Rev Immunol, 2012. **12**(8): p. 581-91.
14. Zhang Y and Yew WW, *Mechanisms of drug resistance in Mycobacterium tuberculosis*. Int J Tuberc Lung Dis, 2009. **13**(11): p. 1320-30.
15. Smith T, Wolff KA and Nguyen L, *Molecular biology of drug resistance in Mycobacterium tuberculosis*. Curr Top Microbiol Immunol, 2013. **374**: p. 53-80.
16. Lamrabet O and Drancourt M, *Genetic engineering of Mycobacterium tuberculosis: a review*. Tuberculosis (Edinb), 2012. **92**(5): p. 365-76.
17. *WHO Guidelines Approved by the Guidelines Review Committee, in The Use of Delamanid in the Treatment of Multidrug-Resistant Tuberculosis: Interim Policy Guidance*. 2014, World Health Organization: Geneva

18. WHO Guidelines Approved by the Guidelines Review Committee, in *Guidelines for the Programmatic Management of Drug-Resistant Tuberculosis: 2011 Update*. 2011, World Health Organization: Geneva
19. WHO Guidelines Approved by the Guidelines Review Committee, in *The Use of Bedaquiline in the Treatment of Multidrug-Resistant Tuberculosis: Interim Policy Guidance*. 2013, World Health Organization: Geneva
20. Zhang Y and Yew WW, *Mechanisms of drug resistance in Mycobacterium tuberculosis: update 2015*. Int J Tuberc Lung Dis, 2015. **19**(11): p. 1276-89.
21. Strauss JM, Groves MG, Mariappan M and Ellison DW, *Melioidosis in Malaysia. II. Distribution of Pseudomonas pseudomallei in soil and surface water*. Am J Trop Med Hyg, 1969. **18**(5): p. 698-702.
22. Perumal Samy R, Stiles BG, Sethi G and Lim LHK, *Melioidosis: Clinical impact and public health threat in the tropics*. PLoS Negl Trop Dis, 2017. **11**(5): p. e0004738.
23. Wiersinga WJ, Currie BJ and Peacock SJ, *Melioidosis*. N Engl J Med, 2012. **367**(11): p. 1035-44.
24. Cheng AC and Currie BJ, *Melioidosis: epidemiology, pathophysiology, and management*. Clin Microbiol Rev, 2005. **18**(2): p. 383-416.
25. Wiersinga WJ, van der Poll T, White NJ, Day NP and Peacock SJ, *Melioidosis: insights into the pathogenicity of Burkholderia pseudomallei*. Nat Rev Microbiol, 2006. **4**(4): p. 272-82.
26. Price EP, Hornstra HM, Limmathurotsakul D, Max TL, Sarovich DS, Vogler AJ, Dale JL, Ginther JL, Leadem B, Colman RE, Foster JT, Tuanyok A, Wagner DM, Peacock SJ, Pearson T and Keim P, *Within-host evolution of Burkholderia pseudomallei in four cases of acute melioidosis*. PLoS Pathog, 2010. **6**(1): p. e1000725.
27. Mohamed R, Nathan S, Embi N, Razak N and Ismail G, *Inhibition of macromolecular synthesis in cultured macrophages by Pseudomonas pseudomallei exotoxin*. Microbiol Immunol, 1989. **33**(10): p. 811-20.
28. Reckseidler-Zenteno SL, DeVinney R and Woods DE, *The capsular polysaccharide of Burkholderia pseudomallei contributes to survival in serum by reducing complement factor C3b deposition*. Infect Immun, 2005. **73**(2): p. 1106-15.
29. Utaisincharoen P, Tangthawornchaikul N, Kespichayawattana W, Chaisuriya P and Sirisinha S, *Burkholderia pseudomallei interferes with inducible nitric oxide synthase (iNOS) production: a possible mechanism of evading macrophage killing*. Microbiol Immunol, 2001. **45**(4): p. 307-13.
30. Kespichayawattana W, Rattanachetkul S, Wanun T, Utaisincharoen P and Sirisinha S, *Burkholderia pseudomallei induces cell fusion and actin-associated membrane protrusion: a possible mechanism for cell-to-cell spreading*. Infect Immun, 2000. **68**(9): p. 5377-84.
31. Ngauy V, Lemeshev Y, Sadkowski L and Crawford G, *Cutaneous melioidosis in a man who was taken as a prisoner of war by the Japanese during World War II*. J Clin Microbiol, 2005. **43**(2): p. 970-2.
32. White NJ, *Melioidosis*. Lancet, 2003. **361**(9370): p. 1715-22.
33. Propst KL, Troyer RM, Kelliham LM, Schweizer HP and Dow SW, *Immunotherapy markedly increases the effectiveness of antimicrobial therapy for treatment of Burkholderia pseudomallei infection*. Antimicrob Agents Chemother, 2010. **54**(5): p. 1785-92.
34. Estes DM, Dow SW, Schweizer HP and Torres AG, *Present and future therapeutic strategies for melioidosis and glanders*. Expert Rev Anti Infect Ther, 2010. **8**(3): p. 325-38.
35. Titball RW, Burtneck MN, Bancroft GJ and Brett P, *Burkholderia pseudomallei and Burkholderia mallei vaccines: Are we close to clinical trials?* Vaccine, 2017.

36. Gilad J, Harary I, Dushnitsky T, Schwartz D and Amsalem Y, *Burkholderia mallei and Burkholderia pseudomallei as bioterrorism agents: national aspects of emergency preparedness*. Isr Med Assoc J, 2007. **9**(7): p. 499-503.
37. Wertheim HF, Melles DC, Vos MC, van Leeuwen W, van Belkum A, Verbrugh HA and Nouwen JL, *The role of nasal carriage in Staphylococcus aureus infections*. Lancet Infect Dis, 2005. **5**(12): p. 751-62.
38. Pantosti A and Venditti M, *What is MRSA?* Eur Respir J, 2009. **34**(5): p. 1190-6.
39. King MD, Humphrey BJ, Wang YF, Kourbatova EV, Ray SM and Blumberg HM, *Emergence of community-acquired methicillin-resistant Staphylococcus aureus USA 300 clone as the predominant cause of skin and soft-tissue infections*. Ann Intern Med, 2006. **144**(5): p. 309-17.
40. Naimi TS, LeDell KH, Como-Sabetti K, Borchardt SM, Boxrud DJ, Etienne J, Johnson SK, Vandenesch F, Fridkin S, O'Boyle C, Danila RN and Lynfield R, *Comparison of community- and health care-associated methicillin-resistant Staphylococcus aureus infection*. Jama, 2003. **290**(22): p. 2976-84.
41. Francis JS, Doherty MC, Lopatin U, Johnston CP, Sinha G, Ross T, Cai M, Hansel NN, Perl T, Ticehurst JR, Carroll K, Thomas DL, Nuermberger E and Bartlett JG, *Severe community-onset pneumonia in healthy adults caused by methicillin-resistant Staphylococcus aureus carrying the Panton-Valentine leukocidin genes*. Clin Infect Dis, 2005. **40**(1): p. 100-7.
42. Seybold U, Kourbatova EV, Johnson JG, Halvosa SJ, Wang YF, King MD, Ray SM and Blumberg HM, *Emergence of community-associated methicillin-resistant Staphylococcus aureus USA300 genotype as a major cause of health care-associated blood stream infections*. Clin Infect Dis, 2006. **42**(5): p. 647-56.
43. Reddy PN, Srirama K and Dirisala VR, *An Update on Clinical Burden, Diagnostic Tools, and Therapeutic Options of Staphylococcus aureus*. Infect Dis (Auckl), 2017. **10**.
44. Fleming A, *On the Antibacterial Action of Cultures of a Penicillium, with Special Reference to their Use in the Isolation of B. influenzae*. Br J Exp Pathol. 1929 Jun;10(3):226-36.
45. Lyon BR and Skurray R, *Antimicrobial resistance of Staphylococcus aureus: genetic basis*. Microbiol Rev, 1987. **51**(1): p. 88-134.
46. Jevons MP, *"Celbenin" - resistant Staphylococci*. Br Med J. 1961 Jan 14;1(5219):124-5.
47. Blair JM, Webber MA, Baylay AJ, Ogbolu DO and Piddock LJ, *Molecular mechanisms of antibiotic resistance*. Nat Rev Microbiol, 2015. **13**(1): p. 42-51.
48. Pantosti A, Sanchini A and Monaco M, *Mechanisms of antibiotic resistance in Staphylococcus aureus*. Future Microbiol, 2007. **2**(3): p. 323-34.
49. Sievert DM, Rudrik JT, Patel JB, McDonald LC, Wilkins MJ and Hageman JC, *Vancomycin-resistant Staphylococcus aureus in the United States, 2002-2006*. Clin Infect Dis, 2008. **46**(5): p. 668-74.
50. Purrello SM, Garau J, Giamarellou E, Mazzei T, Pea F, Soriano A and Stefani S, *Methicillin-resistant Staphylococcus aureus infections: A review of the currently available treatment options*. J Glob Antimicrob Resist, 2016. **7**: p. 178-186.
51. Martens E and Demain AL, *The antibiotic resistance crisis, with a focus on the United States*. J Antibiot (Tokyo), 2017. **70**(5): p. 520-526.
52. Spoering AL, Vulic M and Lewis K, *GlpD and PIsB participate in persister cell formation in Escherichia coli*. J Bacteriol, 2006. **188**(14): p. 5136-44.
53. Balemans W, Vranckx L, Lounis N, Pop O, Guillemont J, Vergauwen K, Mol S, Gilissen R, Motte M, Lancois D, De Bolle M, Bonroy K, Lill H, Andries K, Bald D and Koul A, *Novel antibiotics targeting respiratory ATP synthesis in Gram-positive pathogenic bacteria*. Antimicrob Agents Chemother, 2012. **56**(8): p. 4131-9.
54. Lewis HC, Molbak K, Reese C, Aarestrup FM, Selchau M, Sorum M and Skov RL, *Pigs as source of methicillin-resistant Staphylococcus aureus CC398 infections in humans, Denmark*. Emerg Infect Dis, 2008. **14**(9): p. 1383-9.

55. Chan DI and Vogel HJ, *Current understanding of fatty acid biosynthesis and the acyl carrier protein*. *Biochem J*, 2010. **430**(1): p. 1-19.
56. White SW, Zheng J, Zhang YM and Rock, *The structural biology of type II fatty acid biosynthesis*. *Annu Rev Biochem*, 2005. **74**: p. 791-831.
57. Smith S, Witkowski A and Joshi AK, *Structural and functional organization of the animal fatty acid synthase*. *Prog Lipid Res*, 2003. **42**(4): p. 289-317.
58. Jornvall H, Persson B, Krook M, Atrian S, Gonzalez-Duarte R, Jeffery J and Ghosh D, *Short-chain dehydrogenases/reductases (SDR)*. *Biochemistry*, 1995. **34**(18): p. 6003-13.
59. Kallberg Y, Oppermann U, Jornvall H and Persson B, *Short-chain dehydrogenases/reductases (SDRs)*. *Eur J Biochem*, 2002. **269**(18): p. 4409-17.
60. Massengo-Tiasse RP and Cronan JE, *Diversity in enoyl-acyl carrier protein reductases*. *Cell Mol Life Sci*, 2009. **66**(9): p. 1507-17.
61. Parikh S, Moynihan DP, Xiao G and Tonge PJ, *Roles of tyrosine 158 and lysine 165 in the catalytic mechanism of InhA, the enoyl-ACP reductase from Mycobacterium tuberculosis*. *Biochemistry*, 1999. **38**(41): p. 13623-34.
62. Lu H and Tonge PJ, *Inhibitors of FabI, an enzyme drug target in the bacterial fatty acid biosynthesis pathway*. *Acc Chem Res*, 2008. **41**(1): p. 11-20.
63. Quemard A, Sacchettini JC, Dessen A, Vilcheze C, Bittman R, Jacobs WR, Jr. and Blanchard JS, *Enzymatic characterization of the target for isoniazid in Mycobacterium tuberculosis*. *Biochemistry*, 1995. **34**(26): p. 8235-41.
64. Rafi S, Novichenok P, Kolappan S, Zhang X, Stratton CF, Rawat R, Kisker C, Simmerling C and Tonge PJ, *Structure of acyl carrier protein bound to FabI, the FASII enoyl reductase from Escherichia coli*. *J Biol Chem*, 2006. **281**(51): p. 39285-93.
65. Rafferty JB, Simon JW, Baldock C, Artymiuk PJ, Baker PJ, Stuitje AR, Slabas AR and Rice DW, *Common themes in redox chemistry emerge from the X-ray structure of oilseed rape (Brassica napus) enoyl acyl carrier protein reductase*. *Structure*, 1995. **3**(9): p. 927-38.
66. Rozwarski DA, Vilcheze C, Sugantino M, Bittman R and Sacchettini JC, *Crystal structure of the Mycobacterium tuberculosis enoyl-ACP reductase, InhA, in complex with NAD+ and a C16 fatty acyl substrate*. *J Biol Chem*, 1999. **274**(22): p. 15582-9.
67. Liu N, Cummings JE, England K, Slayden RA and Tonge PJ, *Mechanism and inhibition of the FabI enoyl-ACP reductase from Burkholderia pseudomallei*. *J Antimicrob Chemother*, 2011. **66**(3): p. 564-73.
68. Massengo-Tiasse RP and Cronan JE, *Vibrio cholerae FabV defines a new class of enoyl-acyl carrier protein reductase*. *J Biol Chem*, 2008. **283**(3): p. 1308-16.
69. Heath RJ and Rock CO, *Microbiology: A triclosan-resistant bacterial enzyme*. *Nature*, 2000. **406**(6792): p. 145-146.
70. Heath RJ, Su N, Murphy CK and Rock CO, *The enoyl-[acyl-carrier-protein] reductases FabI and FabL from Bacillus subtilis*. *J Biol Chem*, 2000. **275**(51): p. 40128-33.
71. Schiebel J, Chang A, Lu H, Baxter MV, Tonge PJ and Kisker C, *Staphylococcus aureus FabI: inhibition, substrate recognition, and potential implications for in vivo essentiality*. *Structure*, 2012. **20**(5): p. 802-13.
72. Robert X and Gouet P, *Deciphering key features in protein structures with the new ENDscript server*. *Nucleic Acids Res*, 2014. **42**(Web Server issue): p. W320-4.
73. Odriozola JM, Ramos JA and Bloch K, *Fatty acid synthetase activity in Mycobacterium smegmatis. Characterization of the acyl carrier protein-dependent elongating system*. *Biochim Biophys Acta*, 1977. **488**(2): p. 207-17.
74. Marrakchi H, Laneelle MA and Daffe M, *Mycolic acids: structures, biosynthesis, and beyond*. *Chem Biol*, 2014. **21**(1): p. 67-85.
75. Bhatt A, Molle V, Besra GS, Jacobs WR, Jr. and Kremer L, *The Mycobacterium tuberculosis FAS-II condensing enzymes: their role in mycolic acid biosynthesis, acid-fastness, pathogenesis and in future drug development*. *Mol Microbiol*, 2007. **64**(6): p. 1442-54.

76. Portevin D, De Sousa-D'Auria C, Houssin C, Grimaldi C, Chami M, Daffe M and Guilhot C, *A polyketide synthase catalyzes the last condensation step of mycolic acid biosynthesis in mycobacteria and related organisms*. Proc Natl Acad Sci U S A, 2004. **101**(1): p. 314-9.
77. Luckner SR, Liu N, am Ende CW, Tonge PJ and Kisker C, *A slow, tight binding inhibitor of InhA, the enoyl-acyl carrier protein reductase from Mycobacterium tuberculosis*. J Biol Chem, 2010. **285**(19): p. 14330-7.
78. Merget B and Sottriffer CA, *Slow-Onset Inhibition of Mycobacterium tuberculosis InhA: Revealing Molecular Determinants of Residence Time by MD Simulations*. PLoS One, 2015. **10**(5).
79. Holden MT, Titball RW, Peacock SJ, Cerdeno-Tarraga AM, Atkins T, Crossman LC, Pitt T, Churcher C, Mungall K, Bentley SD, Sebahia M, Thomson NR, Bason N, Beacham IR, Brooks K, Brown KA, Brown NF, Challis GL, Cherevach I, Chillingworth T, Cronin A, Crossett B, Davis P, DeShazer D, Feltwell T, Fraser A, Hance Z, Hauser H, Holroyd S, Jagels K, Keith KE, Maddison M, Moule S, Price C, Quail MA, Rabinowitsch E, Rutherford K, Sanders M, Simmonds M, Songsivilai S, Stevens K, Tumapa S, Vesaratchavest M, Whitehead S, Yeats C, Barrell BG, Oyston PC and Parkhill J, *Genomic plasticity of the causative agent of melioidosis, Burkholderia pseudomallei*. Proc Natl Acad Sci U S A, 2004. **101**(39): p. 14240-5.
80. Cummings JE, Kingry LC, Rholl DA, Schweizer HP, Tonge PJ and Slayden RA, *The Burkholderia pseudomallei enoyl-acyl carrier protein reductase FabI is essential for in vivo growth and is the target of a novel chemotherapeutic with efficacy*. Antimicrob Agents Chemother, 2014. **58**(2): p. 931-5.
81. Lu H and Tonge PJ, *Mechanism and inhibition of the FabV enoyl-ACP reductase from Burkholderia mallei*. Biochemistry, 2010. **49**(6): p. 1281-9.
82. Hirschbeck MW, Kuper J, Lu H, Liu N, Neckles C, Shah S, Wagner S, Sottriffer CA, Tonge PJ and Kisker C, *Structure of the Yersinia pestis FabV enoyl-ACP reductase and its interaction with two 2-pyridone inhibitors*. Structure, 2012. **20**(1): p. 89-100.
83. Kaneda T, *Iso- and anteiso-fatty acids in bacteria: biosynthesis, function, and taxonomic significance*. Microbiol Rev, 1991. **55**(2): p. 288-302.
84. Heath RJ, Li J, Roland GE and Rock CO, *Inhibition of the Staphylococcus aureus NADPH-dependent enoyl-acyl carrier protein reductase by triclosan and hexachlorophene*. J Biol Chem, 2000. **275**(7): p. 4654-9.
85. Kim SJ, Ha BH, Kim KH, Hong SK, Shin KJ, Suh SW and Kim EE, *Dimeric and tetrameric forms of enoyl-acyl carrier protein reductase from Bacillus cereus*. Biochem Biophys Res Commun, 2010. **400**(4): p. 517-22.
86. Kim KH, Ha BH, Kim SJ, Hong SK, Hwang KY and Kim EE, *Crystal structures of Enoyl-ACP reductases I (FabI) and III (FabL) from B. subtilis*. J Mol Biol, 2011. **406**(3): p. 403-15.
87. Zhang YM, Wu B, Zheng J and Rock CO, *Key residues responsible for acyl carrier protein and beta-ketoacyl-acyl carrier protein reductase (FabG) interaction*. J Biol Chem, 2003. **278**(52): p. 52935-43.
88. Zhang YM, Marrakchi H, White SW and Rock CO, *The application of computational methods to explore the diversity and structure of bacterial fatty acid synthase*. J Lipid Res, 2003. **44**(1): p. 1-10.
89. Parris KD, Lin L, Tam A, Mathew R, Hixon J, Stahl M, Fritz CC, Seehra J and Somers WS, *Crystal structures of substrate binding to Bacillus subtilis holo-(acyl carrier protein) synthase reveal a novel trimeric arrangement of molecules resulting in three active sites*. Structure, 2000. **8**(8): p. 883-895.
90. Nguyen C, Haushalter RW, Lee DJ, Markwick PR, Bruegger J, Caldara-Festin G, Finzel K, Jackson DR, Ishikawa F, O'Dowd B, McCammon JA, Opella SJ, Tsai SC and Burkart MD, *Trapping the dynamic acyl carrier protein in fatty acid biosynthesis*. Nature, 2014. **505**(7483): p. 427-31.

91. Zhang YM, Rao MS, Heath RJ, Price AC, Olson AJ, Rock CO and White SW, *Identification and analysis of the acyl carrier protein (ACP) docking site on beta-ketoacyl-ACP synthase III*. J Biol Chem, 2001. **276**(11): p. 8231-8.
92. Roujeinikova A, Baldock C, Simon WJ, Gilroy J, Baker PJ, Stuitje AR, Rice DW, Slabas AR and Rafferty JB, *X-ray crystallographic studies on butyryl-ACP reveal flexibility of the structure around a putative acyl chain binding site*. Structure, 2002. **10**(6): p. 825-35.
93. Zornetzer GA, Tanem J, Fox BG and Markley JL, *The length of the bound fatty acid influences the dynamics of the acyl carrier protein and the stability of the thioester bond*. Biochemistry, 2010. **49**(3): p. 470-7.
94. Heath RJ, Jackowski S and Rock CO, *Fatty acid and phospholipid metabolism in prokaryotes in Biochemistry of Lipids, Lipoproteins and Membranes*, D.E. Vance and J.E. Vance, Editors. 2002, Elsevier Science B.V.
95. Brinster S, Lamberet G, Staels B, Trieu-Cuot P, Gruss A and Poyart C, *Type II fatty acid synthesis is not a suitable antibiotic target for Gram-positive pathogens*. Nature, 2009. **458**(7234): p. 83-6.
96. Parsons JB, Frank MW, Subramanian C, Saenkham P and Rock CO, *Metabolic basis for the differential susceptibility of Gram-positive pathogens to fatty acid synthesis inhibitors*. Proc Natl Acad Sci U S A, 2011. **108**(37): p. 15378-83.
97. Balemans W, Lounis N, Gilissen R, Guillemont J, Simmen K, Andries K and Koul A, *Essentiality of FASII pathway for Staphylococcus aureus*. Nature, 2010. **463**(7279): p. E3; discussion E4.
98. Singh VK, Hattangady DS, Giotis ES, Singh AK, Chamberlain NR, Stuart MK and Wilkinson BJ, *Insertional inactivation of branched-chain alpha-keto acid dehydrogenase in Staphylococcus aureus leads to decreased branched-chain membrane fatty acid content and increased susceptibility to certain stresses*. Appl Environ Microbiol, 2008. **74**(19): p. 5882-90.
99. Holman RT, Adams CE, Nelson RA, Grater SJ, Jaskiewicz JA, Johnson SB and Erdman JW, Jr., *Patients with anorexia nervosa demonstrate deficiencies of selected essential fatty acids, compensatory changes in nonessential fatty acids and decreased fluidity of plasma lipids*. J Nutr, 1995. **125**(4): p. 901-7.
100. Parsons JB and Rock CO, *Is bacterial fatty acid synthesis a valid target for antibacterial drug discovery?* Curr Opin Microbiol, 2011. **14**(5): p. 544-9.
101. Raetz CR, Reynolds CM, Trent MS and Bishop RE, *Lipid A modification systems in gram-negative bacteria*. Annu Rev Biochem, 2007. **76**: p. 295-329.
102. Maier T, Leibundgut M and Ban N, *The crystal structure of a mammalian fatty acid synthase*. Science, 2008. **321**(5894): p. 1315-22.
103. Bunkoczi G, Pasta S, Joshi A, Wu X, Kavanagh KL, Smith S and Oppermann U, *Mechanism and substrate recognition of human holo ACP synthase*. Chem Biol, 2007. **14**(11): p. 1243-53.
104. Palmer AC and Kishony R, *Opposing effects of target overexpression reveal drug mechanisms*. 2014. **5**: p. 4296.
105. Siritapetawee J, Prinz H, Krittanai C and Suginta W, *Expression and refolding of Omp38 from Burkholderia pseudomallei and Burkholderia thailandensis, and its function as a diffusion porin*. Biochem J, 2004. **384**(Pt 3): p. 609-17.
106. Schweizer HP, *Mechanisms of antibiotic resistance in Burkholderia pseudomallei: implications for treatment of melioidosis*. Future Microbiol, 2012. **7**(12): p. 1389-99.
107. Hartkoorn RC, Uplekar S and Cole ST, *Cross-resistance between clofazimine and bedaquiline through upregulation of MmpL5 in Mycobacterium tuberculosis*. Antimicrob Agents Chemother, 2014. **58**(5): p. 2979-81.
108. Floyd JL, Smith KP, Kumar SH, Floyd JT and Varela MF, *LmrS is a multidrug efflux pump of the major facilitator superfamily from Staphylococcus aureus*. Antimicrob Agents Chemother, 2010. **54**(12): p. 5406-12.

109. Katayama Y, Ito T and Hiramatsu K, *A new class of genetic element, staphylococcus cassette chromosome mec, encodes methicillin resistance in Staphylococcus aureus*. *Antimicrob Agents Chemother*, 2000. **44**(6): p. 1549-55.
110. Mishra NN, Yang SJ, Chen L, Muller C, Saleh-Mghir A, Kuhn S, Peschel A, Yeaman MR, Nast CC, Kreiswirth BN, Crémieux AC and Bayer AS, *Emergence of Daptomycin Resistance in Daptomycin-Naïve Rabbits with Methicillin-Resistant Staphylococcus aureus Prosthetic Joint Infection Is Associated with Resistance to Host Defense Cationic Peptides and mprF Polymorphisms*. *PLoS One*, 2013. **8**(8).
111. Rahman A, Srivastava SS, Sneh A, Ahmed N and Krishnasastri MV, *Molecular characterization of tlyA gene product, Rv1694 of Mycobacterium tuberculosis: a non-conventional hemolysin and a ribosomal RNA methyl transferase*. *BMC Biochem*, 2010. **11**: p. 35.
112. Maus CE, Plikaytis BB and Shinnick TM, *Mutation of tlyA Confers Capreomycin Resistance in Mycobacterium tuberculosis*. *Antimicrob Agents Chemother*, 2005. **49**(2): p. 571-7.
113. Abraham EP and Chain E, *An enzyme from bacteria able to destroy penicillin*. *Nature*, 1940. **146**: p. 837.
114. Thompson PR, Hughes DW and Wright GD, *Regiospecificity of aminoglycoside phosphotransferase from Enterococci and Staphylococci (APH(3')-IIIa)*. *Biochemistry*, 1996. **35**(26): p. 8686-95.
115. Vetting MW, Hegde SS, Javid-Majid F, Blanchard JS and Roderick SL, *Aminoglycoside 2'-N-acetyltransferase from Mycobacterium tuberculosis in complex with coenzyme A and aminoglycoside substrates*. *Nat Struct Biol*, 2002. **9**(9): p. 653-8.
116. Baldock C, Rafferty JB, Sedelnikova SE, Baker PJ, Stuitje AR, Slabas AR, Hawkes TR and Rice DW, *A mechanism of drug action revealed by structural studies of enoyl reductase*. *Science*, 1996. **274**(5295): p. 2107-10.
117. Baldock C, de Boer GJ, Rafferty JB, Stuitje AR and Rice DW, *Mechanism of action of diazaborines*. *Biochem Pharmacol*, 1998. **55**(10): p. 1541-9.
118. Hogenauer G and Woisetschlager M, *A diazaborine derivative inhibits lipopolysaccharide biosynthesis*. *Nature*, 1981. **293**(5834): p. 662-4.
119. Zhang Y, Heym B, Allen B, Young D and Cole S, *The catalase-peroxidase gene and isoniazid resistance of Mycobacterium tuberculosis*. *Nature*, 1992. **358**(6387): p. 591-3.
120. Rozwarski DA, Grant GA, Barton DH, Jacobs WR, Jr. and Sacchettini JC, *Modification of the NADH of the isoniazid target (InhA) from Mycobacterium tuberculosis*. *Science*, 1998. **279**(5347): p. 98-102.
121. Ward WH, Holdgate GA, Rowsell S, McLean EG, Pauptit RA, Clayton E, Nichols WW, Colls JG, Minshull CA, Jude DA, Mistry A, Timms D, Camble R, Hales NJ, Britton CJ and Taylor IW, *Kinetic and structural characteristics of the inhibition of enoyl (acyl carrier protein) reductase by triclosan*. *Biochemistry*, 1999. **38**(38): p. 12514-25.
122. Stewart MJ, Parikh S, Xiao G, Tonge PJ and Kisker C, *Structural basis and mechanism of enoyl reductase inhibition by triclosan*. *J Mol Biol*, 1999. **290**(4): p. 859-65.
123. Parikh SL, Xiao G and Tonge PJ, *Inhibition of InhA, the enoyl reductase from Mycobacterium tuberculosis, by triclosan and isoniazid*. *Biochemistry*, 2000. **39**(26): p. 7645-50.
124. Sullivan TJ, Truglio JJ, Boyne ME, Novichenok P, Zhang X, Stratton CF, Li HJ, Kaur T, Amin A, Johnson F, Slayden RA, Kisker C and Tonge PJ, *High affinity InhA inhibitors with activity against drug-resistant strains of Mycobacterium tuberculosis*. *ACS Chem Biol*, 2006. **1**(1): p. 43-53.
125. Gerusz V, Denis A, Faivre F, Bonvin Y, Oxoby M, Briet S, LeFralliec G, Oliveira C, Desroy N, Raymond C, Peltier L, Moreau F, Escaich S, Vongsouthi V, Floquet S, Drocourt E, Walton A, Prouvensier L, Saccomani M, Durant L, Genevard JM, Sam-Sambo V and Soulama-Mouze C, *From triclosan toward the clinic: discovery of nonbiocidal, potent FabI inhibitors for the treatment of resistant bacteria*. *J Med Chem*, 2012. **55**(22): p. 9914-28.
126. England K, am Ende C, Lu H, Sullivan TJ, Marlenee NL, Bowen RA, Knudson SE, Knudson DL, Tonge PJ and Slayden RA, *Substituted diphenyl ethers as a broad-spectrum platform for the*

- development of chemotherapeutics for the treatment of tularaemia*. J Antimicrob Chemother, 2009. **64**(5): p. 1052-61.
127. Freundlich JS, Wang F, Vilcheze C, Gulten G, Langley R, Schiehser GA, Jacobus DP, Jacobs WR, Jr. and Sacchettini JC, *Triclosan derivatives: towards potent inhibitors of drug-sensitive and drug-resistant Mycobacterium tuberculosis*. ChemMedChem, 2009. **4**(2): p. 241-8.
128. Yum JH, Kim CK, Yong D, Lee K, Chong Y, Kim CM, Kim JM, Ro S and Cho JM, *In vitro activities of CG400549, a novel FabI inhibitor, against recently isolated clinical staphylococcal strains in Korea*. Antimicrob Agents Chemother, 2007. **51**(7): p. 2591-3.
129. Kitagawa H, Kumura K, Takahata S, Iida M and Atsumi K, *4-Pyridone derivatives as new inhibitors of bacterial enoyl-ACP reductase FabI*. Bioorg Med Chem, 2007. **15**(2): p. 1106-16.
130. Schiebel J, Chang A, Shah S, Lu Y, Liu L, Pan P, Hirschbeck MW, Tareilus M, Eltschkner S, Yu W, Cummings JE, Knudson SE, Bommineni GR, Walker SG, Slayden RA, Sotriffer CA, Tonge PJ and Kisker C, *Rational design of broad spectrum antibacterial activity based on a clinically relevant enoyl-acyl carrier protein (ACP) reductase inhibitor*. J Biol Chem, 2014. **289**(23): p. 15987-6005.
131. Li MZ and Elledge SJ, *Harnessing homologous recombination in vitro to generate recombinant DNA via SLIC*. Nat Methods, 2007. **4**(3): p. 251-6.
132. Ho SN, Hunt HD, Horton RM, Pullen JK and Pease LR, *Site-directed mutagenesis by overlap extension using the polymerase chain reaction*. Gene, 1989. **77**(1): p. 51-9.
133. Horton RM, Hunt HD, Ho SN, Pullen JK and Pease LR, *Engineering hybrid genes without the use of restriction enzymes: gene splicing by overlap extension*. Gene, 1989. **77**(1): p. 61-8.
134. Post-Beittenmiller D, Jaworski JG and Ohlrogge JB, *In vivo pools of free and acylated acyl carrier proteins in spinach. Evidence for sites of regulation of fatty acid biosynthesis*. J Biol Chem, 1991. **266**(3): p. 1858-65.
135. van der Linden P, Dobias F, Vitoux H, Kapp U, Jacobs J, Mc Sweeney S, Mueller-Dieckmann C and Carpentier P, *Towards a high-throughput system for high-pressure cooling of cryoprotectant-free biological crystals*. Journal of Applied Crystallography, 2014. **47**(2): p. 584-592.
136. Xu H, Sullivan TJ, Sekiguchi J, Kirikae T, Ojima I, Stratton CF, Mao W, Rock FL, Alley MR, Johnson F, Walker SG and Tonge PJ, *Mechanism and inhibition of saFabI, the enoyl reductase from Staphylococcus aureus*. Biochemistry, 2008. **47**(14): p. 4228-36.
137. Priyadarshi A, Kim EE and Hwang KY, *Structural insights into Staphylococcus aureus enoyl-ACP reductase (FabI), in complex with NADP and triclosan*. Proteins, 2010. **78**(2): p. 480-6.
138. Kalnine NN and Schachman HK, *Quantitative urea gradient gel electrophoresis for studies of dissociation and unfolding of oligomeric proteins*. Biophys Chem, 2002. **101-102**: p. 133-44.
139. Chang A, Schiebel J, Yu W, Bommineni GR, Pan P, Baxter MV, Khanna A, Sotriffer CA, Kisker C and Tonge PJ, *Rational optimization of drug-target residence time: insights from inhibitor binding to the Staphylococcus aureus FabI enzyme-product complex*. Biochemistry, 2013. **52**(24): p. 4217-28.
140. Wuthiekanun V and Peacock SJ, *Management of melioidosis*. Expert Rev Anti Infect Ther, 2006. **4**(3): p. 445-55.
141. Rotz LD, Khan AS, Lillibridge SR, Ostroff SM and Hughes JM, *Public health assessment of potential biological terrorism agents*. Emerg Infect Dis, 2002. **8**(2): p. 225-30.
142. Campbell JW and Cronan JE, Jr., *Bacterial fatty acid biosynthesis: targets for antibacterial drug discovery*. Annu Rev Microbiol, 2001. **55**: p. 305-32.
143. Banerjee A, Dubnau E, Quemard A, Balasubramanian V, Um KS, Wilson T, Collins D, de Lisle G and Jacobs WR, Jr., *inhA, a gene encoding a target for isoniazid and ethionamide in Mycobacterium tuberculosis*. Science, 1994. **263**(5144): p. 227-30.
144. Zhang YM, White SW and Rock CO, *Inhibiting bacterial fatty acid synthesis*. J Biol Chem, 2006. **281**(26): p. 17541-4.
145. Cummings JE, Beaupre AJ, Knudson SE, Liu N, Yu W, Neckles C, Wang H, Khanna A, Bommineni GR, Trunck LA, Schweizer HP, Tonge PJ and Slayden RA, *Substituted diphenyl ethers as a novel*

- chemotherapeutic platform against Burkholderia pseudomallei*. Antimicrob Agents Chemother, 2014. **58**(3): p. 1646-51.
146. Escaich S, Prouvensier L, Saccomani M, Durant L, Oxoby M, Gerusz V, Moreau F, Vongsouthi V, Maher K, Morrissey I and Soulama-Mouze C, *The MUTO56399 inhibitor of FabI is a new antistaphylococcal compound*. Antimicrob Agents Chemother, 2011. **55**(10): p. 4692-7.
147. Heath RJ, Rubin JR, Holland DR, Zhang E, Snow ME and Rock CO, *Mechanism of triclosan inhibition of bacterial fatty acid synthesis*. J Biol Chem, 1999. **274**(16): p. 11110-4.
148. Sivaraman S, Sullivan TJ, Johnson F, Novichenok P, Cui G, Simmerling C and Tonge PJ, *Inhibition of the bacterial enoyl reductase FabI by triclosan: a structure-reactivity analysis of FabI inhibition by triclosan analogues*. J Med Chem, 2004. **47**(3): p. 509-18.
149. Lai CT, Lic HJ, Yu W, Shah S, Bommineni GR, Perrone V, Garcia-Diaz M, Tonge PJ and Simmerling C, *Rational modulation of the induced-fit conformational change for slow-onset inhibition in M. tuberculosis InhA*. Biochemistry, 2015. **54**(30): p. 4683-91.
150. Lu H and Tonge PJ, *Drug-target residence time: critical information for lead optimization*. Curr Opin Chem Biol, 2010. **14**(4): p. 467-74.
151. Yu W, Neckles C, Chang A, Bommineni GR, Spagnuolo L, Zhang Z, Liu N, Lai C, Truglio J and Tonge PJ, *A [(32)P]NAD(+)-based method to identify and quantitate long residence time enoyl-acyl carrier protein reductase inhibitors*. Anal Biochem, 2015. **474**: p. 40-9.
152. de Sanctis D, Beteva A, Caserotto H, Dobias F, Gabadinho J, Giraud T, Gobbo A, Guijarro M, Lentini M, Lavault B, Mairs T, McSweeney S, Petitdemange S, Rey-Bakaikoa V, Surr J, Theveneau P, Leonard GA and Mueller-Dieckmann C, *ID29: a high-intensity highly automated ESRF beamline for macromolecular crystallography experiments exploiting anomalous scattering*. J Synchrotron Radiat, 2012. **19**(Pt 3): p. 455-61.
153. Mueller U, Darowski N, Fuchs MR, Forster R, Hellmig M, Paithankar KS, Puhlinger S, Steffien M, Zocher G and Weiss MS, *Facilities for macromolecular crystallography at the Helmholtz-Zentrum Berlin*. J Synchrotron Radiat, 2012. **19**(Pt 3): p. 442-9.
154. Kabsch W, *XDS*. Acta Crystallogr D Biol Crystallogr, 2010. **66**(Pt 2): p. 125-32.
155. Leslie AGW, *Recent changes to the MOSFLM package for processing film and image plate data*. 1992.
156. *The CCP4 suite: programs for protein crystallography*. Acta Crystallogr D Biol Crystallogr, 1994. **50**(Pt 5): p. 760-3.
157. Evans P, *Scaling and assessment of data quality*. Acta Crystallogr D Biol Crystallogr, 2006. **62**(Pt 1): p. 72-82.
158. Evans PR and Murshudov GN, *How good are my data and what is the resolution?* Acta Crystallogr D Biol Crystallogr, 2013. **69**(Pt 7): p. 1204-14.
159. McCoy AJ, Grosse-Kunstleve RW, Adams PD, Winn MD, Storoni LC and Read RJ, *Phaser crystallographic software*. J Appl Crystallogr, 2007. **40**(Pt 4): p. 658-674.
160. Emsley P and Cowtan K, *Coot: model-building tools for molecular graphics*. Acta Crystallogr D Biol Crystallogr, 2004. **60**(Pt 12 Pt 1): p. 2126-32.
161. Murshudov GN, Skubak P, Lebedev AA, Pannu NS, Steiner RA, Nicholls RA, Winn MD, Long F and Vagin AA, *REFMAC5 for the refinement of macromolecular crystal structures*. Acta Crystallogr D Biol Crystallogr, 2011. **67**(Pt 4): p. 355-67.
162. Adams PD, Afonine PV, Bunkoczi G, Chen VB, Davis IW, Echols N, Headd JJ, Hung LW, Kapral GJ, Grosse-Kunstleve RW, McCoy AJ, Moriarty NW, Oeffner R, Read RJ, Richardson DC, Richardson JS, Terwilliger TC and Zwart PH, *PHENIX: a comprehensive Python-based system for macromolecular structure solution*. Acta Crystallogr D Biol Crystallogr, 2010. **66**(Pt 2): p. 213-21.
163. Afonine PV, Grosse-Kunstleve RW, Echols N, Headd JJ, Moriarty NW, Mustyakimov M, Terwilliger TC, Urzhumtsev A, Zwart PH and Adams PD, *Towards automated crystallographic structure refinement with phenix.refine*. Acta Crystallogr D Biol Crystallogr, 2012. **68**(Pt 4): p. 352-67.

164. Schrödinger L, *The PyMOL Molecular Graphics System, version 1.8 ed.* 2015.
165. Pan P, Knudson SE, Bommineni GR, Li HJ, Lai CT, Liu N, Garcia-Diaz M, Simmerling C, Patil SS, Slayden RA and Tonge PJ, *Time-dependent diaryl ether inhibitors of InhA: structure-activity relationship studies of enzyme inhibition, antibacterial activity, and in vivo efficacy.* ChemMedChem, 2014. **9**(4): p. 776-91.
166. am Ende CW, Knudson SE, Liu N, Childs J, Sullivan TJ, Boyne M, Xu H, Gegina Y, Knudson DL, Johnson F, Peloquin CA, Slayden RA and Tonge PJ, *Synthesis and in vitro antimycobacterial activity of B-ring modified diaryl ether InhA inhibitors.* Bioorg Med Chem Lett, 2008. **18**(10): p. 3029-33.
167. Kapoor M, Reddy CC, Krishnasastry MV, Surolia N and Surolia A, *Slow-tight-binding inhibition of enoyl-acyl carrier protein reductase from Plasmodium falciparum by triclosan.* Biochem J, 2004. **381**(Pt 3): p. 719-24.
168. Morrison JF and Walsh CT, *Slow and Tight Inhibition*, in *Enzyme Kinetics and Mechanisms*, K.B. Taylor, Editor. 2002, Springer Netherlands: Dordrecht. p. 122-146.
169. Mima T and Schweizer HP, *The BpeAB-OprB efflux pump of Burkholderia pseudomallei 1026b does not play a role in quorum sensing, virulence factor production, or extrusion of aminoglycosides but is a broad-spectrum drug efflux system.* Antimicrob Agents Chemother, 2010. **54**(8): p. 3113-20.
170. Knudson SE, Cummings JE, Bommineni GR, Pan P, Tonge PJ and Slayden RA, *Formulation studies of InhA inhibitors and combination therapy to improve efficacy against Mycobacterium tuberculosis.* Tuberculosis (Edinb), 2016. **101**: p. 8-14.
171. Heath RJ, Yu YT, Shapiro MA, Olson E and Rock CO, *Broad spectrum antimicrobial biocides target the FabI component of fatty acid synthesis.* J Biol Chem, 1998. **273**(46): p. 30316-20.
172. Sivaraman S, Zwahlen J, Bell AF, Hedstrom L and Tonge PJ, *Structure-activity studies of the inhibition of FabI, the enoyl reductase from Escherichia coli, by triclosan: kinetic analysis of mutant FabIs.* Biochemistry, 2003. **42**(15): p. 4406-13.
173. Chhibber M, Kumar G, Parasuraman P, Ramya TN, Surolia N and Surolia A, *Novel diphenyl ethers: design, docking studies, synthesis and inhibition of enoyl ACP reductase of Plasmodium falciparum and Escherichia coli.* Bioorg Med Chem, 2006. **14**(23): p. 8086-98.
174. Sun S, Canning CB, Bhargava K, Sun X, Zhu W, Zhou N, Zhang Y and Zhou K, *Polybrominated diphenyl ethers with potent and broad spectrum antimicrobial activity from the marine sponge Dysidea.* Bioorg Med Chem Lett, 2015. **25**(10): p. 2181-3.
175. Kamsri P, Koochatammakun N, Srisupan A, Meewong P, Punkvang A, Saparpakorn P, Hannongbua S, Wolschann P, Prueksaaron S, Leartsakulpanich U and Pungpo P, *Rational design of InhA inhibitors in the class of diphenyl ether derivatives as potential anti-tubercular agents using molecular dynamics simulations.* SAR QSAR Environ Res, 2014. **25**(6): p. 473-88.
176. Copeland RA, *Evaluation of enzyme inhibitors in drug discovery. A guide for medicinal chemists and pharmacologists.* Methods Biochem Anal, 2005. **46**: p. 1-265.
177. Copeland RA, *Conformational adaptation in drug-target interactions and residence time.* Future Med Chem, 2011. **3**(12): p. 1491-501.
178. Tummino PJ and Copeland RA, *Residence time of receptor-ligand complexes and its effect on biological function.* Biochemistry, 2008. **47**(20): p. 5481-92.
179. Li HJ, Lai CT, Pan P, Yu W, Liu N, Bommineni GR, Garcia-Diaz M, Simmerling C and Tonge PJ, *A structural and energetic model for the slow-onset inhibition of the Mycobacterium tuberculosis enoyl-ACP reductase InhA.* ACS Chem Biol, 2014. **9**(4): p. 986-93.
180. Schoop A and Dey F, *On-rate based optimization of structure-kinetic relationship--surfing the kinetic map.* Drug Discov Today Technol, 2015. **17**: p. 9-15.
181. Mehboob S, Truong K, Santarsiero BD and Johnson ME, *Structure of the Francisella tularensis enoyl-acyl carrier protein reductase (FabI) in complex with NAD(+) and triclosan.* Acta Crystallogr Sect F Struct Biol Cryst Commun, 2010. **66**(Pt 11): p. 1436-40.

182. Lu H, England K, am Ende C, Truglio JJ, Luckner S, Reddy BG, Marlenee NL, Knudson SE, Knudson DL, Bowen RA, Kisker C, Slayden RA and Tonge PJ, *Slow-onset inhibition of the FabI enoyl reductase from francisella tularensis: residence time and in vivo activity*. ACS Chem Biol, 2009. **4**(3): p. 221-31.
183. Maity K, Banerjee T, Prabakaran N, Surolia N, Surolia A and Suguna K, *Effect of substrate binding loop mutations on the structure, kinetics, and inhibition of enoyl acyl carrier protein reductase from Plasmodium falciparum*. IUBMB Life, 2011. **63**(1): p. 30-41.
184. Copeland RA, Pompliano DL and Meek TD, *Drug-target residence time and its implications for lead optimization*. Nat Rev Drug Discov, 2006. **5**(9): p. 730-9.
185. Zhang R and Monsma F, *The importance of drug-target residence time*. Curr Opin Drug Discov Devel, 2009. **12**(4): p. 488-96.
186. Markgren PO, Schaal W, Hamalainen M, Karlen A, Hallberg A, Samuelsson B and Danielson UH, *Relationships between structure and interaction kinetics for HIV-1 protease inhibitors*. J Med Chem, 2002. **45**(25): p. 5430-9.
187. Walkup GK, You Z, Ross PL, Allen EK, Daryae F, Hale MR, O'Donnell J, Ehmann DE, Schuck VJ, Buurman ET, Choy AL, Hajec L, Murphy-Benenato K, Marone V, Patey SA, Grosser LA, Johnstone M, Walker SG, Tonge PJ and Fisher SL, *Translating slow-binding inhibition kinetics into cellular and in vivo effects*. Nat Chem Biol, 2015. **11**(6): p. 416-23.
188. Kees KL, Musser JH, Chang J, Skowronek M and Lewis AJ, *Synthesis and antiallergic activity of a novel series of 5-lipoxygenase inhibitors*. J Med Chem, 1986. **29**(11): p. 2329-34.
189. Maiti D and Buchwald SL, *Cu-catalyzed arylation of phenols: synthesis of sterically hindered and heteroaryl diaryl ethers*. J Org Chem, 2010. **75**(5): p. 1791-4.
190. Karlowsky JA, Kaplan N, Hafkin B, Hoban DJ and Zhanel GG, *AFN-1252, a FabI inhibitor, demonstrates a Staphylococcus-specific spectrum of activity*. Antimicrob Agents Chemother, 2009. **53**(8): p. 3544-8.
191. Hafkin B, Kaplan N and Murphy B, *Efficacy and Safety of AFN-1252, the First Staphylococcus-Specific Antibacterial Agent, in the Treatment of Acute Bacterial Skin and Skin Structure Infections, Including Those in Patients with Significant Comorbidities*. Antimicrob Agents Chemother, 2015. **60**(3): p. 1695-701.
192. Rao KN, Lakshminarasimhan A, Joseph S, Lekshmi SU, Lau MS, Takhi M, Sreenivas K, Nathan S, Yusof R, Abd Rahman N, Ramachandra M, Antony T and Subramanya H, *AFN-1252 is a potent inhibitor of enoyl-ACP reductase from Burkholderia pseudomallei--Crystal structure, mode of action, and biological activity*. Protein Sci, 2015. **24**(5): p. 832-40.
193. Copeland RA, *The drug-target residence time model: a 10-year retrospective*. Nat Rev Drug Discov, 2016. **15**(2): p. 87-95.
194. Cusack KP, Wang Y, Hoemann MZ, Marjanovic J, Heym RG and Vasudevan A, *Design strategies to address kinetics of drug binding and residence time*. Bioorg Med Chem Lett, 2015. **25**(10): p. 2019-27.
195. Lewin A and Sharbati-Tehrani S, *[Slow growth rate of mycobacteria. Possible reasons and significance for their pathogenicity]*. Bundesgesundheitsblatt Gesundheitsforschung Gesundheitsschutz, 2005. **48**(12): p. 1390-9.
196. Chieng S, Carreto L and Nathan S, *Burkholderia pseudomallei transcriptional adaptation in macrophages*. BMC Genomics, 2012. **13**: p. 328.
197. Domingue G, Costerton JW and Brown MR, *Bacterial doubling time modulates the effects of opsonisation and available iron upon interactions between Staphylococcus aureus and human neutrophils*. FEMS Immunol Med Microbiol, 1996. **16**(3-4): p. 223-8.
198. Pan P and Tonge PJ, *Targeting InhA, the FASII enoyl-ACP reductase: SAR studies on novel inhibitor scaffolds*. Curr Top Med Chem, 2012. **12**(7): p. 672-93.
199. Bundtzen RW, Gerber AU, Cohn DL and Craig WA, *Postantibiotic suppression of bacterial growth*. Rev Infect Dis, 1981. **3**(1): p. 28-37.

200. Vauquelin G, *Rebinding: or why drugs may act longer in vivo than expected from their in vitro target residence time*. *Expert Opin Drug Discov*, 2010. **5**(10): p. 927-41.
201. Vauquelin G and Charlton SJ, *Long-lasting target binding and rebinding as mechanisms to prolong in vivo drug action*. *Br J Pharmacol*, 2010. **161**(3): p. 488-508.
202. Marrakchi H, Laneelle G and Quemard A, *InhA, a target of the antituberculous drug isoniazid, is involved in a mycobacterial fatty acid elongation system, FAS-II*. *Microbiology*, 2000. **146 (Pt 2)**: p. 289-96.
203. Yao J and Rock CO, *Exogenous fatty acid metabolism in bacteria*. *Biochimie*, 2017.

7 Appendix

7.1 Abbreviations

(a)SEC	(analytical) Size-exclusion chromatography
ACC	Acetyl-CoA carboxylase
ACP (AcpM)	Acyl-carrier protein (of <i>Mycobacterium tuberculosis</i>)
AcpS	ACP synthase
Ala (A)	Alanine
Arg (R)	Arginine
ASL	Active-site loop
Asn (N)	Asparagine
Asp (D)	Aspartate
BCA	Bicinchoninic acid
BCFA	Branched-chain fatty acid
BESSY	Berliner Elektronenspeicherring-Gesellschaft für Synchrotronstrahlung
BM(PEG)₂	Bis-(maleimido)-diethylene glycol
BMB	Bis-(maleimido)-butane
BMH	Bis-(maleimido)-hexane
BMOE	Bis-(maleimido)-ethane
CFU	Colony-forming units
CoA	Coenzyme A
CSGE	Conformation-sensitive gel electrophoresis
Cys (C)	Cysteine
DESY	Deutsches Elektronen-Synchrotron
DNA	Deoxyribonucleic acid
DPE	Diphenyl ether
EMBL	European Molecular Biology Laboratory
ENR	Enoyl-ACP Reductase
ESRF	European Synchrotron Radiation Facility
FA	Fatty acid
FabA/FabZ (HadAB/BC)	β -hydroxyacyl-ACP dehydratase (of <i>Mycobacterium tuberculosis</i>)
FabB/FabF (KasA/B)	β -ketoacyl-ACP synthase I/II (of <i>Mycobacterium tuberculosis</i>)
FabD	Malonyl-CoA:ACP transacylase

FabG (MabA)	β -ketoacyl-ACP reductase (of <i>Mycobacterium tuberculosis</i>)
FabH	β -ketoacyl-ACP synthase III
FabI (InhA)	Enoyl-ACP reductase (of <i>Mycobacterium tuberculosis</i>)
FAS	Fatty-acid synthesis
FQ	Fluoroquinolone
Gln (Q)	Glutamine
Glu (E)	Glutamate
Gly (G)	Glycine
HD-N-	Hexadienyl-N-
His (H)	Histidine
Ile (I)	Isoleucine
INH	Isonicotinylhydrazide
Leu (L)	Leucine
Lys (K)	Lysine
MA	Mycolic acid
Met (M)	Methionine
mFAS	Mammalian fatty-acid synthase
MRSA (CA-/HA-)	Methicillin-resistant <i>Staphylococcus aureus</i> (community-acquired/ hospital-acquired)
NAD(P)	Nicotinamide adenine dinucleotide (phosphate)
OD₆₀₀	Optical Density at 600 nm
PAE	Post-antibiotic effect
PBP	Penicillin-binding protein
PCR	Polymerase chain reaction
Phe (F)	Phenylalanine
PKS	Polyketide synthase
Pro (P)	Proline
RMP	Rifampicin
RNS	Reactive nitrogen species
rRNA	Ribosomal ribonucleic acid
SBL	Substrate-binding loop
SCFA	Straight-chain fatty acid
SDR	Short-chain dehydrogenase reductase
SDS-PAGE	Sodium dodecyl sulfate polyacrylamide gel electrophoresis

Ser (S)	Serine
sfp	Surfactin biosynthesis-related protein
SKR	Structure-kinetic relationship
TB (MDR-/RR-/XDR)	Tuberculosis (multidrug-resistant/ rifampicin-resistant/ extensively drug-resistant)
TCL	Triclosan
Thr (T)	Threonine
t_R	Residence time
Trp (W)	Tryptophan
Tyr (Y)	Tyrosine
UFA	Unsaturated fatty acid
Val (V)	Valine
VRE	Vancomycin-resistant enterococcus
WHO	World Health Organisation

7.2 Screen compositions

BMOE-BMB FINESCREEN

Well	Composition		
A1	10% tacsimate pH 7.0	0.1 M sodium cacodylate pH 6.5	27% PEG 4000
A2	15% tacsimate pH 7.0	0.1 M sodium cacodylate pH 6.5	27% PEG 4000
A3	20% tacsimate pH 7.0	0.1 M sodium cacodylate pH 6.5	27% PEG 4000
A4	25% tacsimate pH 7.0	0.1 M sodium cacodylate pH 6.5	24% PEG 4000
A5	30% tacsimate pH 7.0	0.1 M sodium cacodylate pH 6.5	20% PEG 4000
A6	15% tacsimate pH 7.0	0.05 M sodium cacodylate pH 6.5	27% PEG 4000
A7	15% tacsimate pH 7.0	0.1 M sodium cacodylate pH 6.5	27% PEG 4000
A8	15% tacsimate pH 7.0	0.15 M sodium cacodylate pH 6.5	27% PEG 4000
A9	15% tacsimate pH 7.0	0.2 M sodium cacodylate pH 6.5	27% PEG 4000
A10	15% tacsimate pH 7.0	0.1 M sodium cacodylate pH 6.5	10% PEG 4000
A11	15% tacsimate pH 7.0	0.1 M sodium cacodylate pH 6.5	15% PEG 4000
A12	15% tacsimate pH 7.0	0.1 M sodium cacodylate pH 6.5	20% PEG 4000
B1	15% tacsimate pH 7.0	0.1 M sodium cacodylate pH 6.5	25% PEG 4000
B2	15% tacsimate pH 7.0	0.1 M sodium cacodylate pH 6.5	30% PEG 4000
B3	10% tacsimate pH 7.0	0.1 M sodium cacodylate pH 6.5	30% PEG 4000
B4	15% tacsimate pH 7.0	0.1 M sodium cacodylate pH 6.5	25% PEG 4000
B5	20% tacsimate pH 7.0	0.1 M sodium cacodylate pH 6.5	20% PEG 4000

B6	25% tacsimate pH 7.0	0.1 M sodium cacodylate pH 6.5	15% PEG 4000
B7	30% tacsimate pH 7.0	0.1 M sodium cacodylate pH 6.5	10% PEG 4000
B8		0.1 M citric acid pH 4.0	10% PEG 6000
B9		0.1 M citric acid pH 4.0	20% PEG 6000
B10		0.1 M citric acid pH 4.0	30% PEG 6000
B11		0.1 M citric acid pH 4.0	0.8 M ammonium sulfate
B12		0.1 M citric acid pH 4.0	2M ammonium sulfate
C1		0.1 M citric acid pH 4.0	3.2 M ammonium sulfate
C2		0.1 M citric acid pH 4.0	10% PEG 3350
C3		0.1 M citric acid pH 4.0	20% PEG 3350
C4		0.1 M citric acid pH 4.0	30% PEG 3350
C5		0.1 M citric acid pH 4.0	10% PEG 4000
C6		0.1 M citric acid pH 4.0	20% PEG 4000
C7		0.1 M citric acid pH 4.0	30% PEG 4000
C8	15% tacsimate pH 7.0	0.1 M citric acid pH 4.0	10% PEG 6000
C9	15% tacsimate pH 7.0	0.1 M citric acid pH 4.0	20% PEG 6000
C10	15% tacsimate pH 7.0	0.1 M citric acid pH 4.0	30% PEG 6000
C11	10% tacsimate pH 7.0	0.1 M citric acid pH 4.0	30% PEG 6000
C12	20% tacsimate pH 7.0	0.1 M citric acid pH 4.0	20% PEG 6000
D1	30% tacsimate pH 7.0	0.1 M citric acid pH 4.0	10% PEG 6000
D2	15% tacsimate pH 7.0	0.1 M citric acid pH 4.0	0.8 M ammonium sulfate
D3	15% tacsimate pH 7.0	0.1 M citric acid pH 4.0	2 M ammonium sulfate
D4	12.5 % tacsimate pH 7.0	0.1 M citric acid pH 4.0	2.45 M ammonium sulfate
D5	10% tacsimate pH 7.0	0.1 M citric acid pH 4.0	2.6 M ammonium sulfate
D6	20% tacsimate pH 7.0	0.1 M citric acid pH 4.0	2 M ammonium sulfate
D7	30% tacsimate pH 7.0	0.1 M citric acid pH 4.0	0.8 M ammonium sulfate
D8	15% tacsimate pH 7.0	0.1 M citric acid pH 4.0	10% PEG 3350
D9	15% tacsimate pH 7.0	0.1 M citric acid pH 4.0	20% PEG 3350
D10	15% tacsimate pH 7.0	0.1 M citric acid pH 4.0	30% PEG 3350
D11	10% tacsimate pH 7.0	0.1 M citric acid pH 4.0	30% PEG 3350
D12	20% tacsimate pH 7.0	0.1 M citric acid pH 4.0	20% PEG 3350
E1	30% tacsimate pH 7.0	0.1 M citric acid pH 4.0	10% PEG 3350
E2	10% tacsimate pH 7.0	0.1 M citric acid pH 4.0	30% PEG 4000
E3	20% tacsimate pH 7.0	0.1 M citric acid pH 4.0	20% PEG 4000
E4	30% tacsimate pH 7.0	0.1 M citric acid pH 4.0	10% PEG 4000
E5	15% tacsimate pH 7.0	0.1 M citric acid pH 4.0	10% PEG 4000
E6	15% tacsimate pH 7.0	0.1 M citric acid pH 4.0	20% PEG 4000

E7	15% tacsimate pH 7.0	0.1 M citric acid pH 4.0	30% PEG 4000
E8		0.1 M MES pH 6.5	0.6 M magnesium sulfate
E9		0.1 M MES pH 6.5	1 M magnesium sulfate
E10		0.1 M MES pH 6.5	1.3 M magnesium sulfate
E11		0.1 M MES pH 6.5	1.6 M magnesium sulfate
E12		0.1 M citric acid pH 4.0	10% MPD
F1		0.1 M citric acid pH 4.0	20% MPD
F2		0.1 M citric acid pH 4.0	30% MPD
F3		0.1 M citric acid pH 4.0	40% MPD
F4	0.2 M potassium acetate	0.1 M MES pH 6.0	18% PEG 4000
F5	0.4 M potassium acetate	0.1 M MES pH 6.0	18% PEG 4000
F6	0.6 M potassium acetate	0.1 M MES pH 6.0	18% PEG 4000
F7	1M potassium acetate	0.1 M MES pH 6.0	18% PEG 4000
F8	2M potassium acetate	0.1 M MES pH 6.0	18% PEG 4000
F9	0.4 M potassium acetate	0.1 M MES pH 6.0	10% PEG 4000
F10	0.4 M potassium acetate	0.1 M MES pH 6.0	20% PEG 4000
F11	0.4 M potassium acetate	0.1 M MES pH 6.0	30% PEG 4000
F12	0.2 M potassium acetate	0.1 M MES pH 6.0	35% PEG 4000
G1	0.4 M potassium acetate	0.1 M MES pH 6.0	30% PEG 4000
G2	0.6 M potassium acetate	0.1 M MES pH 6.0	25% PEG 4000
G3	1M potassium acetate	0.1 M MES pH 6.0	20% PEG 4000
G4	2M potassium acetate	0.1 M MES pH 6.0	10% PEG 4000
G5	0.2 M potassium acetate	0.1 M MES pH 6.0	18% PEG 3350
G6	0.4 M potassium acetate	0.1 M MES pH 6.0	18% PEG 3350
G7	0.6 M potassium acetate	0.1 M MES pH 6.0	18% PEG 3350
G8	1M potassium acetate	0.1 M MES pH 6.0	18% PEG 3350
G9	2M potassium acetate	0.1 M MES pH 6.0	18% PEG 3350
G10	0.4 M potassium acetate	0.1 M MES pH 6.5	0.6 M magnesium sulfate
G11	0.4 M potassium acetate	0.1 M MES pH 6.5	1M magnesium sulfate
G12	0.4 M potassium acetate	0.1 M MES pH 6.5	1.4 M magnesium sulfate
H1	0.8 M potassium acetate	0.1 M MES pH 6.5	1.2 M magnesium sulfate
H2	0.2 M potassium acetate	0.1 M MES pH 6.0	30% MPD
H3	0.8 M potassium acetate	0.1 M MES pH 6.0	25% MPD
H4	1.2 M potassium acetate	0.1 M MES pH 6.0	20% MPD
H5	2.4 M potassium acetate	0.1 M MES pH 6.0	10% MPD
H6	0.2 M potassium acetate	0.1 M citric acid pH 4.0	30% MPD
H7	1.4 M potassium acetate	0.1 M citric acid pH 4.0	20% MPD

H8	2.6 M potassium acetate	0.1 M citric acid pH 4.0	10% MPD
H9	0.4 M potassium acetate	0.1 M citric acid pH 4.0	10% MPD
H10	0.4 M potassium acetate	0.1 M citric acid pH 4.0	20% MPD
H11	0.4 M potassium acetate	0.1 M citric acid pH 4.0	30% MPD
H12	0.4 M potassium acetate	0.1 M citric acid pH 4.0	40% MPD

CRYSTAL POWER

Well	Composition		
A1		0.1 M Hepes pH 7.0	0.6 M Na/K tartrate
A2		0.1 M Hepes pH 7.0	0.8 M Na/K tartrate
A3		0.1 M Hepes pH 7.0	1M Na/K tartrate
A4		0.1 M Hepes pH 7.5	0.6 M Na/K tartrate
A5		0.1 M Hepes pH 7.5	0.8 M Na/K tartrate
A6		0.1 M Hepes pH 7.5	1M Na/K tartrate
A7		0.1 M Hepes pH 8.0	0.6 M Na/K tartrate
A8		0.1 M Hepes pH 8.0	0.8 M Na/K tartrate
A9	0.0018M magnesium chloride 0.00225 M spermine	0.05 M sodium cacodylate pH 6.0	9% isopropanol
A10	0.0018M magnesium chloride 0.00225 M spermine	0.05 M sodium cacodylate pH 6.0	18% isopropanol
A11	0.01 M magnesium chloride 0.00225 M spermine	0.05 M sodium cacodylate pH 6.0	9% isopropanol
A12	0.01 M magnesium chloride 0.00225 M spermine	0.05 M sodium cacodylate pH 6.0	18% isopropanol
B1	0.0018M magnesium chloride 0.00225 M spermine	0.05 M sodium cacodylate pH 6.5	9% isopropanol
B2	0.0018M magnesium chloride 0.00225 M spermine	0.05 M sodium cacodylate pH 6.5	18% isopropanol
B3	0.01 M magnesium chloride 0.00225 M spermine	0.05 M sodium cacodylate pH 6.5	9% isopropanol
B4	0.01 M magnesium chloride 0.00225 M spermine	0.05 M sodium cacodylate pH 6.5	18% isopropanol
B5	0.6 M sodium tartrate	0.1 M Tris pH 7.5	
B6	0.8 M sodium tartrate	0.1 M Tris pH 7.5	
B7	1M sodium tartrate	0.1 M Tris pH 7.5	
B8	0.6 M sodium tartrate	0.1 M Tris pH 8.0	

B9	0.8 M sodium tartrate	0.1 M Tris pH 8.0	
B10	1 M sodium tartrate	0.1 M Tris pH 8.0	
B11	0.6 M sodium tartrate	0.1 M Tris pH 8.5	
B12	0.8 M sodium tartrate	0.1 M Tris pH 8.5	8% PEG 4000
C1	0.5 M potassium thiocyanate	0.1 M Hepes pH 7.0	18% PEG 4000
C2	0.5 M potassium thiocyanate	0.1 M Hepes pH 7.0	28% PEG 4000
C3	0.5 M potassium thiocyanate	0.1 M Hepes pH 7.0	8% PEG 4000
C4	0.5 M potassium thiocyanate	0.1 M Hepes pH 7.5	18% PEG 4000
C5	0.5 M potassium thiocyanate	0.1 M Hepes pH 7.5	28% PEG 4000
C6	0.5 M potassium thiocyanate	0.1 M Hepes pH 7.5	18% PEG 4000
C7	0.5 M potassium thiocyanate	0.1 M Hepes pH 8.0	28% PEG 4000
C8	0.5 M potassium thiocyanate	0.1 M Hepes pH 8.0	0.6 M Na/K tartrate
C9		0.1 M Hepes pH 7.0	0.8 M Na/K tartrate
C10		0.1 M Hepes pH 7.0	1M Na/K tartrate
C11		0.1 M Hepes pH 7.0	0.6 M Na/K tartrate
C12		0.1 M Hepes pH 7.5	0.8 M Na/K tartrate
D1		0.1 M Hepes pH 7.5	1M Na/K tartrate
D2		0.1 M Hepes pH 7.5	0.6 M Na/K tartrate
D3		0.1 M Hepes pH 8.0	0.8 M Na/K tartrate
D4		0.1 M Hepes pH 8.0	
D5	0.0018M magnesium chloride 0.00225 M spermine	0.05 M sodium cacodylate pH 6.0	9% isopropanol
D6	0.0018M magnesium chloride 0.00225 M spermine	0.05 M sodium cacodylate pH 6.0	18% isopropanol
D7	0.01 M magnesium chloride 0.00225 M spermine	0.05 M sodium cacodylate pH 6.0	9% isopropanol
D8	0.01 M magnesium chloride 0.00225 M spermine	0.05 M sodium cacodylate pH 6.0	18% isopropanol
D9	0.0018M magnesium chloride 0.00225 M spermine	0.05 M sodium cacodylate pH 6.5	9% isopropanol
D10	0.0018M magnesium chloride 0.00225 M spermine	0.05 M sodium cacodylate pH 6.5	18% isopropanol
D11	0.01 M magnesium chloride 0.00225 M spermine	0.05 M sodium cacodylate pH 6.5	9% isopropanol
D12	0.01 M magnesium chloride 0.00225 M spermine	0.05 M sodium cacodylate pH 6.5	18% isopropanol
E1	0.6 M sodium tartrate	0.1 M Tris pH 7.5	

E2	0.8 M sodium tartrate	0.1 M Tris pH 7.5	
E3	1M sodium tartrate	0.1 M Tris pH 7.5	
E4	0.6 M sodium tartrate	0.1 M Tris pH 8.0	
E5	0.8 M sodium tartrate	0.1 M Tris pH 8.0	
E6	1M sodium tartrate	0.1 M Tris pH 8.0	
E7	0.6 M sodium tartrate	0.1 M Tris pH 8.5	
E8	0.8 M sodium tartrate	0.1 M Tris pH 8.5	8% PEG 4000
E9	0.5 M potassium thiocyanate	0.1 M Hepes pH 7.0	18% PEG 4000
E10	0.5 M potassium thiocyanate	0.1 M Hepes pH 7.0	28% PEG 4000
E11	0.5 M potassium thiocyanate	0.1 M Hepes pH 7.0	8% PEG 4000
E12	0.5 M potassium thiocyanate	0.1 M Hepes pH 7.5	18% PEG 4000
F1	0.5 M potassium thiocyanate	0.1 M Hepes pH 7.5	28% PEG 4000
F2	0.5 M potassium thiocyanate	0.1 M Hepes pH 7.5	18% PEG 4000
F3	0.5 M potassium thiocyanate	0.1 M Hepes pH 8.0	28% PEG 4000
F4	0.5 M potassium thiocyanate	0.1 M Hepes pH 8.0	0.6 M Na/K tartrate
F5		0.1 M Hepes pH 7.0	0.8 M Na/K tartrate
F6		0.1 M Hepes pH 7.0	1M Na/K tartrate
F7		0.1 M Hepes pH 7.0	0.6 M Na/K tartrate
F8		0.1 M Hepes pH 7.5	0.8 M Na/K tartrate
F9		0.1 M Hepes pH 7.5	1M Na/K tartrate
F10		0.1 M Hepes pH 7.5	0.6 M Na/K tartrate
F11		0.1 M Hepes pH 8.0	0.8 M Na/K tartrate
F12		0.1 M Hepes pH 8.0	
G1	0.0018 M magnesium chloride 0.00225 M spermine	0.05 M sodium cacodylate pH 6.0	9% isopropanol
G2	0.0018M magnesium chloride 0.00225 M spermine	0.05 M sodium cacodylate pH 6.0	18% isopropanol
G3	0.01 M magnesium chloride 0.00225 M spermine	0.05 M sodium cacodylate pH 6.0	9% isopropanol
G4	0.01 M magnesium chloride 0.00225 M spermine	0.05 M sodium cacodylate pH 6.0	18% isopropanol
G5	0.0018M magnesium chloride 0.00225 M spermine	0.05 M sodium cacodylate pH 6.5	9% isopropanol
G6	0.0018M magnesium chloride 0.00225 M spermine	0.05 M sodium cacodylate pH 6.5	18% isopropanol
G7	0.01 M magnesium chloride 0.00225 M spermine	0.05 M sodium cacodylate pH 6.5	9% isopropanol

G8	0.01 M magnesium chloride 0.00225 M spermine	0.05 M sodium cacodylate pH 6.5	18% isopropanol
G9	0.6 M sodium tartrate	0.1 M Tris pH 7.5	
G10	0.8 M sodium tartrate	0.1 M Tris pH 7.5	
G11	1 M sodium tartrate	0.1 M Tris pH 7.5	
G12	0.6 M sodium tartrate	0.1 M Tris pH 8.0	
H1	0.8 M sodium tartrate	0.1 M Tris pH 8.0	
H2	1 M sodium tartrate	0.1 M Tris pH 8.0	
H3	0.6 M sodium tartrate	0.1 M Tris pH 8.5	
H4	0.8 M sodium tartrate	0.1 M Tris pH 8.5	8% PEG 4000
H5	0.5 M potassium thiocyanate	0.1 M Hepes pH 7.0	18% PEG 4000
H6	0.5 M potassium thiocyanate	0.1 M Hepes pH 7.0	28% PEG 4000
H7	0.5 M potassium thiocyanate	0.1 M Hepes pH 7.0	8% PEG 4000
H8	0.5 M potassium thiocyanate	0.1 M Hepes pH 7.5	18% PEG 4000
H9	0.5 M potassium thiocyanate	0.1 M Hepes pH 7.5	28% PEG 4000
H10	0.5 M potassium thiocyanate	0.1 M Hepes pH 7.5	18% PEG 4000
H11	0.5 M potassium thiocyanate	0.1 M Hepes pH 8.0	28% PEG 4000
H12	0.5 M potassium thiocyanate	0.1 M Hepes pH 8.0	

CRYSTAL SHOWER

Well	Composition	
A1	0.1 M calcium chloride	20% PEG 3350
A2	0.2 M calcium chloride	20% PEG 3350
A3	0.1 M lithium nitrate	20% PEG 3350
A4	0.2 M lithium nitrate	20% PEG 3350
A5	0.1 M calcium chloride	10% PEG 8000
A6	0.2 M calcium chloride	10% PEG 8000
A7	0.1 M lithium nitrate	10% PEG 8000
A8	0.2 M lithium nitrate	10% PEG 8000
A9	0.1 M calcium chloride	20% PEG 4000
A10	0.2 M calcium chloride	20% PEG 4000
A11	0.1 M lithium nitrate	20% PEG 4000
A12	0.2 M lithium nitrate	20% PEG 4000
B1	0.1 M zinc acetate dihydrate	20% PEG 3350
B2	0.2 M zinc acetate dihydrate	20% PEG 3350
B3	0.1 M zinc acetate dihydrate	10% PEG 8000

B4	0.2 M zinc acetate dihydrate		10% PEG 8000
B5	0.1 M zinc acetate dihydrate		20% PEG 4000
B6	0.2 M zinc acetate dihydrate		20% PEG 4000
B7	0.1 M calcium chloride	0.1 M MES pH 6.0	20% PEG 3350
B8	0.2 M calcium chloride	0.1 M MES pH 6.0	20% PEG 3350
B9	0.1 M lithium nitrate	0.1 M MES pH 6.0	20% PEG 3350
B10	0.2 M lithium nitrate	0.1 M MES pH 6.0	20% PEG 3350
B11	0.1 M calcium chloride	0.1 M MES pH 6.0	10% PEG 8000
B12	0.2 M calcium chloride	0.1 M MES pH 6.0	10% PEG 8000
C1	0.1 M lithium nitrate	0.1 M MES pH 6.0	10% PEG 8000
C2	0.2 M lithium nitrate	0.1 M MES pH 6.0	10% PEG 8000
C3	0.1 M calcium chloride	0.1 M MES pH 6.0	20% PEG 4000
C4	0.2 M calcium chloride	0.1 M MES pH 6.0	20% PEG 4000
C5	0.1 M lithium nitrate	0.1 M MES pH 6.0	20% PEG 4000
C6	0.2 M lithium nitrate	0.1 M MES pH 6.0	20% PEG 4000
C7	0.1 M zinc acetate dihydrate	0.1 M MES pH 6.0	20% PEG 3350
C8	0.2 M zinc acetate dihydrate	0.1 M MES pH 6.0	20% PEG 3350
C9	0.1 M zinc acetate dihydrate	0.1 M MES pH 6.0	10% PEG 8000
C10	0.2 M zinc acetate dihydrate	0.1 M MES pH 6.0	10% PEG 8000
C11	0.1 M zinc acetate dihydrate	0.1 M MES pH 6.0	20% PEG 4000
C12	0.2 M zinc acetate dihydrate	0.1 M MES pH 6.0	20% PEG 4000
D1	0.1 M calcium chloride	0.1 M sodium acetate pH 4.5	20% PEG 3350
D2	0.2 M calcium chloride	0.1 M sodium acetate pH 4.5	20% PEG 3350
D3	0.1 M lithium nitrate	0.1 M sodium acetate pH 4.5	20% PEG 3350
D4	0.2 M lithium nitrate	0.1 M sodium acetate pH 4.5	20% PEG 3350
D5	0.1 M calcium chloride	0.1 M sodium acetate pH 4.5	10% PEG 8000
D6	0.2 M calcium chloride	0.1 M sodium acetate pH 4.5	10% PEG 8000
D7	0.1 M lithium nitrate	0.1 M sodium acetate pH 4.5	10% PEG 8000
D8	0.2 M lithium nitrate	0.1 M sodium acetate pH 4.5	10% PEG 8000
D9	0.1 M calcium chloride	0.1 M sodium acetate pH 4.5	20% PEG 4000
D10	0.2 M calcium chloride	0.1 M sodium acetate pH 4.5	20% PEG 4000
D11	0.1 M lithium nitrate	0.1 M sodium acetate pH 4.5	20% PEG 4000
D12	0.2 M lithium nitrate	0.1 M sodium acetate pH 4.5	20% PEG 4000
E1	0.1 M zinc acetate dihydrate	0.1 M sodium acetate pH 4.5	20% PEG 3350
E2	0.2 M zinc acetate dihydrate	0.1 M sodium acetate pH 4.5	20% PEG 3350
E3	0.1 M zinc acetate dihydrate	0.1 M sodium acetate pH 4.5	10% PEG 8000
E4	0.2 M zinc acetate dihydrate	0.1 M sodium acetate pH 4.5	10% PEG 8000

E5	0.1 M zinc acetate dihydrate	0.1 M sodium acetate pH 4.5	20% PEG 4000
E6	0.2 M zinc acetate dihydrate	0.1 M sodium acetate pH 4.5	20% PEG 4000
E7	0.1 M calcium chloride	0.1 M sodium citrate pH 5.6	20% PEG 3350
E8	0.2 M calcium chloride	0.1 M sodium citrate pH 5.6	20% PEG 3350
E9	0.1 M lithium nitrate	0.1 M sodium citrate pH 5.6	20% PEG 3350
E10	0.2 M lithium nitrate	0.1 M sodium citrate pH 5.6	20% PEG 3350
E11	0.1 M calcium chloride	0.1 M sodium citrate pH 5.6	10% PEG 8000
E12	0.2 M calcium chloride	0.1 M sodium citrate pH 5.6	10% PEG 8000
F1	0.1 M lithium nitrate	0.1 M sodium citrate pH 5.6	10% PEG 8000
F2	0.2 M lithium nitrate	0.1 M sodium citrate pH 5.6	10% PEG 8000
F3	0.1 M calcium chloride	0.1 M sodium citrate pH 5.6	20% PEG 4000
F4	0.2 M calcium chloride	0.1 M sodium citrate pH 5.6	20% PEG 4000
F5	0.1 M lithium nitrate	0.1 M sodium citrate pH 5.6	20% PEG 4000
F6	0.2 M lithium nitrate	0.1 M sodium citrate pH 5.6	20% PEG 4000
F7	0.1 M zinc acetate dihydrate	0.1 M sodium citrate pH 5.6	20% PEG 3350
F8	0.2 M zinc acetate dihydrate	0.1 M sodium citrate pH 5.6	20% PEG 3350
F9	0.1 M zinc acetate dihydrate	0.1 M sodium citrate pH 5.6	10% PEG 8000
F10	0.2 M zinc acetate dihydrate	0.1 M sodium citrate pH 5.6	10% PEG 8000
F11	0.1 M zinc acetate dihydrate	0.1 M sodium citrate pH 5.6	20% PEG 4000
F12	0.2 M zinc acetate dihydrate	0.1 M sodium citrate pH 5.6	20% PEG 4000
G1	0.1 M calcium acetate		20% PEG 3350
G2	0.2 M calcium acetate		20% PEG 3350
G3	0.1 M calcium acetate		10% PEG 8000
G4	0.2 M calcium acetate		10% PEG 8000
G5	0.1 M calcium acetate		20% PEG 4000
G6	0.2 M calcium acetate		20% PEG 4000
G7	0.1 M calcium acetate	0.1 M MES pH 6.0	20% PEG 3350
G8	0.2 M calcium acetate	0.1 M MES pH 6.0	20% PEG 3350
G9	0.1 M calcium acetate	0.1 M MES pH 6.0	10% PEG 8000
G10	0.2 M calcium acetate	0.1 M MES pH 6.0	10% PEG 8000
G11	0.1 M calcium acetate	0.1 M MES pH 6.0	20% PEG 4000
G12	0.2 M calcium acetate	0.1 M MES pH 6.0	20% PEG 4000
H1	0.1 M calcium acetate	0.1 M sodium acetate pH 4.5	20% PEG 3350
H2	0.2 M calcium acetate	0.1 M sodium acetate pH 4.5	20% PEG 3350
H3	0.1 M calcium acetate	0.1 M sodium acetate pH 4.5	10% PEG 8000
H4	0.2 M calcium acetate	0.1 M sodium acetate pH 4.5	10% PEG 8000
H5	0.1 M calcium acetate	0.1 M sodium acetate pH 4.5	20% PEG 4000

H6	0.2 M calcium acetate	0.1 M sodium acetate pH 4.5	20% PEG 4000
H7	0.1 M calcium acetate	0.1 M sodium citrate pH 5.6	20% PEG 3350
H8	0.2 M calcium acetate	0.1 M sodium citrate pH 5.6	20% PEG 3350
H9	0.1 M calcium acetate	0.1 M sodium citrate pH 5.6	10% PEG 8000
H10	0.2 M calcium acetate	0.1 M sodium citrate pH 5.6	10% PEG 8000
H11	0.1 M calcium acetate	0.1 M sodium citrate pH 5.6	20% PEG 4000
H12	0.2 M calcium acetate	0.1 M sodium citrate pH 5.6	20% PEG 4000

HD-N-1b FINESCREEN I

Well	Composition	
A1	0.1 M MES pH 6.0	10% PEG 3350
A2	0.1 M MES pH 6.0	20% PEG 3350
A3	0.1 M MES pH 6.0	30% PEG 3350
A4	0.1 M MES pH 6.5	10% PEG 3350
A5	0.1 M MES pH 6.5	20% PEG 3350
A6	0.1 M MES pH 6.5	30% PEG 3350
A7	0.1 M citric acid pH 4.0	10% PEG 3350
A8	0.1 M citric acid pH 4.0	20% PEG 3350
A9	0.1 M citric acid pH 4.0	30% PEG 3350
A10	0.1 M citric acid pH 5.0	10% PEG 3350
A11	0.1 M citric acid pH 5.0	20% PEG 3350
A12	0.1 M citric acid pH 5.0	30% PEG 3350
B1	0.1 M Bis-tris pH 5.5	10% PEG 3350
B2	0.1 M Bis-tris pH 5.5	20% PEG 3350
B3	0.1 M Bis-tris pH 5.5	30% PEG 3350
B4	0.1 M HEPES pH 7.5	10% PEG 3350
B5	0.1 M HEPES pH 7.5	20% PEG 3350
B6	0.1 M HEPES pH 7.5	30% PEG 3350
B7	0.1 M MES pH 6.0	20% MPD
B8	0.1 M MES pH 6.0	40% MPD
B9	0.1 M MES pH 6.0	60% MPD
B10	0.1 M MES pH 6.5	20% MPD
B11	0.1 M MES pH 6.5	40% MPD
B12	0.1 M MES pH 6.5	60% MPD
C1	0.1 M citric acid pH 4.0	20% MPD
C2	0.1 M citric acid pH 4.0	40% MPD

C3		0.1 M citric acid pH 4.0	60% MPD
C4		0.1 M citric acid pH 5.0	20% MPD
C5		0.1 M citric acid pH 5.0	40% MPD
C6		0.1 M citric acid pH 5.0	60% MPD
C7		0.1 M Bis-tris pH 5.5	20% MPD
C8		0.1 M Bis-tris pH 5.5	40% MPD
C9		0.1 M Bis-tris pH 5.5	60% MPD
C10		0.1 M Hepes pH 7.5	20% MPD
C11		0.1 M Hepes pH 7.5	40% MPD
C12		0.1 M Hepes pH 7.5	60% MPD
D1		0.1 M sodium acetate pH 4.6	10% PEG 3350
D2		0.1 M sodium acetate pH 4.6	20% PEG 3350
D3		0.1 M sodium acetate pH 4.6	30% PEG 3350
D4		0.1 M sodium acetate pH 5.5	10% PEG 3350
D5		0.1 M sodium acetate pH 5.5	20% PEG 3350
D6		0.1 M sodium acetate pH 5.5	30% PEG 3350
D7	1M sodium malonate pH 6.0	0.1 M sodium acetate pH 4.6	10% PEG 3350
D8	1M sodium malonate pH 6.0	0.1 M sodium acetate pH 4.6	20% PEG 3350
D9	1M sodium malonate pH 6.0	0.1 M sodium acetate pH 4.6	30% PEG 3350
D10	1M sodium malonate pH 6.0	0.1 M sodium acetate pH 5.5	10% PEG 3350
D11	1M sodium malonate pH 6.0	0.1 M sodium acetate pH 5.5	20% PEG 3350
D12	1M sodium malonate pH 6.0	0.1 M sodium acetate pH 5.5	30% PEG 3350
E1	1M sodium malonate pH 7.0	0.1 M sodium acetate pH 4.6	10% PEG 3350
E2	1M sodium malonate pH 7.0	0.1 M sodium acetate pH 4.6	20% PEG 3350
E3	1M sodium malonate pH 7.0	0.1 M sodium acetate pH 4.6	30% PEG 3350
E4	1M sodium malonate pH 7.0	0.1 M sodium acetate pH 5.5	10% PEG 3350
E5	1M sodium malonate pH 7.0	0.1 M sodium acetate pH 5.5	20% PEG 3350
E6	1M sodium malonate pH 7.0	0.1 M sodium acetate pH 5.5	30% PEG 3350
E7	1M sodium malonate pH 5.0	0.1 M sodium acetate pH 4.6	
E8	1M sodium malonate pH 6.0	0.1 M sodium acetate pH 4.6	
E9	1M sodium malonate pH 7.0	0.1 M sodium acetate pH 4.6	
E10	1M sodium malonate pH 5.0	0.1 M sodium acetate pH 5.5	
E11	1M sodium malonate pH 6.0	0.1 M sodium acetate pH 5.5	
E12	1M sodium malonate pH 7.0	0.1 M sodium acetate pH 5.5	
F1	0.1 M magnesium chloride	0.1 M MES pH 6.0	
F2	0.2 M magnesium chloride	0.1 M MES pH 6.0	
F3	0.1 M magnesium chloride	0.1 M MES pH 6.5	

F4	0.2 M magnesium chloride	0.1 M MES pH 6.5
F5	0.1 M magnesium chloride	0.1 M citric acid pH 4.0
F6	0.2 M magnesium chloride	0.1 M citric acid pH 4.0
F7	0.1 M magnesium chloride	0.1 M citric acid pH 5.0
F8	0.2 M magnesium chloride	0.1 M citric acid pH 5.0
F9	0.1 M magnesium chloride	0.1 M Bis-tris pH 5.5
F10	0.2 M magnesium chloride	0.1 M Bis-tris pH 5.5
F11	0.1 M magnesium chloride	0.1 M Hepes pH 7.5
F12	0.2 M magnesium chloride	0.1 M Hepes pH 7.5
G1	0.1 M magnesium chloride	0.1 M sodium acetate pH 4.6
G2	0.2 M magnesium chloride	0.1 M sodium acetate pH 4.6
G3	0.1 M magnesium chloride	0.1 M sodium acetate pH 5.5
G4	0.2 M magnesium chloride	0.1 M sodium acetate pH 5.5
G5	0.5 M ammonium chloride	0.1 M MES pH 6.0
G6	1M ammonium chloride	0.1 M MES pH 6.0
G7	0.5 M ammonium chloride	0.1 M MES pH 6.5
G8	1M ammonium chloride	0.1 M MES pH 6.5
G9	0.5 M ammonium chloride	0.1 M citric acid pH 4.0
G10	1M ammonium chloride	0.1 M citric acid pH 4.0
G11	0.5 M ammonium chloride	0.1 M citric acid pH 5.0
G12	1M ammonium chloride	0.1 M citric acid pH 5.0
H1	0.5 M ammonium chloride	0.1 M Bis-tris pH 5.5
H2	1M ammonium chloride	0.1 M Bis-tris pH 5.5
H3	0.5 M ammonium chloride	0.1 M Hepes pH 7.5
H4	1M ammonium chloride	0.1 M Hepes pH 7.5
H5	0.5 M ammonium chloride	0.1 M sodium acetate pH 4.6
H6	1M ammonium chloride	0.1 M sodium acetate pH 4.6
H7	0.5 M ammonium chloride	0.1 M sodium acetate pH 5.5
H8	1M ammonium chloride	0.1 M sodium acetate pH 5.5
H9	1.5 M ammonium sulfate	0.1 M MES pH 6.0
H10	2M ammonium sulfate	0.1 M MES pH 6.0
H11	1.5 M ammonium sulfate	0.1 M MES pH 6.5
H12	2M ammonium sulfate	0.1 M MES pH 6.5

HD-N-Ib FINESCREEN II

Well Composition

A1	1.5 M ammonium sulfate	0.1 M sodium acetate pH 4.6	
A2	2M ammonium sulfate	0.1 M sodium acetate pH 4.6	
A3	1.5 M ammonium sulfate	0.1 M sodium acetate pH 5.5	
A4	2M ammonium sulfate	0.1 M sodium acetate pH 5.5	
A5	1.3 M Na/K tartrate	0.1 M MES pH 6.0	
A6	1.8 M Na/K tartrate	0.1 M MES pH 6.0	
A7	1.3 M Na/K tartrate	0.1 M MES pH 6.5	
A8	1.8 M Na/K tartrate	0.1 M MES pH 6.5	
A9	1.3 M Na/K tartrate	0.1 M citric acid pH 4.0	
A10	1.8 M Na/K tartrate	0.1 M citric acid pH 4.0	
A11	1.3 M Na/K tartrate	0.1 M citric acid pH 5.0	
A12	1.8 M Na/K tartrate	0.1 M citric acid pH 5.0	
B1	1.3 M Na/K tartrate	0.1 M Bis-tris pH 5.5	
B2	1.8 M Na/K tartrate	0.1 M Bis-tris pH 5.5	
B3	1.3 M Na/K tartrate	0.1 M HEPES pH 7.5	
B4	1.8 M Na/K tartrate	0.1 M HEPES pH 7.5	
B5	1.3 M Na/K tartrate	0.1 M sodium acetate pH 4.6	
B6	1.8 M Na/K tartrate	0.1 M sodium acetate pH 4.6	
B7	1.3 M Na/K tartrate	0.1 M sodium acetate pH 5.5	
B8	1.8 M Na/K tartrate	0.1 M sodium acetate pH 5.5	
B9	1M sodium malonate dibasic	0.1 M MES pH 6.0	
B10	2M sodium malonate dibasic	0.1 M MES pH 6.0	
B11	1M sodium malonate dibasic	0.1 M MES pH 6.5	
B12	2M sodium malonate dibasic	0.1 M MES pH 6.5	
C1	1M sodium malonate dibasic	0.1 M citric acid pH 4.0	
C2	2M sodium malonate dibasic	0.1 M citric acid pH 4.0	
C3	1M sodium malonate dibasic	0.1 M citric acid pH 5.0	
C4	2M sodium malonate dibasic	0.1 M citric acid pH 5.0	
C5	1M sodium malonate dibasic	0.1 M Bis-tris pH 5.5	
C6	2M sodium malonate dibasic	0.1 M Bis-tris pH 5.5	
C7	1M sodium malonate dibasic	0.1 M HEPES pH 7.5	
C8	2M sodium malonate dibasic	0.1 M HEPES pH 7.5	
C9	1M sodium malonate dibasic	0.1 M sodium acetate pH 4.6	
C10	2M sodium malonate dibasic	0.1 M sodium acetate pH 4.6	
C11	1M sodium malonate dibasic	0.1 M sodium acetate pH 5.5	
C12	2M sodium malonate dibasic	0.1 M sodium acetate pH 5.5	
D1		1M K/Na phosphate pH 5.0	25 % MPD

D2	1 M K/Na phosphate pH 5.0	50 % MPD
D3	1.5 M K/Na phosphate pH 5.0	25 % MPD
D4	1.2 M K/Na phosphate pH 5.0	40 % MPD
D5	1 M K/Na phosphate pH 5.6	25 % MPD
D6	1 M K/Na phosphate pH 5.6	50 % MPD
D7	1.5 M K/Na phosphate pH 5.6	25 % MPD
D8	1.2 M K/Na phosphate pH 5.6	40 % MPD
D9	1 M K/Na phosphate pH 6.2	25 % MPD
D10	0.8 M K/Na phosphate pH 6.2	40 % MPD
D11	1 M K/Na phosphate pH 6.2	25 % MPD
D12	0.8 M K/Na phosphate pH 6.2	40 % MPD
E1	1 M K/Na phosphate pH 6.8	25 % MPD
E2	1 M K/Na phosphate pH 6.8	50 % MPD
E3	1.5 M K/Na phosphate pH 6.8	25 % MPD
E4	1.2 M K/Na phosphate pH 6.8	40 % MPD
E5	1 M K/Na phosphate pH 7.5	25 % MPD
E6	1 M K/Na phosphate pH 7.5	50 % MPD
E7	1.5 M K/Na phosphate pH 7.5	25 % MPD
E8	1.2 M K/Na phosphate pH 7.5	40 % MPD
E9	1 M K/Na phosphate pH 8.2	25 % MPD
E10	1 M K/Na phosphate pH 8.2	50 % MPD
E11	1.5 M K/Na phosphate pH 8.2	25 % MPD
E12	1.2 M K/Na phosphate pH 8.2	40 % MPD
F1	1 M K/Na phosphate pH 5.0	10 % PEG 3350
F2	1 M K/Na phosphate pH 5.0	25 % PEG 3350
F3	1.5 M K/Na phosphate pH 5.0	10 % PEG 3350
F4	1.2 M K/Na phosphate pH 5.0	20 % PEG 3350
F5	1 M K/Na phosphate pH 5.6	10 % PEG 3350
F6	1 M K/Na phosphate pH 5.6	25 % PEG 3350
F7	1.5 M K/Na phosphate pH 5.6	10 % PEG 3350
F8	1.2 M K/Na phosphate pH 5.6	20 % PEG 3350
F9	0.8 M K/Na phosphate pH 6.2	10 % PEG 3350
F10	0.8 M K/Na phosphate pH 6.2	20 % PEG 3350
F11	1 M K/Na phosphate pH 6.2	5 % PEG 3350
F12	1 M K/Na phosphate pH 6.2	12 % PEG 3350
G1	1 M K/Na phosphate pH 6.8	10 % PEG 3350
G2	1 M K/Na phosphate pH 6.8	25 % PEG 3350

G3		1.5 M K/Na phosphate pH 6.8	10% PEG 3350
G4		1.2 M K/Na phosphate pH 6.8	20% PEG 3350
G5		1 M K/Na phosphate pH 7.5	10% PEG 3350
G6		1 M K/Na phosphate pH 7.5	25% PEG 3350
G7		1.5 M K/Na phosphate pH 7.5	10% PEG 3350
G8		1.2 M K/Na phosphate pH 7.5	20% PEG 3350
G9		1 M K/Na phosphate pH 8.2	10% PEG 3350
G10		1 M K/Na phosphate pH 8.2	25% PEG 3350
G11		1.5 M K/Na phosphate pH 8.2	10% PEG 3350
G12		1.2 M K/Na phosphate pH 8.2	20% PEG 3350
H1	1 M sodium tartrate dibasic	0.1 M MES pH 6.0	
H2	1 M sodium tartrate dibasic	0.1 M MES pH 6.5	
H3	1 M sodium tartrate dibasic	0.1 M citric acid pH 4.0	
H4	1 M sodium tartrate dibasic	0.1 M citric acid pH 5.0	
H5	1 M sodium tartrate dibasic	0.1 M Bis-tris pH 5.5	
H6	1 M sodium tartrate dibasic	0.1 M Hepes pH 7.5	
H7	1 M sodium tartrate dibasic	0.1 M sodium acetate pH 4.6	
H8	1 M sodium tartrate dibasic	0.1 M sodium acetate pH 5.5	
H9	1.5 M ammonium sulfate	0.1 M citric acid pH 4.0	
H10	2 M ammonium sulfate	0.1 M citric acid pH 4.0	
H11	1.5 M ammonium sulfate	0.1 M citric acid pH 5.0	
H12	2 M ammonium sulfate	0.1 M citric acid pH 5.0	

HD-N-1b FINESCREEN III

Well	Composition		
A1	1.5 M ammonium sulfate	0.1 M Bis-tris pH 5.5	
A2	2 M ammonium sulfate	0.1 M Bis-tris pH 5.5	
A3	1.5 M ammonium sulfate	0.1 M Hepes pH 7.5	
A4	2 M ammonium sulfate	0.1 M Hepes pH 7.5	
A5	0.1 M magnesium chloride	0.1 M MES pH 6.0	20% PEG 3350
A6	0.1 M magnesium chloride	0.1 M MES pH 6.5	20% PEG 3350
A7	0.1 M magnesium chloride	0.1 M citric acid pH 4.0	20% PEG 3350
A8	0.1 M magnesium chloride	0.1 M citric acid pH 5.0	20% PEG 3350
A9	0.1 M magnesium chloride	0.1 M Bis-tris pH 5.5	20% PEG 3350
A10	0.1 M magnesium chloride	0.1 M Hepes pH 7.5	20% PEG 3350
A11	0.1 M magnesium chloride	0.1 M sodium acetate pH 4.6	20% PEG 3350

A12	0.1 M magnesium chloride	0.1 M sodium acetate pH 5.5	20% PEG 3350
B1	0.1 M magnesium chloride	0.1 M MES pH 6.0	40% MPD
B2	0.1 M magnesium chloride	0.1 M MES pH 6.5	40% MPD
B3	0.1 M magnesium chloride	0.1 M citric acid pH 4.0	40% MPD
B4	0.1 M magnesium chloride	0.1 M citric acid pH 5.0	40% MPD
B5	0.1 M magnesium chloride	0.1 M Bis-tris pH 5.5	40% MPD
B6	0.1 M magnesium chloride	0.1 M HEPES pH 7.5	40% MPD
B7	0.1 M magnesium chloride	0.1 M sodium acetate pH 4.6	40% MPD
B8	0.1 M magnesium chloride	0.1 M sodium acetate pH 5.5	40% MPD
B9	0.2 M ammonium chloride	0.1 M MES pH 6.0	20% PEG 3350
B10	0.2 M ammonium chloride	0.1 M MES pH 6.5	20% PEG 3350
B11	0.2 M ammonium chloride	0.1 M citric acid pH 4.0	20% PEG 3350
B12	0.2 M ammonium chloride	0.1 M citric acid pH 5.0	20% PEG 3350
C1	0.2 M ammonium chloride	0.1 M Bis-tris pH 5.5	20% PEG 3350
C2	0.2 M ammonium chloride	0.1 M HEPES pH 7.5	20% PEG 3350
C3	0.2 M ammonium chloride	0.1 M sodium acetate pH 4.6	20% PEG 3350
C4	0.2 M ammonium chloride	0.1 M sodium acetate pH 5.5	20% PEG 3350
C5	0.2 M ammonium chloride	0.1 M MES pH 6.0	40% MPD
C6	0.2 M ammonium chloride	0.1 M MES pH 6.5	40% MPD
C7	0.2 M ammonium chloride	0.1 M citric acid pH 4.0	40% MPD
C8	0.2 M ammonium chloride	0.1 M citric acid pH 5.0	40% MPD
C9	0.2 M ammonium chloride	0.1 M Bis-tris pH 5.5	40% MPD
C10	0.2 M ammonium chloride	0.1 M HEPES pH 7.5	40% MPD
C11	0.2 M ammonium chloride	0.1 M sodium acetate pH 4.6	40% MPD
C12	0.2 M ammonium chloride	0.1 M sodium acetate pH 5.5	40% MPD
D1	1.8 M ammonium sulfate	0.1 M MES pH 6.0	20% PEG 3350
D2	1.8 M ammonium sulfate	0.1 M MES pH 6.5	20% PEG 3350
D3	1.8 M ammonium sulfate	0.1 M citric acid pH 4.0	20% PEG 3350
D4	1.8 M ammonium sulfate	0.1 M citric acid pH 5.0	20% PEG 3350
D5	1.8 M ammonium sulfate	0.1 M Bis-tris pH 5.5	20% PEG 3350
D6	1.8 M ammonium sulfate	0.1 M HEPES pH 7.5	20% PEG 3350
D7	1.8 M ammonium sulfate	0.1 M sodium acetate pH 4.6	20% PEG 3350
D8	1.8 M ammonium sulfate	0.1 M sodium acetate pH 5.5	20% PEG 3350
D9	1.8 M ammonium sulfate	0.1 M MES pH 6.0	40% MPD
D10	1.8 M ammonium sulfate	0.1 M MES pH 6.5	40% MPD
D11	1.8 M ammonium sulfate	0.1 M citric acid pH 4.0	40% MPD
D12	1.8 M ammonium sulfate	0.1 M citric acid pH 5.0	40% MPD

E1	1.8 M ammonium sulfate	0.1 M Bis-tris pH 5.5	40% MPD
E2	1.8 M ammonium sulfate	0.1 M Hepes pH 7.5	40% MPD
E3	1.8 M ammonium sulfate	0.1 M sodium acetate pH 4.6	40% MPD
E4	1.8 M ammonium sulfate	0.1 M sodium acetate pH 5.5	40% MPD
E5	1 M Na/K tartrate	0.1 M MES pH 6.0	20% PEG 3350
E6	1 M Na/K tartrate	0.1 M MES pH 6.5	20% PEG 3350
E7	1 M Na/K tartrate	0.1 M citric acid pH 4.0	20% PEG 3350
E8	1 M Na/K tartrate	0.1 M citric acid pH 5.0	20% PEG 3350
E9	1 M Na/K tartrate	0.1 M Bis-tris pH 5.5	20% PEG 3350
E10	1 M Na/K tartrate	0.1 M Hepes pH 7.5	20% PEG 3350
E11	1 M Na/K tartrate	0.1 M sodium acetate pH 4.6	20% PEG 3350
E12	1 M Na/K tartrate	0.1 M sodium acetate pH 5.5	20% PEG 3350
F1	1 M Na/K tartrate	0.1 M MES pH 6.0	40% MPD
F2	1 M Na/K tartrate	0.1 M MES pH 6.5	40% MPD
F3	1 M Na/K tartrate	0.1 M citric acid pH 4.0	40% MPD
F4	1 M Na/K tartrate	0.1 M citric acid pH 5.0	40% MPD
F5	1 M Na/K tartrate	0.1 M Bis-tris pH 5.5	40% MPD
F6	1 M Na/K tartrate	0.1 M Hepes pH 7.5	40% MPD
F7	1 M Na/K tartrate	0.1 M sodium acetate pH 4.6	40% MPD
F8	1 M Na/K tartrate	0.1 M sodium acetate pH 5.5	40% MPD
F9	1.5 M sodium malonate dibasic	0.1 M MES pH 6.0	20% PEG 3350
F10	1.5 M sodium malonate dibasic	0.1 M MES pH 6.5	20% PEG 3350
F11	1.5 M sodium malonate dibasic	0.1 M citric acid pH 4.0	20% PEG 3350
F12	1.5 M sodium malonate dibasic	0.1 M citric acid pH 5.0	20% PEG 3350
G1	1.5 M sodium malonate dibasic	0.1 M Bis-tris pH 5.5	20% PEG 3350
G2	1.5 M sodium malonate dibasic	0.1 M Hepes pH 7.5	20% PEG 3350
G3	1.5 M sodium malonate dibasic	0.1 M sodium acetate pH 4.6	20% PEG 3350
G4	1.5 M sodium malonate dibasic	0.1 M sodium acetate pH 5.5	20% PEG 3350
G5	1.5 M sodium malonate dibasic	0.1 M MES pH 6.0	40% MPD
G6	1.5 M sodium malonate dibasic	0.1 M MES pH 6.5	40% MPD
G7	1.5 M sodium malonate dibasic	0.1 M citric acid pH 4.0	40% MPD
G8	1.5 M sodium malonate dibasic	0.1 M citric acid pH 5.0	40% MPD
G9	1.5 M sodium malonate dibasic	0.1 M Bis-tris pH 5.5	40% MPD
G10	1.5 M sodium malonate dibasic	0.1 M Hepes pH 7.5	40% MPD
G11	1.5 M sodium malonate dibasic	0.1 M sodium acetate pH 4.6	40% MPD
G12	1.5 M sodium malonate dibasic	0.1 M sodium acetate pH 5.5	40% MPD
H1	0.7 M sodium tartrate dibasic	0.1 M MES pH 6.0	20% PEG 3350

H2	0.7 M sodium tartrate dibasic	0.1 M citric acid pH 5.0	20% PEG 3350
H3	0.7 M sodium tartrate dibasic	0.1 M Bis-tris pH 5.5	20% PEG 3350
H4	0.7 M sodium tartrate dibasic	0.1 M Hepes pH 7.5	20% PEG 3350
H5	0.7 M sodium tartrate dibasic	0.1 M sodium acetate pH 4.6	20% PEG 3350
H6	0.7 M sodium tartrate dibasic	0.1 M sodium acetate pH 5.5	20% PEG 3350
H7	0.7 M sodium tartrate dibasic	0.1 M MES pH 6.0	40% MPD
H8	0.7 M sodium tartrate dibasic	0.1 M citric acid pH 5.0	40% MPD
H9	0.7 M sodium tartrate dibasic	0.1 M Bis-tris pH 5.5	40% MPD
H10	0.7 M sodium tartrate dibasic	0.1 M Hepes pH 7.5	40% MPD
H11	0.7 M sodium tartrate dibasic	0.1 M sodium acetate pH 4.6	40% MPD
H12	0.7 M sodium tartrate dibasic	0.1 M sodium acetate pH 5.5	40% MPD

HD-N-1B SUPERFINESCREEN

Well	Composition		
A1	0.5 M ammonium sulfate	0.05 M Hepes pH 7.5	10% MPD
A2	0.5 M ammonium sulfate	0.05 M Hepes pH 7.5	20% MPD
A3	0.5 M ammonium sulfate	0.05 M Hepes pH 7.5	30% MPD
A4	0.5 M ammonium sulfate	0.05 M Hepes pH 7.5	40% MPD
A5	0.5 M ammonium sulfate	0.05 M Hepes pH 7.5	45% MPD
A6	0.5 M ammonium sulfate	0.1 M Hepes pH 7.5	10% MPD
A7	0.5 M ammonium sulfate	0.1 M Hepes pH 7.5	20% MPD
A8	0.5 M ammonium sulfate	0.1 M Hepes pH 7.5	30% MPD
A9	0.5 M ammonium sulfate	0.1 M Hepes pH 7.5	40% MPD
A10	0.5 M ammonium sulfate	0.1 M Hepes pH 7.5	45% MPD
A11	0.5 M ammonium sulfate	0.15 M Hepes pH 7.5	10% MPD
A12	0.5 M ammonium sulfate	0.15 M Hepes pH 7.5	20% MPD
B1	0.5 M ammonium sulfate	0.15 M Hepes pH 7.5	30% MPD
B2	0.5 M ammonium sulfate	0.15 M Hepes pH 7.5	40% MPD
B3	0.5 M ammonium sulfate	0.15 M Hepes pH 7.5	45% MPD
B4	0.8 M ammonium sulfate	0.05 M Hepes pH 7.5	10% MPD
B5	0.8 M ammonium sulfate	0.05 M Hepes pH 7.5	20% MPD
B6	0.8 M ammonium sulfate	0.05 M Hepes pH 7.5	30% MPD
B7	0.8 M ammonium sulfate	0.05 M Hepes pH 7.5	40% MPD
B8	0.8 M ammonium sulfate	0.05 M Hepes pH 7.5	45% MPD
B9	0.8 M ammonium sulfate	0.1 M Hepes pH 7.5	10% MPD
B10	0.8 M ammonium sulfate	0.1 M Hepes pH 7.5	20% MPD

B11	0.8 M ammonium sulfate	0.1 M Hepes pH 7.5	30% MPD
B12	0.8 M ammonium sulfate	0.1 M Hepes pH 7.5	40% MPD
C1	0.8 M ammonium sulfate	0.1 M Hepes pH 7.5	45% MPD
C2	0.8 M ammonium sulfate	0.15 M Hepes pH 7.5	10% MPD
C3	0.8 M ammonium sulfate	0.15 M Hepes pH 7.5	20% MPD
C4	0.8 M ammonium sulfate	0.15 M Hepes pH 7.5	30% MPD
C5	0.8 M ammonium sulfate	0.15 M Hepes pH 7.5	40% MPD
C6	0.8 M ammonium sulfate	0.15 M Hepes pH 7.5	45% MPD
C7	1.2 M ammonium sulfate	0.05 M Hepes pH 7.5	10% MPD
C8	1.2 M ammonium sulfate	0.05 M Hepes pH 7.5	20% MPD
C9	1.2 M ammonium sulfate	0.05 M Hepes pH 7.5	30% MPD
C10	1.2 M ammonium sulfate	0.05 M Hepes pH 7.5	40% MPD
C11	1.2 M ammonium sulfate	0.05 M Hepes pH 7.5	45% MPD
C12	1.2 M ammonium sulfate	0.1 M Hepes pH 7.5	10% MPD
D1	1.2 M ammonium sulfate	0.1 M Hepes pH 7.5	20% MPD
D2	1.2 M ammonium sulfate	0.1 M Hepes pH 7.5	30% MPD
D3	1.2 M ammonium sulfate	0.1 M Hepes pH 7.5	40% MPD
D4	1.2 M ammonium sulfate	0.1 M Hepes pH 7.5	45% MPD
D5	1.2 M ammonium sulfate	0.15 M Hepes pH 7.5	10% MPD
D6	1.2 M ammonium sulfate	0.15 M Hepes pH 7.5	20% MPD
D7	1.2 M ammonium sulfate	0.15 M Hepes pH 7.5	30% MPD
D8	1.2 M ammonium sulfate	0.15 M Hepes pH 7.5	40% MPD
D9	1.2 M ammonium sulfate	0.15 M Hepes pH 7.5	45% MPD
D10	1.5 M ammonium sulfate	0.05 M Hepes pH 7.5	10% MPD
D11	1.5 M ammonium sulfate	0.05 M Hepes pH 7.5	20% MPD
D12	1.5 M ammonium sulfate	0.05 M Hepes pH 7.5	30% MPD
E1	1.5 M ammonium sulfate	0.05 M Hepes pH 7.5	40% MPD
E2	1.5 M ammonium sulfate	0.05 M Hepes pH 7.5	45% MPD
E3	1.5 M ammonium sulfate	0.1 M Hepes pH 7.5	10% MPD
E4	1.5 M ammonium sulfate	0.1 M Hepes pH 7.5	20% MPD
E5	1.5 M ammonium sulfate	0.1 M Hepes pH 7.5	30% MPD
E6	1.5 M ammonium sulfate	0.1 M Hepes pH 7.5	40% MPD
E7	1.5 M ammonium sulfate	0.1 M Hepes pH 7.5	45% MPD
E8	1.5 M ammonium sulfate	0.15 M Hepes pH 7.5	10% MPD
E9	1.5 M ammonium sulfate	0.15 M Hepes pH 7.5	20% MPD
E10	1.5 M ammonium sulfate	0.15 M Hepes pH 7.5	30% MPD
E11	1.5 M ammonium sulfate	0.15 M Hepes pH 7.5	40% MPD

E12	1.5 M ammonium sulfate	0.15 M Hepes pH 7.5	45 % MPD
F1	1.8 M ammonium sulfate	0.05 M Hepes pH 7.5	10 % MPD
F2	1.8 M ammonium sulfate	0.05 M Hepes pH 7.5	20 % MPD
F3	1.8 M ammonium sulfate	0.05 M Hepes pH 7.5	30 % MPD
F4	1.8 M ammonium sulfate	0.05 M Hepes pH 7.5	40 % MPD
F5	1.8 M ammonium sulfate	0.05 M Hepes pH 7.5	45 % MPD
F6	1.8 M ammonium sulfate	0.1 M Hepes pH 7.5	10 % MPD
F7	1.8 M ammonium sulfate	0.1 M Hepes pH 7.5	20 % MPD
F8	1.8 M ammonium sulfate	0.1 M Hepes pH 7.5	30 % MPD
F9	1.8 M ammonium sulfate	0.1 M Hepes pH 7.5	40 % MPD
F10	1.8 M ammonium sulfate	0.15 M Hepes pH 7.5	10 % MPD
F11	1.8 M ammonium sulfate	0.15 M Hepes pH 7.5	20 % MPD
F12	1.8 M ammonium sulfate	0.15 M Hepes pH 7.5	30 % MPD
G1	2M ammonium sulfate	0.05 M Hepes pH 7.5	10 % MPD
G2	2M ammonium sulfate	0.05 M Hepes pH 7.5	20 % MPD
G3	2M ammonium sulfate	0.05 M Hepes pH 7.5	30 % MPD
G4	2M ammonium sulfate	0.05 M Hepes pH 7.5	40 % MPD
G5	2M ammonium sulfate	0.1 M Hepes pH 7.5	10 % MPD
G6	2M ammonium sulfate	0.1 M Hepes pH 7.5	20 % MPD
G7	2M ammonium sulfate	0.1 M Hepes pH 7.5	30 % MPD
G8	2M ammonium sulfate	0.1 M Hepes pH 7.5	35 % MPD
G9	2M ammonium sulfate	0.15 M Hepes pH 7.5	10 % MPD
G10	2M ammonium sulfate	0.15 M Hepes pH 7.5	20 % MPD
G11	2M ammonium sulfate	0.15 M Hepes pH 7.5	25 % MPD
G12	2M ammonium sulfate	0.15 M Hepes pH 7.5	30 % MPD
H1	2.4 M ammonium sulfate	0.05 M Hepes pH 7.5	10 % MPD
H2	2.4 M ammonium sulfate	0.05 M Hepes pH 7.5	20 % MPD
H3	2.4 M ammonium sulfate	0.05 M Hepes pH 7.5	25 % MPD
H4	2.4 M ammonium sulfate	0.05 M Hepes pH 7.5	30 % MPD
H5	2.4 M ammonium sulfate	0.1 M Hepes pH 7.5	10 % MPD
H6	2.4 M ammonium sulfate	0.1 M Hepes pH 7.5	20 % MPD
H7	2.4 M ammonium sulfate	0.1 M Hepes pH 7.5	25 % MPD
H8	2.4 M ammonium sulfate	0.15 M Hepes pH 7.5	10 % MPD
H9	2.4 M ammonium sulfate	0.15 M Hepes pH 7.5	15 % MPD
H10	2.4 M ammonium sulfate	0.15 M Hepes pH 7.5	20 % MPD
H11	1.8 M ammonium sulfate	0.1 M Hepes pH 7.5	40 % MPD
H12	1.8 M ammonium sulfate	0.1 M Hepes pH 7.5	40 % MPD

HD-N-SAACP-SAFABI FINESCREEN I

Well	Composition		
A1	0.1 M citric acid pH 4.0	1.5 M sodium chloride	
A2	0.1 M citric acid pH 4.0	2 M sodium chloride	
A3	0.1 M citric acid pH 4.0	2.5 M sodium chloride	
A4	0.1 M citric acid pH 5.0	1.5 M sodium chloride	
A5	0.1 M citric acid pH 5.0	2M sodium chloride	
A6	0.1 M citric acid pH 5.0	2.5 M sodium chloride	
A7	0.1 M citric acid pH 6.0	1.5 M sodium chloride	
A8	0.1 M citric acid pH 6.0	2 M sodium chloride	
A9	0.1 M citric acid pH 6.0	2.5 M sodium chloride	
A10	0.1 M citric acid pH 4.0	2.4 M ammonium sulfate	
A11	0.1 M citric acid pH 4.0	2.8 M ammonium sulfate	
A12	0.1 M citric acid pH 4.0	3.2 M ammonium sulfate	
B1	0.1 M citric acid pH 5.0	2.4 M ammonium sulfate	
B2	0.1 M citric acid pH 5.0	2.8 M ammonium sulfate	
B3	0.1 M citric acid pH 5.0	3.2 M ammonium sulfate	
B4	0.1 M citric acid pH 6.0	2.4 M ammonium sulfate	
B5	0.1 M citric acid pH 6.0	2.8 M ammonium sulfate	
B6	0.1 M citric acid pH 6.0	3.2 M ammonium sulfate	
B7	0.1 M citric acid pH 4.0	0.8 M sodium phosphate monobasic	
B8	0.1 M citric acid pH 4.0	1.2 M sodium phosphate monobasic	
B9	0.1 M citric acid pH 5.0	0.8 M sodium phosphate monobasic	
B10	0.1 M citric acid pH 5.0	1.2 M sodium phosphate monobasic	
B11	0.1 M citric acid pH 6.0	0.8 M sodium phosphate monobasic	
B12	0.1 M citric acid pH 6.0	1.2 M sodium phosphate monobasic	
C1	0.1 M citric acid pH 4.0	1 M ammonium phosphate monobasic	
C2	1.6 M magnesium sulfate	0.1 M citric acid pH 4.0	2 M ammonium phosphate monobasic
C3	1.2 M magnesium sulfate	0.1 M citric acid pH 5.0	1 M ammonium phosphate monobasic
C4	1.6 M magnesium sulfate	0.1 M citric acid pH 5.0	2 M ammonium phosphate monobasic
C5	1.2 M magnesium sulfate	0.1 M citric acid pH 6.0	1 M ammonium phosphate monobasic
C6	1.6 M magnesium sulfate	0.1 M citric acid pH 6.0	2 M ammonium phosphate monobasic
C7	1.2 M magnesium sulfate	0.1 M Tris pH 8.5	1.5 M sodium chloride
C8	1.6 M magnesium sulfate	0.1 M Tris pH 8.5	2 M sodium chloride
C9	1.2 M magnesium sulfate	0.1 M Tris pH 8.5	2.5 M sodium chloride
C10	1.6 M magnesium sulfate	0.1 M Tris pH 8.5	2.4 M ammonium sulfate
C11	1.2 M magnesium sulfate	0.1 M Tris pH 8.5	2.8 M ammonium sulfate

C12	1.6 M magnesium sulfate	0.1 M Tris pH 8.5	3.2 M ammonium sulfate
D1	1.2 M magnesium sulfate	0.1 M Tris pH 8.5	0.8 M sodium phosphate monobasic
D2	1.6 M magnesium sulfate	0.1 M Tris pH 8.5	1.2 M sodium phosphate monobasic
D3	1.2 M magnesium sulfate	0.1 M Tris pH 8.5	1 M ammonium phosphate monobasic
D4	0.15 M potassiumbromide	0.1 M Tris pH 8.5	2 M ammonium phosphate monobasic
D5	0.15 M potassiumbromide	0.1 M Hepes pH 7.5	1.5 M sodium chloride
D6	0.15 M potassiumbromide	0.1 M Hepes pH 7.5	2 M sodium chloride
D7	0.15 M potassiumbromide	0.1 M Hepes pH 7.5	2.5 M sodium chloride
D8	1.6 M magnesium sulfate	0.1 M Hepes pH 7.5	2.4 M ammonium sulfate
D9	1.2 M magnesium sulfate	0.1 M Hepes pH 7.5	2.8 M ammonium sulfate
D10	1.6 M magnesium sulfate	0.1 M Hepes pH 7.5	3.2 M ammonium sulfate
D11	1.2 M magnesium sulfate	0.1 M Hepes pH 7.5	0.8 M sodium phosphate monobasic
D12	1.6 M magnesium sulfate	0.1 M Hepes pH 7.5	1.2 M sodium phosphate monobasic
E1	1.2 M magnesium sulfate	0.1 M Hepes pH 7.5	1 M ammonium phosphate monobasic
E2	1.6 M magnesium sulfate	0.1 M Hepes pH 7.5	2 M ammonium phosphate monobasic
E3	1.2 M magnesium sulfate	0.1 M bicine pH 9.0	1.5 M sodium chloride
E4	1.6 M magnesium sulfate	0.1 M bicine pH 9.0	2M sodium chloride
E5	1.2 M magnesium sulfate	0.1 M bicine pH 9.0	2.5 M sodium chloride
E6	1.6 M magnesium sulfate	0.1 M bicine pH 9.0	2.4 M ammonium sulfate
E7	1.2 M magnesium sulfate	0.1 M bicine pH 9.0	2.8 M ammonium sulfate
E8	1.6 M magnesium sulfate	0.1 M bicine pH 9.0	3.2 M ammonium sulfate
E9	1.2 M magnesium sulfate	0.1 M bicine pH 9.0	0.8 M sodium phosphate monobasic
E10	0.4 M calcium chloride	0.1 M bicine pH 9.0	1.2 M sodium phosphate monobasic
E11	0.4 M calcium chloride	0.1 M bicine pH 9.0	1 M ammonium phosphate monobasic
E12	0.4 M calcium chloride	0.1 M bicine pH 9.0	2 M ammonium phosphate monobasic
F1	0.4 M calcium chloride	0.1 M MES pH 6.5	
F2		0.1 M MES pH 6.5	10% PEG 3350
F3		0.1 M citric acid pH 4.0	
F4		0.1 M citric acid pH 4.0	15% PEG 3350
F5		0.1 M citric acid pH 5.0	
F6		0.1 M citric acid pH 5.0	15% PEG 3350
F7		0.1 M citric acid pH 6.0	
F8		0.1 M citric acid pH 6.0	15% PEG 3350
F9		0.1 M Tris pH 8.5	
F10		0.1 M Tris pH 8.5	15% PEG 3350
F11		0.1 M Hepes pH 7.5	
F12		0.1 M Hepes pH 7.5	12% PEG 3350

G1	0.1 M Bicine pH 9.0	
G2	0.1 M Bicine pH 9.0	15 % PEG 3350
G3		20 % PEG 2000 MME
G4		30 % PEG 2000 MME
G5		20 % PEG 3350
G6		30 % PEG 3350
G7	0.1 M MES pH 6.5	
G8	0.1 M MES pH 6.5	8 % PEG 2000 MME
G9	0.1 M citric acid pH 4.0	
G10	0.1 M citric acid pH 4.0	12 % PEG 2000 MME
G11	0.1 M citric acid pH 5.0	
G12	0.1 M citric acid pH 5.0	12 % PEG 2000 MME
H1	0.1 M citric acid pH 6.0	
H2	0.1 M citric acid pH 6.0	12 % PEG 2000 MME
H3	0.1 M Tris pH 8.5	
H4	0.1 M Tris pH 8.5	12 % PEG 2000 MME
H5	0.1 M Hepes pH 7.5	
H6	0.1 M Hepes pH 7.5	10 % PEG 2000 MME
H7	0.1 M Bicine pH 9.0	
H8	0.1 M Bicine pH 9.0	12 % PEG 2000 MME
H9	0.1 M sodium acetate pH 4.6	18 % PEG 2000 MME
H10	0.1 M sodium acetate pH 4.6	18 % PEG 3350
H11	0.1 M sodium acetate pH 4.6	18 % PEG 4000
H12	0.1 M sodium acetate pH 4.6	18 % PEG 8000

HD-N-SAAP-FAFI FINESCREEN II

<i>Well</i>	<i>Composition</i>	
A1	0.1 M citric acid pH 4.0	1M Na/K tartrate
A2	0.1 M citric acid pH 5.0	1M Na/K tartrate
A3	0.1 M citric acid pH 6.0	1M Na/K tartrate
A4	0.1 M Tris pH 8.5	1M Na/K tartrate
A5	0.1 M Hepes pH 7.5	1M Na/K tartrate
A6	0.1 M Bicine pH 9.0	1M Na/K tartrate
A7	0.1 M MES pH 6.5	1M Na/K tartrate
A8	0.2 M ammonium sulfate	0.1 M sodium acetate pH 5.5
A9	0.2 M ammonium sulfate	0.1 M sodium acetate pH 5.5
		10 % PEG 2000 MME
		20 % PEG 2000 MME

A10	0.2 M ammonium sulfate	0.1 M sodium acetate pH 5.5	10 % PEG 3350
A11	0.2 M ammonium sulfate	0.1 M sodium acetate pH 5.5	20 % PEG 3350
A12	0.2 M ammonium sulfate	0.1 M sodium acetate pH 5.5	10 % PEG 4000
B1	0.2 M ammonium sulfate	0.1 M sodium acetate pH 5.5	20 % PEG 4000
B2	0.2 M ammonium sulfate	0.1 M sodium acetate pH 5.5	10 % PEG 8000
B3	0.2 M ammonium sulfate	0.1 M sodium acetate pH 5.5	20 % PEG 8000
B4	0.2 M lithium sulfate	0.1 M Bis-tris pH 5.5	15 % PEG 2000 MME
B5	0.2 M lithium sulfate	0.1 M Bis-tris pH 5.5	25 % PEG 2000 MME
B6	0.2 M lithium sulfate	0.1 M Bis-tris pH 5.5	15 % PEG 3350
B7	0.2 M lithium sulfate	0.1 M Bis-tris pH 5.5	25 % PEG 3350
B8	0.2 M lithium sulfate	0.1 M Bis-tris pH 5.5	15 % PEG 4000
B9	0.2 M lithium sulfate	0.1 M Bis-tris pH 5.5	25 % PEG 4000
B10	0.2 M lithium sulfate	0.1 M Bis-tris pH 5.5	15 % PEG 8000
B11	0.2 M lithium sulfate	0.1 M Bis-tris pH 5.5	25 % PEG 8000
B12	0.2 M ammonium sulfate	0.1 M Bis-tris pH 5.5	15 % PEG 2000 MME
C1	0.2 M ammonium sulfate	0.1 M Bis-tris pH 5.5	25 % PEG 2000 MME
C2	0.2 M ammonium sulfate	0.1 M Bis-tris pH 5.5	15 % PEG 3350
C3	0.2 M ammonium sulfate	0.1 M Bis-tris pH 5.5	25 % PEG 3350
C4	0.2 M ammonium sulfate	0.1 M Bis-tris pH 5.5	15 % PEG 4000
C5	0.2 M ammonium sulfate	0.1 M Bis-tris pH 5.5	25 % PEG 4000
C6	0.2 M ammonium sulfate	0.1 M Bis-tris pH 5.5	15 % PEG 8000
C7	0.2 M ammonium sulfate	0.1 M Bis-tris pH 5.5	25 % PEG 8000
C8	0.4 M sodium acetate	0.1 M sodium citrate pH 5.6	10 % PEG 2000 MME
C9	0.4 M sodium acetate	0.1 M sodium citrate pH 5.6	20 % PEG 2000 MME
C10	0.4 M sodium acetate	0.1 M sodium citrate pH 5.6	10 % PEG 3350
C11	0.4 M sodium acetate	0.1 M sodium citrate pH 5.6	20 % PEG 3350
C12	0.4 M sodium acetate	0.1 M sodium citrate pH 5.6	10 % PEG 4000
D1	0.4 M sodium acetate	0.1 M sodium citrate pH 5.6	20 % PEG 4000
D2	0.4 M sodium acetate	0.1 M sodium citrate pH 5.6	10 % PEG 8000
D3	0.4 M sodium acetate	0.1 M sodium citrate pH 5.6	20 % PEG 8000
D4	0.2 M proline	0.1 M HEPES pH 7.5	10 % PEG 2000 MME
D5	0.2 M proline	0.1 M HEPES pH 7.5	10 % PEG 3350
D6	0.2 M proline	0.1 M HEPES pH 7.5	10 % PEG 4000
D7	0.2 M proline	0.1 M HEPES pH 7.5	10 % PEG 8000
D8	0.2 M proline	0.1 M citric acid pH 4.0	10 % PEG 2000 MME
D9	0.2 M proline	0.1 M citric acid pH 5.0	10 % PEG 3350
D10	0.2 M proline	0.1 M citric acid pH 6.0	10 % PEG 3350

D11	0.2 M proline	0.1 M Tris pH 8.5	10 % PEG 3350
D12	0.2 M proline	0.1 M Hepes pH 7.5	10 % PEG 3350
E1	0.2 M proline	0.1 M Bicine pH 9.0	10 % PEG 3350
E2	0.2 M proline	0.1 M MES pH 6.5	10 % PEG 3350
E3	0.8 M potassium phosphate monobasic	0.1 M Hepes pH 7.5	0.8 M sodium phosphate monobasic
E4	1M potassium phosphate monobasic	0.1 M Hepes pH 7.5	0.6 M sodium phosphate monobasic
E5	0.8 M potassium phosphate monobasic	0.1 M Hepes pH 7.5	1M sodium phosphate monobasic
E6	0.8 M potassium thiocyanate	0.1 M Hepes pH 7.5	
E7	1.2 M potassium thiocyanate	0.1 M Hepes pH 7.5	
E8	0.8 M potassium thiocyanate	0.1 M Hepes pH 7.5	10 % PEG 3350
E9	1.2 M potassium thiocyanate	0.1 M Hepes pH 7.5	10 % PEG 3350
E10	0.8 M potassium thiocyanate	0.1 M Hepes pH 7.5	20 % PEG 3350
E11	1M potassium thiocyanate	0.1 M Hepes pH 7.5	18 % PEG 3350
E12	0.2 M zinc acetate	0.1 M imidazole pH 8.0	2 M sodium chloride
F1	0.2 M zinc acetate	0.1 M imidazole pH 8.0	2.5 M sodium chloride
F2	0.2 M zinc acetate	0.1 M imidazole pH 8.0	3M sodium chloride
F3	0.2 M zinc acetate	0.1 M Hepes pH 7.5	2M sodium chloride
F4	0.2 M zinc acetate	0.1 M Hepes pH 7.5	2.5 M sodium chloride
F5	0.2 M zinc acetate	0.1 M Hepes pH 7.5	3M sodium chloride
F6	0.2 M lithium sulfate	0.1 M Tris pH 7.0	0.8 M Na/K tartrate
F7	0.2 M lithium sulfate	0.1 M Tris pH 7.0	1M Na/K tartrate
F8	0.2 M lithium sulfate	0.1 M Tris pH 7.0	1.2 M Na/K tartrate
F9	0.2 M lithium sulfate	0.1 M Hepes pH 7.5	0.8 M Na/K tartrate
F10	0.2 M lithium sulfate	0.1 M Hepes pH 7.5	1M Na/K tartrate
F11	0.2 M lithium sulfate	0.1 M Hepes pH 7.5	1.2 M Na/K tartrate
F12	0.2 M lithium sulfate	0.1 M sodium acetate pH 5.5	0.8 M Na/K tartrate
G1	0.2 M lithium sulfate	0.1 M sodium acetate pH 5.5	1M Na/K tartrate
G2	0.2 M lithium sulfate	0.1 M sodium acetate pH 5.5	1.2 M Na/K tartrate
G3	0.2 M lithium sulfate	0.1 M Bis-tris pH 5.5	0.8 M Na/K tartrate

G4	0.2 M lithium sulfate	0.1 M Bis-tris pH 5.5	1M Na/K tartrate
G5	0.2 M lithium sulfate	0.1 M Bis-tris pH 5.5	1.2 M Na/K tartrate
G6	0.2 M lithium sulfate	0.1 M citric acid pH 4.0	0.8 M Na/K tartrate
G7	0.2 M lithium sulfate	0.1 M citric acid pH 4.0	1M Na/K tartrate
G8	0.2 M lithium sulfate	0.1 M citric acid pH 4.0	1.2 M Na/K tartrate
G9	0.2 M lithium sulfate	0.1 M citric acid pH 5.0	0.8 M Na/K tartrate
G10	0.2 M lithium sulfate	0.1 M citric acid pH 5.0	1M Na/K tartrate
G11	0.2 M lithium sulfate	0.1 M citric acid pH 5.0	1.2 M Na/K tartrate
G12	0.2 M lithium sulfate	0.1 M citric acid pH 6.0	0.8 M Na/K tartrate
H1	0.2 M lithium sulfate	0.1 M citric acid pH 6.0	1M Na/K tartrate
H2	0.2 M lithium sulfate	0.1 M citric acid pH 6.0	1.2 M Na/K tartrate
H3	0.2 M magnesium acetate	0.1 M sodium cacodylate pH 6.5	10% PEG 2000 MME
H4	0.2 M magnesium acetate	0.1 M sodium cacodylate pH 6.5	20% PEG 2000 MME
H5	0.2 M magnesium acetate	0.1 M sodium cacodylate pH 6.5	10% PEG 3350
H6	0.2 M magnesium acetate	0.1 M sodium cacodylate pH 6.5	20% PEG 3350
H7	0.2 M magnesium acetate	0.1 M sodium cacodylate pH 6.5	10% PEG 4000
H8	0.2 M magnesium acetate	0.1 M sodium cacodylate pH 6.5	20% PEG 4000
H9	0.2 M magnesium acetate	0.1 M sodium cacodylate pH 6.5	15% PEG 8000
H10		0.1 M HEPES pH 7.5	5% PEG 8000 15% ethylene glycol
H11		0.1 M HEPES pH 7.5	15% PEG 8000 5% ethylene glycol
H12		0.1 M HEPES pH 7.5	10% PEG 8000 8% ethylene glycol

THERMOFLUOR ADVANCE

Well	Composition
A1	
A2	0.1 M citric acid pH 4.0
A3	0.1 M sodium acetate pH 4.5
A4	0.1 M citric acid pH 5.0
A5	0.1 M MES pH 6.0
A6	0.1 M potassium phosphate pH 6.0
A7	0.1 M citric acid pH 6.0
A8	0.1 M Bis-tris pH 6.5
A9	0.1 M sodium cacodylate pH 6.5

A10		0.1 M sodium phosphate pH 7.0
A11		0.1 M potassium phosphate pH 7.0
A12		0.1 M Hepes pH 7.0
B1		0.1 M Mops pH 7.0
B2		0.1 M ammonium acetate pH 7.3 [4]
B3		0.1 M Tris pH 7.5
B4		0.1 M sodium phosphate pH 7.5
B5		0.1 M imidazole pH 8.0
B6		0.1 M Hepes pH 8.0
B7		0.1 M Tris pH 8.0
B8		0.1 M Tricine pH 8.0
B9		0.1 M Bicine pH 8.0
B10		0.1 M Bicine pH 8.5
B11		0.1 M Tris pH 8.5
B12		0.1 M Bicine pH 9.0
C1	0.15 M sodium chloride	
C2	0.15 M sodium chloride	0.1 M citric acid pH 4.0
C3	0.15 M sodium chloride	0.1 M sodium acetate pH 4.5
C4	0.15 M sodium chloride	0.1 M citric acid pH 5.0
C5	0.15 M sodium chloride	0.1 M MES pH 6.0
C6	0.15 M sodium chloride	0.1 M potassium phosphate pH 6.0
C7	0.15 M sodium chloride	0.1 M citric acid pH 6.0
C8	0.15 M sodium chloride	0.1 M Bis-tris pH 6.5
C9	0.15 M sodium chloride	0.1 M sodium cacodylate pH 6.5
C10	0.15 M sodium chloride	0.1 M sodium phosphate pH 7.0
C11	0.15 M sodium chloride	0.1 M potassium phosphate pH 7.0
C12	0.15 M sodium chloride	0.1 M Hepes pH 7.0
D1	0.15 M sodium chloride	0.1 M Mops pH 7.0
D2	0.15 M sodium chloride	0.1 M ammonium acetate pH 7.3 [4]
D3	0.15 M sodium chloride	0.1 M Tris pH 7.5
D4	0.15 M sodium chloride	0.1 M sodium phosphate pH 7.5
D5	0.15 M sodium chloride	0.1 M imidazole pH 8.0
D6	0.15 M sodium chloride	0.1 M Hepes pH 8.0
D7	0.15 M sodium chloride	0.1 M Tris pH 8.0
D8	0.15 M sodium chloride	0.1 M Tricine pH 8.0
D9	0.15 M sodium chloride	0.1 M Bicine pH 8.0
D10	0.15 M sodium chloride	0.1 M Bicine pH 8.5

D11	0.15 M sodium chloride	0.1 M Tris pH 8.5
D12	0.15 M sodium chloride	0.1 M Bicine pH 9.0
E1	0.25 M sodium chloride	
E2	0.25 M sodium chloride	0.1 M citric acid pH 4.0
E3	0.25 M sodium chloride	0.1 M sodium acetate pH 4.5
E4	0.25 M sodium chloride	0.1 M citric acid pH 5.0
E5	0.25 M sodium chloride	0.1 M MES pH 6.0
E6	0.25 M sodium chloride	0.1 M potassium phosphate pH 6.0
E7	0.25 M sodium chloride	0.1 M citric acid pH 6.0
E8	0.25 M sodium chloride	0.1 M Bis-tris pH 6.5
E9	0.25 M sodium chloride	0.1 M sodium cacodylate pH 6.5
E10	0.25 M sodium chloride	0.1 M sodium phosphate pH 7.0
E11	0.25 M sodium chloride	0.1 M potassium phosphate pH 7.0
E12	0.25 M sodium chloride	0.1 M Hepes pH 7.0
F1	0.25 M sodium chloride	0.1 M Mops pH 7.0
F2	0.25 M sodium chloride	0.1 M ammonium acetate pH 7.3 [4]
F3	0.25 M sodium chloride	0.1 M Tris pH 7.5
F4	0.25 M sodium chloride	0.1 M sodium phosphate pH 7.5
F5	0.25 M sodium chloride	0.1 M imidazole pH 8.0
F6	0.25 M sodium chloride	0.1 M Hepes pH 8.0
F7	0.25 M sodium chloride	0.1 M Tris pH 8.0
F8	0.25 M sodium chloride	0.1 M Tricine pH 8.0
F9	0.25 M sodium chloride	0.1 M Bicine pH 8.0
F10	0.25 M sodium chloride	0.1 M Bicine pH 8.5
F11	0.25 M sodium chloride	0.1 M Tris pH 8.5
F12	0.25 M sodium chloride	0.1 M Bicine pH 9.0
G1		0.02 M Hepes pH 7.5
G2		0.05 M Hepes pH 7.5
G3		0.1 M Hepes pH 7.5
G4		0.25 M Hepes pH 7.5
G5		0.02 M sodium phosphate pH 7.5
G6		0.05 M sodium phosphate pH 7.5
G7		0.1 M sodium phosphate pH 7.5
G8		0.2 M sodium phosphate pH 7.5
G9		0.02 M Tris pH 8.0
G10		0.05 M Tris pH 8.0
G11		0.1 M Tris pH 8.0

G12		0.25 M Tris pH 8.0
H1	0.05 M sodium chloride	0.05 M Hepes pH 7.5
H2	0.125M sodium chloride	0.05 M Hepes pH 7.5
H3	0.25 M sodium chloride	0.05 M Hepes pH 7.5
H4	0.5 M sodium chloride	0.05 M Hepes pH 7.5
H5	0.75 M sodium chloride	0.05 M Hepes pH 7.5
H6	1M sodium chloride	0.05 M Hepes pH 7.5
H7	0.05 M sodium chloride	0.05 M Tris pH 8.0
H8	0.125M sodium chloride	0.05 M Tris pH 8.0
H9	0.25 M sodium chloride	0.05 M Tris pH 8.0
H10	0.5 M sodium chloride	0.05 M Tris pH 8.0
H11	0.75 M sodium chloride	0.05 M Tris pH 8.0
H12	1M sodium chloride	0.05 M Tris pH 8.0

THERMOFLUOR STANDARD

Well	Composition	Well	Composition
A1	0.1 M citric acid pH 4.5	E1	0.1 M sodium cacodylate pH 6.0
A2	0.1 M Bis-tris pH 7.0	E2	0.1 M Bis-trispropane pH 7.0
A3	0.1 M imidazole pH 6.5	E3	0.1 M Mops pH 7.0
A4	0.1 M Hepes pH 8.0	E4	0.1 M Bicine pH 9.0
A5	0.1 M Tris pH 8.5	E5	0.1 M glycyl-glycine pH 8.5
B1	0.1 M acetat pH 4.6	F1	0.1 M sodium cacodylate pH 6.5
B2	0.1 M Ada pH 6.5	F2	0.1 M Pipes pH 6.5
B3	0.1 M imidazole pH 8.0	F3	0.1 M Mops pH 7.5
B4	0.1 M Hepes pH 8.5	F4	0.1 M Tris pH 7.0
B5	0.1 M Tris pH 9.0	F5	0.1 M Ches pH 9.0
C1	0.1 M MES pH 5.5	G1	0.1 M Bis-tris pH 5.5
C2	0.1 M Ada pH 7.0	G2	0.1 M Pipes pH 7.0
C3	0.1 M sodium potassium phosphate pH 6.8	G3	0.1 M Hepes pH 7.0
C4	0.1 M Bicine pH 8.0	G4	0.1 M Tris pH 7.5
C5	0.1 M Taps pH 8.0	G5	0.1 M Ches pH 9.5
D1	0.1 M MES pH 6.5	H1	0.1 M Bis-tris pH 6.5
D2	0.1 M Bis-trispropane pH 6.0	H2	0.1 M Pipes pH 7.5
D3	0.1 M sodium potassium phosphate pH 7.5	H3	0.1 M Hepes pH 7.5
D4	0.1 M Bicine pH 8.5	H4	0.1 M Tris pH 8.0
D5	0.1 M Taps pH 9.0	H5	0.1 M Caps pH 9.8

7.3 Construct list

Designation	Variant/ mutation	Species	Vector	Modifications
saACP_S36C	S36C	<i>S. aureus</i>	pET23b	C-term 5xHis-tag
saACP_E41C	E41C	<i>S. aureus</i>	pET23b	C-term 5xHis-tag
saACP_E47C	E47C	<i>S. aureus</i>	pET23b	C-term 5xHis-tag
saFabI_K17C	K17C	<i>S. aureus</i>	pETM-11	N-term 6xHis-tag
saFabI_K50C	K50C	<i>S. aureus</i>	pETM-11	N-term 6xHis-tag
saFabI_R194C	R194C	<i>S. aureus</i>	pETM-11	N-term 6xHis-tag
saFabI_Y173Q	Y173Q	<i>S. aureus</i>	pETM-11	N-term 6xHis-tag
saFabI_Y9/39/ 63/123S	Y9S Y39S Y63S Y123S	<i>S. aureus</i>	pETM-11	N-term 6xHis-tag
saFabI_Y9/39/ 63/123/147S	Y9S Y39S Y63S Y123S Y147S	<i>S. aureus</i>	pETM-11	N-term 6xHis-tag
saACP-ecFabI-II	12 aa connecting linker region (GNGSGGSGSGNG)	<i>E. coli/S. aureus</i>	pET23b	C-term 5xHis-tag
saACP-saFabI-Ib	10 aa connecting linker region (GNGGSGGRGG)	<i>S. aureus</i>	pETM-11	N-term 6xHis-tag
saACP-saFabI-IIb	12 aa connecting linker region (GGNGSGGSGGSG)	<i>S. aureus</i>	pETM-11	N-term 6xHis-tag
saACP-saFabI-Ib- 15₁	15 aa connecting linker region (GGNGGSGGNSGGRGG)	<i>S. aureus</i>	pETM-11	N-term 6xHis-tag
saACP-saFabI-Ib- 20₁ ("20₁-VI")	20 aa connecting linker region (GGNGGSGGNGGSGGNG GRGG)	<i>S. aureus</i>	pETM-11	N-term 6xHis-tag
saACP-saFabI-Ib- 20₁' ("20₁-III")	20 aa connecting linker region (GGNGGSAGNGGSGGNG GRGG)	<i>S. aureus</i>	pETM-11	N-term 6xHis-tag
saACP-saFabI-Ib_ E41C_K50C	10 aa connecting linker region (GNGGSGGRGG). E41C _{ACP} K50C _{FabI}	<i>S. aureus</i>	pETM-11	N-term 6xHis-tag

saACP-saFabI-Ib_ E47C_K17C	10 aa connecting linker region (GNGGSGGRGG). E47C _{ACP} K17C _{FabI}	<i>S. aureus</i>	pETM-11	N-term 6xHis-tag
CoaA	Burkart lab. San Diego. USA	<i>E. coli</i>	pMAL-c2X	N-term MBP-tag
CoaD	Burkart lab. San Diego. USA	<i>E. coli</i>	pMAL-c2X	N-term MBP-tag
CoaE	Burkart lab. San Diego. USA	<i>E. coli</i>	pMAL-c2X	N-term MBP-tag

7.4 Data collection parameters from additional data sets

Collection parameter	Data sets		
	<i>[InhA·</i> <i>NAD⁺·101JS] #1</i>	<i>[InhA·</i> <i>NAD⁺·101JS] #2</i>	<i>[saFabI·</i> <i>NADP⁺·101JS]</i>
Beamline	ESRF ID30A-3/ MASSIF-3	ESRF ID30	BESSY BL 14.1
Wavelength (Å)	0.96770	0.96770	0.91841
Detector	Dectris Eiger 4M	Dectris PILATUS3 2M	Dectris PILATUS 6M
Detector distance (mm)	160.96	280.89	319.81
Number of images	1200	1800	1800
Oscillation (°)	0.15	0.1	0.1
Exposure time (s)	0.01	0.015	0.5

7.5 Silver-stained SDS gel prepared from crystals of the fusion construct “Ib”

MW (kDa)

130

100

70

55

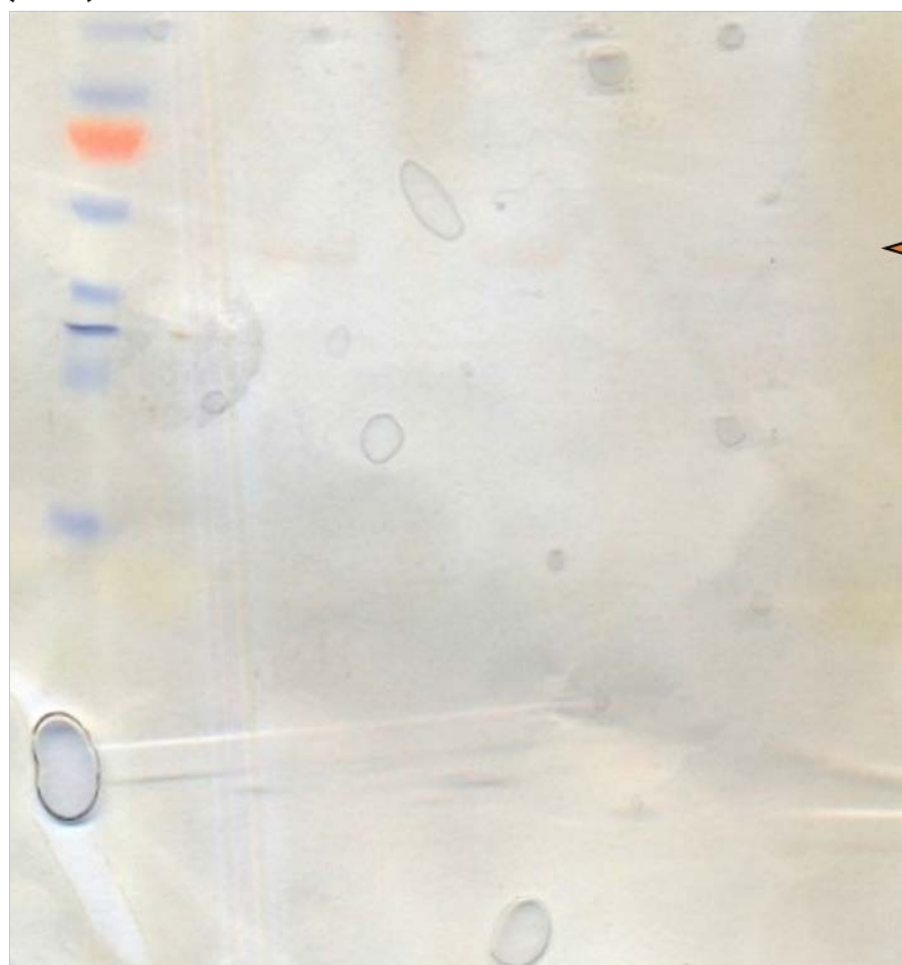
40

35

25

15

10

**M****1****2****3**

The samples were prepared from crystals obtained from the modification reaction of *construct Ib* described in **Chapter 3.5.8**. Each sample contained two (*3*) or three (*1*, *2*) dissolved crystals from different crystallisation conditions, which had previously displayed weak ($R_{\max} \approx 20 \text{ \AA}$) protein diffraction at the synchrotron. (*1*) 0.1 M HEPES, pH 7.5, 0.8 M sodium citrate; 0.05 – 0.1 mm in size; (*2*) 1.2 M K_2HPO_4 ; 0.1 – 0.2 mm in size; (*3*) 0.1 M imidazole, pH 8.0, 1 M sodium citrate; 0.05 – 0.1 mm in size.

7.6 Statement of individual author contributions and of legal second publication rights

Publication (complete reference):					
Rationalizing the Binding Kinetics for the Inhibition of the <i>Burkholderia pseudomallei</i> FabI1 Enoyl-ACP Reductase;					
<i>Carla Neckles, Sandra Eltschkner, Jason E. Cummings, Maria Hirschbeck, Fereidoon Daryaei, Gopal R. Bommineni, Zhuo Zhang, Lauren Spagnuolo, Weixuan Yu, Shabnam Davoodi, Richard A. Slayden, Caroline Kisker and Peter J. Tonge;</i>					
Biochemistry 2017, 56, 1865–1878					
Participated in	Author Initials, Responsibility decreasing from left to right				
Study Design Methods Development	CN, PJT	SE, CK	RAS		
Data Collection	CN, SE, MH, JEC	FD, GRB, ZZ, LS, WY, SD			
Data Analysis and Interpretation	CN, SE, JEC, PJT, CK, RAS	MH, FD	WY		
Manuscript Writing Writing of Introduction Writing of Materials & Methods Writing of Discussion Writing of First Draft	CN, PJT CN, SE, JEC CN, SE, JEC, PJT, CK, RAS CN	MH SE		JEC	

Explanations (if applicable):

The doctoral researcher and the primary supervisor confirm the correctness of the above-mentioned assessment.

Sandra Eltschkner

Würzburg

Doctoral Researcher's Name

Date

Place

Signature

Caroline Kisker

Würzburg

Primary Supervisor's Name

Date

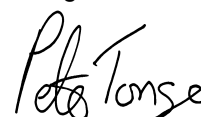
Place

Signature

Peter Tonge

June 1, 2017

Stony Brook



Additional Supervisor's Name

Date

Place

Signature

7.6.1 *Statement of individual author contributions to figures/tables/chapters included in the manuscripts*

Publication (complete reference):					
Rationalizing the Binding Kinetics for the Inhibition of the <i>Burkholderia pseudomallei</i> FabI1 Enoyl-ACP Reductase;					
<i>Carla Neckles, Sandra Eltschkner, Jason E. Cummings, Maria Hirschbeck, Fereidoon Daryaei, Gopal R. Bommineni, Zhuo Zhang, Lauren Spagnuolo, Weixuan Yu, Shabnam Davoodi, Richard A. Slayden, Caroline Kisker and Peter J. Tonge;</i>					
Biochemistry 2017, 56, 1865–1878					
Figure	Author Initials, Responsibility decreasing from left to right				
1	CN, PJT				
2	CN, FD				
3	CN, PJT, FD	WY, LS			
4	SE, CK	MH			
5	SE, CK	MH			
6	JEC, RAS	GRB, LS, ZZ			
7	CN, PJT, FD				
S1	CN				
S2	SE, CK	MH			
S3	SE, CK	MH			
S4	SE, CK	MH			
Table					
1	CN, PJT, FD, JEC, RAS	LS, WY, SD			
S1	SE, CK	MH			
S2	CN, PJT, FD				
Scheme					
1	PJT				
S1	LS, CN, GRB, ZZ				

Explanations (if applicable):

I also confirm my primary supervisor's acceptance.

Sandra Eltschkner

Würzburg

Doctoral Researcher's Name

Date

Place

Signature

LIST OF PUBLICATIONS

Peer-reviewed publications

Spagnuolo L.A., Eltschkner S., Yu W., Daryae F., Davoodi S., Knudson S.E., Allen E.K., Merino J., Pschibul A., Moree B., Thivalapill N., Truglio J.J., Salafsky J., Slayden R.A., Kisker C. and Tonge P.J., *Evaluating the Contribution of Transition-State Destabilization to Changes in the Residence Time of Triazole-Based InhA Inhibitors*. J Am Chem Soc, 2017. **139**(9): p. 3417-3429.

Neckles C., Eltschkner S., Cummings J.E., Hirschbeck M., Daryae F., Bommineni G.R., Zhang Z., Spagnuolo L., Yu W., Davoodi S., Slayden R.A., Kisker C. and Tonge P.J., *Rationalizing the Binding Kinetics for the Inhibition of the Burkholderia pseudomallei FabI1 Enoyl-ACP Reductase*. Biochemistry, 2017. **56**(13): p. 1865-1878.

Schiebel J., Chang A., Shah S., Lu Y., Liu L., Pan P., Hirschbeck M.W., Tareilus M., Eltschkner S., Yu W., Cummings J.E., Knudson S.E., Bommineni G.R., Walker S.G., Slayden R.A., Sotriffer C.A., Tonge P.J. and Kisker C., *Rational design of broad spectrum antibacterial activity based on a clinically relevant enoyl-acyl carrier protein (ACP) reductase inhibitor*. J Biol Chem, 2014. **289**(23): p. 15987-6005.

Congress contributions

Eltschkner S., Yu W., Pschibul A., Kisker C., Tonge P.J., *“Structural characterisation of novel potent inhibitors for treatment of TB infections”*, **23rd Annual Conference of the German Crystallographic Society**, Göttingen, Germany, 2015

Eltschkner S., Volkers G., Palm G.J., Hinrichs W., *“Testing surface-entropy reduction to improve crystal quality of the TetX monooxygenase”*, **15th Heart of Europe Biocrystallography Meeting**, Beilngries, Germany, 2012

ACKNOWLEDGEMENTS

I would like to express my sincere gratitude towards all the people who accompanied me on my way and who have a great share in the successful completion of my work.

In the first instance, I thank *Caroline Kisker* who offered me the opportunity to make a new start on my doctoral thesis in a friendly and fruitful working environment. I'm thankful for her encouragement to develop my own ideas, her interest in discussing and looking at – albeit in “stereo view” – structural data and for being a marvellous mentor not only concerning scientific questions.

I thank the members of my thesis committee, *Christoph Sotriffer*, *Peter Tonge* and *Winfried Hinrichs* for their kind support, the valuable discussions and the productive collaboration.

Special thanks are due to *Lauren Spagnuolo*, *Carla Neckles* and *Benjamin Merget* with whom it was a great pleasure to discuss and to find explanations for our observations.

All members of the structural biology groups contributed to create a friendly working environment and were always helpful with problems. Particularly, I thank *Wolfgang Kölmel*, who not only offered me great insights into the details of data processing, but always had a good advice when things turned out to be difficult. We had a great time spending our coffee breaks sitting outside on the lawn.

I thank *Petra Hänzelmann*, whose valuable suggestions immensely alleviated the work in the lab, whom I could always bother with my questions and who was a humorous bench neighbour. Additionally, I thank *Antje Schäfer* for her helpful advice in daily lab life and her great empathy. I thank *Carolyn Delto* who managed to give me some understanding of sophisticated cloning procedures and for the nice conversations about anything under the sun.

I appreciate the valuable suggestions and help regarding crystallographic issues which I received from *Jochen Kuper* and *Hermann Schindelin*.

Many thanks I owe to *Christin Schäfer*, who was always kind and helpful, especially during my first months in the lab when I got lost sometimes. I thank *Johannes Schiebel* for introducing me to my current project and who was always happy to discuss old and new results.

I thank my master student *Annica Pschibul* and my bachelor student *Jonas Weinrich* who dedicated their time and their keen interest to parts of my project. It was a great pleasure to supervise two such talented students.

I thank my dear friends *Max-Christian*, *Marten* and *Carmen* who have been accompanying me for many years and who were always there for me and endorsed me to keep track of the important things in life.

I thank *my family* for all their support and for making me the person I am. I am grateful for their love, their belief in me and their support in pursuing the things that are important for me.

At the end, I am thankful for all the smaller and bigger coincidences, which guided me the path I am on.

AFFIDAVIT

I hereby confirm that my thesis entitled

“Targeting the Bacterial Fatty-Acid Synthesis Pathway: Towards the Development of Slow-Onset Inhibitors and the Characterisation of Protein-Protein Interactions”

is the result of my own work. I did not receive any help or support from commercial consultants. All sources and / or materials applied are listed and specified in the thesis.

Furthermore, I confirm that this thesis has not yet been submitted as part of another examination process neither in identical nor in similar form.

Place, Date

Signature

EIDESSTÄTTLICHE ERKLÄRUNG

Hiermit erkläre ich an Eides statt, die Dissertation

„Die bakterielle Fettsäurebiosynthese als Zielobjekt zur Entwicklung langsam bindender Inhibitoren und zur Charakterisierung von Protein-Protein-Wechselwirkungen“

eigenständig, d.h. insbesondere selbständig und ohne Hilfe eines kommerziellen Promotionsberaters, angefertigt und keine anderen als die von mir angegebenen Quellen und Hilfsmittel verwendet zu haben.

Ich erkläre außerdem, dass die Dissertation weder in gleicher noch in ähnlicher Form bereits in einem anderen Prüfungsverfahren vorgelegen hat.

Ort, Datum

Unterschrift